

DOCUMENTATION PAGE

Form Approved
ANSI Z39-18



PB96-191465

JULY 8, 1996

FINAL

1992-1996

SYNTHESIS OF PASSIVE AND ACTIVE BRACING
IN ACTIVE STRUCTURES

G

NSF

MSS-9207252

CHRIS P. PANTELIDES

SHYH-RONG TZAN

UNIVERSITY OF UTAH
DEPT. OF CIVIL & ENVIRONMENTAL ENGR.
3220 MEB
SALT LAKE CITY, UT 84112

UUCE 96-01

KEN CHONG
NATIONAL SCIENCE FOUNDATION
4201 WILSON BLVD.
RM 545, ARLINGTON, VA 22230

SEE ATTACHED

STRUCTURES, CONTROL, EARTHQUAKES, OPTIMIZATION

15. NUMBER OF PAGES

292

16. PRICE CODE

UNCLASSIFIED

UNCLASSIFIED

UNCLASSIFIED

20. LIMITATION OF ABSTRACT

UL

Page Intentionally Left Blank



PB96-191465

**SYNTHESIS OF PASSIVE AND ACTIVE BRACING
IN ACTIVE STRUCTURES**

**Prepared for
National Science Foundation**

July 8, 1996

by

Chris P. Pantelides, Ph.D., P.E.

Shyh-Rong Tzan, Ph.D.

**Earthquake Research Program
Research Report UUCE 96-01
Department of Civil and Environment Engineering
University of Utah
Salt Lake City, Utah 84112**



PB96-191465

**SYNTHESIS OF PASSIVE AND ACTIVE BRACING
IN ACTIVE STRUCTURES**

**Prepared for
National Science Foundation**

May 22, 1996

by

Chris P. Pantelides, Ph.D., P.E.

Shyh-Rong Tzan, Ph.D.

**Earthquake Research Program
Research Report UUCE 96-01
Department of Civil and Environment Engineering
University of Utah
Salt Lake City, Utah 84112**

**PROTECTED UNDER INTERNATIONAL COPYRIGHT
ALL RIGHTS RESERVED.
NATIONAL TECHNICAL INFORMATION SERVICE
U.S. DEPARTMENT OF COMMERCE**

ABSTRACT

The seismic resistance achieved by optimizing the design of the conventional members of a structure equipped with structural control is evaluated. Viscoelastic (VE) dampers and active bracing system (ABS) are studied individually, as well as combined as a hybrid system for their effectiveness in reducing the response of seismic structures. Two convex models are used to estimate the maximum response of structural systems subjected to uncertain seismic excitations. A reduction factor is used to calibrate the convex models for a specific excitation. An average reduction factor is also defined by averaging a set of excitation-specific reduction factors. The average reduction factor can be used for unknown excitations with an assumed energy bound and certain common earthquake characteristics.

A procedure for achieving the structural design of actively controlled structures has been developed. A modified iterated simulated annealing (MISA) method has been established for optimal design of structural systems under dynamic constraints. In performing the optimization, the MISA method employs two desirable features; the first is to achieve an automatic reduction of the search range, and the second is to perform sensitivity analysis for the design variables. The optimal designs using classical optimization methods for problems with dynamic constraints are compared with those of the MISA method.

The optimal design of the members of both conventional structures and structures equipped with active bracing systems, known as active structures, is presented for uncertain excitations. Three approaches are used for obtaining the optimal structural design: (1) analysis using the time-history of an actual ground motion (AR), (2) analysis using the global energy-bound convex model adjusted with an excitation-specific reduction factor (RGEB), and (3) analysis using the global energy-bound convex model adjusted with an average reduction factor (ARGEB) for a set of excitations with common characteristics. The optimal structures obtained using the RGEB and ARGEB convex models have different sizes for their conventional members from the optimal design based on a time-history analysis of the actual earthquake (AR).

Structures with different levels of inherent structural damping are used to investigate the merits of simultaneous structure-control optimization in the case where the viscoelastic dampers and active control systems are present. A comparison between optimal designs of structures with conventional members only, and active structures indicates that the latter are more efficient by combining the conventional and active members. Inelastic material behavior is modeled for both conventional and active structures. The effects of inelastic material behavior are investigated in terms of the structural response, control force requirements, energy balance of the structural systems and number of yield events.

ACKNOWLEDGMENT

This material is based upon work supported by the National Science Foundation under Grant No. MSS-9207252.

Any opinions, findings, and conclusions or recommendations expressed in this material are those of the authors and do not necessarily reflect the views of the National Science Foundation.

TABLE OF CONTENTS

ABSTRACT		i
ACKNOWLEDGMENT		iii
LIST OF FIGURES		viii
LIST OF TABLES		xviii
 Chapter		
1 INTRODUCTION		1
Literature Survey		4
Structural Control Systems		5
Convex Models		7
Optimization		9
Active Structures		12
Objectives		15
2 ALGORITHMS FOR PASSIVE/ACTIVE STRUCTURAL CONTROL		17
Passive Structural Control System		17
Existing Models		19
Proposed Model		21
Active Structural Control System		22
Existing Models		24
Lyapunov Method for Evaluating the Weighting Matrices		26
Drift Performance Index		27
Velocity Performance Index		28
3 CONVEX MODELS AND OPTIMAL STRUCTURAL DESIGN		30
Energy-bound Convex Models		30
Global Energy-bound Convex Model (GEB)		33
Local Energy-bound Convex Model (LEB)		36
Structural Optimization		38
Simulated Annealing Methods		41
Existing Methods		41
Modified Iterated Simulated Annealing Method (MISA)		43
4 DYNAMIC RESPONSE OF STRUCTURES WITH PASSIVE/ACTIVE STRUCTURAL CONTROL		50

Properties of Viscoelastic Damper	52
Frequency Dependence of VE Materials	52
Placement of VE dampers	64
Design of VE damper	74
Parametric Study of Active Bracing System	77
Performance of Different Control Algorithms	79
Combined Performance of VE Dampers and ABS	85
5 PERFORMANCE OF CONVEX MODELS	108
Energy-bound Convex Models and Dynamic Magnification Factor	108
Energy-bound Convex Models Adjusted with a Reduction Factor	115
Energy-bound Convex Models using Average Reduction Factor	129
ARGEB and ARLEB Convex Models for Impulse Excitations	133
ARGEB Convex Model for Past Earthquake Records	139
ARGEB Convex Model for Artificial Earthquakes	143
Global Energy-bound Convex Model for Active Structural Control	149
6 OPTIMAL DESIGN OF CONVENTIONAL AND ACTIVE STRUCTURES	153
Structural Optimization	153
Ten-bar Truss with Static Constraints	154
Two-story Frame with Dynamic Constraints	159
Ten-story Frame with Dynamic Constraints	172
Optimal Structures using Convex Models	181
Optimal Design of Conventional Structure for El-Centro Earthquake ..	182
Optimal Design of Conventional Structure for San Fernando Earthquake	187
Optimal Design of Conventional Structure for Artificial Earthquake ...	191
Optimal Design of Active Structure for El-Centro Earthquake	191
Optimal Design of Active Structure for San Fernando and Artificial Earthquakes	197
Optimal Designs of Active Structures	200
7 INELASTIC ANALYSIS OF CONVENTIONAL AND ACTIVE STRUCTURES	210
Inelastic Analysis of Framed Structures	210
Conventional Structures	213
Active Structures	221
8 CONCLUSIONS	239
 Appendices	
A. ACTIVE CONTROL ALGORITHMS	244
B. RUNGE-KUTTA METHOD	254
C. DIRECT STIFFNESS METHOD AND GUYAN REDUCTION	258
D. SENSITIVITY ANALYSIS FOR STRUCTURAL DESIGN	264

E. CLASSICAL OPTIMIZATION METHODS	267
F. MISA PROGRAM	277
REFERENCES	283

LIST OF FIGURES

<u>Figure</u>	<u>Page</u>
2.1 Typical viscoelastic damper construction	18
2.2 Active bracing system	23
3.1 Annealing procedure for optimization of structural design	44
3.2 Automatic reduction of the search range used in the present method	47
4.1 Numerical examples: (a) eight-story shear building, (b) ten-story frame, and (c) five-story shear building	51
4.2 Effective damping ratio of the eight-story shear building equipped with one VE damper on the first floor for different excitation frequencies: (a) 1st mode and (b) 2nd mode; - - - - = constant values of shear storage and loss moduli, ——— = varying values using equation (2.4), ··>···· = proposed method using equation (2.5)	54
4.3 Effective damping ratio of the ten-story frame equipped with one VE damper on the first floor for different excitation frequencies: (a) 1st mode and (b) 2nd mode; - - - - = constant values of shear storage and loss moduli, ——— = varying values using equation (2.4), ··>···· = proposed method using equation (2.5)	55
4.4 Maximum responses of the eight-story shear building equipped with one VE damper on the first floor for a sine wave excitation with varying frequency: (a) displacement and (b) drift; - - - - = constant values of shear storage and loss moduli, ——— = varying values using equation (2.4), ····· = proposed method using equation (2.5)	56
4.4 (Continued) (c) velocity and (d) acceleration; - - - - = constant values of shear storage and loss moduli, ——— = varying values using equation (2.4), ····· = proposed method using equation (2.5)	57

4.5	Maximum responses of the ten-story frame equipped with one VE damper on the first floor for a sine wave excitation with varying frequency: (a) displacement and (b) drift; - - - = constant values of shear storage and loss moduli, ——— = varying values using equation (2.4), ····· = proposed method using equation (2.5)	58
4.5	(Continued) (c) velocity and (d) acceleration; - - - = constant values of shear storage and loss moduli, ——— = varying values using equation (2.4), ····· = proposed method using equation (2.5)	59
4.6	Seismic excitations: (a) S00E record of the May 18, 1940 El-Centro earthquake (Imperial Valley record), and (b) S16E record of the Feb. 2, San Fernando earthquake (Pacoima Dam record)	62
4.7	Effective damping ratio as a function of the location and number of VE dampers for: (a) five-story shear building, (b) eight-story shear building, and (c) ten-story frame; \diamond = one VE damper on each floor, \square = all VE dampers on first floor	65
4.8	Seismic excitations: (a) N90W record of the Sep. 19, 1985 Mexico City earthquake (Cuerrero-Michoacan Coast record) and (b) S90N record of the Jan. 17, Northridge earthquake (Santa Monica station, City Hall record)	67
4.9	Spectrum amplitude of the excitation: (a) 1940 El-Centro earthquake shown in Figure 4.6(a), and (b) 1971 San Fernando earthquake shown in Figure 4.6(b)	68
4.9	(Continued) (c) 1985 Mexico City earthquake shown in Figure 4.8(a), and (d) 1994 Northridge earthquake shown in Figure 4.8(b)	69
4.10	Displacement reduction for the structure with one VE damper on the first floor: (a) five-story shear building, (b) eight-story shear building, and (c) ten-story frame; \boxtimes = Northridge earthquake, \blacksquare = Mexico City earthquake, \square = San Fernando earthquake, \boxminus = El-Centro earthquake	70
4.11	Comparison of: (a) displacement, (b) drift, (c) velocity, and (d) acceleration of eight-story building for El-Centro earthquake; \ominus = uncontrolled ($\xi_1 = 2.50\%$), \boxminus = AC on the first floor ($\xi_1 = 7.14\%$), \blacktriangle = VE on the three lower floors ($\xi_1 = 7.04\%$), \blacklozenge = VE on the four lower floors ($\xi_1 = 8.4\%$)	87

4.12	Comparison of: (a) displacement, (b) drift, (c) velocity, and (d) acceleration of eight-story building for San Fernando earthquake; \ominus = uncontrolled ($\xi_1 = 2.50\%$), \boxminus = AC on the first floor ($\xi_1 = 7.14\%$), \boxplus = VE on the three lower floors ($\xi_1 = 7.04\%$), \boxtimes = VE on the four lower floors ($\xi_1 = 8.14\%$)	88
4.13	Comparison of: (a) displacement, (b) drift, (c) velocity, and (d) acceleration of eight-story building for Mexico City earthquake; \ominus = uncontrolled ($\xi_1 = 2.50\%$), \boxminus = AC on the first floor ($\xi_1 = 7.14\%$), \boxplus = VE on the three lower floors ($\xi_1 = 7.04\%$), \boxtimes = VE on the four lower floors ($\xi_1 = 8.14\%$)	89
4.14	Comparison of: (a) displacement, (b) drift, (c) velocity, and (d) acceleration of eight-story building for Northridge earthquake; \ominus = uncontrolled ($\xi_1 = 2.50\%$), \boxminus = AC on the first floor ($\xi_1 = 7.14\%$), \boxplus = VE on the three lower floors ($\xi_1 = 7.04\%$), \boxtimes = VE on the four lower floors ($\xi_1 = 8.14\%$)	90
4.15	Eight-story shear building with six different arrangements of ABS and VE dampers	92
4.16	Comparison of: (a) displacement, (b) drift, (c) velocity, and (d) acceleration of eight-story building for El-Centro earthquake; \ominus = uncontrolled, \boxminus = Case (1) of Figure 4.15, \boxplus = Case (2) of Figure 4.15, \boxtimes = Case (3) of Figure 4.15	94
4.17	Comparison of: (a) displacement, (b) drift, (c) velocity, and (d) acceleration of eight-story building for San Fernando earthquake; \ominus = uncontrolled, \boxminus = Case (1) of Figure 4.15, \boxplus = Case (2) of Figure 4.15, \boxtimes = Case (3) of Figure 4.15	95
4.18	Comparison of: (a) displacement, (b) drift, (c) velocity, and (d) acceleration of eight-story building for Mexico City earthquake; \ominus = uncontrolled, \boxminus = Case (1) of Figure 4.15, \boxplus = Case (2) of Figure 4.15, \boxtimes = Case (3) of Figure 4.15	96
4.19	Comparison of: (a) displacement, (b) drift, (c) velocity, and (d) acceleration of eight-story building for Northridge earthquake; \ominus = uncontrolled, \boxminus = Case (1) of Figure 4.15, \boxplus = Case (2) of Figure 4.15, \boxtimes = Case (3) of Figure 4.15	97
4.20	Maximum control force for: (a) 1940 El-Centro earthquake and (b) 1971 San Fernando earthquake; \boxtimes = 1st floor control force, \boxplus = 2nd floor control force	98

4.20	(Continued) (c) 1985 Mexico City earthquake and (d) 1994 Northridge earthquake; \boxtimes = 1st floor control force, \boxminus = 2nd floor control force	99
4.21	Energy time-history for 1940 El-Centro earthquake: (a) without an ABS or VE damper, (b) one ABS on the first floor	103
4.21	(Continued) (c) one ABS and one VE damper on the first floor, (d) one ABS on the first floor and one VE damper on the first and second floors	104
4.22	Comparison of kinetic energy for: (a) 1940 El-Centro earthquake and (b) 1971 San Fernando earthquake; = without control, _____ = one ABS and one VE damper on the first floor	105
4.22	(Continued) (c) 1985 Mexico City earthquake and (d) 1994 Northridge earthquake; = without control, _____ = one ABS and one VE damper on the first floor	106
5.1	Dynamic magnification factor for rectangular impulse: _____ = actual response, = global energy-bound convex model, ----- = local energy-bound convex model	110
5.2	Eight impulses	110
5.3	Dynamic magnification factor for sine-wave impulse: _____ = actual response, = global energy-bound convex model, ----- = local energy-bound convex model	111
5.4	Dynamic magnification factor for impulse \odot of Figure 5.2: _____ = actual response, = global energy-bound convex model, ----- = local energy-bound convex model	111
5.5	Displacement time-history of a SDOF system with damping level of 5 % of critical for the 1940 El-Centro earthquake; _____ = actual record (AR), - - - - = global energy-bound convex model (GEB), = local energy-bound convex model (LEB)	114
5.6	Displacement time-history of a SDOF system with damping level of 10 % of critical for the 1940 El-Centro earthquake; _____ = actual record (AR), = global energy-bound convex model (GEB), - - - - = local energy-bound convex model (LEB)	114
5.7	Global energy-bound reduction factor of the rectangular impulsive excitation: (a) displacement, (b) velocity, and (c) acceleration; \ominus = damping level of 2 % of critical, \boxminus = damping level of 6 % of critical, \boxplus = damping level of 10 % of critical	117

5.8	Global energy-bound reduction factor of the two-peak impulsive excitation: (a) displacement, (b) velocity, and (c) acceleration; \ominus = damping level of 2 % of critical, \boxminus = damping level of 6 % of critical, \blacktriangleleft = damping level of 10 % of critical	118
5.9	Global energy-bound reduction factor of the 1940 El-Centro earthquake: (a) displacement, (b) velocity, and (c) acceleration; \ominus = damping level of 2 % of critical, \boxminus = damping level of 6 % of critical, \blacktriangleleft = damping level of 10 % of critical	119
5.10	Global energy-bound reduction factor of the 1971 San Fernando earthquake: (a) displacement, (b) velocity, and (c) acceleration; \ominus = damping level of 2 % of critical, \boxminus = damping level of 6 % of critical, \blacktriangleleft = damping level of 10 % of critical	120
5.11	Local energy-bound reduction factor of the rectangular impulse: (a) displacement, (b) velocity, and (c) acceleration; \ominus = damping level of 2 % of critical, \boxminus = damping level of 6 % of critical, \blacktriangleleft = damping level of 10 % of critical	121
5.12	Comparison of the global energy-bound reduction factor for the rectangular impulse: (a) data-base, and (b) calibration curve	124
5.13	Comparison of the local energy-bound reduction factor for the rectangular impulse: (a) data-base, and (b) calibration curve	125
5.14	Ten-story frame	127
5.15	Average reduction factor for global energy-bound of impulsive excitations of Figure 5.2: (a) displacement, (b) velocity, and (c) acceleration; \ominus = damping level of 2 % of critical, \boxminus = damping level of 6 % of critical, \blacktriangleleft = damping level of 10 % of critical	132
5.16	Maximum dynamic response of the eight-story building to a rectangular impulse: (a) velocity, (b) acceleration; \ominus = actual response (AR), \boxminus = GEB convex model, \blacktriangleleft = RGEB convex model	136
5.17	Maximum dynamic response of the eight-story building to a rectangular impulse: (a) displacement, (b) velocity, (c) acceleration; \ominus = actual response (AR), \boxminus = RGEB convex model, \blacktriangleleft = ARGEB convex model	138
5.18	Artificial earthquakes of Group 1: (a) spectrum, (b)-(g) artificial earthquakes	144

5.19	Artificial earthquakes of Group 2: (a) spectrum, (b)-(g) artificial earthquakes	146
5.20	Artificial earthquakes of Group 3: (a) spectrum, (b)-(g) artificial earthquakes	147
5.21	Artificial earthquake using the spectrum of Figure 5.19(a)	150
5.22	Comparison of the predicted response with the actual record: (a) displacement, (b) velocity; —●— = actual record (AR), —□— = estimated results obtained by the ARGEB convex model of artificial earthquakes in Group 2	150
6.1	Ten-bar truss: (a) dimensions and degrees-of-freedom, (b) loading and design variables	155
6.2	Iteration history for five-variable optimal design of ten-bar truss using the ISA method (-----) and the modified iterated simulated annealing (MISA) method (————)	157
6.3	Two-story frame: (a) dimensions and degrees-of-freedom, (b) loading and design variables	160
6.4	Artificial excitations using an amplitude envelope function: (a) artificial earthquake I (equation (6.2b)), (b) artificial earthquake II (equation (6.2c)) .	161
6.5	Time-dependent variation of amplitude envelope function (equation (6.2c)) for artificial earthquake	163
6.6	Disjoint feasible region of the two-story frame subjected to artificial earthquake I; —2.54 — = second floor drift constraint, ----150---- = combined stress constraint in columns of the first floor	165
6.7	Disjoint feasible region of the two-story frame subjected to artificial earthquake II; —2.54 — = second floor drift constraint, ----150---- = combined stress constraint in columns of the first floor	169
6.8	Iteration history for four-variable optimal design of two-story frame using the MISA method	173
6.9	Ten-story frame: (a) dimensions and degrees-of-freedom, (b) loading and design variables	174
6.10	Feasible region of ten-story frame constrained by drift on: (a) first, (b) third, (c) fourth, and (d) fifth floors	175

6.11	Feasible region of ten-story frame constrained by combined stress in columns of the first floor	177
6.12	Disjoint feasible of the ten-story frame constrained by the drift constraint on the third, fourth, and fifth floors and the combined stress constraint in columns of the first floor	178
6.13	Artificial earthquake IV using the amplitude envelope function of equation (6.2c)	185
6.14	Interstory drift of the ten-story frame: (a) AR design for 1940 El-Centro of Table 6.11 (Building I) and (b) ARGEb convex model design of Table 6.11 (Building II); \boxtimes = artificial earthquake shown in Figure 6.13, \boxplus = scaled record of 1994 Northridge earthquake, \blacksquare = scaled record of 1971 San Fernando earthquake, \square = 1940 El-Centro earthquake record	186
6.15	Interstory drift of the ten-story frame: (a) AR design for 1971 San Fernando of Table 6.13 (Building III) and (b) ARGEb convex model design of Table 6.13 (Building IV); \boxplus = scaled record of 1994 Northridge earthquake, \boxtimes = 1971 San Fernando earthquake record	190
6.16	Interstory drift of the ten-story frame with two ABS: (a) AR design for 1940 El-Centro of Table 6.16 (Building V) and (b) ARGEb convex model design of Table 6.16 (Building VI); \boxtimes = artificial earthquake shown in Figure 6.13, \boxplus = scaled record of 1994 Northridge earthquake, \blacksquare = scaled record of 1971 San Fernando earthquake, \square = 1940 El-Centro earthquake record	195
6.17	Maximum control force of the ten-story frame with two ABS: (a) Building V (AR analysis for 1940 El-Centro) and (b) Building VI (ARGEb convex model); \boxtimes = artificial earthquake shown in Figure 6.13, \boxplus = scaled record of 1994 Northridge earthquake, \blacksquare = scaled record of 1971 San Fernando earthquake, \square = 1940 El-Centro earthquake record	196
6.18	Comparison of the effective damping vs. optimal volume: \blacklozenge = conventional structure, \ominus = active structure with two ABS	206
6.19	Comparison of the effective damping vs. optimal volume: \blacklozenge = conventional structure, \ominus = active structure with two VE dampers	206
6.20	Comparison of the effective damping vs. optimal volume: \blacklozenge = conventional structure, \ominus = active structure with one ABS and one VE ..	207
6.21	Comparison of the effective damping vs. optimal volume of active structures: \times = two ABS, \blacklozenge = two VE dampers, \ominus = one ABS and one VE damper	207

6.22	Additional damping of the active structures; ■ = two ABS (Case 1), □ = two VE dampers (Case 2), ▣ = one ABS and one VE damper (Case 3)	209
6.23	Reduction of the structural volume; ■ = two ABS (Case 1), □ = two VE dampers (Case 2), ▣ = one ABS and one VE damper (Case 3)	209
7.1	Yield surface and sign convention for moment	211
7.2	Bilinear model for the inelastic structure; (a) parallel components, (b) moment-curvature relationship	212
7.3	Maximum displacement of the ten-story frame for the 1971 San Fernando earthquake; (a) elastic analysis, (b) inelastic analysis	215
7.4	Maximum drift of the ten-story frame for the 1971 San Fernando earthquake; (a) elastic analysis, (b) inelastic analysis	215
7.5	Maximum velocity of the ten-story frame for the 1971 San Fernando earthquake; (a) elastic analysis, (b) inelastic analysis	216
7.6	Maximum acceleration of the ten-story frame for the 1971 San Fernando earthquake; (a) elastic analysis, (b) inelastic analysis	216
7.7	Maximum displacement of the ten-story frame for the scaled record of El-Centro earthquake; (a) elastic analysis, (b) inelastic analysis	217
7.8	Maximum drift of the ten-story frame for the scaled record of El-Centro earthquake; (a) elastic analysis, (b) inelastic analysis	217
7.9	Maximum velocity of the ten-story frame for the scaled record of El-Centro earthquake; (a) elastic analysis, (b) inelastic analysis	218
7.10	Maximum acceleration of the ten-story frame for the scaled record of El-Centro earthquake; (a) elastic analysis, (b) inelastic analysis	218
7.11	Maximum displacement of the ten-story frame for the scaled record of Northridge earthquake; (a) elastic analysis, (b) inelastic analysis	219
7.12	Maximum drift of the ten-story frame for the scaled record of Northridge earthquake; (a) elastic analysis, (b) inelastic analysis	219
7.13	Maximum velocity of the ten-story frame for the scaled record of Northridge earthquake; (a) elastic analysis, (b) inelastic analysis	220

7.14	Maximum acceleration of the ten-story frame for the scaled record of Northridge earthquake; (a) elastic analysis, (b) inelastic analysis	220
7.15	Displacement time-history of the 10th floor of the structure: (a) 1971 San Fernando earthquake, (b) scaled record of 1940 El-Centro earthquake, (c) scaled record of 1994 Northridge earthquake; = elastic analysis, = inelastic analysis	222
7.16	Permanent deformation of the elastic-plastic structure; (a) the 1971 San Fernando earthquake, (b) the scaled record of the 1940 El-Centro earthquake, (c) the scaled record of the 1994 Northridge earthquake	223
7.17	Energy time-history for the 1971 San Fernando earthquake: (a) elastic analysis; (b) inelastic analysis	224
7.18	Energy time-history for the scaled record of the 1940 El-Centro earthquake: (a) elastic analysis; (b) inelastic analysis	225
7.19	Energy time-history for the scaled record of the 1994 Northridge earthquake: (a) elastic analysis; (b) inelastic analysis	226
7.20	Yield events of the inelastic ten-story frame subjected to the actual record of 1971 San Fernando earthquake: (a) no control, (b) structure with two ABS structural controls, (c) structure with four ABS structural control	228
7.21	Yield events occurring in the beam members of the inelastic ten-story frame subjected to the actual record of 1971 San Fernando earthquake: (a) no control, (b) structure with two ABS structural controls, (c) structure with four ABS structural control	230
7.22	Yield events occurring in the column members of the inelastic ten-story frame subjected to the actual record of 1971 San Fernando earthquake: (a) no control, (b) structure with two ABS structural controls, (c) structure with four ABS structural control	231
7.23	Yield events of the inelastic ten-story frame subjected to the scaled record of 1940 El-Centro earthquake: (a) no control, (b) structure with two ABS structural controls, (c) structure with four ABS structural control	232
7.24	Yield events occurring in the beam members of the inelastic ten-story frame subjected to the scaled record of 1940 El-Centro earthquake: (a) no control, (b) structure with two ABS structural controls, (c) structure with four ABS structural control	233

7.25	Yield events occurring in the column members of the inelastic ten-story frame subjected to the scaled record of 1940 El-Centro earthquake: (a) no control, (b) structure with two ABS structural controls, (c) structure with four ABS structural control	234
7.26	Yield events of the inelastic ten-story frame subjected to the scaled record of 1994 Northridge earthquake: (a) no control, (b) structure with two ABS structural controls, (c) structure with four ABS structural control	235
7.27	Yield events occurring in the beam members of the inelastic ten-story frame subjected to the actual record of 1971 San Fernando earthquake: (a) no control, (b) structure with two ABS structural controls, (c) structure with four ABS structural control	236
7.28	Yield events occurring in the column members of the inelastic ten-story frame subjected to the scaled record of 1994 Northridge earthquake: (a) no control, (b) structure with two ABS structural controls, (c) structure with four ABS structural control	237
C.1	Local freedom numbers for: (a) truss and (b) frame elements	260
F.1	Execution order of the MISA program	279

LIST OF TABLES

<u>Table</u>	<u>Page</u>
3.1 Comparison of the existing annealing methods and the proposed method	46
4.1 Maximum response for structures equipped with one VE damper on the first floor subjected to a sinusoidal base acceleration	60
4.2 Maximum response for structures equipped with one VE damper on the first floor subjected to a multiple-frequency base acceleration	61
4.3 Maximum response for structures equipped with one VE damper on the first floor subjected to the 1940 El-Centro earthquake	63
4.4 Maximum response for structures equipped with one VE damper on the first floor subjected to the 1971 San Fernando earthquake	63
4.5 Top floor displacement as compared to the uncontrolled response with the addition of VE dampers	71
4.6 Top floor velocity as compared to the uncontrolled response with the addition of VE dampers	72
4.7 Top floor acceleration as compared to the uncontrolled response with the addition of VE dampers	73
4.8 Optimal designs for the minimum cross-sectional area of VE damper for the eight-story shear building (m ²)	75
4.9 Optimal designs for the minimum cross-sectional area of VE damper for the eight-story shear building with minimum side constraint equal to zero (m ²) ..	76
4.10 Optimal designs for the minimum cross-sectional area of VE damper for the ten-story frame (m ²)	76
4.11 Optimal design of VE dampers for an expected damping level	78
4.12 Comparison of the control forces, damping ratios, and weighting matrices for the 1940 El-Centro earthquake record	80
4.13 Lyapunov matrix for the eight-story building equipped with an ABS on the first floor	81
4.14 Lyapunov matrix for the eight-story building equipped with an ABS on the first and second floors	82

4.15	Comparison of the required maximum control force and number of controllers for 30 % reduction of the eighth floor displacement of the eight-story building	84
4.16	Effective damping ratio for the hybrid ABS-VE damper systems	93
4.17	Maximum absolute energy distribution for the hybrid ABS-VE damper systems	102
5.1	Comparison of energy-bound convex models with actual record at the transition point	112
5.2	Member sizes for ten-story frame	128
5.3	Maximum response of the ten-story frame for the 1940 El-Centro earthquake record	128
5.4	Displacement response of the eight-story building for impulses with the same global energy-bound	134
5.5	Displacement reduction factor for the RGEB and ARGEB convex models for each mode for the eight-story shear building	134
5.6	Displacement response of the eight-story building for impulses with the same local energy-bound	140
5.7	Displacement reduction factor for the RLEB and ARLEB convex models for each mode for the eight-story shear building	140
5.8	Past earthquake records used to investigate the ARGEB convex model	141
5.9	Subsets of earthquakes used in the ARGEB convex model	141
5.10	Response ratio for maximum response using the RGEB and the ARGEB convex models for past earthquake records	142
5.11	Artificial earthquakes used in the ARGEB convex model	148
5.12	Response ratio for maximum response using the RGEB and the ARGEB convex models for artificial earthquakes	148
5.13	Maximum response of the ten-story frame with two ABS for the 1940 El-Centro earthquake record	152
6.1	Five-variable optimal design of ten-bar truss with static constraints	158
6.2	Ten-variable optimal design of ten-bar truss with static constraints	158
6.3	Optimal design of the two-story frame subjected to artificial earthquake I	166
6.4	Results for two-story frame subjected to artificial earthquake I for different initial designs	167

6.5	Optimal design of the two-story frame subjected to artificial earthquake II ..	170
6.6	Results for two-story frame subjected to artificial earthquake II for different initial designs	170
6.7	Optimal design of two-story frame for the 1940 El-Centro earthquake	171
6.8	Two-variable optimal design of ten-story frame subjected to the 1940 El-Centro earthquake	179
6.9	Eight-variable optimal design of ten-story frame subjected to the 1940 El-Centro earthquake	179
6.10	Results for eight-variable ten-story frame for different initial designs	180
6.11	The optimal design of the ten-story conventional structure subjected to the 1940 El-Centro earthquake	183
6.12	Peak acceleration and global energy-bound of the excitations for verifying the structure designed by the ARGEB convex model of subset S7 of Table 5.9	184
6.13	The optimal design of the ten-story conventional structure subjected to the 1971 San Fernando earthquake	188
6.14	Peak acceleration and global energy-bound of the excitations for verifying the structure designed by the ARGEB convex model of subset S6 of Table 5.9	189
6.15	The optimal design of the ten-story conventional structure subjected to the artificial earthquake III	192
6.16	The optimal design of the ten-story active structure subjected to the 1940 El-Centro earthquake	194
6.17	The optimal design of the ten-story active structure subjected to the 1971 San Fernando earthquake	198
6.18	The optimal design of the ten-story active structure subjected to the artificial earthquake III	199
6.19	Optimal designs of the ten-story frame with different levels of the inherent structural damping	202
6.20	Optimal designs of ten-story frame with two ABS	203
6.21	Optimal designs of ten-story frame with two VE dampers	204
6.22	Optimal designs of ten-story frame with one ABS and one VE damper	205
7.1	Moments of inertia and yield moments of the structural elements of Building V in Table 6.15	213

7.2	Peak acceleration and global energy-bound of the excitations for investigating the inelastic behavior of Building V in Table 6.15	214
7.3	Average response ratios as compared to the uncontrolled structure with the addition of active bracing systems	227
7.4	Yielding events of the inelastic structure equipped with a certain number of active bracing systems	238
F.1	Input order for required data in the MISA program	278
F.2	Description for input data in the MISA program	281

CHAPTER 1

INTRODUCTION

The criteria for designing buildings and other structures are based on the requirements of safety, serviceability, and resistance to self-straining forces. Safety of structures is ensured by supporting all loads, including gravity and lateral loads, to avoid exceeding the allowable stresses for the materials of construction in the structural members and connections. Serviceability of structural systems and their components is achieved by providing adequate stiffness, to limit transverse deflections, lateral drift and vibration. Provision always needs to be made for self-straining forces arising from assumed differential settlements of foundations, and dimensional changes such as temperature differentials, moisture expansion, shrinkage, and creep. In addition, structures capable of supporting safely all conventional loads may still suffer local damage, that is, the loss of load resistance in an element or small portion of the structure.

The most common method of achieving structural integrity is through an arrangement of the structural elements that provides stability to the entire structural system. Basically, such an arrangement consists of the provision of sufficient continuity and energy-absorbing capability in the components and connections of the structure. This scheme provides a means to transfer loads from any locally damaged region to adjacent

regions capable of resisting these loads without collapse. The designing concepts and guidelines for the provision of general structural integrity are outlined in the commentary of the ASCE 7-95 Standard (1996).

Until recently, the structural integrity of buildings, bridges, and other constructed facilities has been achieved by building structures that rely on their mass and solidity to resist outside forces. The drawback of this kind of design is that these structures do not have the ability to adapt to extraordinary dynamic loads. With the need for structural integrity other factors are currently gaining prominence, such as increased flexibility, increased safety levels and performance requirements, and demands for better utilization of material and lower cost. As a result, new ideas for structural integrity and structural motion control have been developed. These new inventions can be divided into two main categories: the passive control devices, such as friction dampers, viscoelastic (VE) dampers and passive tuned mass dampers, and active control (AC) devices such as active mass dampers, pulse generators, variable stiffness devices, and active bracing systems.

VE dampers dissipate energy in the form of heat or friction. They are usually used in large numbers for more effectiveness. Initially, VE dampers were mainly introduced in the design of buildings to reduce floor accelerations due to windstorms within acceptable levels of human comfort. The twin towers of the World Trade Center in New York have 10,000 VE dampers installed throughout the height of each of the towers which were installed in 1969 (Wiesner, 1986). In 1982, a passive damping system was designed for the Columbia Center in Seattle, Washington with 260 VE dampers. The VE dampers were located alongside the main diagonal bracing members in the core of the building, and were larger than those used at the World Trade Center, hence a smaller number were

required. VE dampers have been considered lately for seismic structures.

An AC system uses a microcomputer that executes the control algorithm and controls the motion of the hydraulic system to supply reasonable control forces for the structure. In a narrow eleven-story building, which is 13×43 ft in plan and 108 ft high, two active mass drivers were installed on the top floor by Kajima Corporation in Japan in 1990 to control lateral and torsional vibrations (ENR, 1990). Kajima's system has worked successfully several times already during recent earthquakes that occurred in Japan.

Viscoelastic dampers and the active bracing system (ABS) have been shown to be effective in reducing the seismic response of both reinforced concrete and structural steel frames. The performance of the systems can be predicted adequately through simplified analytical procedures. The addition of VE dampers could assist the AC system in improving the damping ability of the structure, which should reduce the required control forces and the cost of the AC system. On the other hand, the addition of the AC system could improve the velocity performance of the VE dampers and reduce the possibility of shear failure of the viscoelastic material in case of large deformations. In the present work, VE dampers and the ABS are studied together as a hybrid system for their combined effectiveness in reducing the response of seismic structures.

Integration of passive and active devices with conventional structural systems at the design stage has not gained much attention. Soong and Manolis (1987) have envisaged a future type of structure, an active structure, having two types of load resisting members : the traditional passive members that are designed to support static design loads, and active members that will assist the structure in resisting dynamic loads.

The U. S. National Workshop on Structural Control Research (1990) has acknowledged the need for the study of active structures by encouraging that more attention should be given to "smart structures" research, including active elements embedded within truss elements. In addition, it was recognized that hybrid control approaches which combine passive and active members seem to offer opportunities for improving performance over either active or passive approaches taken individually.

At the latest Applied Technology Council Conference (ATC 17-1, 1993) on seismic isolation, passive energy dissipation, and active control, the issue of hybrid control systems has been addressed. A system proposed by Riley et al. (1993) used a sliding base isolated structure which combines sliding bearings with active servo-hydraulic actuators operating in parallel with the sliding bearings. Experimental shake table tests have verified the concept. Another concept uses a hybrid control system which connects the rubber-bearing isolators of a base-isolated building to an actuator (Yang et al., 1993). Simulation results indicate that a nonlinear control method is effective for hybrid control of seismic structures equipped with such a system.

Literature Survey

Analysis of structural response to dynamic excitations such as shock, blast, wind, and earthquake is important in the design of structural systems. Examples include buildings under loads generated due to blast or explosion (Norris et al., 1959), dynamic loads in automobiles, traveling cranes, and other mobile machinery (Humar, 1990). Impulsive loads are also important in the field of earthquake engineering, where it is

assumed that the earthquake acceleration consists of a series of impulses distributed randomly in time (Housner and Jennings, 1964). In the following section, several fields of research are reviewed: (1) structural control systems including passive and active controls, (2) convex modeling for estimating the structural response, (3) optimization methods, and (4) active structures.

Structural Control Systems

The first study of the active control system for civil engineering structures was proposed by Yao (1972). Martin and Soong (1976) used a combination of structural flexibility concepts and classical optimal control theory to investigate real-time controllability, control implementation, and the economics of an active control system. The idea of combining structural optimization and structural control was conceived by Kirsch and Moses (1977). Their effort was directed towards either reduction of internal forces or minimization of the cross-sectional area of an actively controlled continuous beam, under a given loading condition.

In the area of active control systems for civil engineering structures, Yang (1982) has presented a transfer matrix approach for the application of the active mass damper and active tendon systems to seismic buildings. A random vibration analysis was formulated to obtain the frequency response of the structure. The transfer matrix approach has been applied to tall buildings in along-wind motion by Yang and Samali (1983). The performance of the active tendon and active mass damper systems was investigated. A methodology to analyze the problem by using a large number of modes has been presented. The transfer approach was used to determine the power spectral density of the

building response directly without computing the natural frequency.

Cheng and Pantelides (1986) have used the transfer matrix approach for simultaneous optimization and active control of tall buildings subjected to stochastic earthquake excitations. The control forces were generated by active tendons and active mass dampers. They attempted to optimize a performance index based on the weight and stiffness of the structure subject to structural response performance and control force constraints. Recently, several optimal control algorithms and control parameters for stable controllers were proposed (Yang et al., 1987, 1991, 1992a, 1992b, and Soong, 1990). In those studies, the instantaneous optimal open-loop, closed-loop, and open-closed-loop controls were presented for simplifying the traditional control algorithm of the linear quadratic regulator method. An energy consideration method and Lyapunov's criteria were used to define the control parameters for dynamic stability.

A full-scale test with an active bracing system on a five-story building was conducted by Soong et al. and Reinhorn et al. in 1991 and 1992 respectively. A procedure of designing a full-scale ABS for an earthquake resistant building was presented. The classic optimal control algorithm of linear quadratic regulator and two modified control algorithms were implemented.

The first building equipped with viscoelastic (VE) dampers was the twin towers of the World Trade Center, New York in 1969 for reduction of wind-load effects (Wiesner, 1986). The total damping of the building was determined from experimental work and found to be in the range of 2.5 to 3.0 % of critical damping. The properties of VE dampers and the evaluation of the VE damping effect for seismic structures were investigated by Zhang et al. in 1989. The stiffness and damping ratio of the VE dampers

were estimated using an energy-based theory. The advantage of the VE dampers in reducing the structural response was proven by numerical examples. In the meantime, structural response control by adding VE dampers was also presented by Zhang in 1990. The number, size, and optimal location of VE dampers for supporting the structure, and their effects on stiffness and damping ratio were studied by Zhang and Soong in 1992. The effect of temperature on VE dampers and the frequency dependent properties of VE dampers were investigated by Chang et al. (1992, 1994, and 1995) and by Kasai et al. (1993). A full-scale vibrational test of VE dampers was investigated by Lai et al. (1995).

The idea of combining VE dampers and active tendons in a structure for reduction of seismic response was presented by Pantelides in 1991. It was shown that the reduction of the structure's response can be achieved more efficiently with the above combination. The two systems could be used to resist various levels of intensity of external loads. The VE dampers could be used to resist windstorms or moderate earthquakes, while in a strong earthquake VE dampers and AC systems would be operating together.

Convex Models

The maximum response of structures to uncertain dynamic forces has been examined using probabilistic methods and Fourier amplitude spectrum envelope methods (Shinozuka, 1970). Another method uses limited deterministic information which characterizes the dynamic force (Drenick, 1970, 1973); a "critical excitation" is sought within the set of allowable dynamic forces such that it maximizes the structural response. Ben-Haim and Elishakoff (1990) have used convex models to represent uncertain dynamic forces in applications ranging from vehicle vibration to impact loading of shells. A convex

model of uncertainty is a set of functions specified by global characteristics such as input load functions, spectral properties, or functions of bounded energy. In effect, the convex model constrains uncertainty within a known bound.

A study of the dynamics and failure of a thin circular cylindrical shell with axisymmetric initial imperfections was performed by Elishakoff and Ben-Haim (1993). The most significant N Fourier coefficients of the initial imperfection profile were assumed to fall in an ellipsoidal set in N -dimensional Euclidean space. Convex methods have been compared to probabilistic methods in structural dynamics (Elishakoff, 1990). Convex models have also been used to model uncertain imperfections in multimode dynamic buckling of cylindrical shells under symmetric radial impulsive loads (Lindberg, 1992 a, b). The maximum possible buckling deformations for any imperfection within uniform bounds could be made comparable to the deformations from the probabilistic models at a reliability of 99.5 %. The convex model has the advantage that its numerical evaluation and interpretation is much simpler than the probabilistic model. In addition, the convex model solution provides a means for quality control of each and every shell by simply recording the uniform bounds from imperfection measurements. More recently, convex models have been used to model material uncertainty in the vibrations of viscoelastic structure (Elishakoff et al. 1994). A safety factor based on convex modelling has been proposed (Elishakoff, 1994). The probabilistic and convex modelling of acoustically excited structures have been studied by Elishakoff and Zhu (1994).

Convex models of uncertainty have been compared to stochastic models (Ben-Haim, 1994 a). It was found that analogous stochastic and convex models of uncertainty may lead to very different predictions in the range of the response of linear dynamic

systems with uncertain or time-varying disturbances. In a related development, convex models were used to evaluate the least time to failure of linear elastic systems with uncertain time-varying input (Ben-Haim, 1994 b). The uncertainty of the load history was represented by an ellipsoidal Fourier-bound convex model. Recently, Ben-Haim et al. (1994) have used several convex models to describe earthquake excitation uncertainties and to predict maximum structural responses to earthquake loads. The concept of convex modeling and its relationship with the theory of probability and fuzzy sets was described by Elishakoff (1995). A convex model of the base acceleration in terms of an upper bound was used along with linear programming to obtain the least favorable structural response.

Convex models specify uncertainties in the absence of detailed probabilistic information about the possible values of the variables of interest. The concept of convex modeling provides an alternative way of analysis of uncertainty when a limited amount of information is available. In addition, the subjective design decisions that result when using convex models to include uncertainty do not involve the element of chance.

Optimization

Modern literature on the topic of design optimization has seen an increase since the advent of the computer in the last half-century. Accurate and automated optimization methods originated from many fields as discussed by Haug and Arora (1979), and Schmit (1981). Optimization algorithms include: (1) mathematical programming methods, (2) optimality criteria methods, (3) approximation methods, and methods involving random sequences of designs.

Mathematical programming methods were described by Zoutendijk (1960). Finite

element analysis methods have been combined with mathematical programming algorithms for structural optimization (Gellatly and Gallagher, 1966). Optimization research in aerospace vehicle design, based on the combined technique of fully stressed design with mathematical programming, was used to design the size and materials of the structure in the 1970s (Heldenfels, 1973). Mathematical programming methods are currently used as tools for design synthesis (Vanderplaats, 1984a, 1984b).

Prager and Marcal (1971), Taylor (1969), Khot et al. (1979), and Kiusalaas (1972) have studied the optimal design of structures using the optimality criteria method. Procedures for finding the minimum weight design using the optimality criteria method were developed by Venkayya (1971), Gellatly and Berke (1971), Dobbs and Nelson (1976), and Fleury (1980).

Approximation methods are based on Taylor series truncation techniques of the objective and constraints, and include sequential linear programming (Kelley, 1960) and sequential quadratic programming (Vanderplaats, 1984b). Finally, methods involving random sequences of designs include genetic algorithms that emulate the natural selection process of nature and operate on a principle of survival of the fittest (Goldberg, 1989), and simulated annealing algorithms that emulate the reduction of the temperature in a bar that goes from a high to a low temperature (Kirkpatrick et al., 1983).

Optimization techniques have for the most part focused on structural optimization of systems with static constraints. When dynamic or time-varying constraints are imposed, the feasible region usually becomes disjoint. It is well known that when the feasible region is not convex, as in the case of disjoint spaces, some local minima may appear. This situation arises in structures undergoing dynamic loading. Cassis (1974) described this

phenomenon in detail for planar frames subjected to horizontal vibrations at their foundation. Estimates for the maximum number of disjoint feasible regions in the optimization of structural systems subjected to harmonic loads have also been developed (Johnson, 1976; Johnson et al., 1976; Mills-Curran and Schmit, 1985).

In the area of minimum weight design of damped structures subjected to dynamic loads, Cassis and Schmit (1976) discussed the disjoint nature of the feasible region for some combinations of constraints and loadings. The optimum structural design for dynamic response constraints with deterministic and nondeterministic loadings was presented by Yamakawa in 1984. The objective function was replaced by the dynamic response peaks using the root-mean-square values of selected displacements. A solution of the dynamic constraints problem based on upper bound approximations for the behavior constraints was developed by Mills-Curran and Schmit (1985). Dynamic stability constraints were included in a structure-controller synthesis by solving an approximate problem at each design iteration by Thomas and Schmit (1991).

The simulated annealing method involves random sequences of candidate designs with a probabilistic acceptance criterion of a better design at each subsequent iteration. Ackley (1987) developed the iterated simulated annealing method (ISA) and the stochastic hillclimbing method (SHC). In the SHC method the probability evaluation of a new design is held constant for the duration of the search. In the ISA method the probability evaluation of a new design starts at a high value of any adjustable parameter determining the acceptability of the design (temperature) and is reduced by a decay rate during the search.

The simulated annealing method was used by Salama et al. (1988) to determine the

optimal placement of discrete actuators and sensors for truss structures. The simulated annealing technique has been used for the optimal placement design of active/passive members of a truss structure by Chen et al. in 1991. The optimal design of steel frames with discrete member sizes using the simulated annealing method was developed by Balling in 1991. Simulated annealing is useful in combinatorial problems like the “traveling salesman” and circuit design problems (Nemhauser and Wolsey, 1988).

The simultaneous control and optimization problem has been studied by Komkov (1983) and Haftka et al. (1985 and 1986). It was shown that changes that are small in the configuration of the structure result in large changes in the control force requirements. In addition, they showed that the magnitude of the control forces in a system that has been optimized can be reduced by minor changes in stiffness or mass. Hale et al. (1985), suggest that the objective function to be optimized should contain a cost term that depends on the structural configuration. Their work produced plots of contours of different costs versus design parameters.

Active Structures

Active structures are structural systems which are composed of two types of load resisting members: (a) conventional static members such as beams and columns that are designed to support static design loads; (b) active members such as active mass dampers, active braces, or active variable stiffness members that are designed to resist dynamic loads such as those that a structure may experience in a strong earthquake. The concept of the active structure has important implications for the design of new structures in seismic regions that are to be equipped with active systems. The new structure must be

designed to utilize efficiently both the properties of the conventional static members and the dynamic properties of the active members. Recent progress in the area of active structural control has brought the application of active systems from theory and experiment to actual implementation (Kobori, 1994, and Housner et al., 1994).

The concept of the active structure was introduced by Soong and Manolis (1987). A structure was optimally designed in terms of minimizing structural cost while simultaneously the optimal control force for the active control system was obtained. The structural cost was expressed as the structural volume, the structural design variables were defined as the member areas, and the control variables were the optimal control forces. The general theory of optimal control of parametric systems was used to formulate the active structure optimization solution. The formulation resulted in a system of nonlinear coupled equations whose solution was accomplished iteratively using nonlinear programming and steepest descent methods.

Cha, Pitarresi, and Soong (1988) presented a numerical design procedure that optimizes the structural and controller parameters simultaneously. The problem was treated as one of the general theory of optimal control of parametric systems. The procedure searches and updates both the structural parameters and control parameters using a conjugate gradient technique, thus resulting in only one global optimization. Furthermore, the procedure is not limited to linear structural behavior or linear control laws. Numerical examples of active structures including a simple steel frame subjected to a sinusoidal base excitation, and a king-post bridge beam subjected to a moving load of constant magnitude and a given velocity have been carried out. It was demonstrated that the numerical procedure is effective in the design of the structural cross-section, the

required control force, as well as the placement of the active members.

The design of active structures was also addressed by Cheng and Pantelides (1988), and Pantelides (1990), who formulated the solution in two stages: (a) the optimal control forces were expressed in closed-form as implicit functions of the design variables (equivalent to the moments of inertia of the structural members); (b) the design variables were modified iteratively in order to minimize the structural volume with constraints imposed on the structural displacements, frequencies, and maximum level of control forces. The definition of the active structure can be extended to include in addition to the active control systems not only purely static members (Soong and Manolis, 1987), but also passive control members such as viscoelastic dampers (Tzan and Pantelides, 1994).

The design methods for active structures developed by Soong and Manolis (1987) and Pantelides (1990), use a time-dependent record of a past earthquake or an artificial earthquake acceleration as the excitation which is known in advance; the resulting computational effort required for the optimization process is rather costly. This situation is common in the structural optimization not only of active structures but also of traditional deterministic structures which are designed for earthquakes (Bhatti and Pister, 1981, Balling et al., 1983, and Truman and Petruska, 1992). The method proposed in this report seeks to replace the dynamic optimization of either traditional deterministic structures or active structures by a simpler static optimization. This can be achieved if the time-dependent displacements, member stresses, and control forces could be replaced by a maximum value representing an upper bound of the structural response to the earthquake.

Objectives

The seismic resistance achieved using structural control when the conventional structural members are optimized is evaluated in this research. The concept of an energy-bound convex model is utilized to obtain the maximum dynamic response and simplify the design for earthquake excitations. The convex model of the earthquake excitation is more general than a single earthquake record and that is the primary reason for utilizing it. A procedure for achieving the structural design of actively controlled structures is developed. The optimal design of a structure equipped with either an active bracing system or a set of viscoelastic dampers, known as an active structure, is investigated.

The following objectives are discussed in the indicated chapters of the report.

- (1) **Theory development:** The frequency dependent properties of stiffness and damping of the viscoelastic (VE) dampers, and control algorithms for the active bracing system (ABS) are studied in Chapter 2. The convex model, which is based on the assumption that the energy of the excitation is bounded, is derived in Chapter 3. The structural optimization procedure for the optimal design of conventional or active structures is described in Chapter 3.
- (2) **Theory verification:** The optimal material properties of VE dampers and control parameters of the active bracing system are investigated in Chapter 4. The effectiveness of reducing the response of seismic structures by combining the VE dampers and the ABS as a hybrid system is also studied. In Chapter 5, two convex models, the global energy-bound and the local energy-bound convex models, are used to estimate the maximum response of single-degree-of-freedom (SDOF) and multiple-degrees-of-freedom (MDOF) structural systems subjected to uncertain

dynamic excitations. A reduction factor is defined for a specific excitation by dividing the results obtained from the convex model by the maximum response obtained from the time-history analysis of the actual record. An average reduction factor, defined by averaging the reduction factors from a set of excitations with common characteristic, is developed for the uncertain excitations.

- (3) **Optimal structural design:** A modified annealing strategy is developed for structural optimization problems with dynamic constraints in Chapter 6. The optimal structural designs obtained using the method developed here are compared with classical optimization methods such as the state space method, the method of modified feasible directions, the sequential linear programming method, and the sequential quadratic programming method. The constraints obtained from both the time-history analysis of the actual record and the convex models are studied. The optimal design of a structure equipped with either a number of active bracing systems or a number of VE dampers, known as an active structure, is also investigated in Chapter 6. The structure is designed using past earthquake records as well as artificial earthquake excitations.
- (4) **Inelastic behavior of structures:** An inelastic analysis based on a bilinear elastic-plastic model is carried out for both conventional and active structures in Chapter 7. The behavior of the inelastic models is investigated in terms of the response, control force requirements, energy of the structural systems and number of yield events.
- (5) **Conclusions:** Finally, a brief summary and the conclusions learned from this study are presented in Chapter 8.

CHAPTER 2

ALGORITHMS FOR PASSIVE/ACTIVE STRUCTURAL CONTROL

A type of passive structural control system, the viscoelastic (VE) damper, is discussed in this chapter. The active bracing system (ABS) is considered as the active control system. The existing and proposed algorithms for both control systems are introduced in this chapter.

Passive Structural Control System

Passive structural control is defined as the result of using energy absorbing devices to reduce the structural response due to either wind or seismic loads. The passive control devices do not require external power. A viscoelastic (VE) damper for use in seismic structures is studied as a passive control system and is shown in Figure 2.1. A hysteretic damping model was used to describe the behavior of the VE damper in terms of constant damping (Zhang and Soong, 1992). The response of the VE damper is controlled by two variables - the excitation frequency and the ambient temperature. In the following section, the influence of the excitation frequency is considered while the temperature is assumed constant.

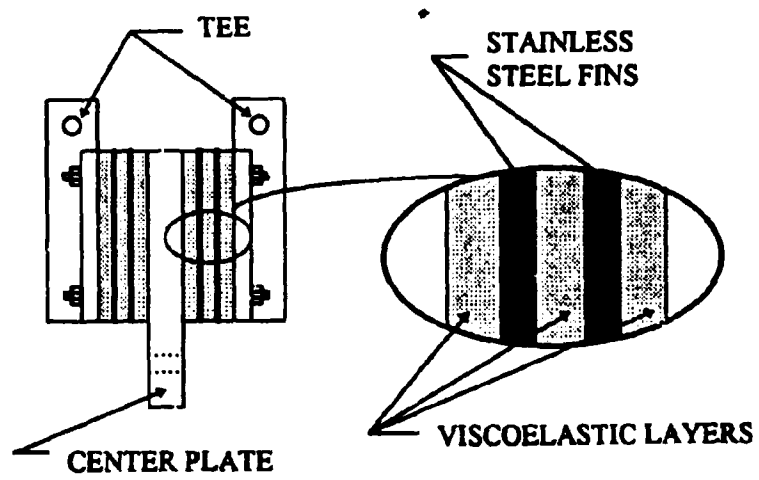


Figure 2.1 Typical viscoelastic damper construction

Existing Models

The viscoelastic (VE) damper can be considered as a kind of energy absorber which can be described as a combined device of a viscous damper and a spring unit. Therefore, the additional damping and stiffness due to the VE damper become an important topic in studying the material properties of the VE damper.

In previous research, the additional stiffness, k_d , due to the VE damper has been presented by Zhang (1990) as

$$k_d = \frac{\sqrt{G'^2 + G''^2}}{t} A \beta \quad (2.1)$$

where G' and G'' are the shear storage and shear loss moduli respectively, A and t are the cross-section area and the thickness of the VE damper; $\beta = \cos \theta$, and θ is the damper inclination with respect to the horizontal direction.

The added modal damping ratio due to the VE damper was proposed by Chang et al. (1992) and is defined as

$$\xi = \frac{\eta \phi^T K_d \phi}{2 \phi^T K_s \phi} = \frac{\eta}{2} \left(1 - \frac{\phi^T K_o \phi}{\phi^T K_s \phi} \right) \equiv \frac{\eta}{2} \left(1 - \frac{\omega_o^2}{\omega_s^2} \right) \quad (2.2)$$

where ϕ is the mode shape vector; K_o , K_s , and K_d are the stiffness matrices due to the damper-brace elastic stiffness, the stiffness matrix of the structure without VE dampers

and the stiffness of the structure with VE dampers, respectively; ω_0 and ω_1 are the natural frequency of the structure without and with VE dampers; $\eta = G^* / G'$ is the damping loss factor.

Equation (2.2) provides the calculation of the modal damping ratio for the structure whose inherent structural damping ratio is zero. A modified formula of the effective damping for the structure with nonzero inherent structural damping level was proposed by Chang et al. in 1994 as

$$\xi = \xi_0 \left(1 - \frac{\phi^T K_s \phi}{\phi^T K_s \phi} \right) + \frac{\eta \phi^T K_s \phi}{2 \phi^T K_s \phi} \quad (2.3)$$

where ξ_0 is the damping ratio of the structure without any VE dampers, and the other quantities were defined in equation (2.2).

The parameters G' and G^* are both frequency dependent, and a model which expresses these two parameters in terms of the excitation frequency was proposed by Kasai et al. (1993) as

$$G'(\omega) = G \frac{[1 + b\omega^\alpha \cos(\alpha\pi/2)][1 + a\omega^\alpha \cos(\alpha\pi/2)] + [ab\omega^{2\alpha} \sin^2(\alpha\pi/2)]}{[1 + a\omega^\alpha \cos(\alpha\pi/2)]^2 + [a\omega^\alpha \sin(\alpha\pi/2)]^2} \quad (2.4a)$$

$$G^*(\omega) = G \frac{[b\omega^\alpha \sin(\alpha\pi/2)][1 + a\omega^\alpha \cos(\alpha\pi/2)] - [a\omega^\alpha \sin(\alpha\pi/2)][1 + b\omega^\alpha \cos(\alpha\pi/2)]}{[1 + a\omega^\alpha \cos(\alpha\pi/2)]^2 + [a\omega^\alpha \sin(\alpha\pi/2)]^2} \quad (2.4b)$$

where ω is the excitation frequency, and a , b , G , and α are constants. It should be noted that in real earthquakes more than one excitation frequency is present; therefore G' and G'' can not be determined uniquely for design purposes by using equation (2.4).

Proposed Model

The well known situation of *resonance*, during which the excitation frequency equals the natural vibration frequency of the structure, should be prevented in structural design. In this section, multiple-degree-of-freedom (MDOF) structures are considered under seismic excitations and equations (2.1), (2.3), and (2.4) are modified for narrow-band frequency excitations. The VE damper contributions to the damping and stiffness are derived based on the values of parameters G' and G'' at the values of the natural frequencies of the structure.

A frequency-dependent calculation for the damping loss factor and the damping ratio is proposed as

$$\xi_j(\omega_{a,j}) = \xi_{a,j} \left(1 - \frac{\phi^T K_b \phi}{\phi^T K_s \phi} \right) + \frac{\eta(\omega_{a,j}) \phi^T K_b \phi}{2 \phi^T K_s \phi} \quad (2.5a)$$

$$\eta(\omega_{a,j}) = \frac{G''(\omega_{a,j})}{G'(\omega_{a,j})} \quad (2.5b)$$

where G' and G'' can be found by substituting $\omega_{a,j}$, the j th mode natural frequency of the structure, into equations (2.4a) and (2.4b) respectively. Thus, the damping contribution of the first n modes is uniquely determined through the damping ratio of equation (2.5) and is

considered invariant with respect to the remaining excitation frequencies. The stiffness of the VE damper can also be expressed as a function of structural frequencies as

$$k_d = \frac{\sqrt{G'(\omega_{s,1})^2 + G''(\omega_{s,1})^2}}{l} A \beta \quad (2.6)$$

It should be noted that only the fundamental mode parameters, $G'(\omega_{s,1})$ and $G''(\omega_{s,1})$ are used to determine the VE damper stiffness.

Active Structural Control System

Significant progress has been made in recent years in the application of control theory to civil structures (Wiesner, 1986). The active structural control system considered herein is the active bracing system (ABS) as shown in Figure 2.2. The ABS has been studied both theoretically and experimentally and has been tested successfully on a full-scale structure (Soong and Reinhorn, 1993 and Reinhorn et al., 1992). The optimal control forces from the ABS can be obtained using various techniques which have been established specifically for civil structures (Pantelides, 1991). The linear quadratic regulator (Soong, 1990) and instantaneous optimal control (Yang et al., 1987) algorithms have been used for seismic structures with an ABS.

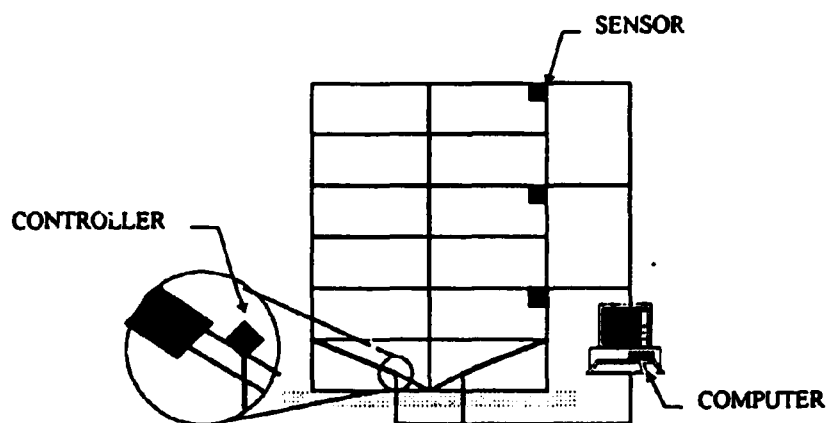


Figure 2.2 Active bracing system

Existing Models

The standard quadratic performance index for the linear quadratic regulator (LQR) is given as (Soong, 1990)

$$J = \frac{1}{2} \int_0^{t_f} [z^T(t)Qz(t) + u^T(t)Ru(t)] dt \quad (2.7)$$

in which t_f = earthquake duration, $z^T(t)$ is the transpose of the state vector $z^T(t) = \{x(t), \dot{x}(t)\}^T$ and $x(t)$ and $\dot{x}(t)$ are the relative displacement and velocity response of the structure; Q and R are the weighting matrices chosen by the designer. The optimal control force, $u^*(t)$, can be obtained by minimizing J subject to the constraint of the equation of motion which in state form can be expressed as

$$\dot{z}(t) = Az(t) + Bu(t) + HF(t) \quad (2.8a)$$

$$A = \begin{bmatrix} O & I \\ -M^{-1}K & -M^{-1}C \end{bmatrix}; \quad B = \begin{bmatrix} O \\ M^{-1}b \end{bmatrix}; \quad H = \begin{bmatrix} O \\ M^{-1}\delta \end{bmatrix} \quad (2.8b)$$

where M , C and K are the $N \times N$ mass, damping, and stiffness matrices, N being the number of degrees of freedom; O and I are the null and identity matrices; b is an $N \times m$ matrix which defines the ABS locations with respect to the structure's topology, m being the number of controllers; δ is the effective loading vector which for earthquake excitations is $\delta^T = \{-m_1, -m_2, \dots, -m_n\}$ where m_i = mass of the i th floor, $F(t)$ is the ground base-

acceleration. The result of the minimization is given by

$$u^*(t) = -\frac{1}{2}R^{-1}B^T P(t)z(t) \quad (2.9a)$$

$$PA + A^T P - \frac{1}{2}PBR^{-1}B^T P - 2Q = 0 \quad (2.9b)$$

The unknown matrix $P(t)$ can be found by assuming that it is constant with respect to time from equation (2.9b). Matrix Q could be assigned to be any positive semidefinite matrix. One way of simplifying the control procedure is to define $Q = I$, the identity matrix. Weighting matrix R is assigned to be an identity matrix multiplied by a constant r , as shown in the numerical examples.

The time-dependent performance index, $J(t)$, for instantaneous optimal control (IOC) was defined as (Yang et al., 1987)

$$J(t) = z^T(t)Qz(t) + u^T(t)Ru(t) \quad (2.10)$$

The optimal control forces, $u^*(t)$, are obtained by minimizing $J(t)$ subject to the constraint of the equation of motion of the dynamic system represented by equation (2.8). The result of the minimization is

$$u^*(t) = -\frac{\Delta t}{2}R^{-1}B^T Qz(t) \quad (2.11)$$

The time-step at which the control force is evaluated is denoted by Δt . The details of the LQR and IOC control algorithms are discussed in Appendix A.

Matrix Q in equation (2.11) is usually assigned to be an identity matrix and R is a diagonal matrix multiplied by a constant, r , at the nonzero elements of the diagonal. Therefore, the equation of motion can be expressed as

$$M\ddot{x}(t) + C^* \dot{x}(t) + Kx(t) = \delta F(t) \quad (2.12a)$$

$$C^* = C + C_{ABS} \quad (2.12b)$$

$$C_{ABS} = \frac{\Delta t}{2r} bb^T M^{-1} \quad (2.12c)$$

where C_{ABS} is the equivalent damping matrix due to the presence of the active structural control. Equation (2.12) can be used to obtain the response of a structure equipped with an ABS control system during a horizontal earthquake.

Lyapunov Method for Evaluating the Weighting Matrices

A new method for obtaining the Q weighting matrix is presented here by using Lyapunov's criteria for dynamic stability of a dynamic system. Substitution of equation (2.11) into equation (2.10) gives

$$J(t) = z^T(t) [Q + Q^T S Q] z(t) \quad (2.13a)$$

$$S = \left(\frac{\Delta t}{2} \right)^2 B R^{-1} B^T \quad (2.13b)$$

A necessary and sufficient condition for obtaining a dynamically stable structure-control system is that the term in brackets in equation (2.13a) satisfies Lyapunov's criteria for dynamic stability. The use of the Lyapunov-base Q matrix is necessary when the IOC is employed in a hysteretic inelastic structural system (Yang et al., 1992 a). This requirement can be expressed as

$$A^T[Q + Q^T S Q] + [Q + Q^T S Q]A = -I. \quad (2.14)$$

The weighting matrix Q can be found from equation (2.14) which is then substituted in equation (2.11) to obtain the optimal control force. Note that equation (2.14) differs from the result of Yang et al. (1992 a) in that both terms of equation (2.10) are considered in the present derivation of weighting matrix Q . The weighting matrix R is still assumed to be a diagonal matrix multiplied by a constant at the nonzero elements of the diagonal. The elements of R are defined for a specific structure in the numerical examples.

Drift Performance Index (DPI)

A performance index for optimal control is proposed in terms of the magnitude of drift displacements as

$$J(t) = \Delta z^T(t) Q \Delta z(t) + u^T(t) R u(t) \quad (2.15a)$$

$$\Delta z(t) = Dz(t), \quad D = \begin{bmatrix} d & \mathbf{O} \\ \mathbf{O} & d \end{bmatrix}, \quad d = \begin{bmatrix} 1 & 0 & 0 & \dots \\ -1 & 1 & 0 & \dots \\ 0 & -1 & 1 & \dots \\ \dots & \dots & \dots & \dots \end{bmatrix} \quad (2.15b)$$

where matrix D defines the relationship between displacement and interstory drift. The optimal control force can be obtained as

$$u^*(t) = \frac{-\Delta t}{2} R^{-1} B^T Q^* z(t); \quad Q^* = D^T Q D \quad (2.16)$$

The identity matrix is used for weighting matrix Q , and a diagonal matrix is used for weighting matrix R . The elements of R are defined for the specific structure in the numerical examples.

Velocity Performance index (VPI)

A control performance index is proposed for reduction of the velocity and acceleration response of the structure. The feedback measurements required are those of velocity and acceleration (\dot{z} feedback) which are easier to obtain than displacement and velocity (z feedback). The performance index is defined as

$$J = \frac{1}{2} \int_0^{t_f} \left[\dot{z}^T(t) Q \dot{z}(t) + u^T(t) R u(t) \right] dt \quad (2.17)$$

in which t_f = earthquake duration, \dot{z}^T is the transpose of the velocity state vector, $\dot{z}^T(t) = \{\dot{x}(t), \ddot{x}(t)\}^T$, and $\ddot{x}(t)$ is the acceleration vector. The optimal control force can be obtained as

$$u^*(t) = R^{-1} B^T P(t) \dot{z}(t) \quad (2.18)$$

where matrix P is the Riccati matrix using the assumption that it is a constant. The Riccati matrix can be found from the following:

$$PA^{-1} + PA^{-1}CP + (A^T)^{-1}P - (A^T)^{-1}Q = 0 \quad (2.19a)$$

$$C = BR^{-1}B^T \quad (2.19b)$$

The weighting matrix, Q , is defined as the identity matrix, and matrix R is assumed as a diagonal matrix. Equation (2.19) can be solved by the Runge-Kutta four-order method which is discussed in Appendix B.

CHAPTER 3

CONVEX MODELS AND OPTIMAL STRUCTURAL DESIGN

The energy-bound convex models for estimating the maximum dynamic response of the structure for an uncertain earthquake excitation are discussed in this chapter. The structural optimization using the modified annealing strategy is also presented for the optimal design of conventional or active structures.

Energy-bound Convex Models

A convex model is a method of quantifying uncertainty, in this case the uncertain nature of earthquakes or impulses, without resorting to the traditional concepts of probability, but rather by defining a set of functions which have certain convex global characteristics or bounds (Ben-Haim and Elishakoff, 1990; Ben-Haim, 1994 b). The application of convex models to quantify uncertainty is well suited in situations in which only a limited amount of information is available for the variables of interest, which is exactly the case for structural systems subjected to uncertain excitations such as earthquakes. In effect, the convex model constrains the uncertainty, inherent in earthquake excitations, within a bound that is defined in terms of either a function of

bounded energy, or an envelope function with upper and lower limits.

It was shown in the previous section that the structural response of an actively controlled structure can be obtained from either equation (2.8) or equation (2.12). Numerical simulations have shown that the results obtained by either method are practically identical. The natural frequencies of the physical structure are basically the same and the mode shapes are not changed significantly for the levels of damping considered herein (Pantelides, 1987). Equation (2.12) is used in its normalized form with respect to the mass matrix to represent the structural response of the controlled structure. Let the natural frequencies of the N degree-of-freedom controlled structure be $\omega_1, \dots, \omega_N$, the corresponding mode shapes be ϕ_1, \dots, ϕ_N , and the corresponding modal matrix be $\Phi = [\phi_1, \dots, \phi_1, \dots, \phi_N]$. The normalized equation of motion is expressed as

$$\ddot{y}_i + 2\omega_i \xi_i \dot{y}_i + \omega_i^2 y_i = \phi_i f(t) \quad (3.1a)$$

where the normalized properties with respect to the mass matrix are

$$\Phi^T M \Phi = I; \quad \Phi^T K \Phi = \begin{bmatrix} \omega_1^2 & & & & 0 \\ & \ddots & & & \\ & & \omega_i^2 & & \\ & & & \ddots & \\ 0 & & & & \omega_N^2 \end{bmatrix};$$

$$\Phi^T C^* \Phi = \begin{bmatrix} 2\omega_1 \xi_1^* & & & & 0 \\ & \ddots & & & \\ & & 2\omega_i \xi_i^* & & \\ & & & \ddots & \\ 0 & & & & 2\omega_N \xi_N^* \end{bmatrix} \quad (3.1b)$$

$$\xi_i^* = \xi_i + \xi_{c,i}; \quad i = 1, \dots, N \quad (3.1c)$$

where I is an $N \times N$ identity matrix, ξ_i is the i th mode damping ratio of the structure and $\xi_{c,i}$ is the damping in the i th mode introduced by the active/passive control system; ω_i^* is the structural frequency of the controlled structure for the i th normal mode.

Using Duhamel's integral and assuming zero initial conditions, yields for the response of the controlled structure in the i th normal mode

$$y_i(t) = \frac{1}{\omega_{D,i}} \int_0^t \phi_i^T \delta X_g(\tau) e^{-\xi_i^* \omega_i^* (t-\tau)} \sin \omega_{D,i} (t-\tau) d\tau; \quad i = 1, \dots, N \quad (3.2a)$$

$$\omega_{D,i} = \omega_i^* \zeta_i; \quad \zeta_i = \sqrt{1 - (\xi_i^*)^2} \quad (3.2b)$$

The modal amplitude $y_i(t)$ is the response of the i th mode in normal coordinates. Furthermore, the i th mode modal velocity and acceleration for zero initial conditions can be expressed as

$$\dot{y}_i(t) = \frac{e^{-\xi_i^* \omega_i^* t}}{\omega_{D,i}} \left\{ \omega_{D,i} \int_0^t [\phi_i^T f(\tau)] e^{\xi_i^* \omega_i^* \tau} \cos \omega_{D,i} (t-\tau) d\tau - \xi_i^* \omega_i^* \int_0^t [\phi_i^T f(\tau)] e^{\xi_i^* \omega_i^* \tau} \sin \omega_{D,i} (t-\tau) d\tau \right\} \quad (3.3a)$$

$$\begin{aligned} \ddot{y}_i(t) = & \phi_i^T f(t) - 2\xi_i \omega_i e^{-\xi_i \omega_i t} \int_0^t [\phi_i^T f(\tau)] e^{\xi_i \omega_i \tau} \cos \omega_{D,i}(t - \tau) d\tau \\ & + e^{-\xi_i \omega_i t} \left(\frac{(\xi_i \omega_i)^2}{\omega_{D,i}} - \omega_{D,i} \right) \int_0^t [\phi_i^T f(\tau)] e^{\xi_i \omega_i \tau} \sin \omega_{D,i}(t - \tau) d\tau \end{aligned} \quad (3.3b)$$

The displacement, velocity and acceleration in physical coordinates are then obtained from the following superposition equations

$$\mathbf{x}(t) = \Phi \mathbf{y}(t); \quad \dot{\mathbf{x}}(t) = \Phi \dot{\mathbf{y}}(t); \quad \ddot{\mathbf{x}}(t) = \Phi \ddot{\mathbf{y}}(t) \quad (3.4)$$

In what follows, the ground acceleration $\ddot{X}_g(t)$ is assumed to belong to a convex set bounded by either a global energy or a local energy-bound model.

Global Energy-bound Convex Model (GEB)

The convex set of allowed excitations for the global energy-bound convex model (GEB) is expressed as (Ben-Haim and Elishakoff, 1990)

$$F_{GEB} = \left\{ f(t): \int_0^t f(\tau)^T f(\tau) d\tau \leq E_0^2(t) \right\} \quad (3.5)$$

The instantaneous energy of the input excitation defined by equation (3.5) is bounded at each instant, t . For the global energy-bound model the energy bound, $E_0^2(t)$, varies in a given time-interval and its value is the integral or the area of the input energy as expressed

by equation (3.5) up to time t . As time goes to infinity, the bound of the global energy convex model reaches a finite value, $E_0^2(\infty)$ which is larger than any $E_0^2(t)$ for any $t < \infty$. Time is assumed to reach infinity at the end of the earthquake record.

The maximum modal displacement, velocity, and acceleration for each mode I , obtained by using the convex model of equation (3.5), can be found using the theory of convex models (Ben-Haim and Elishakoff, 1990) as follows: From equation (3.2), the maximum modal displacement obtained using the convex model of equation (3.5) is

$$y_{\text{GEB},i} = \max_{f \in F_{\text{conv}}} \frac{1}{\omega_{D,i}} \int_0^t \left\{ \left[\phi_i^T f(\tau) \right] e^{-\zeta_i \omega_{D,i} (t-\tau)} \sin \omega_{D,i} (t-\tau) \right\} d\tau \quad (3.6)$$

Since y_i is a linear function of the excitation $f(\tau)$ and assuming that the excitation set F_{GEB} is convex, the maximum in equation (3.6) occurs on the set of extreme points of F_{GEB} ; the maximizing excitation will satisfy

$$\int_0^t f^T(\tau) f(\tau) d\tau = E_0^2(t) \quad (3.7)$$

According to the Cauchy-Schwarz inequality (Hardy et al., 1934) for arbitrary f_1 and f_2

$$\left(\int_0^t f_1(\tau) f_2(\tau) d\tau \right)^2 \leq \int_0^t f_1^2(\tau) d\tau \int_0^t f_2^2(\tau) d\tau \quad (3.8)$$

with equality only if $f_1(\tau)$ and $f_2(\tau)$ are proportional. Using the result of equation (3.8) in equation (3.6) gives

$$y_{\max,i}(t) = \frac{\rho_{\alpha,i}(t)}{2\omega_{D,i}} \sqrt{\frac{\lambda_d}{\xi_i^2 \omega_i^2}}; \quad \lambda_d = \zeta_i^2 - e^{-2\zeta_i \omega_i t} \left(1 + \zeta_i \xi_i^2 \sin 2\omega_{D,i} t - \xi_i^2 \cos 2\omega_{D,i} t \right) \quad (3.9a)$$

Similarly, results for the maximum modal velocity and acceleration can be obtained as

$$\begin{aligned} \dot{y}_{\max,i}(t) &= \frac{\rho_{\alpha,i}(t)}{2\omega_{D,i}} \sqrt{\frac{\omega_i^2 \lambda_v}{\xi_i^2}}; \\ \lambda_v &= \zeta_i^2 - e^{-2\zeta_i \omega_i t} \left(1 - \zeta_i \xi_i^2 \sin 2(\theta_i - \omega_{D,i} t) - \xi_i^2 \cos 2(\theta_i - \omega_{D,i} t) \right) \\ \theta_i &= \tan^{-1} \left(\frac{\zeta_i}{\xi_i^2} \right) \end{aligned} \quad (3.9b)$$

$$\begin{aligned} \ddot{y}_{\max,i}(t) &= \phi_i^T f(t) - \frac{\rho_{\alpha,i}(t)}{2} \sqrt{\frac{\omega_i^2 \lambda_a}{\xi_i^2 \zeta_i^2}}; \\ \lambda_a &= 1 + \xi_i^2 (3 - 4\xi_i^2) - e^{-2\zeta_i \omega_i t} \left(1 + \zeta_i \xi_i^2 \sin 2(\theta_i + \omega_{D,i} t) - \xi_i^2 \cos 2(\theta_i + \omega_{D,i} t) \right) \\ \theta_i &= \tan^{-1} \left(\frac{2\xi_i^2 \zeta_i}{1 - 2\xi_i^2} \right) \end{aligned} \quad (3.9c)$$

where $\rho_{\alpha,i}(t) = \left(\phi_i^T \phi_i E_0^2(t) \right)^{1/2}$, $\omega_{D,i} = \zeta_i \omega_i$, and $\zeta_i = \sqrt{1 - \xi_i^2}$. The maximum modal responses for displacement, velocity, and acceleration as time goes to infinity can be found as

$$y_{\max,i} = \frac{\rho_{0,i}(\infty)}{2\omega_i \sqrt{\xi_i} \omega_i} \quad (3.10a)$$

$$\dot{y}_{\max,i} = \frac{\rho_{0,i}(\infty)}{2\sqrt{\xi_i} \omega_i} \quad (3.10b)$$

$$\ddot{y}_{\max,i} = \frac{\rho_{0,i}(\infty)}{2} \sqrt{\frac{\omega_i^2 (1 + 4\xi_i^2)}{\xi_i}} \quad (3.10c)$$

where $\rho_{0,i}(\infty) = (\phi_i^T \phi_i E_0^2(\infty))^{1/2}$.

The maximum displacement in physical coordinates can be approximated by the square root of the sum of the squares (SRSS) of the modal responses

$$|x_{\max,j}| \equiv \sqrt{\sum_{i=1}^N \phi_{ji}^2 y_{\max,i}^2}; \quad |\dot{x}_{\max,j}| \equiv \sqrt{\sum_{i=1}^N \phi_{ji}^2 \dot{y}_{\max,i}^2}; \quad |\ddot{x}_{\max,j}| \equiv \sqrt{\sum_{i=1}^N \phi_{ji}^2 \ddot{y}_{\max,i}^2} \quad (3.11)$$

The subscript j denotes the response at the j th floor and i denotes the i th normal mode. N is the number of dynamic modes of the system. However, when the SRSS method is used only the significant modes need to be considered. When major contributing modes have frequencies that are close together, the complete quadratic combination (CQC) method should be used (Der Kiureghian, 1980).

Local Energy-bound Convex Model (LEB)

In the local energy-bound convex model (LEB) the instantaneous energy of the excitation is bounded at each instant. Furthermore, the energy bound, $E_1^2(t)$, can vary

with time. The convex set of allowed excitations is expressed as (Ben-Haim and Elishakoff, 1990)

$$F_{LEB} = \{f(t): f(t)^T f(t) \leq E_L^2(t)\} \quad (3.12)$$

The maximum modal displacement, velocity, and acceleration for each mode i , obtained by using the convex model of equation (3.12) can be found using the theory of convex models as:

$$y_{max,i}(t) = \rho_{L,i}(t) \left\{ \frac{e^{-\zeta_i \omega_i t}}{\omega_{D,i}} \left[|\sin \omega_{D,i} t| \int_0^t e^{\zeta_i \omega_i \tau} |\cos \omega_{D,i} \tau| d\tau + |\cos \omega_{D,i} t| \int_0^t e^{\zeta_i \omega_i \tau} |\sin \omega_{D,i} \tau| d\tau \right] \right\} \quad (3.13a)$$

$$\dot{y}_{max,i}(t) = \rho_{L,i}(t) \left\{ e^{-\zeta_i \omega_i t} \left[\left(\frac{\xi_i^*}{\zeta_i} |\sin \omega_{D,i} t| + |\cos \omega_{D,i} t| \right) \int_0^t e^{\zeta_i \omega_i \tau} |\cos \omega_{D,i} \tau| d\tau + \left(\frac{\xi_i^*}{\zeta_i} |\cos \omega_{D,i} t| + |\sin \omega_{D,i} t| \right) \int_0^t e^{\zeta_i \omega_i \tau} |\sin \omega_{D,i} \tau| d\tau \right] \right\} \quad (3.13b)$$

$$\ddot{y}_{max,i}(t) = \phi_i^T f(t) \pm \rho_{L,i}(t) \omega_i e^{-\zeta_i \omega_i t} \left[\left(\frac{1}{\zeta_i} |\sin \omega_{D,i} t| + 2\xi_i^* |\cos \omega_{D,i} t| \right) \int_0^t e^{\zeta_i \omega_i \tau} |\cos \omega_{D,i} \tau| d\tau + \left(\frac{1}{\zeta_i} |\cos \omega_{D,i} t| + 2\xi_i^* |\sin \omega_{D,i} t| \right) \int_0^t e^{\zeta_i \omega_i \tau} |\sin \omega_{D,i} \tau| d\tau \right] \left(\frac{1}{\zeta_i} |\cos \omega_{D,i} t| + 2\xi_i^* |\sin \omega_{D,i} t| \right) \int_0^t e^{\zeta_i \omega_i \tau} |\sin \omega_{D,i} \tau| d\tau \right] \quad (3.13c)$$

Let $y_{max,i} = \max_{f(t) \in F(t)} |y_{max,i}(t)|$, and $t \rightarrow \infty$; the maximum modal displacement, velocity, and acceleration in the normal coordinates as time goes to infinity can be found as

$$y_{\max,i} = \frac{\rho_{L,i}(\infty)}{\omega_i^2} \left(\frac{1 + e^{-\xi_i \pi / \zeta_i}}{1 - e^{-\xi_i \pi / \zeta_i}} \right) \quad (3.14a)$$

$$\dot{y}_{\max,i} = \frac{2\rho_{L,i}(\infty)}{\omega_i} \left(\frac{\xi_i + \zeta_i e^{-\xi_i \pi / 2\zeta_i}}{1 - e^{-\xi_i \pi / \zeta_i}} \right) \quad (3.14b)$$

$$\ddot{y}_{\max,i} = \rho_{L,i}(\infty) \left(2\xi_i^2 + \frac{1 - 2\xi_i^2 + 4\xi_i^2 \zeta_i e^{-\xi_i \pi / 2\zeta_i} + (1 - 2\xi_i^2) e^{-\xi_i \pi / \zeta_i}}{1 - e^{-\xi_i \pi / \zeta_i}} \right) \quad (3.14c)$$

where $\rho_{L,i}(t) = (\phi_i^T \phi_i E_L^2(t))^{1/2}$, $\rho_{L,i}(\infty) = (\phi_i^T \phi_i E_L^2(\infty))^{1/2}$, $\omega_{D,i} = \zeta_i \omega_i^*$, and $\zeta_i = \sqrt{1 - \xi_i^2}$. Note that the maximum values in equation (3.14) will occur at some time (t_{\max}) which is between $t = 0$ and $t = \infty$; at time t_{\max} , the local energy bound reaches a peak value $E_L^2(\infty)$ which is larger than $E_L^2(t)$ for any other time t . Equation (3.14) can be combined with the SRSS expression of equation (3.11) to obtain the physical displacement, velocity, and acceleration response.

Structural Optimization

The structural optimization problem for a building equipped with an active bracing system is a dynamic one and is formulated as follows. Find the optimal parameters (\underline{A}, r), which are the areas of the structural members and the weighting matrix parameters Q and R that minimize the structural volume $V(\underline{A}, r)$ subject to displacement constraints on the structural response, $x(t)$, stress constraints on the structural members, $\sigma(t)$, and side constraints on the design variables, $\underline{A}_L, \underline{A}_U, r_L, r_U$. The subscript L denotes the lower bound and subscript U is the upper bound of the design variable. Mathematically, this can be expressed as

$$\min. V(\underline{A}, r) \quad (3.15)$$

Subject to

$$x_j(\underline{A}, r, t) \leq x_{all,j}; \quad j = 1, \dots, \bar{j}; \quad t \geq 0 \quad (3.16a)$$

$$\sigma_k(\underline{A}, r, t) \leq \sigma_{all,k}; \quad k = 1, \dots, \bar{k}; \quad t \geq 0 \quad (3.16b)$$

$$\underline{A}_L \leq \underline{A}_k \leq \underline{A}_U; \quad k = 1, \dots, \bar{k}; \quad t \geq 0 \quad (3.16c)$$

$$r_L \leq r \leq r_U \quad (3.16d)$$

where $x_{all,j}$ is the allowable displacement at a certain node of the structure, and \bar{j} is the number of nodes at which displacement constraints are imposed; $\sigma_{all,k}$ is the allowable combined stress in a structural member, and \bar{k} is the number of structural members. Note that if the peak values of the structural response are used that can be obtained from either the GEB or LEB convex models, the quantities on the left hand side of equations (3.16a, b) become time-independent and the optimization problem is reduced to a static one.

The static optimization problem is developed as follows. Minimize the structural volume given in equation (3.15) subject to the constraints

$$x_{j, \text{GEB or LEB}}(\underline{A}, r) \leq x_{all,j}; \quad j = 1, \dots, \bar{j} \quad (3.17a)$$

$$\sigma_{k, \text{GEB or LEB}}(\underline{A}, r) \leq \sigma_{all,k} \quad k = 1, \dots, \bar{k} \quad (3.17b)$$

and also subject to the side constraints of equations (3.16c, d). It is obvious that the

solution of the static optimization problem of equations (3.15, 3.17a, b, and 3.16c, d) is much easier than that of the original dynamic problem, because in the latter the constraints are time-independent. The accuracy of the approximate static optimization problem depends on the relationship between the actual peak values of the structural response and those obtained using the GEB or LEB convex models. Note that for the optimization of conventional structures without ABS, or structures equipped with VE dampers, the same procedure can be used and the problem is also independent of r .

The structural analysis of frame type buildings considered here is carried out using the direct stiffness method (Appendix C), with a capability for computing and enforcing a strength ratio of column to beam greater or equal to unity. The strength ratio of column to beam is necessary in order to enforce the strong-column weak-beam philosophy of the design codes (UBC, 1994). The structural analysis also produces the axial, bending and combined stresses in the structural members.

In what follows the dynamic and approximate static optimization problems are solved. The optimal designs obtained using the convex models are compared to the optimal design obtained using an actual ground acceleration record. The correlation between the static and dynamic active structures that are obtained is observed. Both traditional (VMA, 1993) and the optimization method developed here known as the modified iterated simulated annealing method, are used to obtain the optimal structural designs. Artificial earthquakes, as well as records from past earthquakes are considered.

Simulated Annealing Methods

Since 1983, when the simulated annealing method was introduced (Kirkpatrick et al.), two notable developments most related to the present method evolved. These are Ackley's iterated simulated annealing (ISA) and stochastic hillclimbing (SHC) methods (1987), and Balling's simulated annealing method (1991).

Existing Methods

The iterated simulated annealing (ISA) method has developed from the stochastic hillclimbing (SHC) method. Both the ISA and SHC methods consider a random change to the current design point, and accept the change with a probability, p , determined by a fixed formula of the difference in the objective function values (Ackley, 1987)

$$p = \frac{1}{1 + e^{(V_c - V_o)/T}} \quad (3.18)$$

where V_c is the current value of the objective function from the pre-selected point, V_o is a candidate value of the objective function which is produced by an adjacent point picked randomly, and T is an adjustable parameter which is described as "temperature." Larger values of T may cause the probabilities of acceptance of the current design to reach closer to a 50 % reject and 50 % accept.

In the SHC method, the temperature T of the system is a parameter which is held constant for the duration of the search. In the ISA technique, the temperature is a variable that starts at a high value and is reduced by a decay rate during the search. The system

accepts the almost random moves at the high temperature, and the probability of accepting any move drops at the lower temperature.

A simulated annealing strategy was developed for the discrete optimization of steel frames by Balling (1991). The probabilistic acceptance criterion for determining whether the candidate design should replace the current design or be rejected was formed with a probability

$$p = e^{(-D/BT)} \quad (3.19)$$

where D is the difference in the value of the objective function between the candidate design and the current design, B is a normalization constant which is the running average of D , and T is the strategy temperature which decreases according to a "cooling factor," f , defined as

$$f = \left(\frac{\log(p_s)}{\log(p_f)} \right)^{1/(N-1)} \quad (3.20)$$

In equation (3.20), p_s and p_f are the starting and final acceptance probabilities for an average $D = B$, and N is the number of cycles. In Balling's procedure, the acceptance criterion allows worse designs to be accepted in the initial stages of the optimization.

Modified Iterated Simulated Annealing Method (MISA)

An annealing strategy is employed for problems with dynamic constraints. The reason for using an annealing strategy is that the random sequence of designs is suited for problems with disjoint feasible regions where a local rather than the global minimum might be reached if classical optimization methods were to be used. The proposed algorithm contains elements of existing annealing strategies. Ackley's ISA algorithm (1987) regarding the probability of acceptance and Balling's search strategy (1991) are included as elements of the proposed algorithm.

Figure 3.1 shows the flowchart of the optimal design procedure. The design variables, which are the cross-sectional areas of the members, are determined by a procedure which is based on a random reference number that is requested by the program based on the current time of the computer clock. Two iterations loops are performed which are defined as M and N . M is the maximum value of m which is the counter for the inner loop. The inner loop determines the search direction and M is usually a small number less than 10. N is the maximum value of n which is the counter for the outer loop. The outer loop determines the best design for different annealing probabilities, based on different values of T (temperature); n_1 is the minimum number of runs of the outer loop; k is an integer, and $k \times n_2$ is the number of times required, in addition to n_1 , for the outer loop to converge; n_1 and n_2 must be determined by the user for a particular application. Usually, n_1 is between 75 and 150 and n_2 is between 10 and 25. The value of k is entirely problem dependent. After the outer loop runs $(n_1 + n_2)$ times, the designs at n_1 and $(n_1 + n_2)$ are compared. When these two designs are identical the program stops.

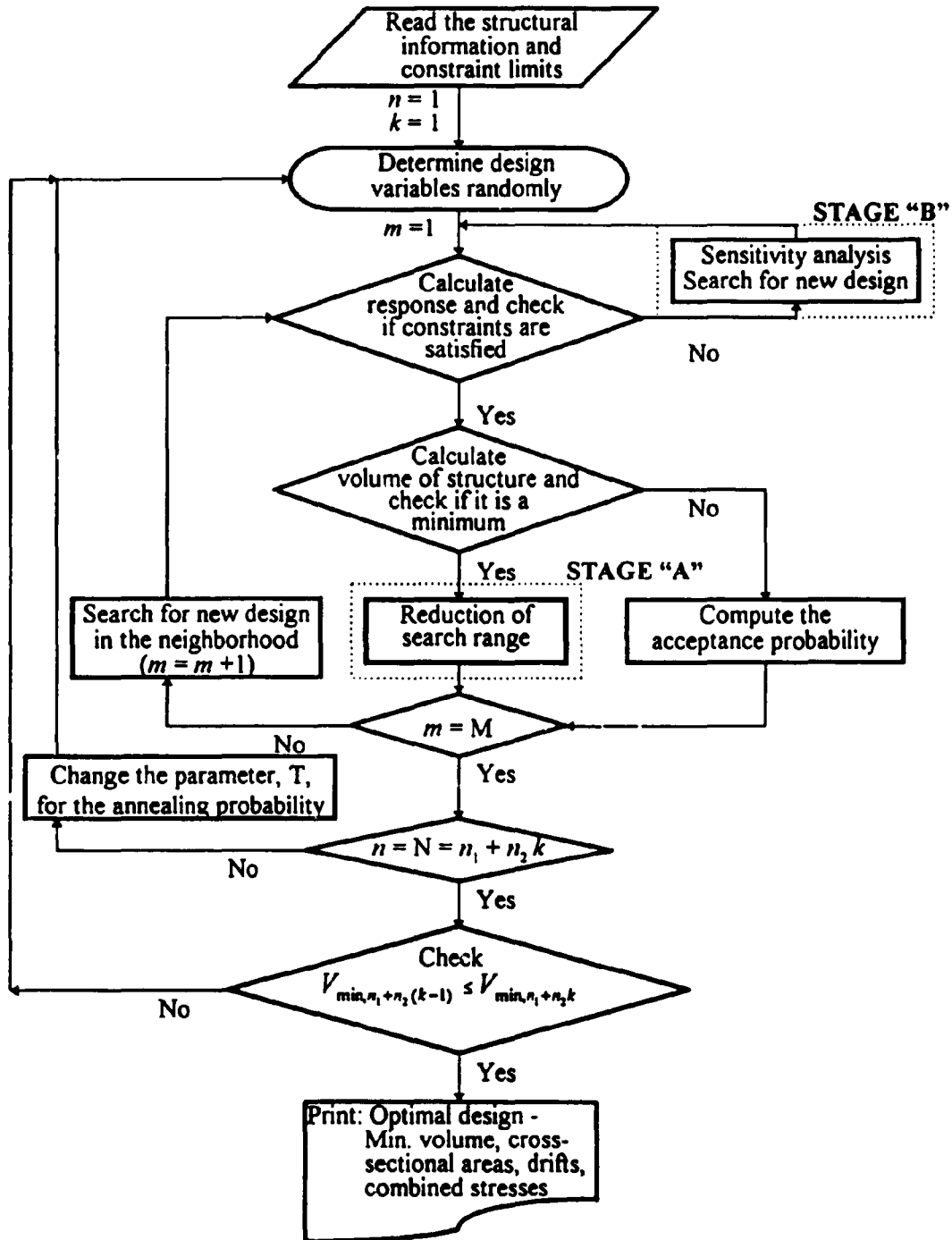


Figure 3.1 Annealing procedure for optimization of structural design

Otherwise, the outer loop is repeated n_2 times, and comparison is made between the designs at $(n_1 + n_2)$ and $(n_1 + 2n_2)$. The algorithm is repeated k times until the two designs converge.

A comparison of the proposed method and the existing methods is shown in Table 3.1. From Table 3.1, it can be observed that the search strategy of the MISA method is similar to the search steps of Balling's method, except that the probability of acceptance is different. Instead of using Balling's probability of acceptance, Ackley's ISA probability is adopted for its simplicity.

Two new procedures are introduced whose purpose is to: (a) achieve reduction of the search range, and (b) use sensitivity analysis for the design variables. Reduction of the search range is achieved in the present method as follows: Assume that a candidate design is found (point C in Figure 3.2) at which the objective function has a smaller value than the previous design (point P in Figure 3.2). When this happens, the search range is reduced to exclude any points outside a region which contains the candidate design (point C). The new search range is increased by an amount X_r and Y_r from point C . The increase for X_r and Y_r in Figure 3.2 is chosen as 15 % of X and Y , respectively. This procedure is performed at stage "A" of the flowchart of Figure 3.1. Since the next point is chosen randomly two situations are possible. First, the new candidate design could end up in the infeasible region in which case the design is rejected and there is no need for reduction of the search range. The second possibility is that the new candidate design is inside the feasible region of the new search range and has a smaller objective function value than point C . In this case, a new search range will be found as described above.

Table 3.1 Comparison of the existing annealing methods and the proposed method

Ackley's method - ISA method	Belling's method	Proposed method
<p>1. (Restart) Set $T=T_{max}$. Select a random point X_c and evaluate V_c.</p> <p>2. (Stochastic Hillclimb) Pick an adjacent point X_s (a random number) and evaluate V_s.</p>	<p>1. Input P_s, P_f, and N by user and compute the starting T and F. Also, initialize C and M to 1 and 0.</p> <p>2. Randomly select each variable until all variable have been selected.</p> <p>3. Generate a random increment between -2 and 2 and create a candidate design by adding this increment to the selected discrete variable. Compute the weight of the candidate design and perform the approximate analysis to evaluate the constraints.</p> <p>4.1 Automatic rejection : If the candidate design is infeasible, reject the candidate design and return to step 2.</p> <p>4.2 Automatic acceptance : If the candidate design is feasible and has a lower weight, accept this candidate design as the current design and return to step 2.</p> <p>4.3 If candidate design is feasible but has a higher weight, update C and M, compute the acceptance probability : $P = \exp(-D/CN)$, and generate a random number, X, which is between zero and one.</p> <p>4.3.1 Probabilistic rejection : If X is greater than or equal to P, reject this candidate design and return to step 2.</p> <p>4.3.2 Probabilistic acceptance : If X is less than P, accept the candidate design as the current design and return to step 2.</p> <p>5. Update the temperature $T = \gamma T$.</p>	<p>1. Set $T = T_{max}$. Select a random point X_c and evaluate the constraints.</p> <p>2. Pick an adjacent point, X_s, which is a random number between $-L$ and L ($L = (A_{max} - A_{min})/S$). S is a constant number used to define the search distance for the designs in the feasible region. Usually, S is defined equal to 20. After repeating steps 2-4 for M loops the program should go to step 5 to update the annealing temperature, T.</p> <p>3. Calculate the response and check the constraints.</p> <p>4.1 If X_s is infeasible, reject this point and use the sensitivity analysis to indicate the variables needed to be changed. Pick a random point between $-l$ and l for the changed variables and go to step 2.</p> <p>Note: $l = (A_{max} - A_{min})/s$, where $s = 5$ is used to define the search distance for the designs in the infeasible region.</p> <p>4.2 If X_s is feasible and V_s is smaller than V_c, accept this point, replace X_c, V_c by X_s, V_s, and return to step 2 if $m < M$, otherwise go to step 5.</p> <p>4.3 If X_s is feasible and V_s larger than V_c, calculate the probability : $P = 1/(1 + \exp((V_s - V_c)/T))$, and select a random number, X, which is between zero and 0.5.</p> <p>4.3.1 If X is larger than or equal to P, reject this point and return to step 2.</p> <p>4.3.2 If X is smaller than P, accept this point and replace X_c, V_c by X_s, V_s. Return to step 2.</p> <p>5. Update the annealing temperature $T = \gamma T$. Stop the program if V_{min} retained the same value during the last N cycles, otherwise go to step 2.</p>
<p>3. Set $X_c = X_s$ and select a new point, X_s, with probability : $1/(1 + \exp((V_s - V_c)/T))$. Repeat step 2 and 3 for K times.</p>		
<p>4. (Anneal/Convergence test) Set $T = \gamma T$. If $T > T_{min}$, go to step 2, otherwise go to step 1.</p>		

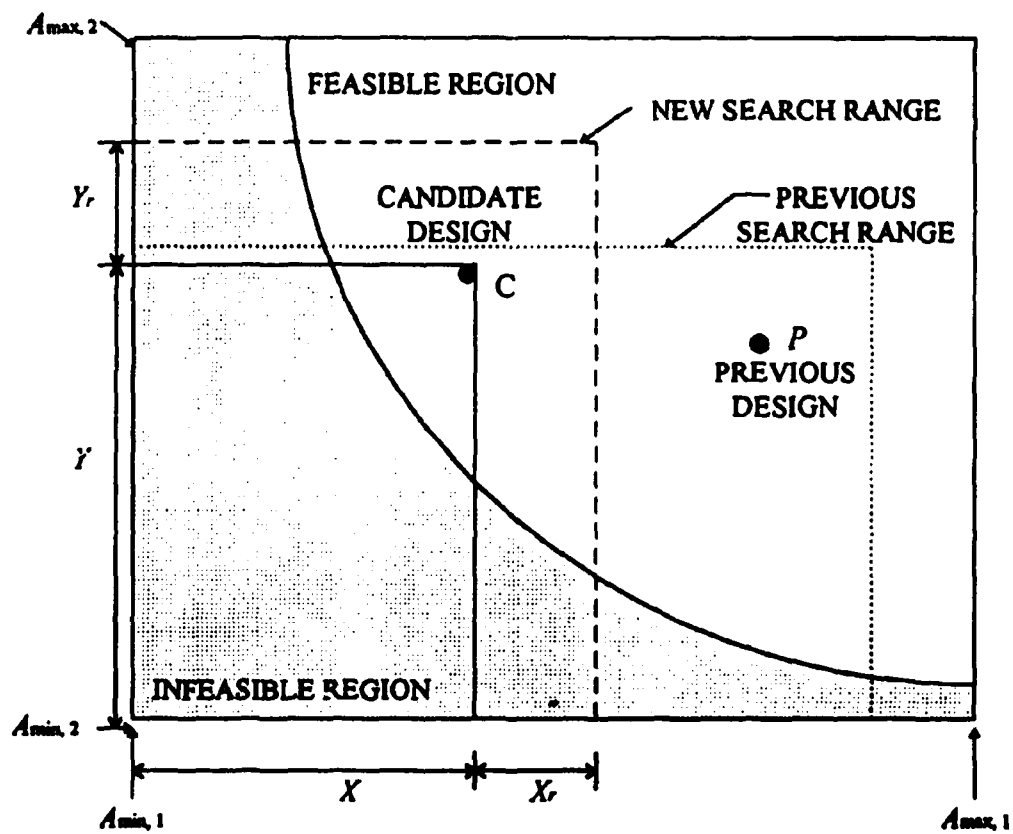


Figure 3.2 Automatic reduction of the search range used in the present method

Sensitivity analysis (Grierson, 1994) is used in order to improve the efficiency of the present method as follows: if a given displacement response violates the constraint, the neighboring structural members are identified by sensitivity analysis and the area of those members is changed by a proportionate random number (Appendix D). A first-order sensitivity analysis of displacement responses is carried out. The purpose of the analysis is to identify the design variables (areas of structural members) that must be modified in the new design, in order to decrease the magnitude of a certain displacement in the most economical way. This sensitivity analysis is performed at stage "B" of the flowchart of Figure 3.1. Thus, even though the determination of the values of the design variable is random, the identification of which variables must be modified is done using sensitivity analysis methods (Grierson, 1994). It was found that by using sensitivity analysis, the expense of multiple trials is avoided and the efficiency of the present method is improved considerably.

The method presented above contains features common to many simulated annealing algorithms. However, it should be pointed out that the design variables are continuous rather than discrete. In addition, the sensitivity information on the design variables reduces the randomness of choosing which variables to modify; however, the numerical values that these variables take are randomly determined. Finally, the automatic reduction of the search range violates symmetry considerations inherent in simulated annealing algorithms. However, the automatic reduction of the search range improves the computational efficiency considerably and is a desirable feature of the present method. Thus, the present method can be characterized as a new method.

The present method was found to be advantageous in certain cases when the constraints were dynamic, as compared to standard mathematical programming methods. Numerical examples are provided to show the performance of the present method as compared to standard optimization methods for optimal design with static or dynamic constraints.

CHAPTER 4

DYNAMIC RESPONSE OF STRUCTURES WITH PASSIVE/ACTIVE STRUCTURAL CONTROL

In this chapter, a hybrid control system is presented that consists of viscoelastic (VE) dampers and active bracing systems (ABS). The performance of the system is predicted adequately through simplified analytical procedures. An eight-story shear building (Yang et al., 1988) and a ten-story frame (Xia et al., 1990) shown in Figure 4.1 are used to evaluate the performance of the passive and active structural control systems. In addition, a five-story experimental shear building shown in Figure 4.1(c) (Zhang and Soong, 1992) is used to study the influence of the location of the viscoelastic (VE) dampers. The structural frequencies of the five-story shear building are 19.27, 56.41, 88.94, 108.64, 145.59 rad/sec., those of the eight-story building are 5.79, 17.18, 27.98, 37.83, 46.39, 53.37, 58.53, 61.70 rad/sec., and those of the ten-story frame are 2.47, 6.99, 12.36, 18.95, 26.09, 34.78, 44.02, 52.80, 62.70, 74.75 rad/sec. Young's modulus for all three building materials equals $206.8E+09$ N/m².

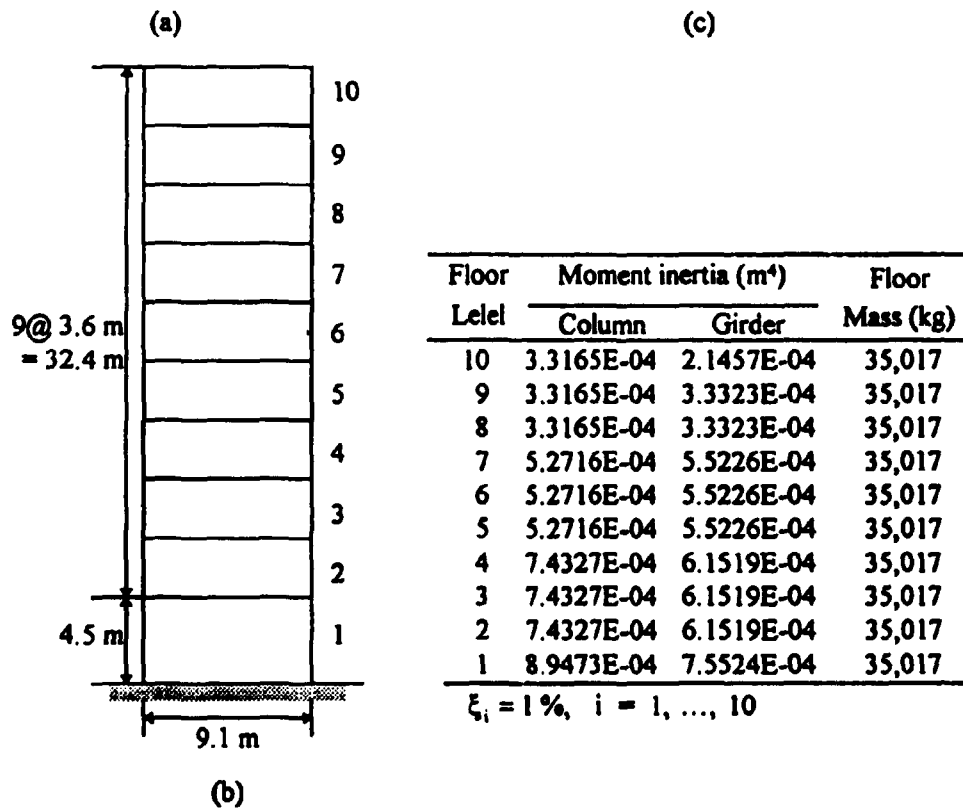
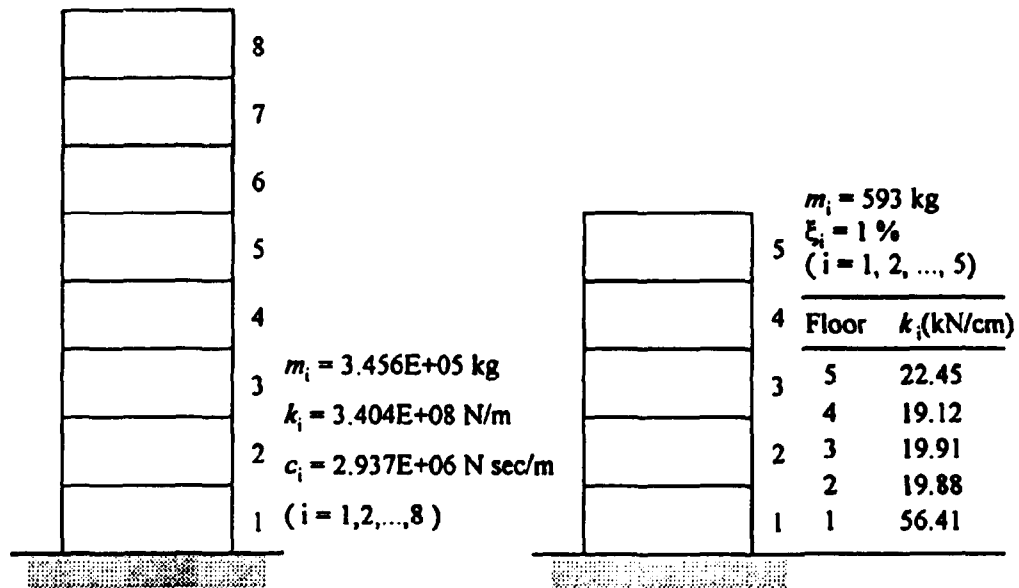


Figure 4.1 Numerical examples: (a) eight-story shear building, (b) ten-story frame, and (c) five-story shear building

Properties of Viscoelastic Damper

Viscoelastic dampers have properties that are both frequency and temperature dependent. It is well known that the location of the VE dampers affects their efficiency in providing seismic resistance. Parametric studies of structures equipped using a number of VE dampers on different floors are performed. The effective damping ratio includes the inherent structural damping ratio and the additional damping introduced by the VE dampers. In this section, the frequency dependence and the location effect of the VE dampers are investigated. Temperature effects are not considered in this study.

Frequency Dependence of VE Damper Materials

The eight-story shear building shown in Figure 4.1(a) is used to calculate the effective damping ratios including the influence of the VE dampers by using three methods. The cross-sectional area of the VE damper is assumed as $A = 0.090 \text{ m}^2$, and its thickness $t = 0.0127 \text{ m}$. In the first method, the values of shear storage and loss moduli, G' and G'' , are fixed as constants, invariant with the excitation frequency (Zhang and Soong, 1992). In the second method, instead of using constants to represent these two parameters, equations (2.4a) and (2.4b) are used (Kasai et al., 1993). A structure-dependent design is presented here for the third method; in this case, the frequencies at which G' and G'' are evaluated are the natural frequencies of the structure. The idea behind the third method is that the majority of the response is concentrated at the natural frequencies of the structure. The three approaches are applied to the eight-story building with one VE damper on the first floor using equations (2.1 - 2.6). The constants, a , b , α ,

and G are used as 0.0347, 4.16, 0.71, and $4.5176E+05$ N/m² respectively. Figure 4.2 shows the first and second mode damping ratio vs. excitation frequency for the three methods; the proposed method (third) gives a lower damping ratio than the first (Zhang and Soong, 1992) which uses constant parameters G' and G'' . On the other hand, the second method shows the variation of the damping ratio with frequency. The proposed method is conservative but still within acceptable limits.

The ten-story frame shown in Figure 4.1(b) is also used in this evaluation. All parameters are the same as mentioned previously except that the area of the VE damper, $A = 0.02$ m², for the lighter frame. Figure 4.3 shows the damping ratio for the first two modes vs. excitation frequency for the three cases. Similar results are observed as was shown in Figure 4.2. Note that the damping ratio shown in Figures 4.2 and 4.3 is the effective damping level which includes the inherent damping of the structure (see Figure 4.1) and the damping due to the presence of the VE dampers.

A single frequency excitation is used to examine the parameters G' and G'' of the VE damper. A sinusoidal base acceleration of magnitude 0.015 g and frequency varying from 0.1 to 50 rad/sec. is used to study the three methods. Two buildings, the eight-story shear building and the ten-story frame, are used in this evaluation. The maximum responses for the first floor interstory drift, and for the displacement, velocity, and acceleration of the top floor are shown in Figures 4.4 and 4.5. The maximum response using the proposed method (third) for both structures was very close to the results obtained by using Kasai's method (second method). The results obtained by using the constant parameters (first method) were found smaller than those obtained by the second

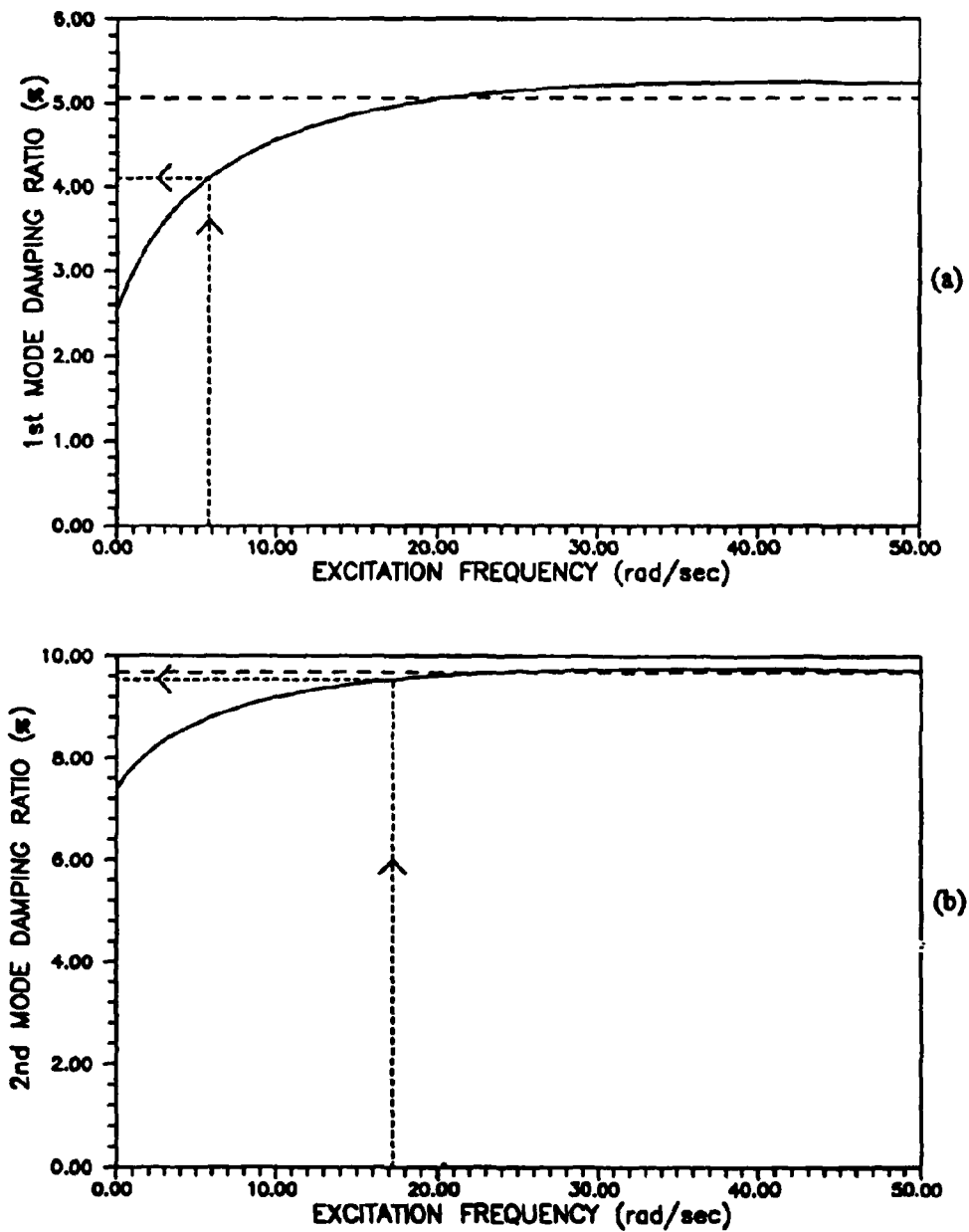


Figure 4.2 Effective damping ratio of the eight-story shear building equipped with one VE damper on the first floor for different excitation frequencies: (a) 1st mode and (b) 2nd mode; - - - - = constant values of shear storage and loss moduli, ——— = varying values using equation (2.4), - · - · - · = proposed method using equation (2.5)

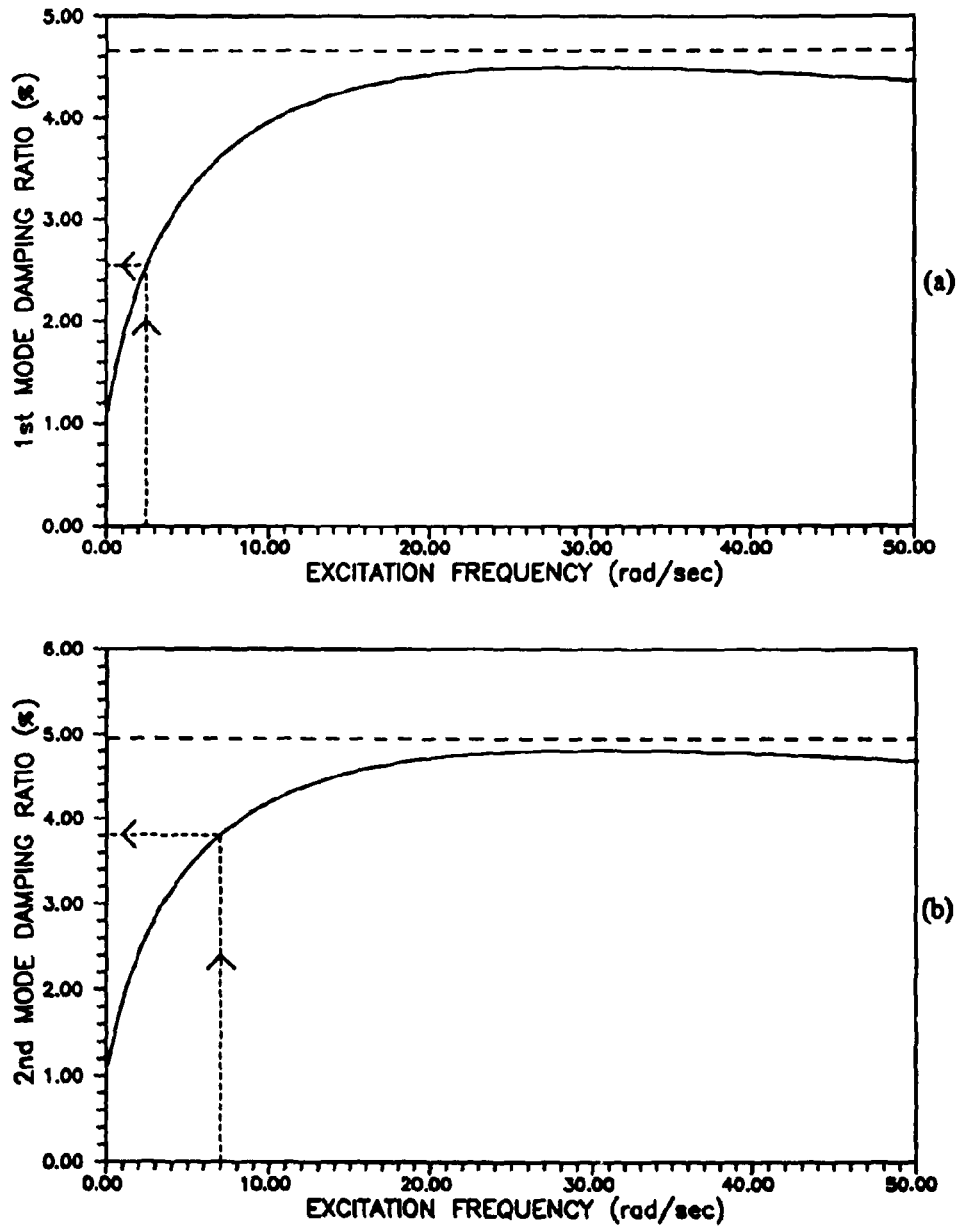


Figure 4.3 Effective damping ratio of the ten-story frame equipped with one VE damper on the first floor for different excitation frequencies: (a) 1st mode and (b) 2nd mode: - - - - = constant values of shear storage and loss moduli, ——— = varying values using equation (2.4), $\dots \rightarrow$ = proposed method using equation (2.5)

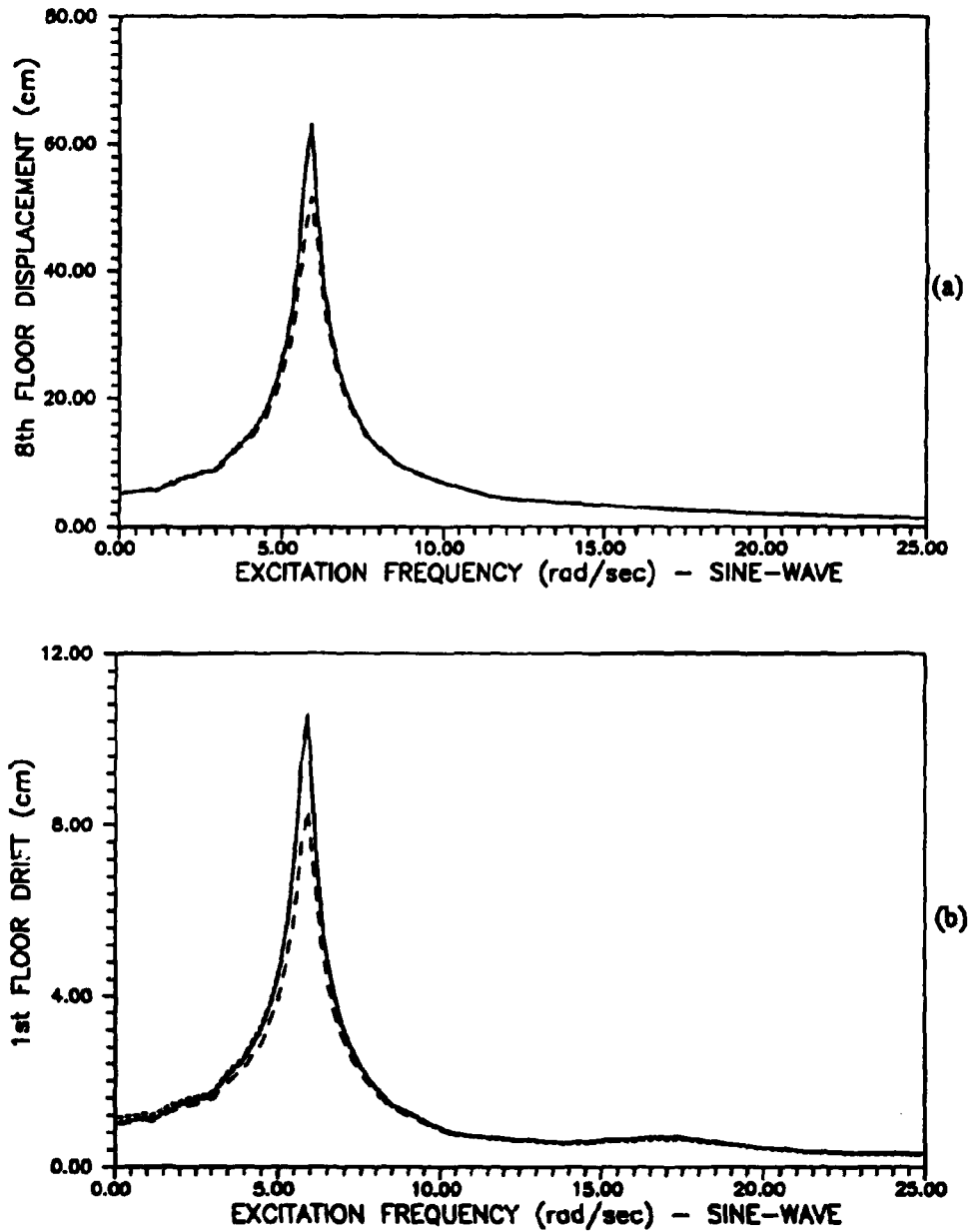


Figure 4.4 Maximum responses of the eight-story shear building equipped with one VE damper on the first floor for a sine wave excitation with varying frequency: (a) displacement and (b) drift; - - - - = constant values of shear storage and loss moduli, ——— = varying values using equation (2.4), ····· = proposed method using equation (2.5)

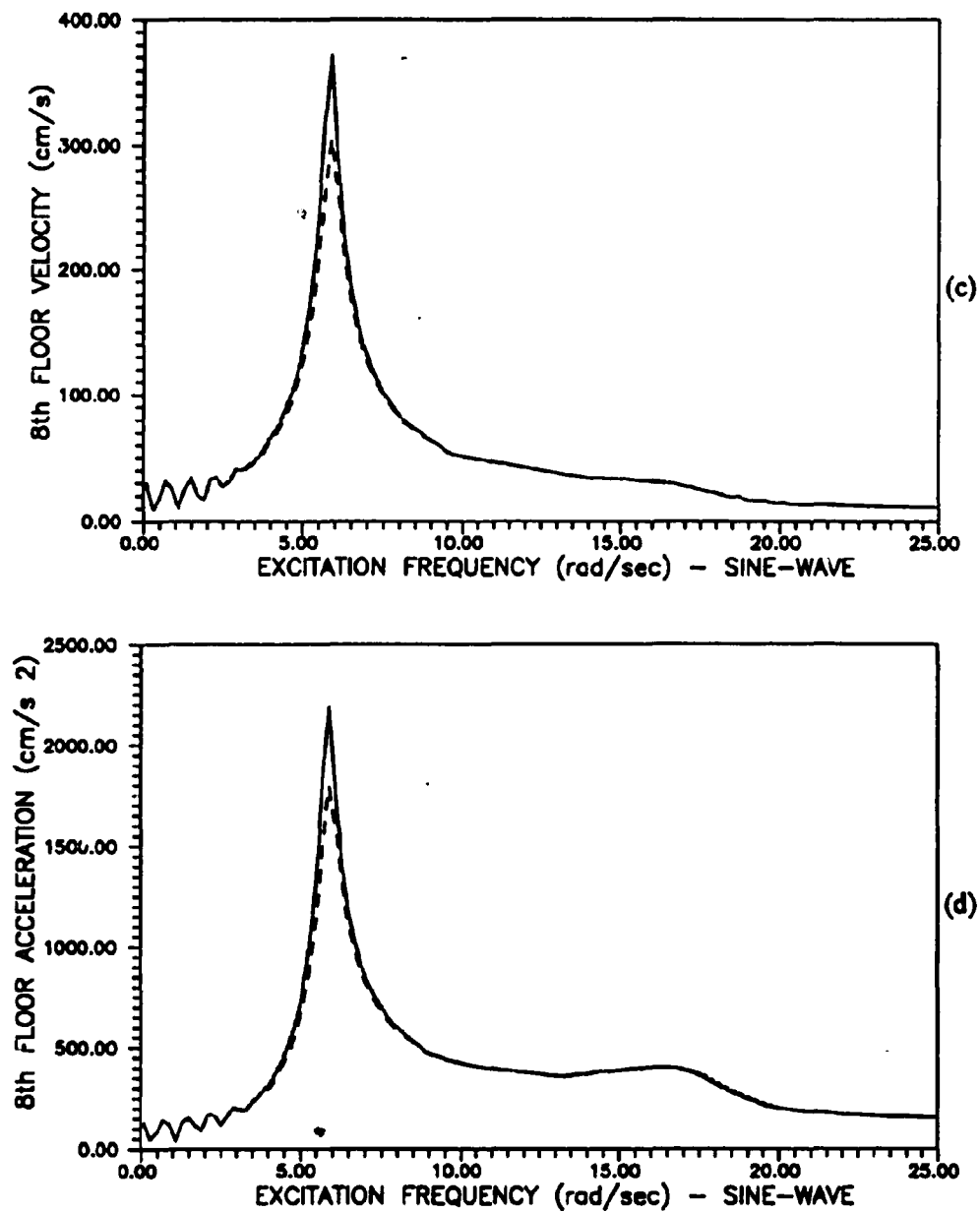


Figure 4.4 (Continued) (c) velocity and (d) acceleration; - - - - = constant values of shear storage and loss moduli, ——— = varying values using equation (2.4), = proposed method using equation (2.5)

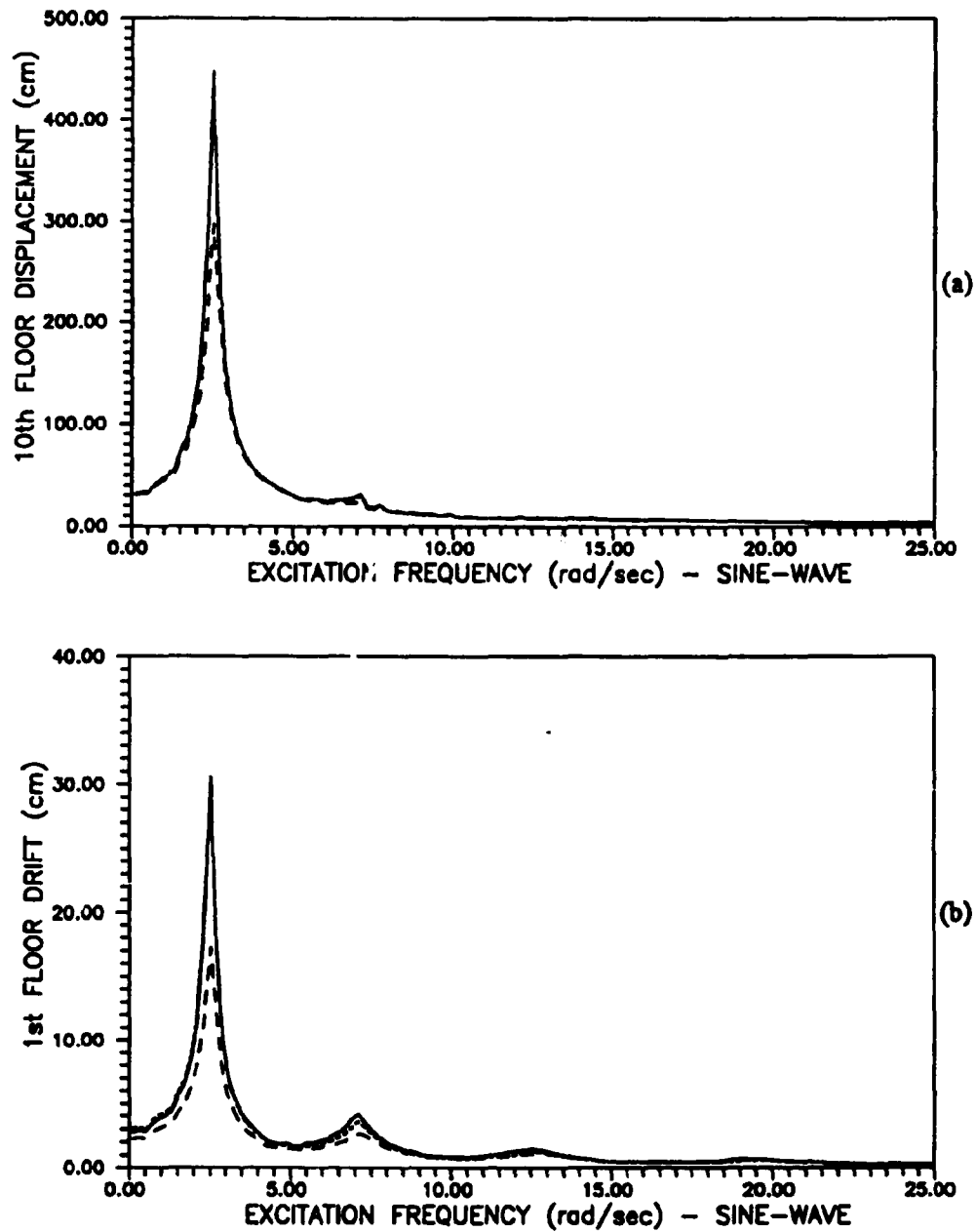


Figure 4.5 Maximum responses of the ten-story frame equipped with one VE damper on the first floor for a sine wave excitation with varying frequency: (a) displacement and (b) drift; ---- = constant values of shear storage and loss moduli, — = varying values using equation (2.4), ····· = proposed method using equation (2.5)

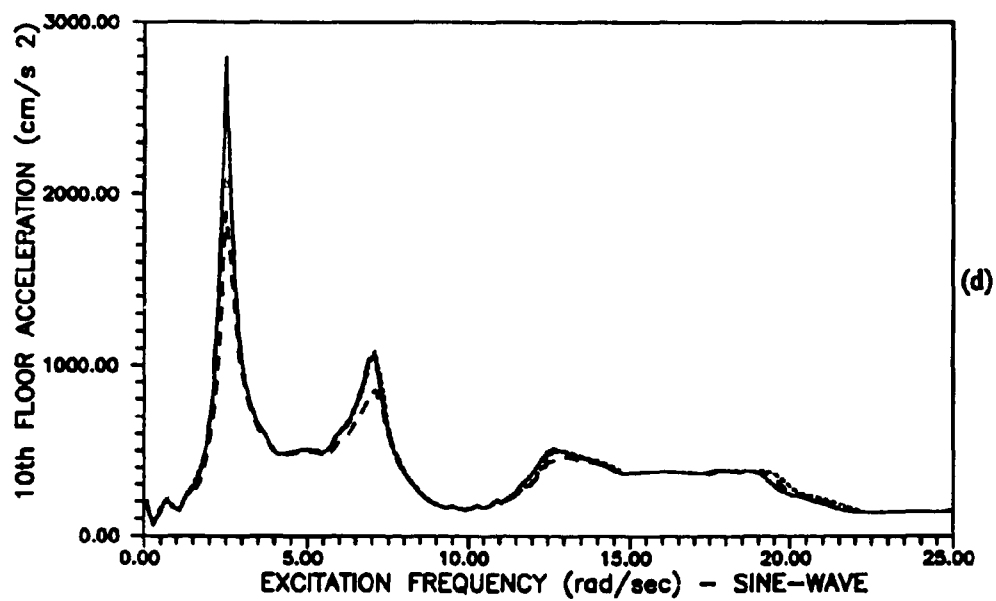
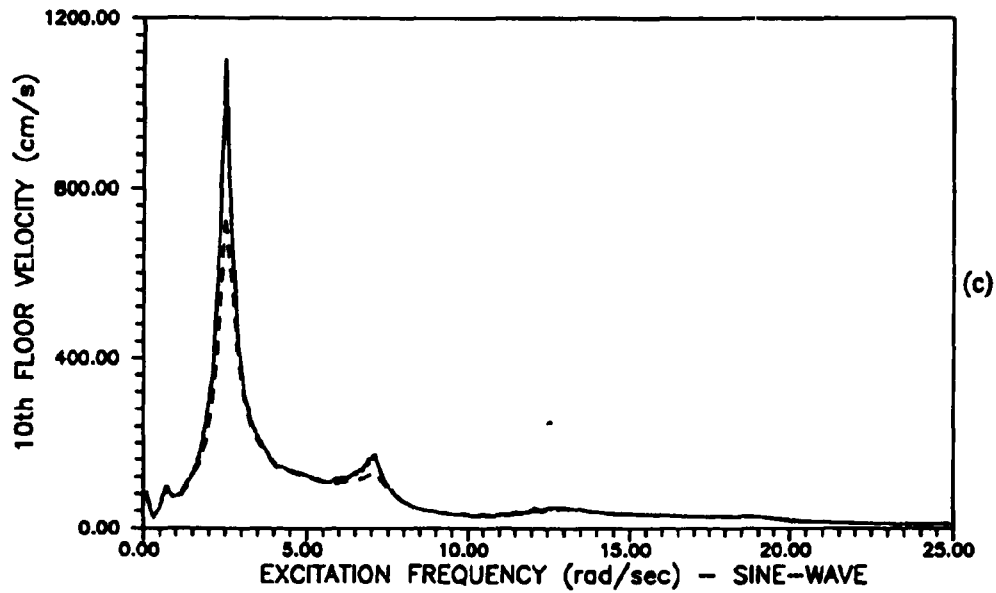


Figure 4.5 (Continued) (c) velocity and (d) acceleration; - - - - = constant values of shear storage and loss moduli, ——— = varying values using equation (2.4), = proposed method using equation (2.5)

method at the excitation frequency close to the fundamental frequency of the structure (resonance condition). The maximum displacement, velocity, and acceleration of the top floor and the first floor interstory drift at the resonance condition are compared in Table 4.1. It can be observed that the results obtained by the proposed method are more conservative than those of the constant assumption of the first method. In addition, the proposed method (third) gives results that are very close to the second method.

A multiple-frequency base acceleration is used to compare the response using the constant assumption of the first method with the method presented here (third method), given as

$$F(t) = 0.0025g [\sin \omega_1 t + 2 \sin \omega_2 t + 3 \sin \omega_3 t]$$

where ω_1 , ω_2 , and ω_3 are the first, second, and third natural frequencies. Note that equation (2.4) for the second method can not be used for this excitation since its derivation is based on a single forcing excitation frequency.

Table 4.1. Maximum response for structures equipped with one VE damper on the first floor subjected to a sinusoidal base acceleration

Properties of VE damper	1st mode total damping (%)	1st floor drift (cm)	Top floor disp. (cm)	Top floor velocity (cm/s)	Top floor accel. (g)
Eight-story Building ($\omega_1 = 5.79$ rad/sec)					
1st method	5.06	8.35	51.62	304.64	1.83
2nd method	4.10	10.52	62.77	370.40	2.23
3rd method	4.10	10.57	62.96	371.59	2.24
Ten-story Frame ($\omega_1 = 2.47$ rad/sec)					
1st method	4.66	17.26	293.02	728.34	1.93
2nd method	2.54	30.53	446.46	1098.74	2.85
3rd method	2.54	30.61	447.19	1100.59	2.85

The maximum responses for both structures are shown in Table 4.2. The responses obtained from the proposed method are larger than those obtained from the constant assumption for both the eight-story building and the ten-story frame for the multiple-frequency base acceleration. In the ten-story frame, the difference of the effective damping level obtained by the two methods is even larger than the eight-story shear building.

Two earthquake records, the S00E component of the May 18, 1940 El-Centro earthquake Imperial Valley record, and the S16E component of the Feb. 9, 1971 San Fernando earthquake Pacoima Dam record, shown in Figure 4.6, are used to evaluate the two methods stated above. The maximum responses of the eight-story shear building and the ten-story frame are shown in Tables 4.3 and 4.4 for the 1940 El-Centro and the 1971 San Fernando earthquakes. Similar results are observed by comparing Tables 4.1 (sinusoidal base acceleration), 4.2 (multiple-frequency base acceleration), and 4.3 and 4.4 (seismic records). It is concluded that in general, the proposed method is conservative for both typical structures regardless of the type of the excitation.

Table 4.2. Maximum response for structures equipped with one VE damper on the first floor subjected to a multiple-frequency base acceleration

Properties of VE damper	1st mode total damping (%)	1st floor drift (cm)	Top floor disp. (cm)	Top floor velocity (cm/s)	Top floor accel. (g)
Eight-story Building					
1st method	5.06	1.41	8.80	49.18	0.47
3rd method	4.10	1.79	10.83	59.09	0.54
Ten-story Frame					
1st method	4.66	0.50	6.60	31.67	0.29
3rd method	2.54	0.61	6.85	32.47	0.29

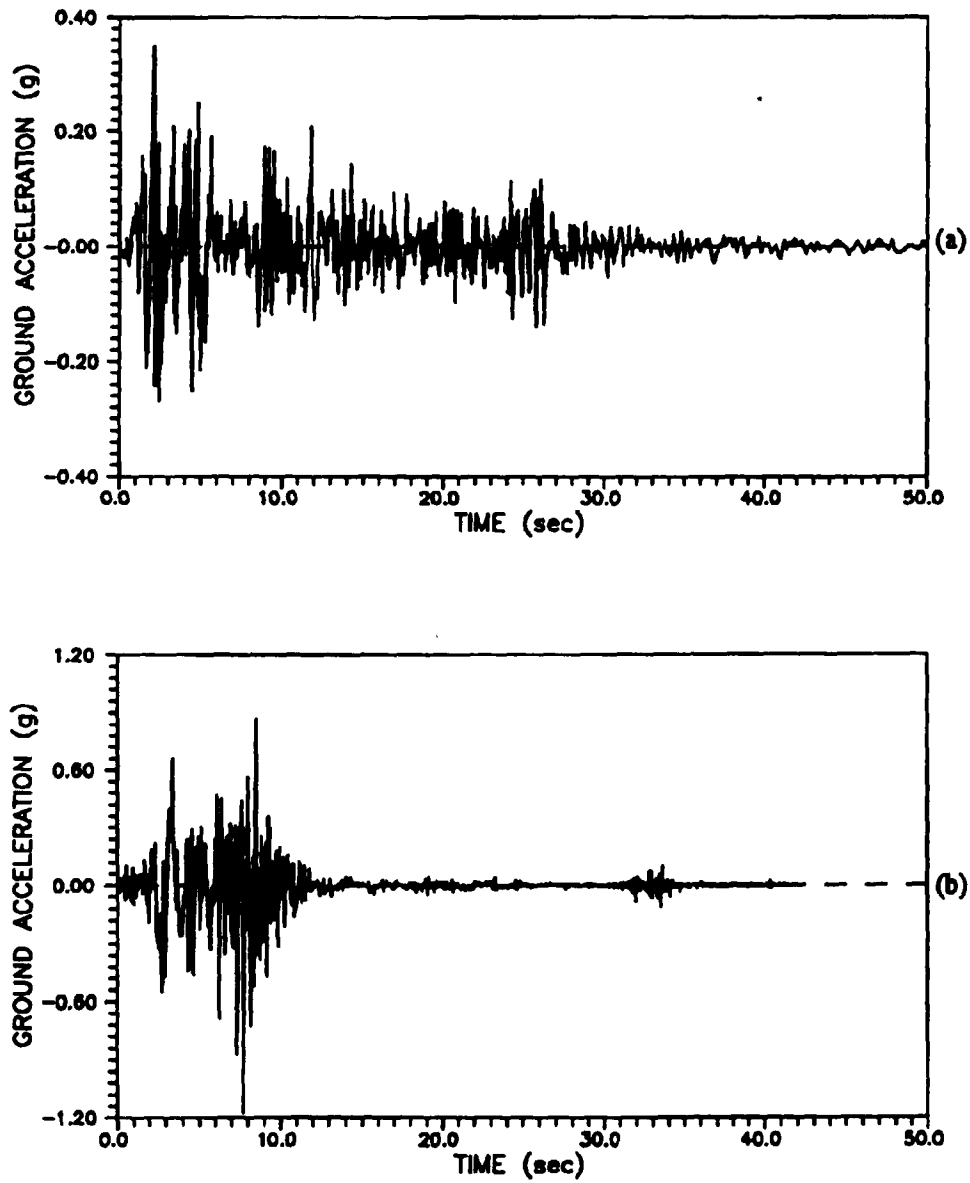


Figure 4.6 Seismic excitations: (a) S00E record of the May 18, 1940 El-Centro earthquake (Imperial Valley record), and (b) S16E record of the Feb. 2, San Fernando earthquake (Pacoima Dam record)

Table 4.3. Maximum response for structures equipped with one VE damper on the first floor subjected to the 1940 El-Centro earthquake

Properties of VE damper	1st mode total damping (%)	1st floor drift (cm)	Top floor disp. (cm)	Top floor elocity (cm/s)	Top floor accel. (g)
Eight-story Building					
1st method	5.06	2.47	15.97	97.39	0.88
3rd method	4.10	2.72	17.17	100.23	0.92
Ten-story Frame					
1st method	4.66	3.90	40.82	128.94	0.67
3rd method	2.54	3.67	45.82	145.04	0.65

Table 4.4. Maximum response for structures equipped with one VE damper on the first floor subjected to the 1971 San Fernando earthquake

Properties of VE damper	1st mode total damping (%)	1st floor drift (cm)	Top floor disp. (cm)	Top floor elocity (cm/s)	Top floor accel. (g)
Eight-story Building					
1st method	5.06	7.11	44.18	248.11	1.94
3rd method	4.10	7.81	46.80	262.63	2.05
Ten-story Frame					
1st method	4.66	4.92	64.01	285.37	1.32
3rd method	2.54	6.32	66.93	301.00	1.52

Placement of VE Dampers

Two shear buildings (Figures 4.1(a) and 4.1(c)) and one ten-story frame (Figure 4.1(b)) have been used to study the response of the structures with a given number of VE dampers at different locations. Two cases are described. In the first case one VE damper is installed at each floor, and in the second case all VE dampers are placed on the first floor. The parameters G' and G'' of the VE dampers are determined by the third method presented in the previous section. The constants, a , b , α , and G of equation (2.4) are assumed as 0.0347, 4.16, 0.71, and $4.5176\text{E}+05$ N/m², respectively. The cross-sectional area of the VE dampers is 0.005 m² for the five-story shear building, 0.09 m² for the eight-story shear building, and 0.02 m² for the ten-story frame. The thickness of the VE dampers for the three structures is identical and equals 0.0127 m. The above dimensions were chosen from relative mass and structural response considerations.

Figure 4.7 shows how the effective damping ratio (which includes the structure's damping) varies with the number and the location of the VE dampers. It is obvious that larger damping ratios can be obtained if the VE dampers are placed on separate floors rather than if they are all concentrated on the first floor. This is more obvious in the cases of the lighter structures, such as the five-story building and the ten-story frame. However, for the eight-story shear building the variation of the effective damping ratios for the two cases is not very significant. The reason for the small difference in the latter case is due to the larger mass of the eight-story shear building. This shows that perhaps more than one damper per floor is needed for the eight-story shear building.

Four earthquake records, the 1940 El-Centro earthquake, 1971 San Fernando

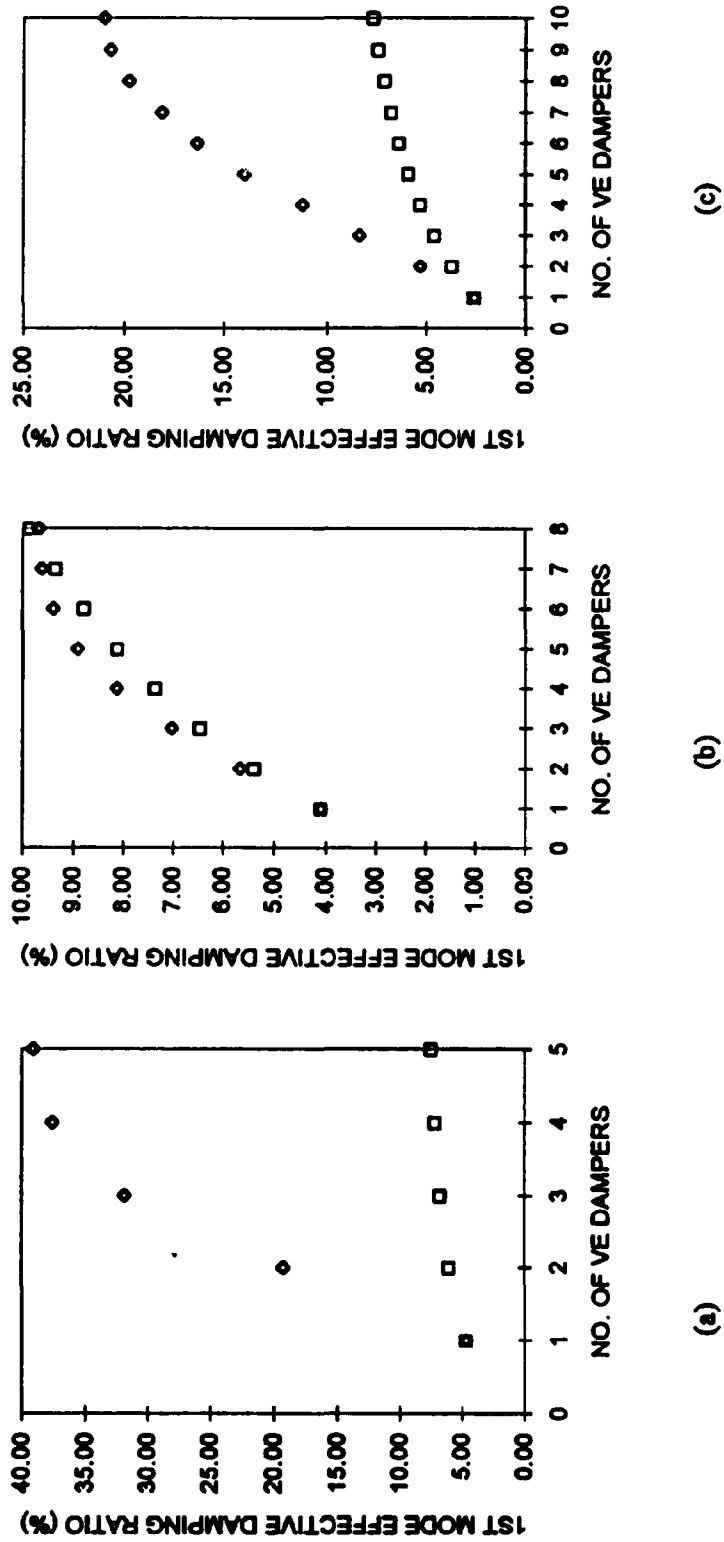


Figure 4.7 Effective damping ratio as a function of the location and number of VE dampers for: (a) five-story shear building, (b) eight-story shear building, and (c) ten-story shear building; \diamond = one VE damper on each floor, \square = all VE dampers on first floor

earthquake, the N90W component of the Sep. 19, 1985 Mexico City (Cuerrero-Michoacan Coast, Mexico) earthquake (Figure 4.8(a)), and the S90N component of the Jan. 17, 1994 Northridge (Santa Monica station at City Hall, CA) earthquake (Figure 4.8(b)) are used to examine the performance of the VE dampers for the three test structures. Figure 4.9 shows the spectral amplitude as a function of the frequency content of the four earthquakes. Figure 4.10 shows the displacement reduction for the three structures stated above, equipped with one VE damper on the first floor. It can be observed that the reduction is largest for the five-story and eight-story shear buildings during the 1994 Northridge earthquake as compared to the other three earthquakes. However, the displacement reduction for the ten-story frame is more efficient during the 1985 Mexico City earthquake. Again, it should be noted that the five-story shear building and ten-story frame are much lighter than the eight-story shear frame. Hence, for larger reduction of the response the latter should be equipped with more than one damper.

The displacement, velocity, and acceleration reduction ratio for the top floor of each of the three structures equipped with a number of VE dampers are shown in Tables 4.5 - 4.7 for the four earthquakes. Greater reductions in the response of the top floor are achieved when the VE dampers are placed one per floor rather than all on the first floor. The displacement responses in Table 4.5 are reduced the most for the five-story and eight-story building subjected to the 1994 Northridge earthquake record. For the ten-story frame the displacement reductions are largest when it is subjected to the 1985 Mexico City earthquake record. In general, the response reduction for each structure with the same number and same location of VE dampers but subjected to different earthquakes is within

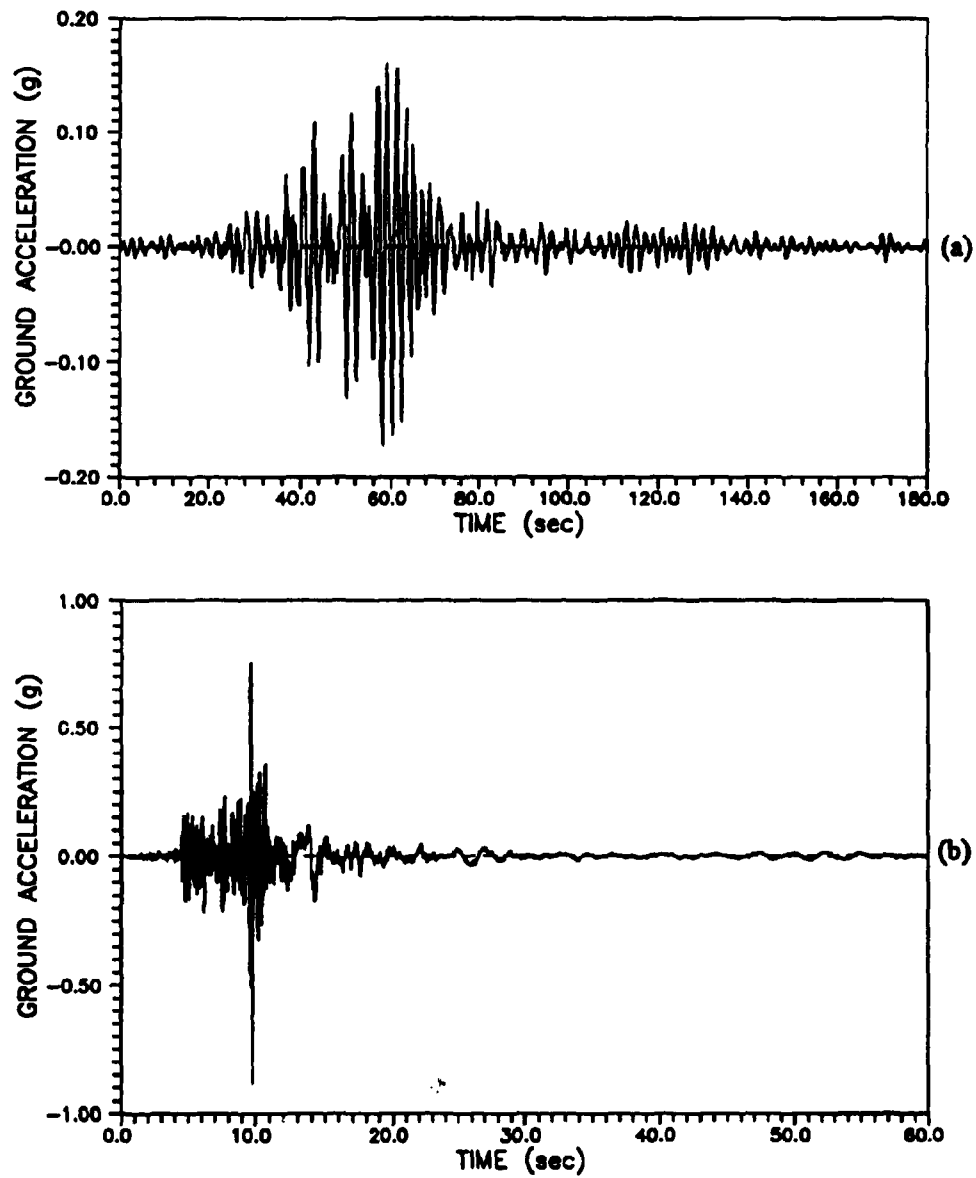


Figure 4.8 Seismic excitations: (a) N90W record of the Sep. 19, 1985 Mexico City earthquake (Cuerrero-Michoacan Coast record) and (b) S90N record of the Jan. 17, Northridge earthquake (Santa Monica station, City Hall record)

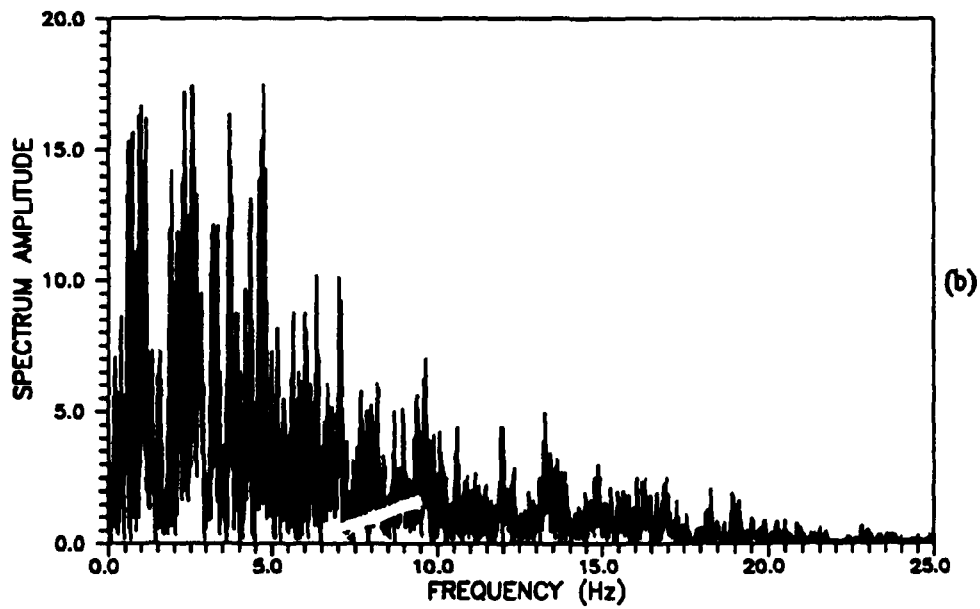
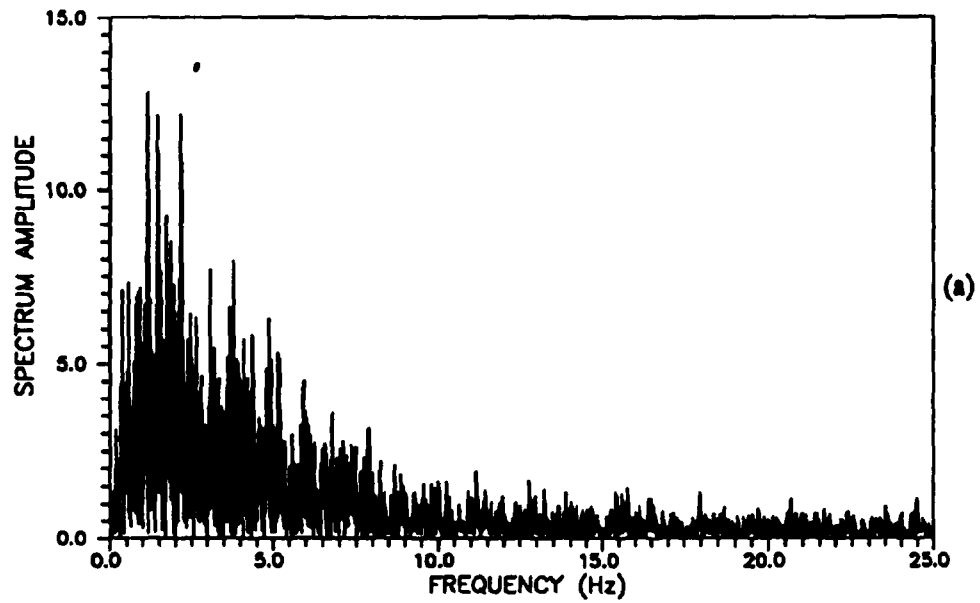


Figure 4.9 Spectrum amplitude of the excitation: (a) 1940 El-Centro earthquake shown in Figure 4.6(a), and (b) 1971 San Fernando earthquake shown in Figure 4.6(b)

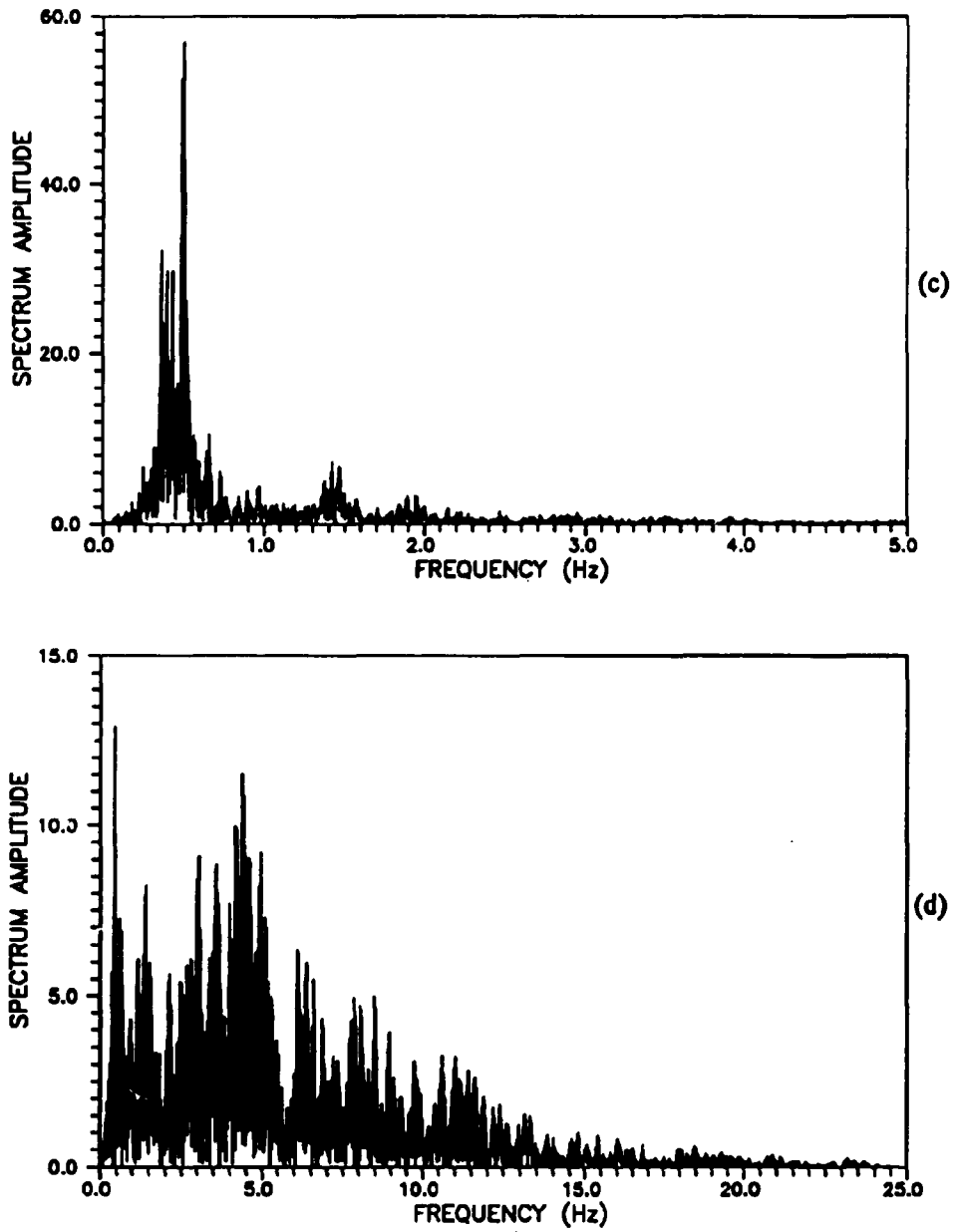


Figure 4.9 (Continued) (c) 1985 Mexico City earthquake shown in Figure 4.8(a), and (d) 1994 Northridge earthquake shown in Figure 4.8(b)

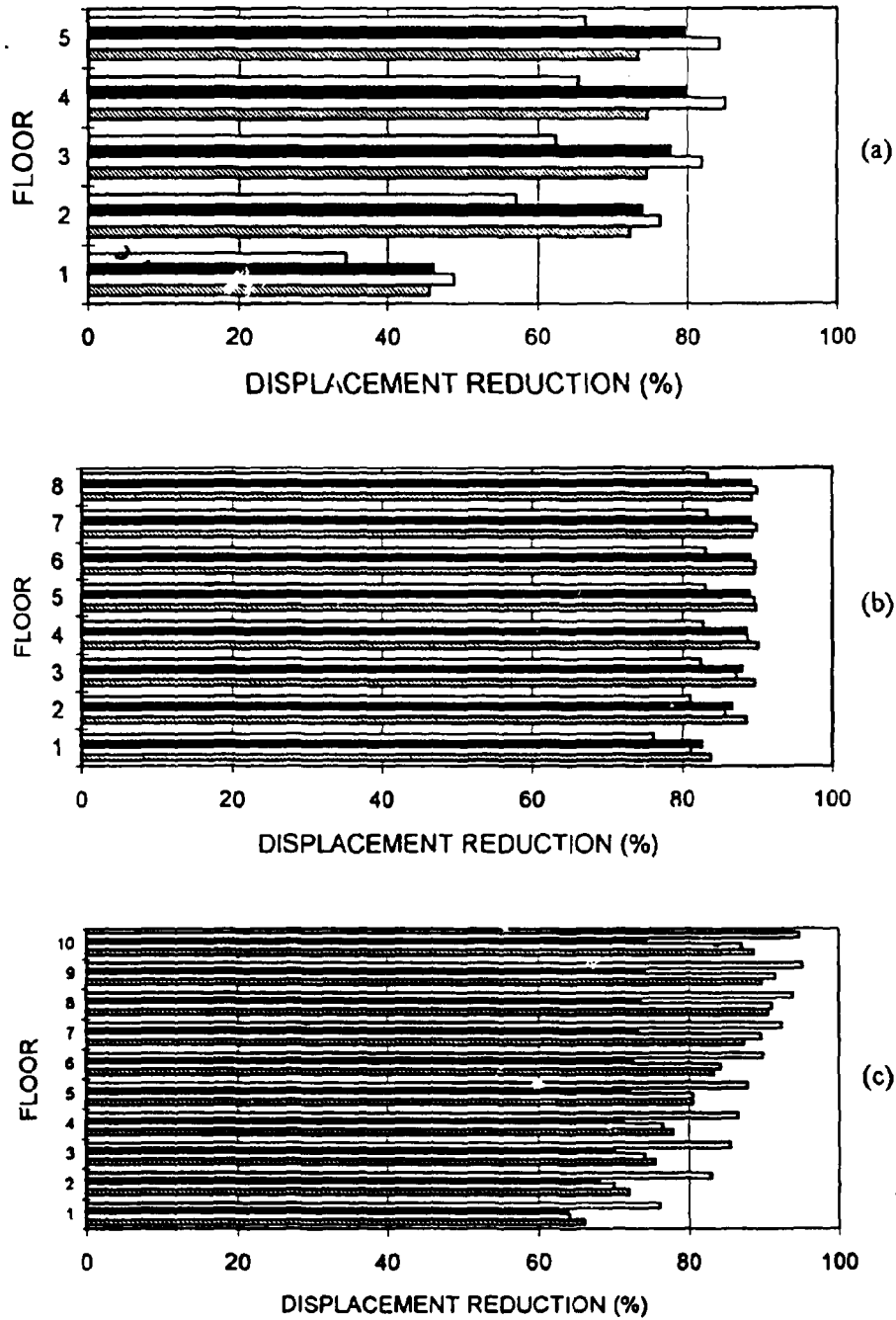


Figure 4.10 Displacement reduction for the structure with one VE damper on the first floor: (a) five-story shear building, (b) eight-story shear building, and (c) ten-story frame; □ = Northridge earthquake, ■ = Mexico City earthquake, ▨ = San Fernando earthquake, ▩ = El-Centro earthquake

Table 4.5. Top floor displacement as compared to the uncontrolled response with the addition of VE dampers

No. of VE dampers	One VE damper per floor					All VE damper on the first floor				
	1st mode damping ratio (%)	EI-Centro (%)	San Fernando (%)	Mexico City (%)	North-ridge (%)	1st mode damping ratio (%)	EI-Centro (%)	San Fernando (%)	Mexico City (%)	North-ridge (%)
Five-story Shear Building										
1	4.66	73	84	80	66	4.66	73	84	80	66
2	19.26	34	41	46	38	6.03	65	77	77	60
3	31.85	20	28	30	24	6.76	61	76	74	58
4	37.63	15	22	24	18	7.20	59	75	73	56
5	39.14	13	19	20	15	7.50	57	75	71	55
Eight-story Shear Building										
1	4.10	89	90	89	83	4.10	89	90	89	83
2	5.68	80	81	79	76	5.40	81	83	81	77
3	7.04	72	74	73	71	6.47	75	77	75	72
4	8.14	67	69	69	68	7.37	70	72	72	70
5	8.92	63	66	67	66	8.13	66	69	69	67
6	9.40	61	65	66	64	8.78	63	66	67	66
7	9.62	59	64	66	64	9.35	61	65	66	64
8	9.68	59	64	65	63	9.85	58	63	65	63
Ten-story Frame										
1	2.54	89	87	74	95	2.54	89	89	74	95
2	5.29	75	81	55	85	3.68	82	84	64	90
3	8.35	64	78	44	76	4.57	78	83	58	87
4	11.17	56	76	37	68	5.28	75	81	55	84
5	14.01	49	74	32	61	5.86	73	80	52	82
6	16.37	44	71	28	56	6.35	71	79	50	82
7	18.13	41	68	26	51	6.75	69	78	49	80
8	19.77	38	63	23	46	7.10	68	78	47	78
9	20.72	35	59	22	42	7.41	67	77	46	77
10	21.03	34	57	21	41	7.67	66	77	45	76

Table 4.6. Top floor velocity as compared to the uncontrolled response with the addition of VE dampers

No. of VE dampers	One VE damper per floor					All VE damper on the first floor				
	1st mode damping ratio (%)	EI-Centro (%)	San Fernando (%)	Mexico City (%)	North-ridge (%)	1st mode damping ratio (%)	EI-Centro (%)	San Fernando (%)	Mexico City (%)	North-ridge (%)
Five-story Shear Building										
1	4.66	81	82	48	62	4.66	82	82	48	62
2	19.26	47	43	23	43	6.03	76	73	41	59
3	31.85	32	31	14	29	6.76	73	68	38	57
4	37.63	26	25	11	22	7.20	71	64	37	56
5	39.14	22	21	10	19	7.50	70	62	37	56
Eight-story Shear Building										
1	4.10	94	92	90	84	4.10	94	92	90	84
2	5.68	92	84	90	78	5.40	92	85	90	78
3	7.04	89	78	90	76	6.47	89	80	90	74
4	8.14	86	74	89	72	7.37	87	76	89	72
5	8.92	83	70	87	69	8.13	85	73	88	70
6	9.40	80	68	86	66	8.78	82	70	87	69
7	9.62	79	66	85	63	9.35	80	68	86	68
8	9.68	78	66	84	63	9.85	79	65	85	67
Ten-story Frame										
1	2.54	77	94	76	87	2.54	77	94	76	87
2	5.29	61	85	57	78	3.68	68	90	66	83
3	8.35	52	80	46	69	4.57	64	87	60	80
4	11.17	47	77	39	62	5.28	61	85	57	77
5	14.01	44	75	34	56	5.86	59	84	54	76
6	16.37	42	73	30	52	6.35	57	83	52	74
7	18.13	38	70	27	48	6.75	56	82	51	73
8	19.77	33	65	24	45	7.10	55	81	49	72
9	20.72	29	61	23	43	7.41	54	80	48	71
10	21.03	28	59	22	41	7.67	53	79	47	70

Table 4.7. Top floor acceleration as compared to the uncontrolled response with the addition of VE dampers

No. of VE dampers	One VE damper per floor					All VE damper on the first floor				
	1st mode damping ratio (%)	El-Centro (%)	San Fernando (%)	Mexico City (%)	North-ridge (%)	1st mode damping ratio (%)	El-Centro (%)	San Fernando (%)	Mexico City (%)	North-ridge (%)
Five-story Shear Building										
1	4.66	82	74	43	76	4.66	82	74	43	76
2	19.26	58	50	20	58	6.03	78	76	39	70
3	31.85	35	40	13	47	6.76	76	76	37	67
4	37.63	30	35	11	37	7.20	76	76	36	66
5	39.14	29	34	9	33	7.50	75	75	35	65
Eight-story Shear Building										
1	4.10	93	85	91	92	4.10	93	85	91	92
2	5.68	87	78	87	90	5.40	88	79	88	87
3	7.04	81	72	86	88	6.47	83	74	86	84
4	8.14	76	68	84	83	7.37	80	70	84	81
5	8.92	73	65	82	80	8.13	76	68	83	79
6	9.40	71	64	81	76	8.78	73	66	82	77
7	9.62	70	64	80	78	9.35	71	64	81	76
8	9.68	69	63	79	78	9.85	69	63	80	75
Ten-story Frame										
1	2.54	78	74	80	91	2.54	78	74	80	91
2	5.29	72	61	64	88	3.68	73	63	71	87
3	8.35	67	60	54	84	4.57	71	59	66	85
4	11.17	61	58	46	82	5.28	69	59	63	84
5	14.01	55	57	40	81	5.86	68	59	61	82
6	16.37	52	56	35	78	6.35	67	58	59	81
7	18.13	49	55	33	79	6.75	66	58	51	81
8	19.77	48	53	30	84	7.10	65	58	57	81
9	20.72	47	52	28	84	7.41	64	58	56	80
10	21.03	49	51	28	84	7.67	63	58	55	80

20 %. However, the velocity and acceleration reductions for the five-story shear building subjected to the 1985 Mexico City earthquake are reduced much more than the other three earthquakes.

Design of VE Damper

An optimization method is investigated to design the minimum size of VE dampers for achieving an expected effective damping ratio of the structural system. The modified method of feasible directions, a subprogram of DOT (Design Optimization Tools) program developed by VMA Engineering (1993), is used to optimize the required cross-sectional area of the VE dampers on the different floors of the structure. The parameters G' and G'' of the VE dampers are determined by the third method presented in the previous section. The constants, a , b , α , and G of equation (2.4) are assumed as 0.0347, 4.16, 0.71, and $4.5176E+05$ N/m², respectively.

The effective damping ratios were obtained from the previous section by using the VE dampers with cross-sectional area equal to 0.09 m² for the eight-story shear building, and 0.02 m² for the ten-story frame. These damping ratios are used to find the optimum area required for the VE dampers. The inherent structural damping level of the first mode equals 2.5 % of critical for the eight-story building and 1 % for the ten-story frame. The thickness of the VE dampers is assumed to be a fixed value and equals 0.0127 m. The side constraints of the maximum and minimum sizes of the VE damper are 5.0 and 0.0001 m² respectively.

Table 4.8 shows the optimal designs for the minimum cross-sectional area of the

Table 4.8 Optimal designs for the minimum cross-sectional area of VE dampers for the eight-story shear building (m²)

Floor	First mode effective damping ratio (%)							
	4.10	5.66	7.02	8.12	8.90	9.37	9.60	9.65
1	0.0849	0.0959	0.1277	0.1499	0.1640	0.1751	0.1775	0.1759
2	-	0.0780	0.0976	0.1244	0.1363	0.1588	0.1437	0.1487
3	-	-	0.0337	0.0583	0.0840	0.0864	0.1030	0.0993
4	-	-	-	0.0001	0.0034	0.0027	0.0152	0.0200
5	-	-	-	-	0.0001	0.0001	0.0001	0.0001
6	-	-	-	-	-	0.0001	0.0001	0.0001
7	-	-	-	-	-	-	0.0001	0.0001
8	-	-	-	-	-	-	-	0.0001
Sum.	0.0849	0.1739	0.2590	0.3327	0.3878	0.4232	0.4397	0.4443
Diff.	0.0051	0.0061	0.0110	0.0273	0.0622	0.1168	0.1903	0.2757

VE damper for an expected effective damping in the first mode of the eight-story building

One to eight dampers are used, one on each floor. The last row in Table 4.8 shows the difference in the total area of the VE dampers between the optimal designs and the designs using the same size for each VE damper. The latter are the damper dimensions used in the previous section, i.e. $A = 0.09 \text{ m}^2$ for the eight-story building. It can be observed that the total value of the cross-sectional area of the VE dampers obtained from the optimal design for a certain number of VE dampers is less than the value using the same size for each VE damper. For example, the required area of VE dampers when the building is equipped with a VE damper at each floor obtained from the optimal design is about 38 % less compared to the design using the same size for each damper. It should be noted that some of the required areas designed by the optimization method reach the side constraints, i.e., the minimum area, which suggests that no VE damper is required at that floor. Table 4.9 shows the designs when the side constraint minimum equals 0.0 m^2 . It can be seen that the total areas of the VE dampers are close to the values shown in Table 4.8, but only a few lower floors are required to be equipped with the VE dampers.

Table 4.9 Optimal designs for the minimum cross-sectional area of VE dampers for the eight-story shear building with minimum side constraint equal to zero (m²)

Floor	First mode effective damping ratio (%)							
	4.10	5.66	7.02	8.12	8.90	9.37	9.60	9.65
1	0.0849	0.0959	0.1277	0.1415	0.1636	0.1760	0.1781	0.1729
2	-	0.0780	0.0976	0.1241	0.1375	0.1532	0.1507	0.1562
3	-	-	0.0337	0.0672	0.0728	0.0944	0.1031	0.1176
4	-	-	-	none	0.0144	none	0.0078	none
5	-	-	-	-	none	none	none	none
6	-	-	-	-	-	none	none	none
7	-	-	-	-	-	-	none	none
8	-	-	-	-	-	-	-	none
Sum.	0.0849	0.1739	0.2590	0.3328	0.3883	0.4236	0.4397	0.4467
Diff.	0.0051	0.0061	0.0110	0.0272	0.0617	0.1164	0.1903	0.2733

The optimal designs for the minimum cross-sectional area of the VE damper for an expected effective damping in the first mode of the ten-story frame are shown in Table 4.10. Similar conclusions about the results can be observed to the conclusions reached about the designs shown in Table 4.8. However, for this ten-story frame a smaller area of VE damper is required for the first floor when more than one floor is equipped with VE dampers. This suggests that the best location of VE dampers might be a floor other than the first.

Table 4.10 Optimal designs for the minimum cross-sectional area of VE dampers for the ten-story frame (m²)

Floor	First mode effective damping ratio (%)									
	2.54	5.29	8.33	11.14	13.97	16.37	18.08	19.72	20.66	20.97
1	0.0194	0.0001	0.0001	0.0001	0.0001	0.0001	0.0001	0.0001	0.0001	0.0001
2	-	0.0299	0.0127	0.0182	0.0150	0.0142	0.0272	0.0274	0.0294	0.0301
3	-	-	0.0315	0.0216	0.0229	0.0328	0.0276	0.0301	0.0307	0.0298
4	-	-	-	0.0280	0.0154	0.0213	0.0176	0.0247	0.0273	0.0213
5	-	-	-	-	0.0340	0.0209	0.0242	0.0217	0.0218	0.0289
6	-	-	-	-	-	0.0182	0.0173	0.0196	0.0229	0.0211
7	-	-	-	-	-	-	0.0099	0.0054	0.0075	0.0076
8	-	-	-	-	-	-	-	0.0105	0.0103	0.0138
9	-	-	-	-	-	-	-	-	0.0008	0.0007
10	-	-	-	-	-	-	-	-	-	0.0001
Sum.	0.0194	0.0300	0.0479	0.0679	0.0874	0.1075	0.1239	0.1395	0.1508	0.1543
Diff.	0.0006	0.0100	0.0121	0.0121	0.0126	0.0125	0.0161	0.0205	0.0292	0.0457

The optimal designs using a constant number of VE dampers but different levels of the effective damping ratio are also investigated. Table 4.11 shows the designs for the 10, 15, 20, and 25 % of critical effective damping ratio by locating one VE damper on the first and second floors of the eight-story building or the ten-story frame. The same table shows the case when one VE damper is located on the first, second, third, and fourth floors of the two structures. The thickness of the VE dampers is assumed to be a fixed value and equals 0.01 m in this study. The side constraints of the maximum and minimum sizes of the VE damper are 5.0 and 0.01 m² respectively. It can be found that by increasing the size of the VE damper one can increase the effective damping level for the same number of VE dampers located in the structure. However, for the same level of effective damping, the structure equipped with VE dampers on the first and second floors only, needs considerably more material than the structure equipped with VE dampers on the first, second, third, and fourth floors. For the ten-story frame, if only the first and second floors are equipped with VE dampers, the structure cannot even reach the effective damping level of 25 % of critical.

Parametric Study of Active Bracing System

The performance of the active bracing system (ABS) is examined by using the linear quadratic regulator (LQR) optimal control method and the instantaneous optimal control (IOC) for the eight-story shear building. Both the identity matrix and the matrix obtained using the Lyapunov method as the weighting matrix Q are used in the IOC. The maximum displacement of the eighth floor is set arbitrarily to 70 % of the uncontrolled

Table 4.12. Comparison of the control forces, damping ratios, and weighting matrices for the 1940 El-Centro earthquake record

Location of Controller Optimal Control Method	w/o Control	ABS on the 1st floor only			ABS on the 1st & 2nd floor		
		LQR	IOC		LQR	IOC	
Q matrix	-	I^1	I	Lyapunov ²	I	I	Lyapunov ³
Constant of R matrix ($r \times I$)	-	1.164E-13	7.20E-16	1.96E-15	2.272E-13	2.25E-15	4.50E-15
1st floor CF (kN)	-	3,176	4,334	3,203	1,642	1,908	1,697
2nd floor CF (kN)	-	-	-	-	1,578	1,593	1,504
Structural damping ratio	2.50 %	2.50 %	2.50 %	2.50 %	2.50 %	2.50 %	2.50 %
ABS damping ratio	-	4.57 %	8.07 %	4.64 %	4.54 %	4.94 %	4.54 %
Total effective damping ratio	2.50 %	7.07 %	10.57 %	7.14 %	7.04 %	7.44 %	7.04 %
Max. Disp. (m) - 8th Fl.	0.193	0.135	0.135	0.134	0.135	0.135	0.135
Max. Vel. (m/s) - 8th Fl.	1.062	0.811	0.885	0.813	0.812	0.809	0.820
Max. Accel. (g) - 8th Fl.	0.990	0.807	0.804	0.808	0.805	0.796	0.809

¹ Identity matrix.

² Matrix based on Lyapunov method for one controller shown in Table 4.13.

³ Matrix based on Lyapunov method for two controllers shown in Table 4.14.

response, i.e., a reduction of 30 % is to be achieved. A total of six cases are studied. In three of the cases, an ABS is placed on the first floor only, and in the remaining three cases an ABS is placed on both the first and second floors. Simulation results are compared in Table 4.12 for the required control force magnitude (CF), effective damping ratio achieved, and maximum response using the 1940 El-Centro earthquake of Figure 4.6(a).

It should be noted that all damping ratios shown in Table 4.12 are referenced to the fundamental mode, but in the analysis all the modes have been considered. The results show that when two controllers are used, the maximum control force per controller is reduced to approximately one-half of the case with only one controller. This is important for design purposes because smaller actuators are more readily available and less costly than larger actuators. Table 4.8 shows that when the Lyapunov-based Q matrix is used in the IOC (obtained from equation (2.14) and shown in Tables 4.13 and 4.14), approximately the same maximum control forces are required to obtain results identical to those using the LQR optimal control; these forces are smaller than those required by using the identity matrix in the IOC.

Performance of Different Control Algorithms

The instantaneous optimal control (IOC) with the Lyapunov-based Q weighting matrix, the drift performance index (DPI) control, and the velocity performance index (VPI) control described in Chapter 2 are compared for the following two cases : (a) for the same level of maximum control force compare the response, and (b) for the same

Table 4.14. Lyapunov matrix for the eight-story building equipped with an ABS on the first and second floors

$$Q = [Q_1 \mid Q_2]$$

$Q_1 =$.58022E+02	.63819E-01	.34343E-01	.77930E-01	.11653E+00	.71723E-01	.71849E-01	.18467E-01
	.63819E-01	.58057E+02	.14224E+00	.13289E+00	.15361E+00	.18856E+00	.69436E-01	.91277E-01
	.34343E-01	.14224E+00	.58157E+02	.20581E+00	.21511E+00	.15548E+00	.19368E+00	.14926E+00
	.77930E-01	.13289E+00	.20581E+00	.58236E+02	.20987E+00	.21890E+00	.23217E+00	.25163E+00
	.11653E+00	.15361E+00	.21511E+00	.20987E+00	.58241E+02	.28703E+00	.28076E+00	.33471E+00
	.71723E-01	.18856E+00	.15548E+00	.21890E+00	.28703E+00	.58301E+02	.38869E+00	.36164E+00
	.71849E-01	.69436E-01	.19368E+00	.23217E+00	.28076E+00	.38869E+00	.58383E+02	.41595E+00
	.18467E-01	.91277E-01	.14926E+00	.25163E+00	.33471E+00	.36164E+00	.41595E+00	.58437E+02
	.61695E-02	.61695E-02	.65465E-02	.57356E-02	.69860E-02	.64041E-02	.59891E-02	.63092E-02
	.63657E-02	.65514E-02	.70890E-02	.64366E-02	.73063E-02	.67878E-02	.67580E-02	.66125E-02
	.64934E-02	.64563E-02	.75627E-02	.69835E-02	.78130E-02	.72767E-02	.72808E-02	.70905E-02
	.66260E-02	.64184E-02	.75197E-02	.74178E-02	.83927E-02	.77804E-02	.76991E-02	.76206E-02
	.63710E-02	.65725E-02	.75948E-02	.73617E-02	.88933E-02	.83007E-02	.81854E-02	.81546E-02
	.65061E-02	.65554E-02	.75826E-02	.73953E-02	.88801E-02	.87845E-02	.86989E-02	.86690E-02
	.68012E-02	.64526E-02	.75501E-02	.74334E-02	.89008E-02	.87646E-02	.91809E-02	.92030E-02
	.65776E-02	.66047E-02	.76137E-02	.74235E-02	.88902E-02	.87831E-02	.91578E-02	.97135E-02
$Q_2 =$.64671E-02	.63657E-02	.64934E-02	.66260E-02	.63710E-02	.65061E-02	.68012E-02	.65776E-02
	.61695E-02	.65514E-02	.70890E-02	.64184E-02	.65725E-02	.65554E-02	.64526E-02	.66047E-02
	.65465E-02	.70890E-02	.75627E-02	.75197E-02	.75948E-02	.75826E-02	.75501E-02	.76137E-02
	.57356E-02	.64366E-02	.69835E-02	.74178E-02	.73617E-02	.73953E-02	.74334E-02	.74235E-02
	.69860E-02	.73063E-02	.78130E-02	.83927E-02	.88933E-02	.8801E-02	.89008E-02	.88902E-02
	.64041E-02	.67878E-02	.72767E-02	.77804E-02	.83007E-02	.87845E-02	.87646E-02	.87831E-02
	.59891E-02	.67580E-02	.72808E-02	.76991E-02	.81854E-02	.86989E-02	.91809E-02	.91578E-02
	.63092E-02	.66125E-02	.70905E-02	.76206E-02	.81546E-02	.86690E-02	.92030E-02	.97135E-02
	.63948E-01	.64342E-01	.64699E-01	.65018E-01	.65276E-01	.65420E-01	.65502E-01	.65517E-01
	.64342E-01	.64342E-01	.64699E-01	.65018E-01	.65276E-01	.65420E-01	.65502E-01	.65517E-01
	.64699E-01	.64342E-01	.18403E+00	.18491E+00	.18570E+00	.18608E+00	.18641E+00	.18656E+00
	.65018E-01	.65018E-01	.18491E+00	.24490E+00	.24580E+00	.24649E+00	.24697E+00	.24722E+00
	.65276E-01	.65276E-01	.18560E+00	.24580E+00	.30582E+00	.30670E+00	.30731E+00	.30765E+00
	.65420E-01	.65420E-01	.18608E+00	.24649E+00	.30670E+00	.36663E+00	.36737E+00	.36774E+00
	.65502E-01	.65502E-01	.18641E+00	.24697E+00	.30731E+00	.36737E+00	.42706E+00	.42747E+00
	.65517E-01	.65517E-01	.18656E+00	.24722E+00	.30765E+00	.36774E+00	.42747E+00	.48680E+00

Table 4.13. Lyapunov matrix for the eight-story building equipped with an ABS on the first floor

$$Q = [Q_1, Q_2]$$

$$Q_1 = \begin{bmatrix} .58022E+02 & .47299E-01 & .38581E-01 & .77748E-01 & .81274E-01 & .78451E-01 & .64961E-01 & -.27569E-03 \\ .47299E-01 & .58050E+02 & .14401E+00 & .12519E+00 & .13091E+00 & .18250E+00 & .64815E-01 & .73539E-01 \\ .38581E-01 & .14401E+00 & .58.50E+02 & .19240E+00 & .20518E+00 & .14368E+00 & .18151E+00 & .13826E+00 \\ .77748E-01 & .12519E+00 & .19240E+00 & .58229E+02 & .20502E+00 & .20568E+00 & .22105E+00 & .24427E+00 \\ .81274E-01 & .13091E+00 & .20518E+00 & .20502E+00 & .58231E+02 & .27936E+00 & .27076E+00 & .32704E+00 \\ .78451E-01 & .18250E+00 & .14368E+00 & .20568E+00 & .27936E+00 & .58291E+02 & .38258E+00 & .35376E+00 \\ .64961E-01 & .38539E-01 & .18151E+00 & .22105E+00 & .27076E+00 & .38258E+00 & .58374E+02 & .41168E+00 \\ -.27569E-03 & .73539E-01 & .13826E+00 & .24427E+00 & .32704E+00 & .35376E+00 & .41168E+00 & .58431E+02 \\ -.36715E-02 & -.37051E-02 & .35314E-02 & .38783E-02 & .35714E-02 & -.35633E-02 & .37909E-02 & -.36182E-02 \\ -.38226E-02 & -.31775E-02 & .33338E-02 & .32093E-02 & .25582E-02 & -.35949E-02 & .32593E-02 & -.29932E-02 \\ -.40124E-02 & -.31643E-02 & .29479E-02 & .26556E-02 & .19120E-02 & -.31671E-02 & .28745E-02 & -.24036E-02 \\ -.34316E-02 & -.33417E-02 & .30651E-02 & .22084E-02 & .14256E-02 & -.25748E-02 & .23870E-02 & -.19036E-02 \\ -.31891E-02 & -.34010E-02 & .30617E-02 & .22599E-02 & .98070E-03 & -.20141E-02 & .18305E-02 & -.14186E-02 \\ -.40564E-02 & -.31130E-02 & .29074E-02 & .22749E-02 & .10574E-02 & -.15465E-02 & .13238E-02 & -.89857E-03 \\ -.38053E-02 & -.32772E-02 & .28984E-02 & .22346E-02 & .10406E-02 & -.15722E-02 & .84997E-03 & -.34797E-03 \\ -.35850E-02 & -.33047E-02 & .29906E-02 & .22574E-02 & .99085E-03 & -.15538E-02 & .88690E-03 & .16091E-03 \end{bmatrix}$$

$$Q_2 = \begin{bmatrix} -.36715E-02 & -.38226E-02 & -.40124E-02 & -.34316E-02 & -.31891E-02 & -.40564E-02 & -.38053E-02 & -.35850E-02 \\ -.37051E-02 & -.31775E-02 & .33338E-02 & .32093E-02 & .25582E-02 & -.35949E-02 & .32593E-02 & -.29932E-02 \\ -.35314E-02 & -.33338E-02 & .29479E-02 & .26556E-02 & .19120E-02 & -.31671E-02 & .28745E-02 & -.24036E-02 \\ -.38783E-02 & .32093E-02 & .26556E-02 & .22084E-02 & .22599E-02 & .98070E-03 & .18305E-02 & .14186E-02 \\ -.35714E-02 & .25582E-02 & .19120E-02 & .14256E-02 & .98070E-03 & .10574E-02 & .10406E-02 & .99085E-03 \\ -.35633E-02 & .35949E-02 & .31671E-02 & .25748E-02 & .20141E-02 & .15465E-02 & .15722E-02 & .15538E-02 \\ -.37909E-02 & .32593E-02 & .28745E-02 & .23870E-02 & .18305E-02 & .13238E-02 & .84997E-03 & .88690E-03 \\ -.36182E-02 & .29932E-02 & .24036E-02 & .19036E-02 & .14186E-02 & .89857E-03 & .34797E-03 & .16091E-03 \\ .52393E-01 & .52793E-01 & .53139E-01 & .53453E-01 & .53693E-01 & .53829E-01 & .53905E-01 & .53911E-01 \\ .52793E-01 & .11247E+00 & .11320E+00 & .11379E+00 & .11426E+00 & .11459E+00 & .11474E+00 & .11481E+00 \\ .53139E-01 & .11320E+00 & .17312E+00 & .17399E+00 & .17468E+00 & .17515E+00 & .17549E+00 & .17563E+00 \\ .53453E-01 & .11379E+00 & .17399E+00 & .23400E+00 & .23490E+00 & .23558E+00 & .23606E+00 & .23631E+00 \\ .53693E-01 & .11426E+00 & .17468E+00 & .23490E+00 & .29491E+00 & .29580E+00 & .29641E+00 & .29675E+00 \\ .53829E-01 & .11459E+00 & .17515E+00 & .23558E+00 & .29580E+00 & .35572E+00 & .35648E+00 & .35684E+00 \\ .53905E-01 & .11474E+00 & .17549E+00 & .23606E+00 & .29641E+00 & .35648E+00 & .41617E+00 & .41659E+00 \\ .53911E-01 & .11481E+00 & .17563E+00 & .23631E+00 & .29675E+00 & .35684E+00 & .41659E+00 & .47591E+00 \end{bmatrix}$$

Table 4.15. Comparison of the required maximum control force and number of controllers for 30 % reduction of the eighth floor displacement of the eight-story building

Location of ABS	Without Control	ABS at 1st fl	ABS at 1st & 2nd fl.		ABS at 1st, 2nd, 3rd, and 4th fl.		
Algorithm		IOC	IOC	VPI	IOC	DPI	VPI
1st Fl. CF (kN)	-	3,202	1,697	6,668	926	2,187	4,527
2nd Fl. CF (kN)	-	-	1,504	6,410	887	1,627	3,581
3rd Fl. CF (kN)	-	-	-	-	818	1,097	3,000
4th Fl. CF (kN)	-	-	-	-	727	518	2,745
Floor	Displacement (m)	Percentage of uncontrolled displacement (%)					
1	0.033	76	74	107	74	73	84
2	0.065	73	73	107	72	77	80
3	0.096	70	70	90	70	71	79
4	0.125	69	70	82	70	71	80
5	0.150	69	70	77	70	71	75
6	0.171	69	70	75	70	70	72
6	0.185	70	70	71	70	70	71
8	0.193	70	70	70	70	70	70
Floor	Velocity (m/s)	Percentage of uncontrolled velocity (%)					
1	0.224	61	74	90	76	59	70
2	0.429	71	68	93	73	61	67
3	0.612	68	69	77	70	62	68
4	0.759	67	68	72	68	65	70
5	0.868	68	69	68	69	70	66
6	0.939	72	72	69	71	75	65
7	1.002	76	76	70	76	78	64
8	1.062	77	77	68	77	77	62
Floor	Acceleration (g)	Percentage of uncontrolled acceleration (%)					
1	0.431	84	99	33	100	44	29
2	0.539	100	96	51	101	66	42
3	0.570	104	103	94	100	85	53
4	0.619	98	97	92	90	90	59
5	0.767	76	77	65	78	76	53
6	0.879	80	80	49	80	75	50
7	0.945	82	82	51	81	76	48
8	0.990	82	82	54	80	77	48

maximum displacement response compare the maximum control force required. The eight-story building subjected to the 1940 El-Centro earthquake is used.

In case (a), except for the acceleration on the lower floors (first to third floor) of the building, the response is reduced better by the IOC algorithm than by the DPI or VPI algorithm. Results for case (b) are shown in Table 4.15. The eighth floor maximum displacement is arbitrarily set to 70 % of the uncontrolled response for all three control algorithms (IOC, DPI, and VPI). Three situations are compared : a single ABS on the first floor, an ABS on the first and second floors, and an ABS on the first, second, third, and fourth floors. In order to reach the 70 % limit, the velocity control (VPI) required at least two controllers, and the drift control (DPI) required four controllers.

Note that the instantaneous optimal control (IOC) algorithm maximum control force when using one controller is 3,202 kN, when using two controllers it is 1,697 kN; and when using four controllers it is 926 kN. The above forces are almost inversely proportional to the number of controllers used. A significant reduction of the acceleration is found when using the velocity control (VPI) algorithm. A similar outcome appears for the drift control (DPI) algorithm as compared to the IOC control. For drift reduction, the DPI performs better than the IOC and VPI algorithms. For velocity and acceleration reduction, the VPI performs better than the IOC and DPI algorithms. However, the control forces required to reduce the maximum displacement to the same level are much larger for the DPI and VPI than those using the IOC algorithm.

To study areas where both moderate and strong earthquakes are expected, the 1940 El-Centro earthquake (Figure 4.6(a)), the 1971 San Fernando earthquake (Figure 4.6(b)), the 1985 Mexico City earthquake (Figure 4.8(a)), and the 1994 Northridge earthquake (Figure 4.8(b)) were used to examine the performance of the ABS and VE dampers. The instantaneous optimal control (IOC) with the Lyapunov-based Q weighting matrix and the VE damper properties used in previous sections are employed for all four earthquake records.

The performance of the ABS is compared to that of the VE dampers in Figures 4.11 - 4.14. The eight-story shear building shown in Figure 4.1(a) is used with the four earthquakes state above. Three cases are examined: (1) one ABS on the first floor, (2) one VE damper on the first, second, and third floors, and (3) one VE damper on the first, second, third, and fourth floors. The first mode effective damping ratio of the three cases, which includes the inherent structural damping and the additional damping due to the ABS or VE damper, equals 7.14, 7.04, and 8.14 % respectively. The control parameters for the ABS are the same as shown in Table 4.12. The thickness and the cross-sectional area of the VE damper equal 0.0127 m and 0.09 m². The material properties of the VE damper remain the same as stated in the previous section on the placement of VE dampers.

It can be observed that the displacement, drift, and velocity responses are effectively reduced. From Figures 4.11(a), 4.11(c), and 4.14(a), the response of the structure equipped with one ABS ($\xi_1=7.14$ %) is even less than the case with four VE dampers ($\xi_1=8.14$ %). In Figures 4.13(a) and 4.13(c), the displacement and velocity

Combined Performance of VE Dampers and ABS

The capability of available actuators for use in the ABS is significant. Currently, actuators can provide control forces up to 1,000 kN with a stroke displacement and velocity well within those expected from structural responses in strong earthquakes. Specially fabricated actuators can reach forces as high as 20,000 kN; actuators can be designed to reach strokes up to ± 2 m and stroke velocities up to 5 m/sec for specific systems (Clark, 1994). For control forces larger than 1,000 kN the cost of the actuator increases rather sharply, and more than one actuator could be used as an alternative. However, the hydraulic systems that include manifolds and oil pumps and the performance characteristics such as the flow rate are required to be at higher levels and must be custom manufactured. Reduction of the required control forces is desirable for containing the ABS cost.

Extensive testing and evaluation of VE dampers at both a reduced and at full scale have proven the feasibility of their use in seismic structures. However, it is known that the damping properties of the VE material are frequency dependent. In addition, the VE material has a finite ability to resist shear strains, and for large deformations beyond the design level it may fail in shear.

The ABS and VE dampers could complement each other. For moderate earthquakes the VE dampers may suffice for reducing the structural response, but for strong earthquakes the ABS may have to be activated. It is apparent that both systems can benefit from the presence of the other. In addition, redundancy is introduced into the protective system.

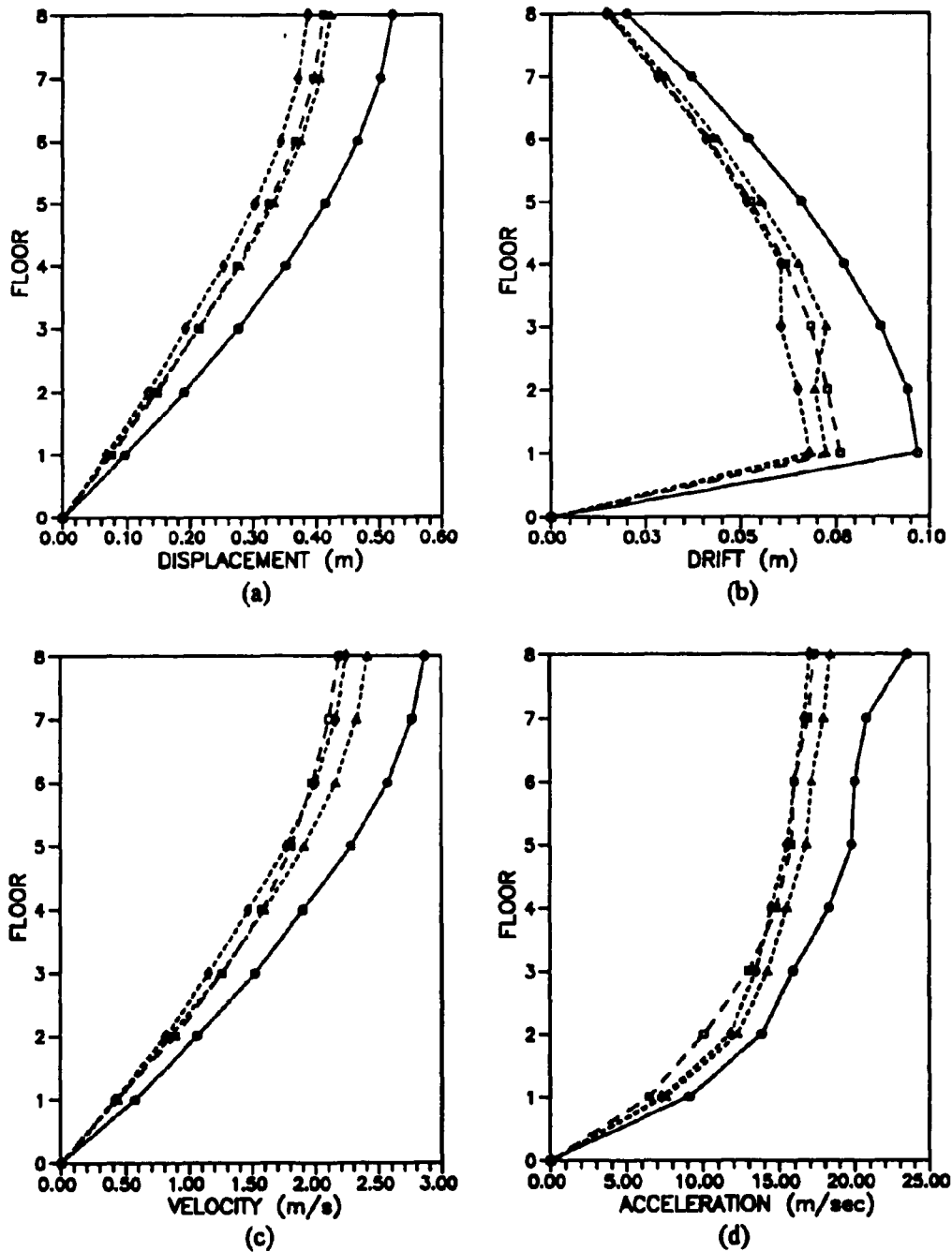


Figure 4.12 Comparison of: (a) displacement, (b) drift, (c) velocity, and (d) acceleration of eight-story building for San Fernando earthquake; $\text{---}\circ\text{---}$ = uncontrolled ($\xi_1 = 2.50\%$), $\text{---}\square\text{---}$ = AC on the first floor ($\xi_1 = 7.14\%$), $\text{---}\triangle\text{---}$ = VE on the three lower floors ($\xi_1 = 7.04\%$), $\text{---}\diamond\text{---}$ = VE on the four lower floors ($\xi_1 = 8.14\%$)

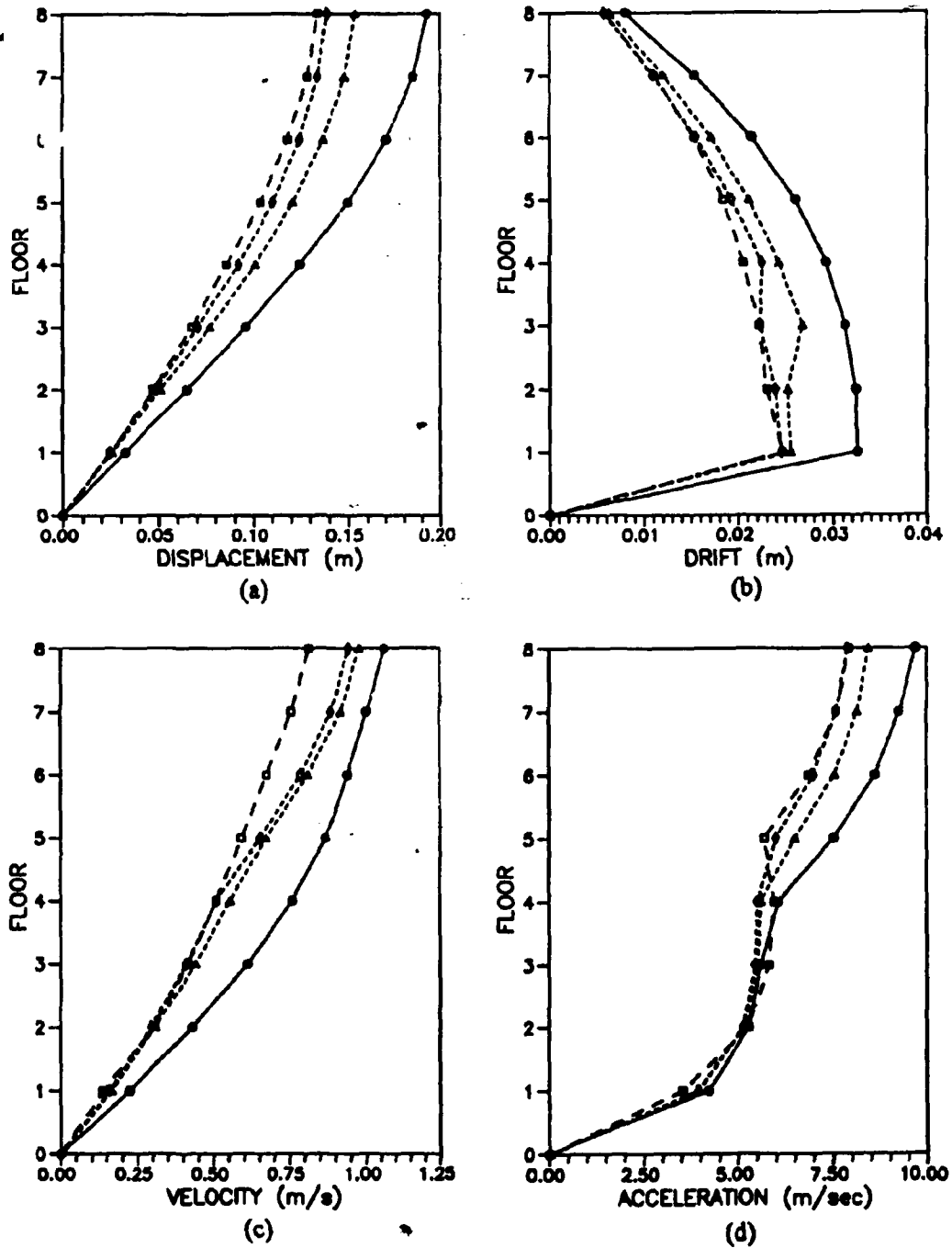


Figure 4.11 Comparison of: (a) displacement, (b) drift, (c) velocity, and (d) acceleration of eight-story building for El-Centro earthquake; $\text{---}\circ\text{---}$ = uncontrolled ($\xi_1 = 2.50\%$), $\text{---}\square\text{---}$ = AC on the first floor ($\xi_1 = 7.14\%$), $\text{---}\triangle\text{---}$ = VE on the three lower floors ($\xi_1 = 7.04\%$), $\text{---}\diamond\text{---}$ = VE on the four lower floors ($\xi_1 = 8.14\%$)

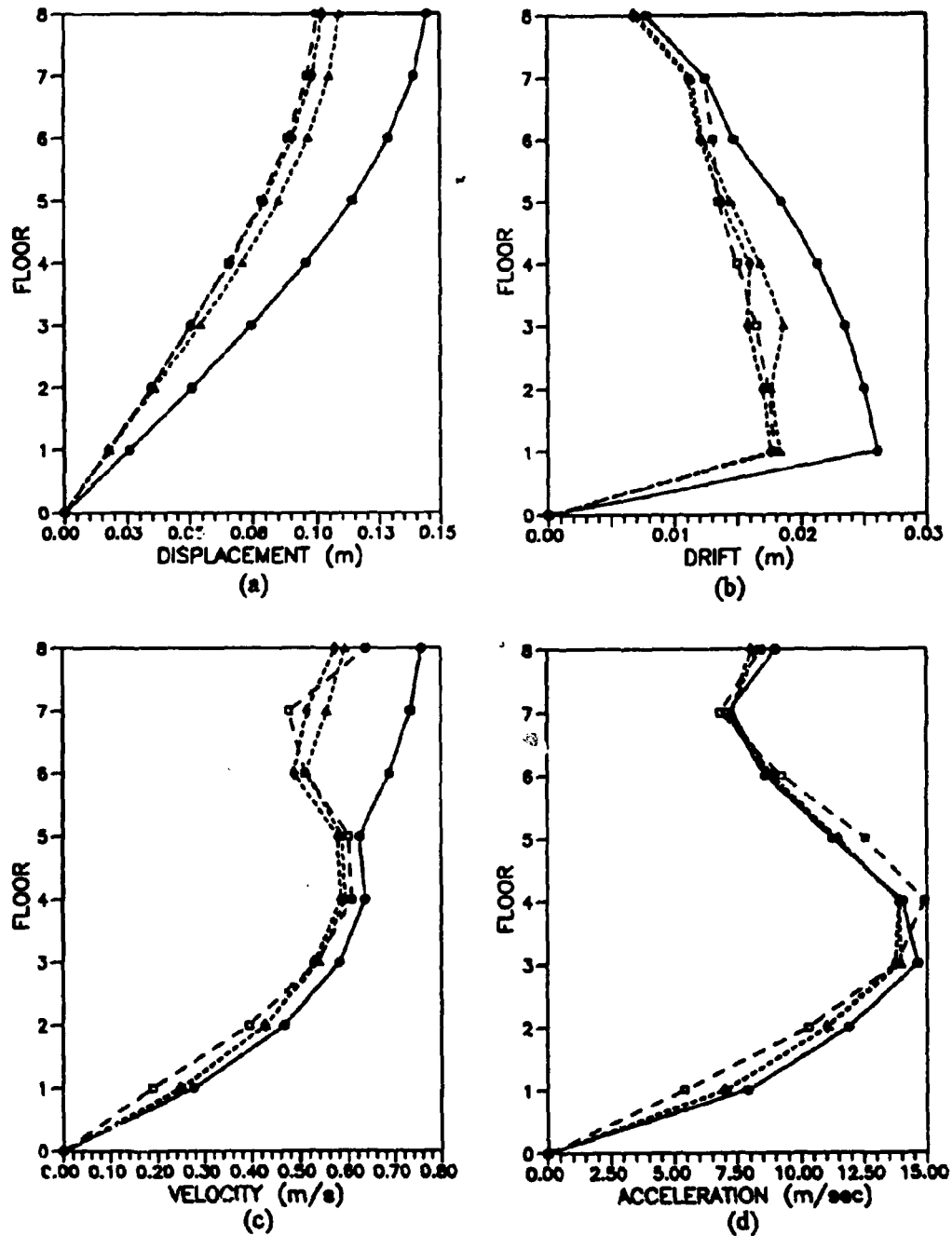


Figure 4.14 Comparison of: (a) displacement, (b) drift, (c) velocity, and (d) acceleration of eight-story building for Northridge earthquake; \circ = uncontrolled ($\xi_1 = 2.50\%$), \square = AC on the first floor ($\xi_1 = 7.14\%$), \triangle = VE on the three lower floors ($\xi_1 = 7.04\%$), \diamond = VE on the four lower floors ($\xi_1 = 8.14\%$)

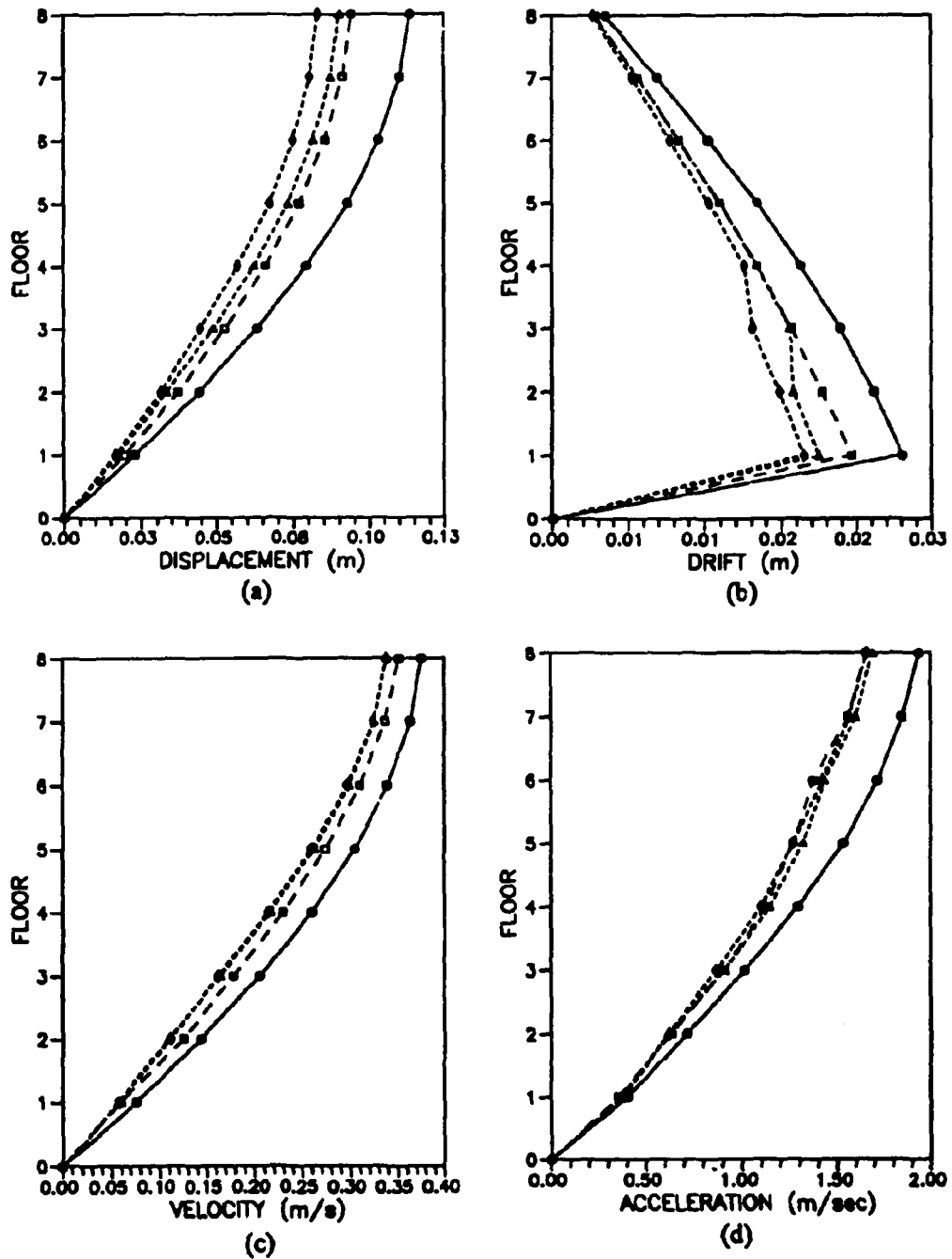


Figure 4.13 Comparison of: (a) displacement, (b) drift, (c) velocity, and (d) acceleration of eight-story building for Mexico City earthquake; $\text{---}\circ\text{---}$ = uncontrolled ($\xi_1 = 2.50\%$), $\text{---}\square\text{---}$ = AC on the first floor ($\xi_1 = 7.14\%$), $\text{---}\triangle\text{---}$ = VE on the three lower floors ($\xi_1 = 7.04\%$), $\text{---}\diamond\text{---}$ = VE on the four lower floors ($\xi_1 = 8.14\%$)

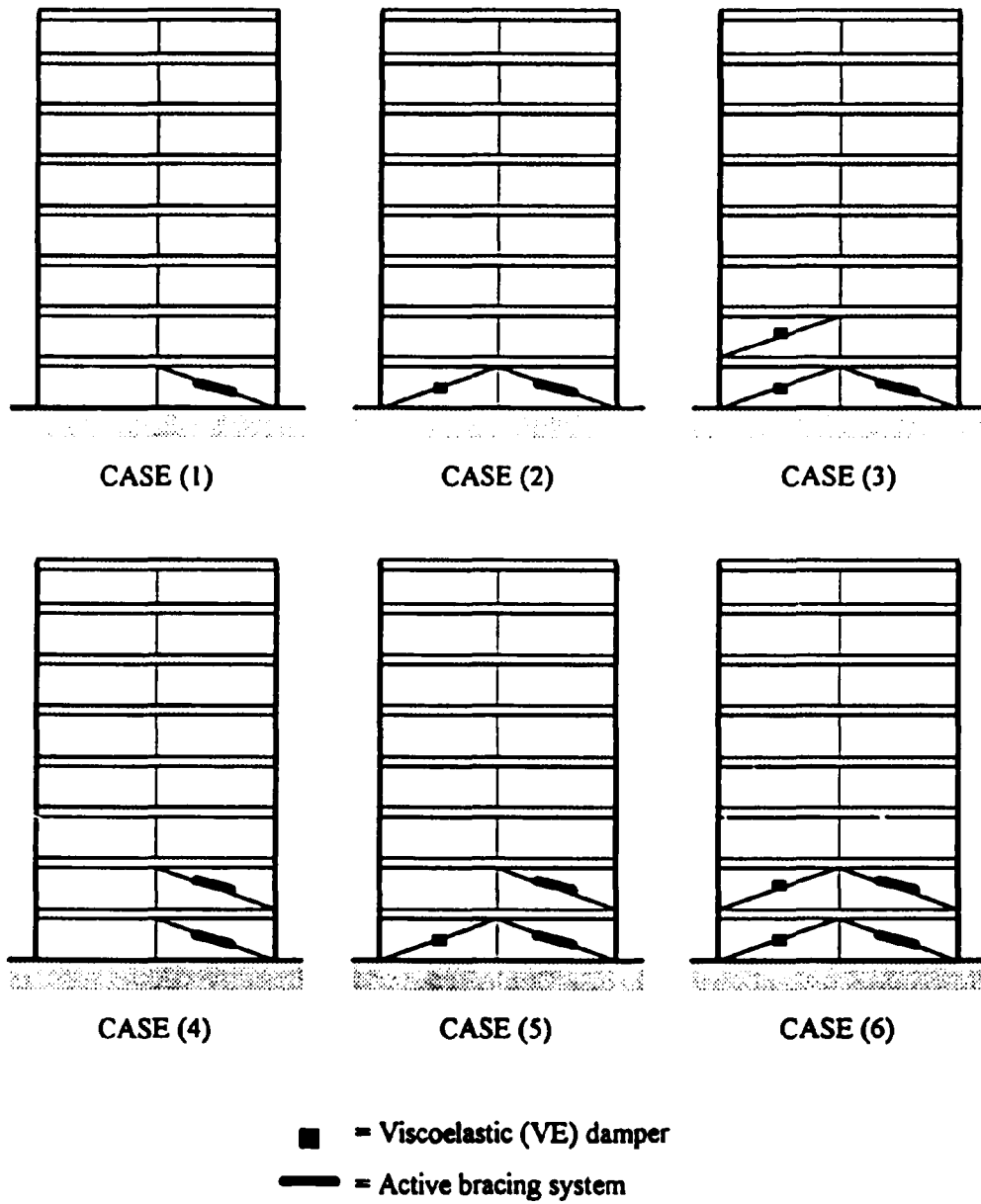


Figure 4.15 Eight-story shear building with six different arrangements of ABS and VE dampers

response for the structure with an ABS on the first floor subjected to the 1985 Mexico City earthquake are slightly larger than the case with three VE dampers ($\xi_1=7.04\%$). This is because the weighting matrices, Q and R , of the ABS were established for the El-Centro earthquake which has significantly different frequency characteristics than those of the Mexico City earthquake (see Figures 4.9(a) and 4.9(c)).

The combined performance of the ABS and VE dampers is studied using six different arrangements (Figure 4.15) for the eight-story building subjected to the four earthquakes. In case (1) one ABS is placed on the first floor; in case (2) one ABS and one VE damper are placed on the first floor; in case (3) one ABS and one VE damper are placed on the first floor and one VE damper is placed on the second floor; in case (4) one ABS is placed on the first and one on the second floor; in case (5) one ABS and one VE damper are placed on the first floor and one ABS is placed on the second floor; in case (6) one ABS and one VE damper are placed on the first and second floors.

The maximum displacement of the eighth floor is set to 70 % of the uncontrolled response for all six cases in Table 4.16 for the 1940 El-Centro earthquake. For the 1971 San Fernando, 1985 Mexico City, and 1994 Northridge earthquakes the same ABS weighting matrices and VE damper properties were used. The range of the displacement response reduction for these three earthquakes is 70 to 80 % for the San Fernando, 75 to 85 % for the Mexico City, and 70 % for the Northridge earthquake compared to the uncontrolled response. The structural damping energy (SDE), VE damper damping energy (VDE), ABS damping energy (ADE), and elastic strain energy (ESE) are determined separately by the absolute energy method (Uang, 1988). In addition, the total

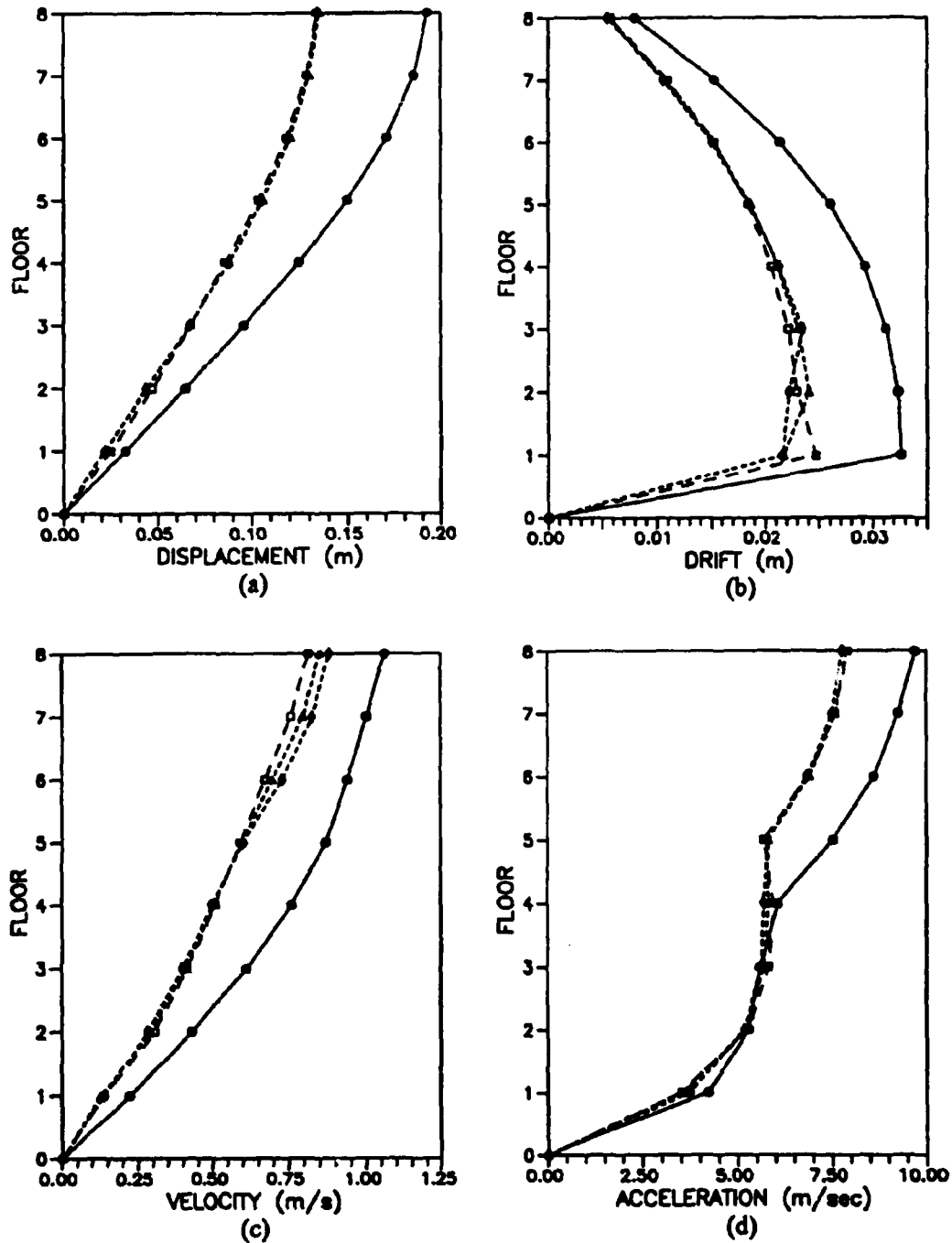


Figure 4.16 Comparison of: (a) displacement, (b) drift, (c) velocity, and (d) acceleration of eight-story building for 1940 El-Centro earthquake; $\text{---}\bigcirc\text{---}$ = uncontrolled, $\text{---}\square\text{---}$ = Case (1) of Figure 4.15, $\text{---}\triangle\text{---}$ = Case (2) of Figure 4.15, $\text{---}\diamond\text{---}$ = Case (3) of Figure 4.15

Table 4.16. Effective damping ratio for the hybrid ABS-VE damper systems

Case	without ABS or VE damper	ABS on the 1st floor only			ABS on the 1st and 2nd floors		
		(1) w/o VE	(2) VE on 1st fl	(3) VE on 1,2 fl.	(4) w/o VE	(5) VE on 1st fl	(6) VE on 1,2 fl.
Structural damping	2.50 %	2.50 %	2.50 %	2.50 %	2.50 %	2.50 %	2.50 %
ABS damping ratio	-	4.64 %	3.09 %	1.88 %	4.54 %	3.11 %	1.81 %
VE damping ratio	-	-	1.60 %	3.10 %	-	1.60 %	3.10 %
Effective damping ratio	2.50 %	7.14 %	7.19 %	7.48 %	7.04 %	7.21 %	7.41 %

damping energy (TDE), input energy (IE), and kinetic energy (KE) are determined. The damping ratio corresponds to the fundamental mode, but in the analysis the damping ratios of all the modes are used. As can be seen from Table 4.16, the total damping ratio for reducing the maximum displacement to a desired level is increased as additional VE dampers are added.

Figures 4.16 - 4.19 show the responses for the uncontrolled case and cases (1), (2), and (3) of Figure 4.15 for the 1940 El-Centro, 1971 San Fernando, 1985 Mexico City, and 1994 Northridge earthquakes, respectively. The maximum displacement of the eighth floor decreases considerably in cases (2) and (3) for all four earthquakes. Comparing Figures 4.16(c) to 4.11(c) and 4.17(c) to 4.12(c) it can be seen that the ABS helps improve the velocity response of the VE damper.

The maximum control force required by the actuator of the ABS has been reduced considerably by introducing one VE damper (cases (2) and (5)), and is further reduced by introducing two VE dampers (cases (3) and (6)) as shown in Figure 4.20. Note that the maximum control force levels are kept within 30 % of the structure's weight for the El-Centro earthquake. Since the peak ground acceleration of the 1971 San Fernando earthquake (1.1 g) is almost three times that of the 1940 El-Centro earthquake (0.34 g) the control force required using the same control parameters is increased by about three

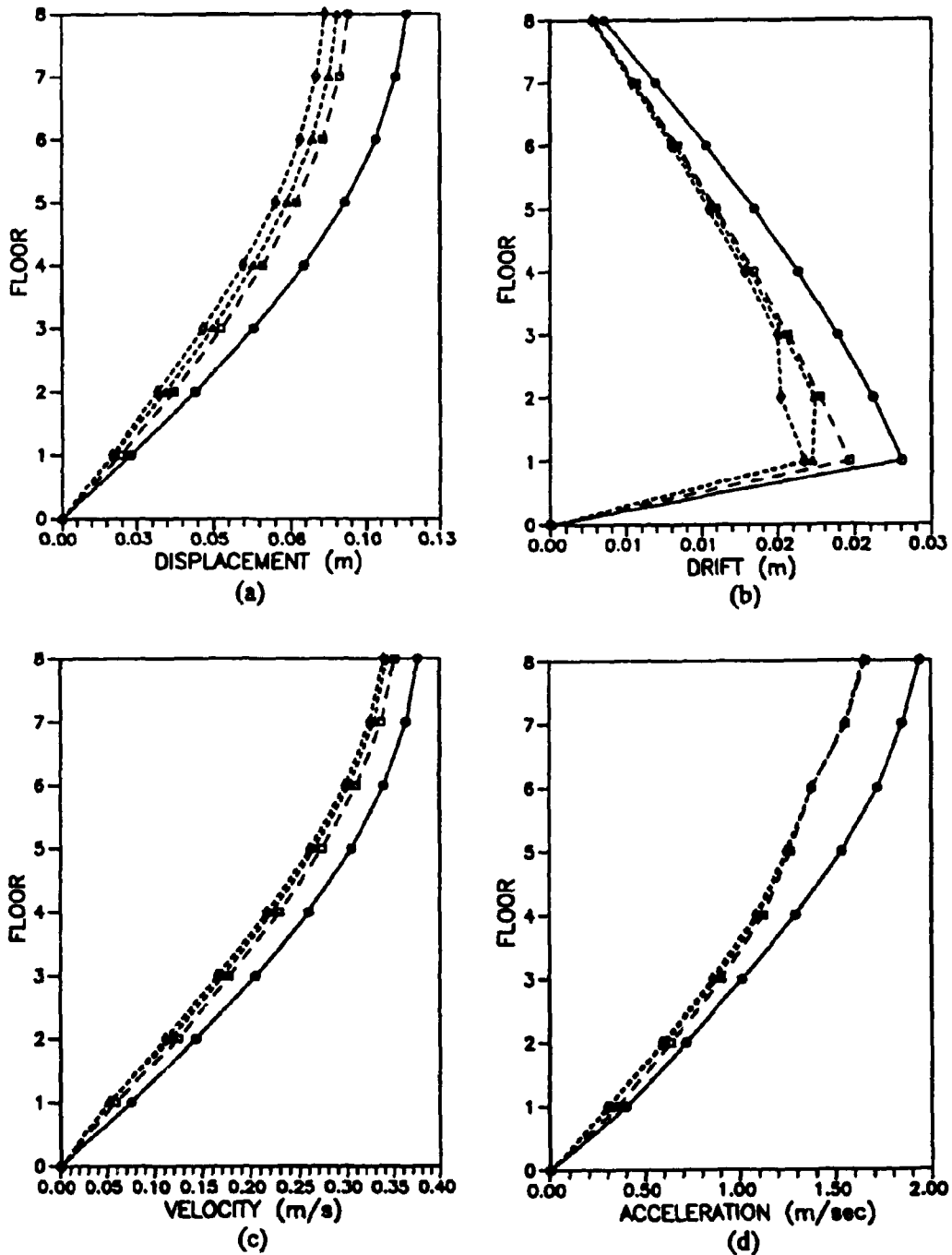


Figure 4.18 Comparison of: (a) displacement, (b) drift, (c) velocity, and (d) acceleration of eight-story building for 1985 Mexico City earthquake; $\text{---}\ominus\text{---}$ = uncontrolled, $\text{---}\square\text{---}$ = Case (1) of Figure 4.15, $\text{---}\triangle\text{---}$ = Case (2) of Figure 4.15, $\text{---}\diamond\text{---}$ = Case (3) of Figure 4.15

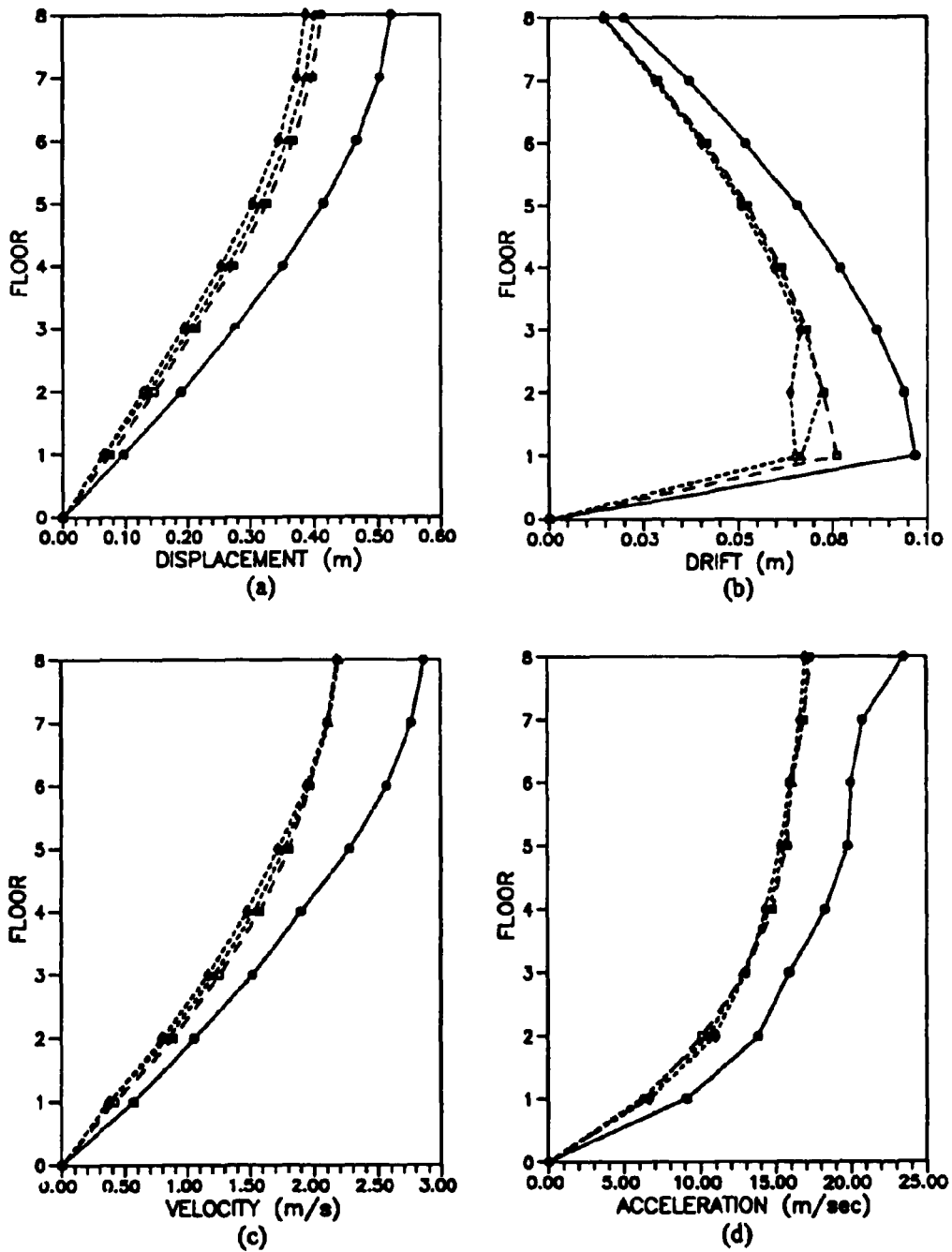


Figure 4.17 Comparison of: (a) displacement, (b) drift, (c) velocity, and (d) acceleration of eight-story building for 1971 San Fernando earthquake; \ominus = uncontrolled, \square = Case (1) of Figure 4.15, \triangle = Case (2) of Figure 4.15, \diamond = Case (3) of Figure 4.15

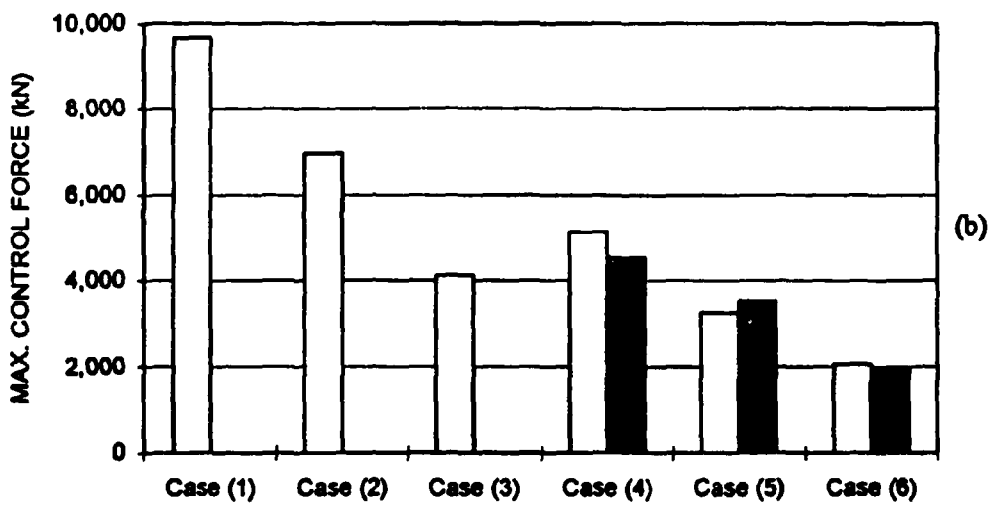
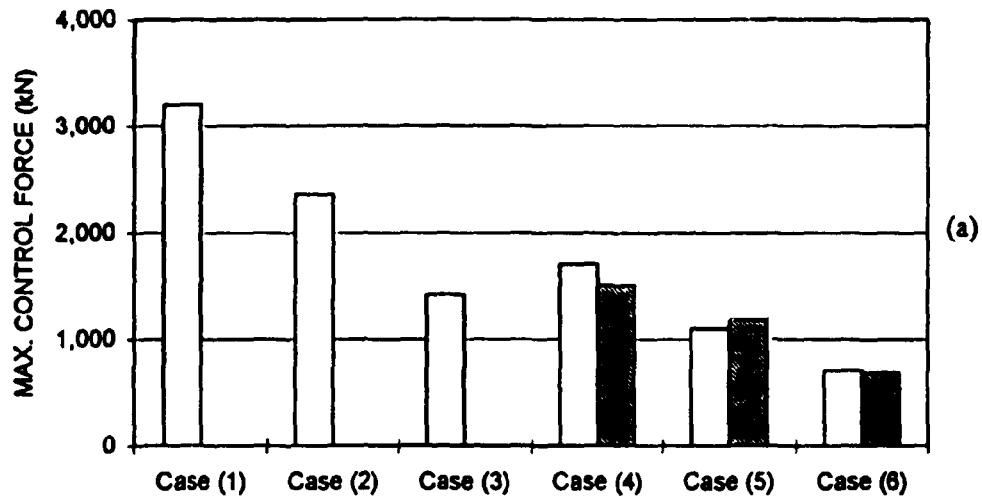


Figure 4.20 Maximum control force for: (a) 1940 El-Centro earthquake and (b) 1971 San Fernando earthquake; □ = 1st floor control force, ■ = 2nd floor control force

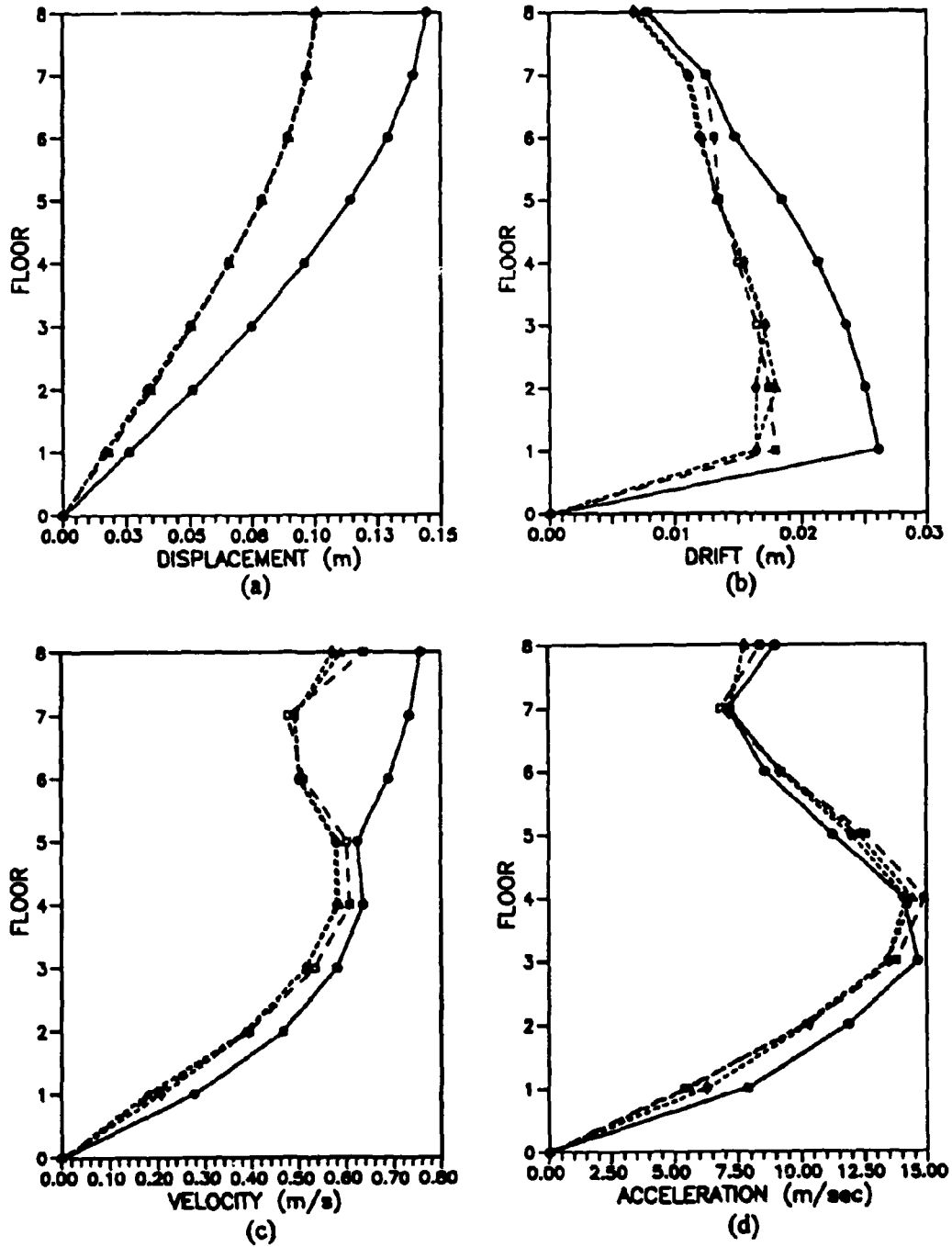


Figure 4.19 Comparison of: (a) displacement, (b) drift, (c) velocity, and (d) acceleration of eight-story building for 1940 Northridge earthquake; —○— = uncontrolled, -□- = Case (1) of Figure 4.15, ...△... = Case (2) of Figure 4.15, -◇- = Case (3) of Figure 4.15

times. Likewise, the peak acceleration of the 1985 Mexico City earthquake (0.17 g) is about one half of the 1940 El-Centro earthquake, thereby the required control force is slightly less than half of that for the El-Centro earthquake (Figure 4.20(c)). However, even though the peak acceleration of the 1994 Northridge earthquake (0.89 g) is about two times larger than that of the El-Centro earthquake, the maximum required control forces are only two-thirds of those required by the El-Centro earthquake. This shows that the ABS will produce a different performance for earthquakes with different characteristics.

From the previous discussion it is obvious that the control forces are rather large. Cases (2) and (3) in Figure 4.20 show how these forces can be substantially reduced by introducing one (case (2)) or two (case (3)) VE dampers. Similar results are obtained if two ABS are used (case (4)), and the required control forces are further reduced if one VE damper is added to the two ABS (case (5)), or two VE dampers are added (case (6)). When two ABS are present, the sum of the required maximum control force from each controller is approximately the same as the maximum control force required when only one ABS is present. The addition of the VE dampers not only brings the ABS within the realm of practicality but also reduces their overall cost. It can also be observed that the additional damping ratio introduced by the ABS is slightly different in cases (1) - (3) and cases (4) - (6) (see Table 4.16). However, the differences in the damping ratio between cases (1) and (4), cases (2) and (5), and cases (3) and (6) are due to the fact that the weighting matrices were modified to obtain the same roof displacement. Similar results can also be observed for all three earthquakes (Figures 4.20(b), 4.20(c), and 4.20(d)).

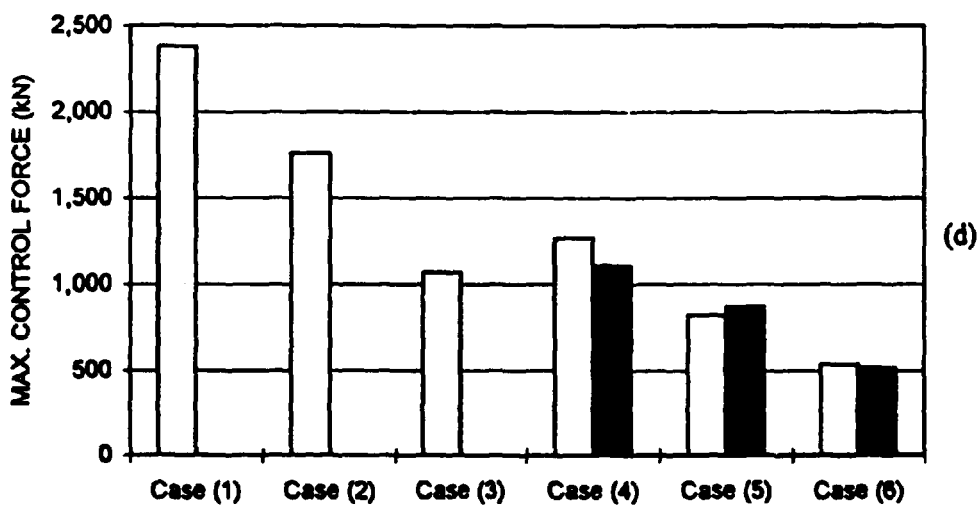
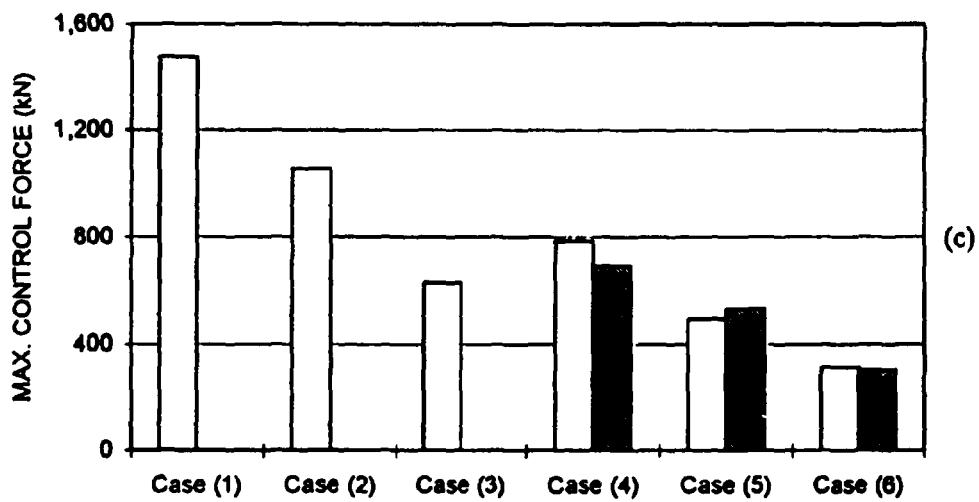


Figure 4.20 (Continued) (c) 1985 Mexico City earthquake and (b) 1994 Northridge earthquake; □ = 1st floor control force, ■ = 2nd floor control force

Table 4.17. Maximum absolute energy distribution for the hybrid ABS-VE damper systems

Case	without ABS or VE damper	ABS on the 1st floor only			ABS on the 1st and 2nd floors		
		(1) w/o VE	(2) VE on 1st fl.	(3) VE on 1,2 fl.	(4) w/o VE	(5) VE on 1st fl.	(6) VE on 1,2 fl.
1940 El-Centro earthquake							
SDE (kN-m)	1,718	677	630	586	663	617	590
ADE (kN-m)	0	829	554	340	936	622	356
VDE kN-m)	0	0	369	672	0	367	678
TDE (kN-m)	1,718	1,506	1,553	1,598	1,600	1,606	1,624
KE (kN-m)	1,102	565	619	645	574	617	650
ESE (kN-m)	1,119	750	754	743	712	726	735
IE (kN-m)	2,279	2,165	2,173	2,188	2,179	2,184	2,195
1971 San Fernando earthquake							
SDE (kN-m)	10,081	3,654	3,421	3,182	3,608	3,355	3,216
ADE (kN-m)	0	4,495	3,083	1,906	5,016	3,398	1,970
VDE kN-m)	0	0	1,972	3,593	0	1,962	3,637
TDE (kN-m)	10,081	8,149	8,476	8,681	8,624	8,715	8,822
KE (kN-m)	7,760	4,579	4,511	4,302	4,626	4,496	4,336
ESE (kN-m)	7,694	5,299	5,100	4,859	5,228	5,059	4,872
IE (kN-m)	13,899	11,428	11,465	11,545	11,531	11,510	11,598
1985 Mexico City earthquake							
SDE (kN-m)	446	256	240	222	252	236	243
ADE (kN-m)	0	436	284	171	455	297	267
VDE kN-m)	0	0	152	279	0	152	156
TDE (kN-m)	446	692	676	671	707	685	667
KE (kN-m)	937	872	876	872	874	876	882
ESE (kN-m)	1,347	1,300	1,301	1,315	1,343	1,348	1,347
IE (kN-m)	1,920	2,057	2,044	2,049	2,112	2,094	2,080
1994 Northridge earthquake							
SDE (kN-m)	1,153	511	453	417	495	443	421
ADE (kN-m)	0	438	298	188	515	345	200
VDE kN-m)	0	0	216	378	0	215	382
TDE (kN-m)	1,153	948	967	983	1,010	1,004	1,003
KE (kN-m)	565	390	363	339	391	363	340
ESE (kN-m)	1,292	1,069	1,066	1057	1,041	1,049	1,049
IE (kN-m)	2,089	1,853	1,851	1,850	1,867	1,864	1,857

Note : SDE = Inherent structural damping energy; ADE = Damping energy due to ABS ;
VDE = Damping energy due to VE dampers; TDE = Total damping energy (SDE+ADE+VDE);
KE = Kinetic energy; ESE = Elastic Strain Energy;
IE = Input energy;

The absolute energy distribution for the eight-story building subjected to the four earthquakes is shown in Table 4.17. It can be seen that the structural damping energy is reduced significantly after adding the active bracing system(s) and is reduced even more with the additional VE damper(s). The VE damper damping energy increases by adding more VE dampers, and the ABS damping energy is decreased. The total damping energy increases from case (1) to case (3) when VE dampers are added. The input energy, elastic strain energy, and kinetic energy are decreased by adding the ABS and VE dampers as compared to the case without ABS or VE dampers.

The input, damping, and elastic strain energy for the structure subjected to the 1971 San Fernando earthquake is about five to six times compared to those of the El-Centro earthquake, and the kinetic energy is even larger. This is true for the structure wither with or without controls. Similar results can be observed when the structure is subjected to the 1985 Mexico City and 1994 Northridge earthquakes. In the case of the Mexico City earthquake, the input energy increases slightly after the addition of the hybrid system, but the damping energy increases significantly.

The energy time-histories of cases (1), (2), and (3) in Table 4.17 for the structure subjected to the 1940 El-Centro earthquake are compared to those of the structure without an ABS system or VE damper, and are shown in Figure 4.21. The ABS and VE dampers contribute a significant amount to the total damping energy as shown in Figures 4.21(b), 4.21(c), and 4.21(d). From these figures it can also be observed that the damping energy of the VE dampers reduces the demand on the ABS system for the same result in response reduction. Figure 4.22 shows the kinetic energy time-histories for the

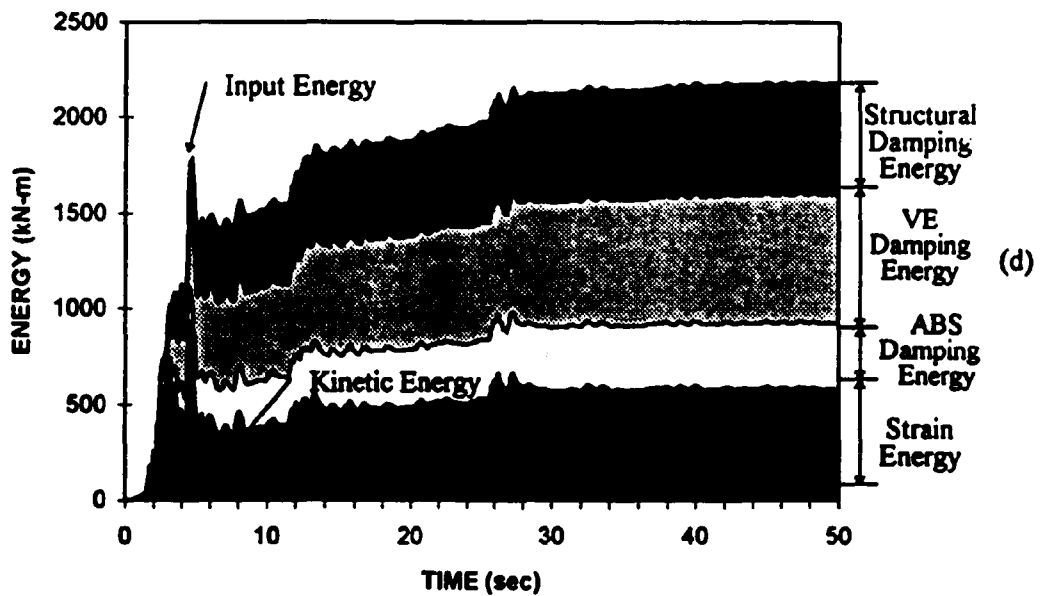
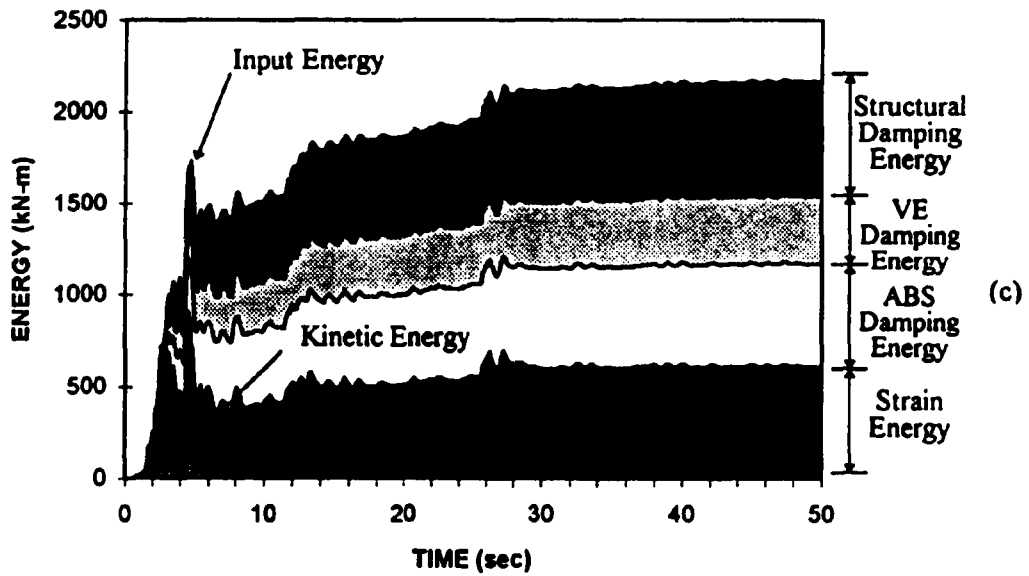


Figure 4.21 (Continued) (c) one ABS and one VE damper on the first floor; (d) one ABS on the first floor and one VE damper on the first and second floor

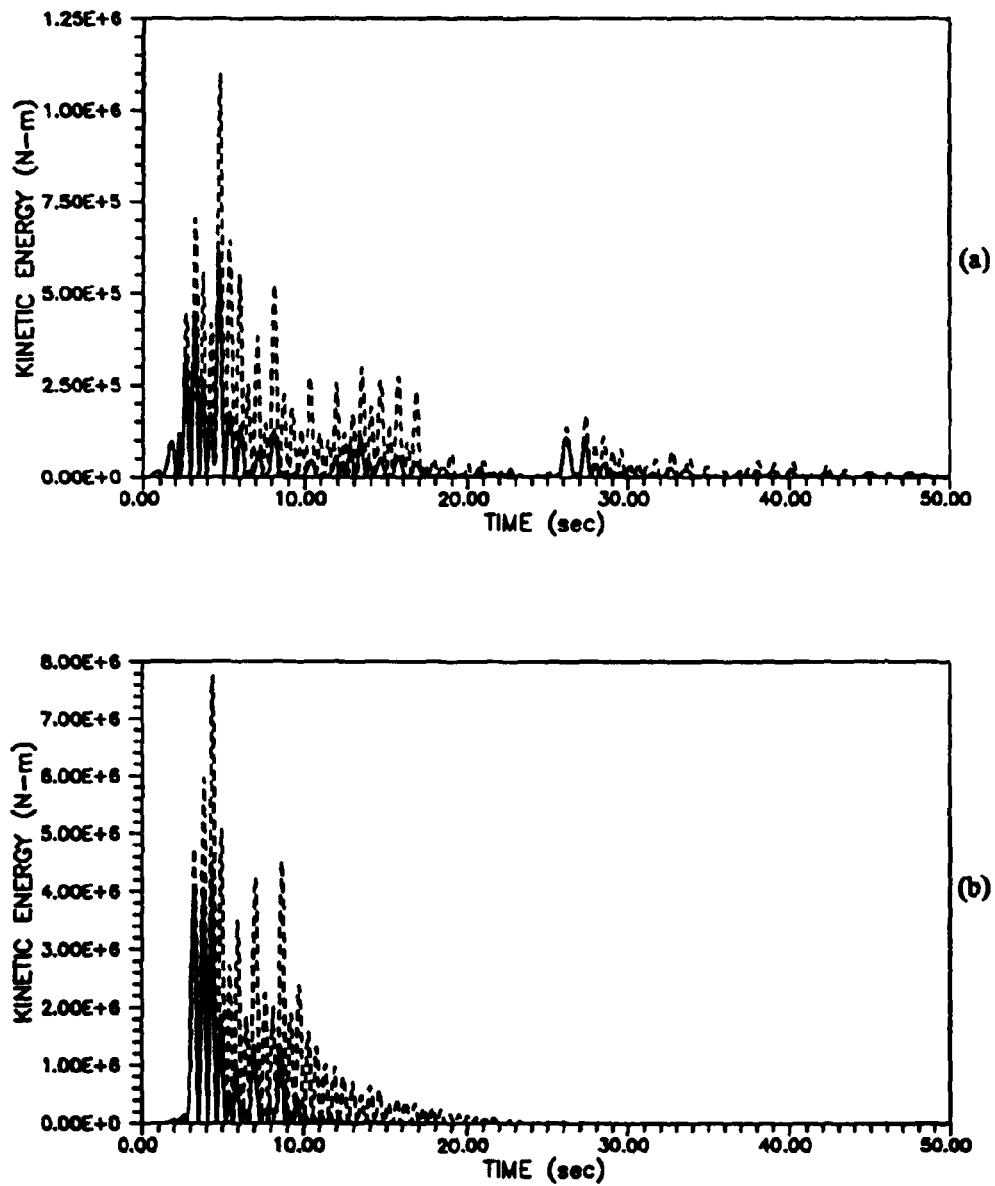


Figure 4.22 Comparison of kinetic energy for: (a) 1940 El-Centro earthquake, and (b) 1971 San Fernando earthquake; = without control, — = one ABS and one VE damper on the first floor

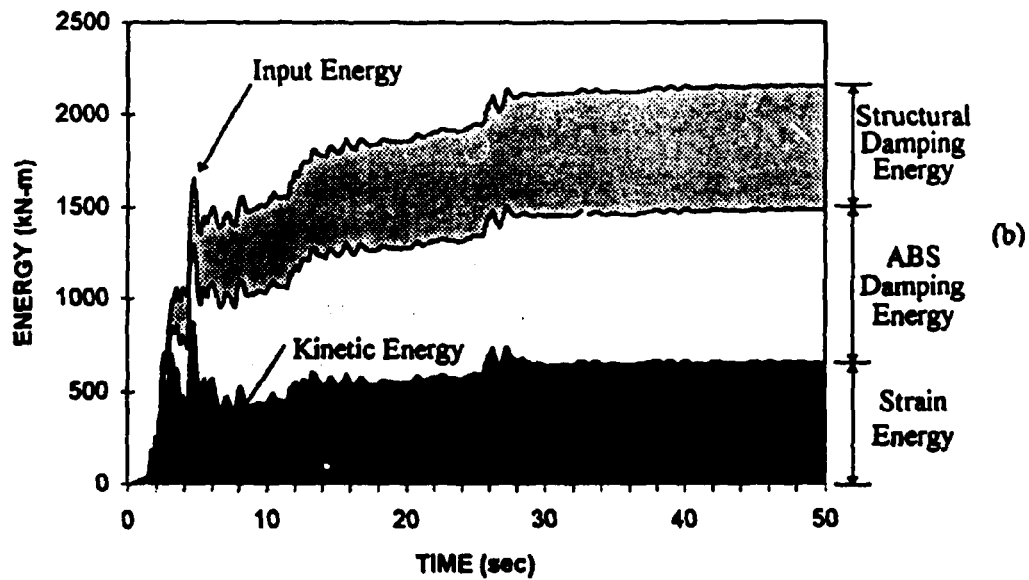
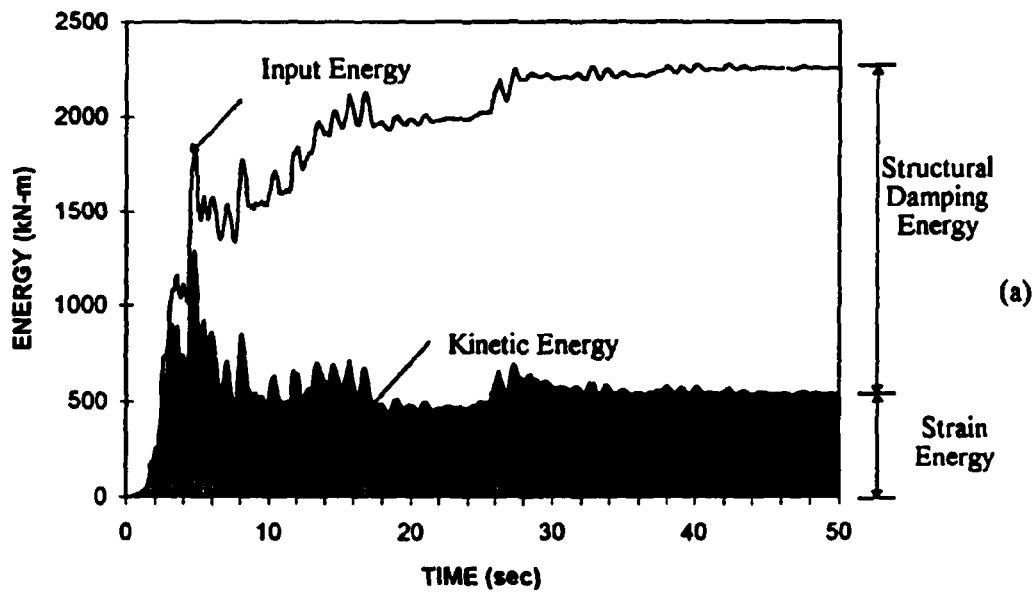


Figure 4.21 Energy time-history for 1940 El-Centro earthquake: (a) without an ABS or VE damper; (b) one ABS on the first floor

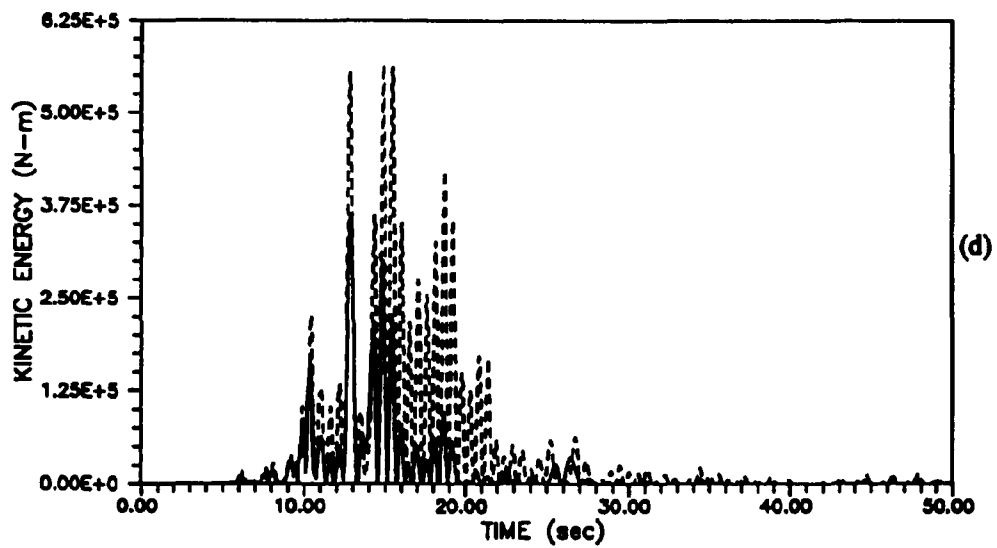
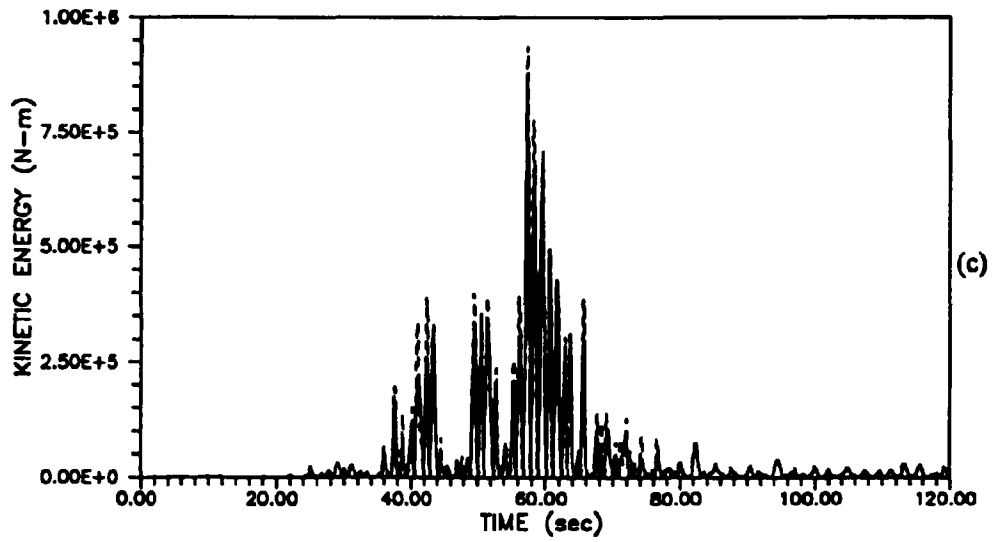


Figure 4.22 (Continued) (c) 1985 Mexico City earthquake and (d) 1994 Northridge earthquake; = without control, — = one AC and one VE damper on the first floor

1940 El-Centro, the 1971 San Fernando, the 1985 Mexico City, and the 1994 Northridge earthquakes, for the uncontrolled case and case (2) (one ABS and one VE damper on the first floor). It can be observed that in the hybrid case a significant reduction of kinetic energy is obtained for all four earthquakes.

CHAPTER 5

PERFORMANCE OF CONVEX MODELS

In this chapter, the energy-bound convex models are used to estimate the maximum response of structures for uncertain dynamic loads. The performance of convex models is investigated for impulses, artificial earthquakes, and several records of past earthquakes. The response using the time-history of the actual record (AR) is compared with the values obtained from the global energy-bound (GEB) and local energy-bound (LEB) convex models of an uncertain excitation.

Energy-bound Convex Models and Dynamic Magnification Factor

First, a single degree-of-freedom system (SDOF) subjected to an uncertain impulsive excitation is used to evaluate the performance of the two convex models. The excitation $f(t)$ in equation (3.1a) is a scalar, it has an uncertain profile, and is assumed to belong to a convex set of dynamic functions. Several excitations were used to evaluate the solution obtained by the convex model.

The dynamic magnification factor, D , is defined as (Clough and Penzien, 1975)

$$D = \left| \frac{x_{\max}}{P_o / k} \right| \quad (5.1)$$

Figure 5.1 shows the displacement response spectra of a rectangular impulse for a damping level of 5 % of critical. The displacement response using the time-history of the actual record (AR), the global (GEB) convex model (equation (3.10)), and local (LEB) convex model (equation (3.14)) is shown. In Figure 5.1, t_1 is the duration of the impulse and T is the structural period. The maximum displacement occurs during the impulse (phase I) when the impulse length ratio, t_1/T , is larger than 0.49; the maximum displacement occurs after the impulse (phase II) if $t_1/T < 0.49$. The other seven impulses shown in Figure 5.2 are also used in this study. Results for a sine-wave impulse are shown in Figure 5.3; results for a two-peak arbitrary impulse (impulse No. ⑥ in Figure 5.2) are displayed in Figure 5.4. It can be observed that the maxima obtained by the global energy-bound (GEB) and local energy-bound (LEB) convex models are much larger than the spectra for the actual record (AR).

The displacement response to the impulses shown in Figure 5.2 was evaluated using the GEB convex model of equation (3.9a), the LEB convex model of equation (3.13a), and a solution as if $f(\dot{t})$ were known with certainty using the time-history analysis of the actual record (AR). Table 5.1 shows the results at the transition point $(t_1/T)_c$ at which the maximum switches from phase II to phase I for the SDOF structure; 1 % and 5 % of critical damping is considered. In Table 5.1, the non-dimensional global energy factor $(E_o)^2(t_1)/P_o^2 t_1$ can be obtained by any of three different conditions: First, the

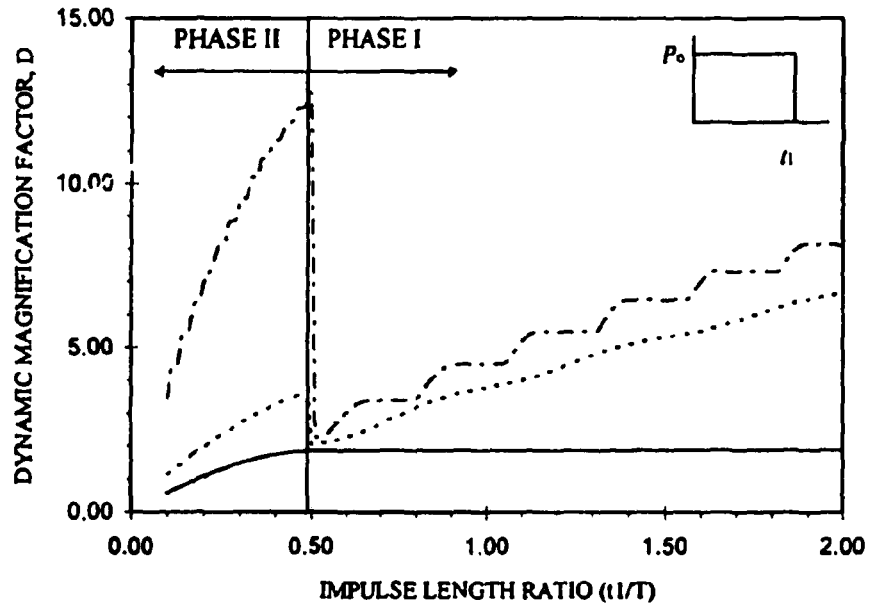


Figure 5.1 Dynamic magnification factor for rectangular impulse: — = actual response, = global energy-bound convex model, - - - - = local energy-bound convex model

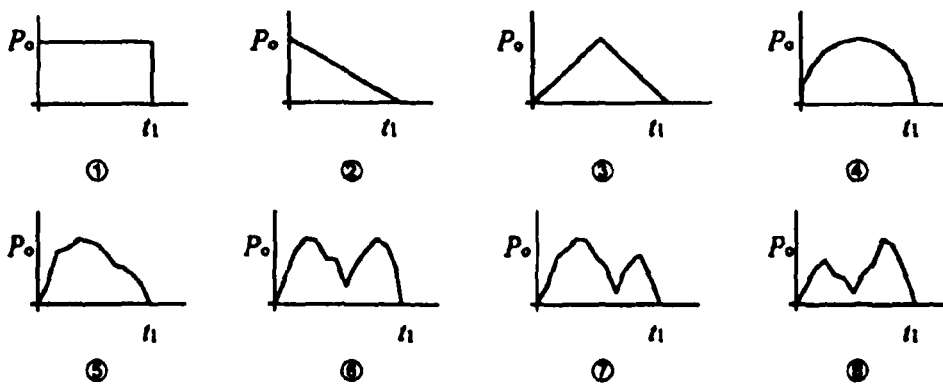


Figure 5.2 Eight impulses

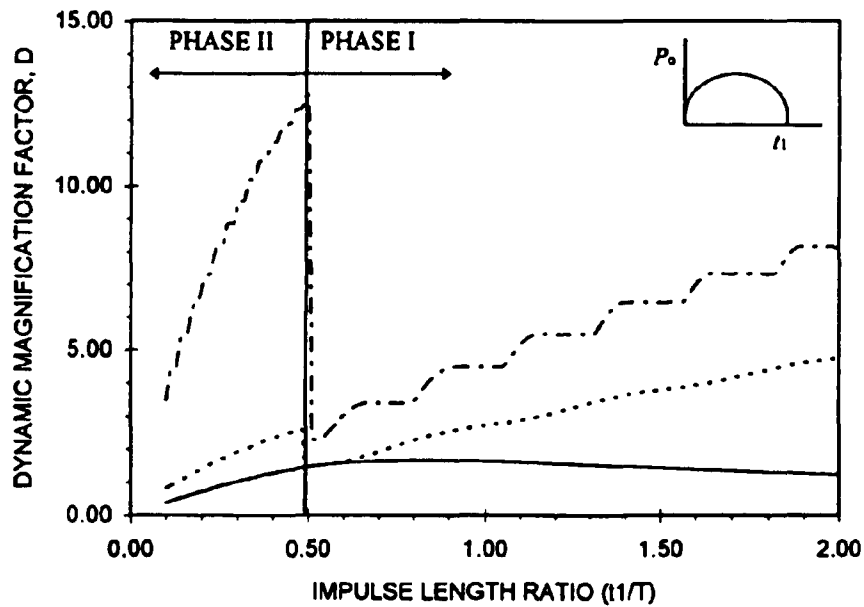


Figure 5.3 Dynamic magnification factor for sine-wave impulse: — = actual response, = global energy-bound convex model, - - - = local energy-bound convex model

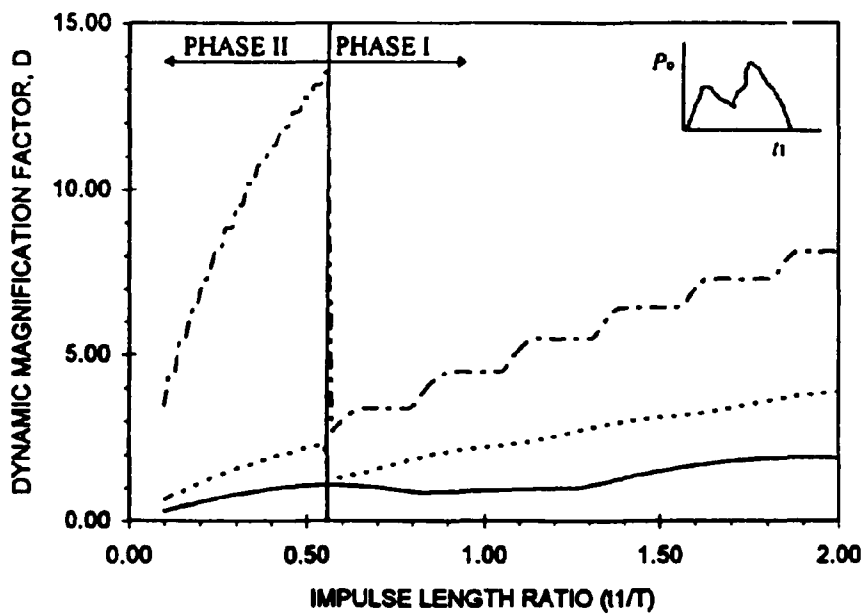

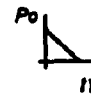
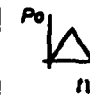
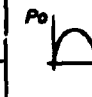
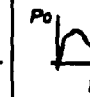
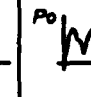
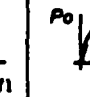
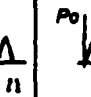


Figure 5.4 Dynamic magnification factor for impulse ① of Figure 5.2: — = actual response, = global energy-bound convex model, - - - = local energy-bound convex model

Table 5.1. Comparison of energy-bound convex models with actual record at the transition point

Impulse								
$E_G^2(t)/P_0^2 t$	1.00	0.33	0.33	0.50	0.49	0.55	0.42	0.35
$E_L^2(t)/P_0^2$	1.00	1.00	1.00	1.00	1.00	1.00	1.00	1.00
Damping ratio = 1 %								
$(t/T)_p$	0.50	0.37	0.49	0.49	0.46	0.51	0.47	0.56
AR	1.97	1.00	1.24	1.53	1.45	1.45	1.28	1.14
GEB	5.52	2.50	3.18	3.89	3.59	4.16	3.42	3.57
GEB/AR	2.80	2.50	2.56	2.54	2.54	2.87	2.66	3.13
LEB	19.49	14.93	19.50	19.50	18.39	19.50	18.30	21.68
LEB/AR	9.89	14.93	17.73	12.75	12.68	13.45	12.30	19.02
Damping ratio = 5 %								
$(t/T)_p$	0.50	0.37	0.48	0.49	0.45	0.5	0.46	0.56
AR	1.86	0.92	1.16	1.45	1.35	1.37	1.20	1.08
GEB	3.76	1.81	2.14	2.66	2.48	2.84	2.33	2.36
GEB/AR	2.03	1.96	1.86	1.84	1.83	2.07	1.95	2.18
LEB	12.74	10.77	12.74	12.74	12.74	12.74	12.31	13.51
LEB/AR	6.85	11.71	10.98	8.79	9.44	9.30	10.26	12.51
Note : AR - Actual record								
GEB - Global energy-bound convex model								
LEB - Local energy-bound convex model								

duration and the maximum force of all impulses is kept the same, while the energy of the impulses is different; Second, the energy and the duration of the impulses are kept the same, while the maximum force is different; Third, the energy and the maximum force of the impulses are kept the same, but the duration of the impulses is different. All three combinations have the same dynamic magnification factors for the actual response and the global energy bound convex model. The GEB convex model gives higher values than the response evaluated using the time-history of the actual record (AR) by an average ratio for the eight impulses, $(\text{GEB}/\text{AR})_d = 1.97$ for the damping level of 5 % of critical.

For the LEB convex model, the nondimensional local energy factor, $E_L^2(t_1) / P_a^2$, which is only related to the maximum value of the excitation, is always equal to 1. The LEB convex model gives much higher values than the response using the actual record, by an average ratio for the eight impulses, $(\text{LEB}/\text{AR})_d = 9.98$ for the damping level of 5 % of critical.

Similar results can be observed when the structure is subjected to past earthquake records. Consider a SDOF structural system subjected to the S00E record of the May 18, 1940 El-Centro earthquake which is shown in Figure 4.6(a). The displacement responses obtained by using the time-history of the actual record (AR), the GEB convex model, and the LEB convex model are shown in Figure 5.5. The fundamental period of the structure is 1.0 sec. and the damping level is 5 % of critical. The maximum responses obtained by the AR, the GEB and LEB convex models analysis equal 0.13, 0.48, and 1.57 meters respectively. The time-history displacement for the structure with a damping level of 10 % of critical is shown in Figure 5.6. The maximum responses obtained by the AR, and

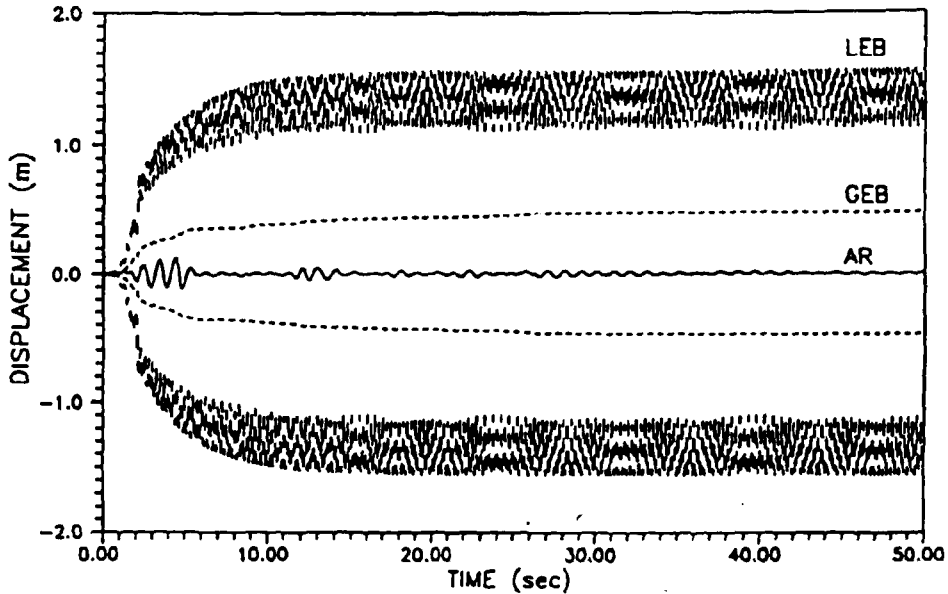


Figure 5.5 Displacement time-history of a SDOF system with damping level of 5 % of critical for the 1940 El-Centro earthquake; — = actual record (AR), = global energy-bound convex model (GEB), - - - = local energy-bound convex model (LEB)

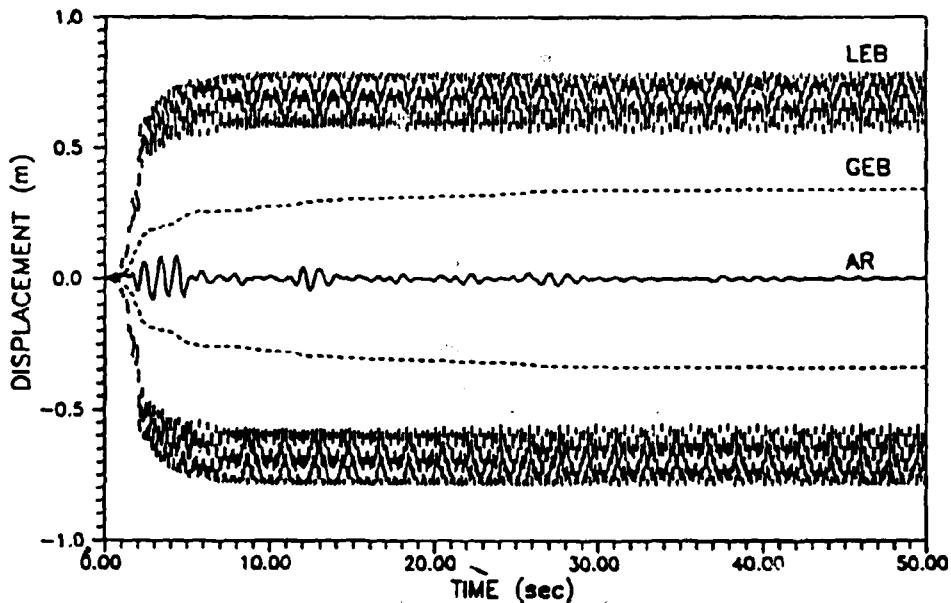


Figure 5.6 Displacement time-history of a SDOF system with damping level of 10 % of critical for the 1940 El-Centro earthquake; — = actual record (AR), = global energy-bound convex model (GEB), - - - = local energy-bound convex model (LEB)

the GEB and LEB convex model analysis equal 0.09, 0.34, and 0.79 meters. Similar results can be observed for the time-history of the velocity and acceleration responses. These results show that the convex models give bounds that are relatively closer to the actual maxima for higher levels of damping. This property is desirable in the design of active structures, which inherently have higher levels of damping.

For the case with a damping level of 5 % of critical, the response obtained by the GEB convex model gives a higher value than the maximum response obtained using the time-history of the actual record (AR) by a ratio, $(\text{GEB}/\text{AR})_d = 3.71$ for the maximum displacement, $(\text{GEB}/\text{AR})_v = 3.30$ for the maximum velocity, and $(\text{GEB}/\text{AR})_a = 2.80$ for the maximum acceleration. For the same damping level, the LEB convex model gives a much higher value than the response using the actual record by a ratio, $(\text{LEB}/\text{AR})_d = 8.76$ for the maximum displacement, $(\text{LEB}/\text{AR})_v = 8.11$ for the maximum velocity, and $(\text{LEB}/\text{AR})_a = 7.50$ for the maximum acceleration. This suggests that a reduction factor could be used to reduce the conservatism of the results obtained by the convex models for the maximum displacement, velocity, and acceleration response.

Energy-bound Convex Models Adjusted with a Reduction Factor

In general, the reduction factor for a given excitation is a function of the period and the damping ratio or the SDOF structure. Consider a given excitation of a certain energy E_G (GEB) or E_L (LEB), for a given structure with mode shapes ϕ_1, \dots, ϕ_N . The results obtained using the global and local energy-bound convex models depend on the natural frequency (period) and the damping of the structure in each mode, as can be

observed from equation (3.10) for the GEB model, and equation (3.14) for the LEB model. The reduction factors are defined at the modal level as the ratios of the response quantity obtained by the convex model divided by the response to the actual excitation record. The reduction factors for the displacement, velocity, and acceleration response obtained by the GEB convex model of equation (3.10) for the rectangular impulse, and impulse No. ④ in Figure 5.2 are shown in Figures 5.7 and 5.8, respectively. A similar procedure can be developed for earthquake records. Figures 5.9 and 5.10 show the reduction factors for displacement, velocity, and acceleration response obtained by the GEB convex model for the 1940 El-Centro (Figure 4.6(a)) and 1971 San Fernando (Figure 4.6(b)) earthquakes. The distribution of the reduction factor is significantly different for the two impulses and is unique for each impulse shape, and this is also true for each earthquake record.

The reduction factors for the response to the rectangular impulse for the LEB convex model of equation (3.14) are shown in Figure 5.11. The reduction factor for displacement is different from those for velocity and acceleration. It can be observed that for higher levels of damping the reduction factor is reduced. These figures can be used to estimate the expected response to an excitation for MDOF structural systems.

For a certain excitation, the reduction factors, which are a function of the excitation shape, the natural period, and the damping ratio of the structure, can be defined for the GEB convex model as

$$A_{0,d} = h_{0,d}(\Gamma, T, \xi); \quad A_{0,v} = h_{0,v}(\Gamma, T, \xi); \quad A_{0,a} = h_{0,a}(\Gamma, T, \xi) \quad (5.2)$$

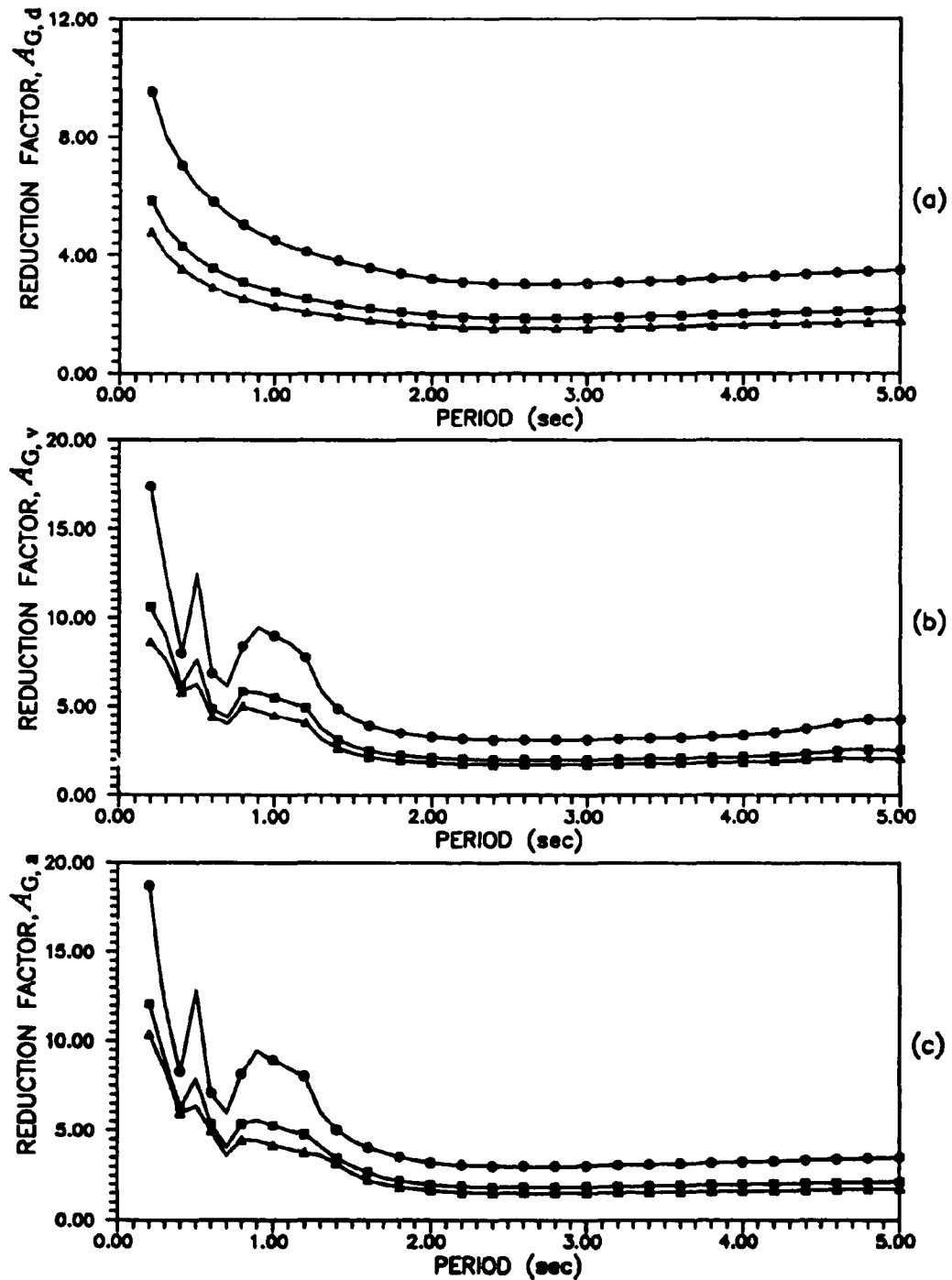


Figure 5.7 Global energy-bound reduction factor of the rectangular impulsive excitation: (a) displacement, (b) velocity, and (c) acceleration; \ominus = damping level of 2 % of critical, \boxminus = damping level of 6 % of critical, \blacktriangle = damping level of 10 % of critical

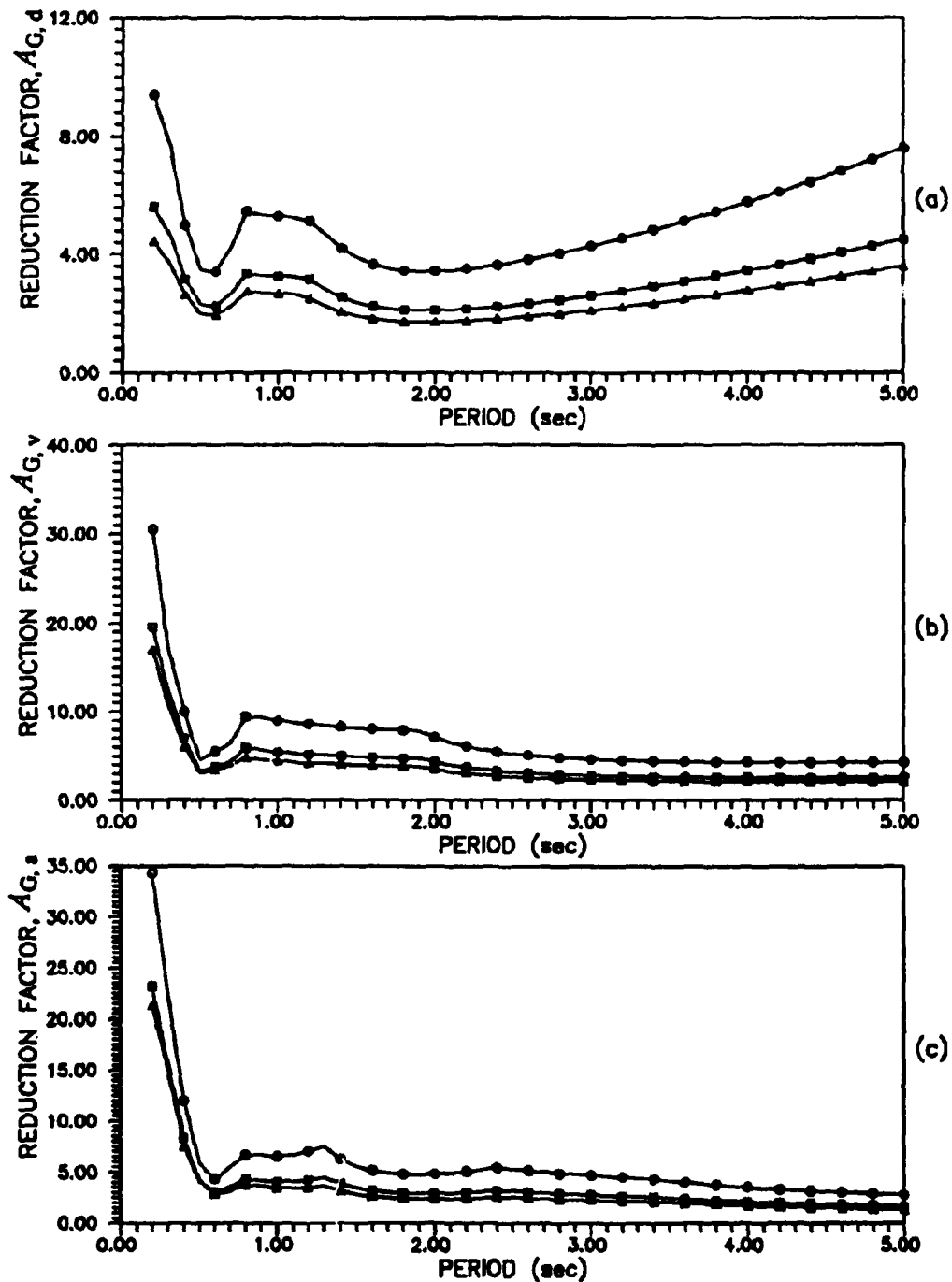


Figure 5.8 Global energy-bound reduction factor of the two-peak impulsive excitation: (a) displacement, (b) velocity, and (c) acceleration; \ominus = damping level of 2 % of critical, \boxminus = damping level of 6 % of critical, \triangle = damping level of 10 % of critical

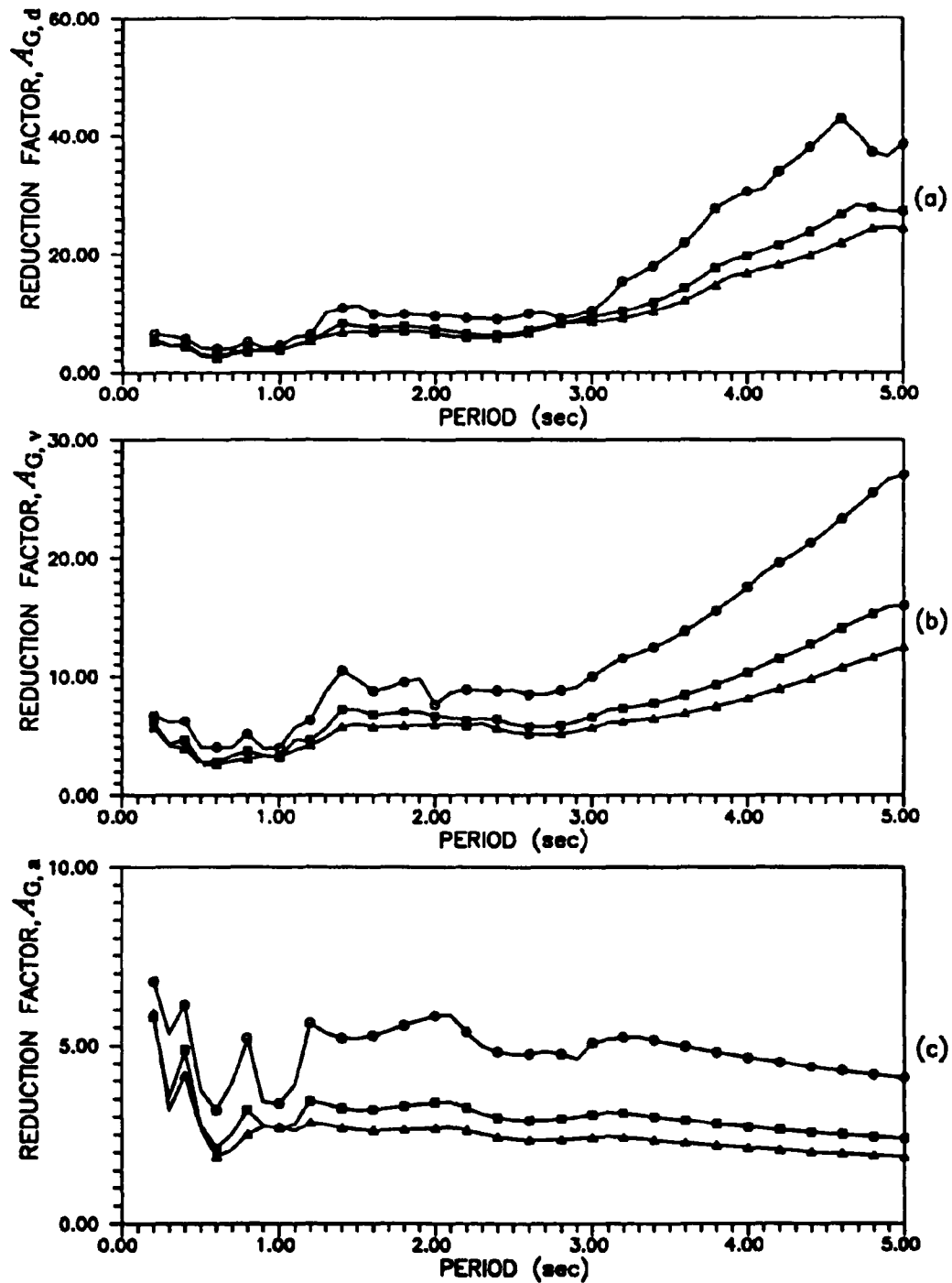


Figure 5.9 Global energy-bound reduction factor of the 1940 El-Centro earthquake: (a) displacement, (b) velocity, and (c) acceleration; \ominus = damping level of 2 % of critical, \boxminus = damping level of 6 % of critical, \triangle = damping level of 10 % of critical

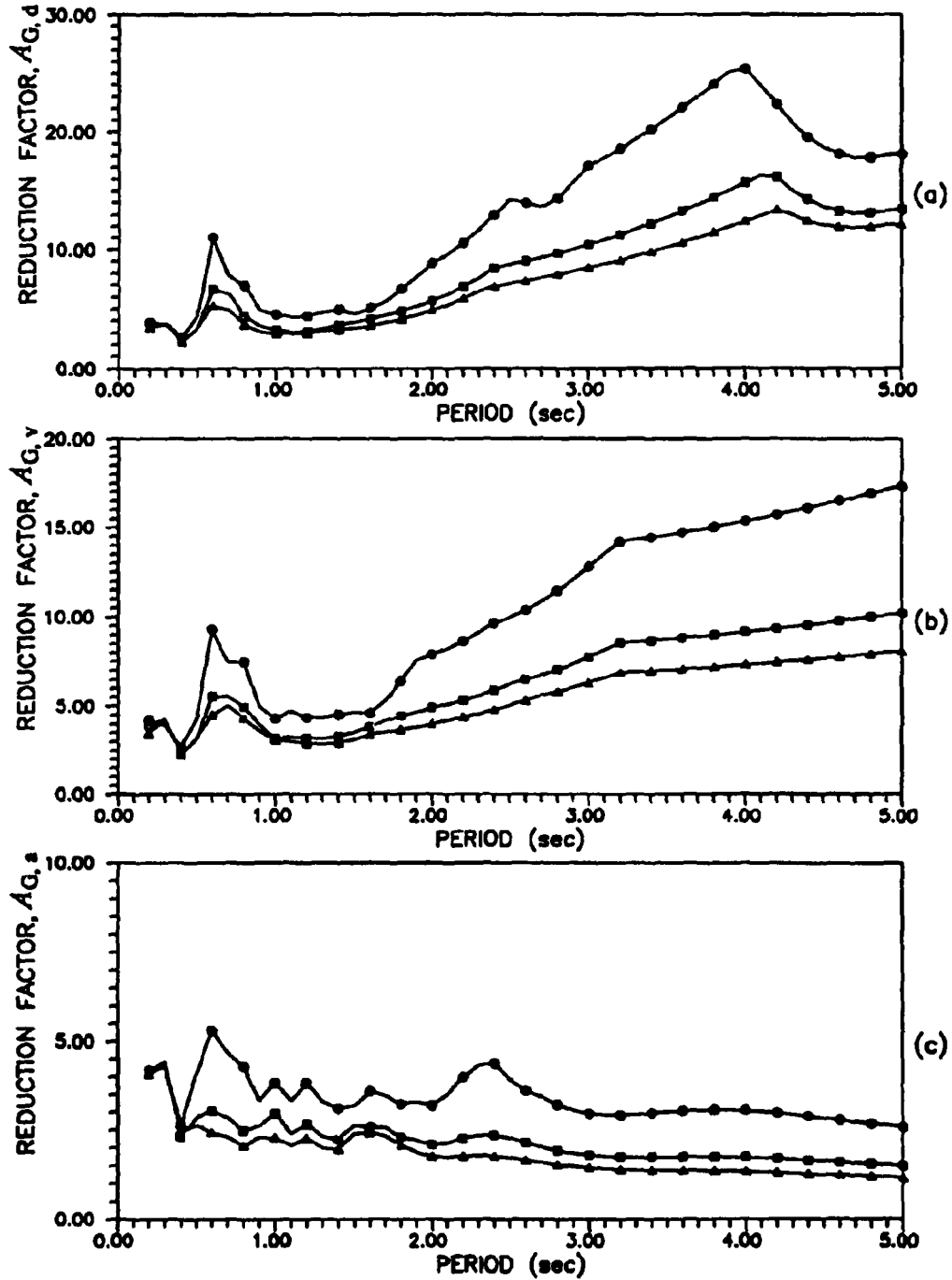


Figure 5.10 Global energy-bound reduction factor of the 1971 San Fernando earthquake: (a) displacement, (b) velocity, and (c) acceleration; \ominus = damping level of 2 % of critical, \boxplus = damping level of 6 % of critical, \triangle = damping level of 10 % of critical

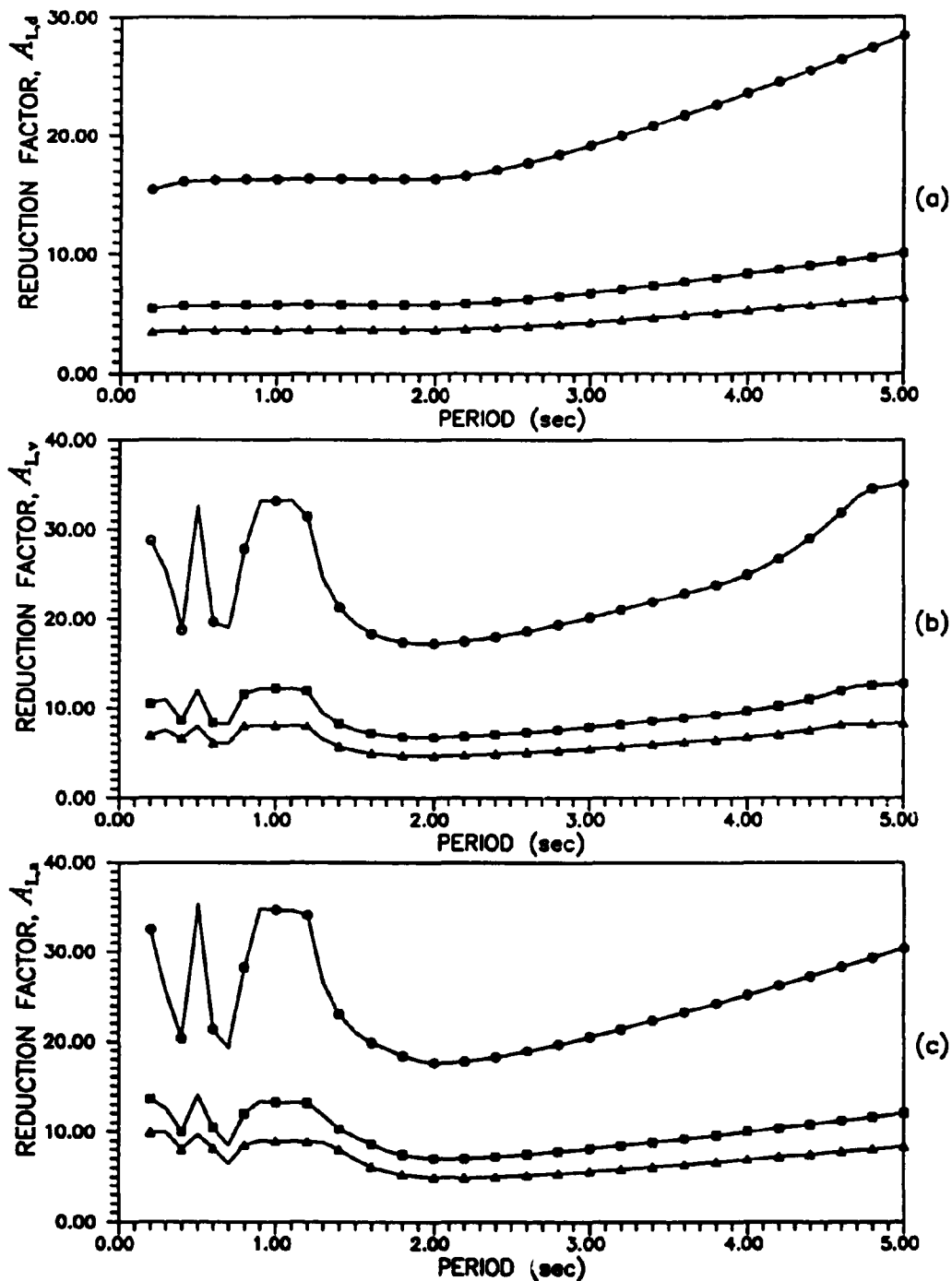


Figure 5.11 Local energy-bound reduction factor of the rectangular impulse: (a) displacement, (b) velocity, and (c) acceleration; \ominus = damping level of 2 % of critical, \boxminus = damping level of 6 % of critical, \triangleleft = damping level of 10 % of critical

and for the LEB convex model as

$$A_{L,d} = h_{L,d}(\Gamma, T, \xi); \quad A_{L,v} = h_{L,v}(\Gamma, T, \xi); \quad A_{L,a} = h_{L,a}(\Gamma, T, \xi) \quad (5.3)$$

where Γ denotes the excitation shape; the subscripts, G and L denote the GEB and LEB convex models; d , v and a , denote the displacement, velocity, and acceleration, respectively.

The models described above are defined as the RGEB convex model (global energy-bound convex model adjusted with an excitation-specific reduction factor) and the RLEB convex model (local energy-bound convex model adjusted with an excitation-specific reduction factor). For each excitation the reduction factor can be obtained from the period and damping ratio for each mode of the structure, and will be different for other excitations. A simple method for obtaining the reduction factor is to create a data-base as a function of period and damping ratio. An interpolation technique can be used to find the value of the reduction factor for a certain period and damping. Another method is to fit a curve to the data-base as a function of the period (frequency) and damping ratio for each mode of the structure. For example, in the case of the rectangular impulse, the reduction factor for the global energy-bound convex model, equation (5.2), can be written as

$$A_0 = a_1(1 + a_2 e^{-\alpha_2 \tau}) (1 + a_4 e^{-\alpha_4 \tau}) \quad (5.4)$$

where the constants, a_1, \dots, a_5 , are equal to: 1.1589, 2.9376, 2.0696, 2.4299, and 19.4258 for the displacement; 1.4910, 4.6422, 1.5463, 1.8052, and 20.9529 for the velocity; and 1.3570, 8.3356, 1.9881, 1.8098, and 27.2092 for the acceleration. The coefficients a_1, \dots, a_5 were obtained using an optimization routine for the best fit between the data-base and the expression in equation (5.4). Figure 5.12 shows the displacement reduction factor of the RGEB convex model using both methods, i.e. the data-base (Figure 5.12(a)), and equation (5.4) (Figure 5.12(b)); the agreement is considered satisfactory.

The reduction factor for the local energy-bound convex model, equation (5.3), in the case of the rectangular impulse can be written as

$$A_L = b_1[\sin(b_2\omega) + b_3e^{-b_4\omega}](1 + b_5e^{-b_6\omega}) \quad (5.5)$$

The constants, b_1, \dots, b_6 , are equal to: 3.8190, 0.1747, 0.5346, 0.6912, 14.3225, and 29.9341 for the displacement; 6.7967, 0.1531, 0.8156, 0.7359, 9.4113, and 31.2581 for the velocity; and 6.4697, -0.3526, 0.9212, -0.1389, 7.9988, and 28.3647 for the acceleration. Coefficients b_1, \dots, b_6 were obtained using an optimization routine for the best fit between the data-base and the expression in equation (5.5). Figure 5.13 shows the displacement reduction factor of the RLEB convex model using both methods, i.e., the data-base (Figure 5.13(a)), and equation (5.5) (Figure 5.13(b)); the agreement is seen to be satisfactory. Similar equations to (5.4) and (5.5) can be derived for the other excitations. The reduction factor for each excitation can be used for the records with the same duration and shape, but different levels of the energy-bound E_G , or E_L . In the

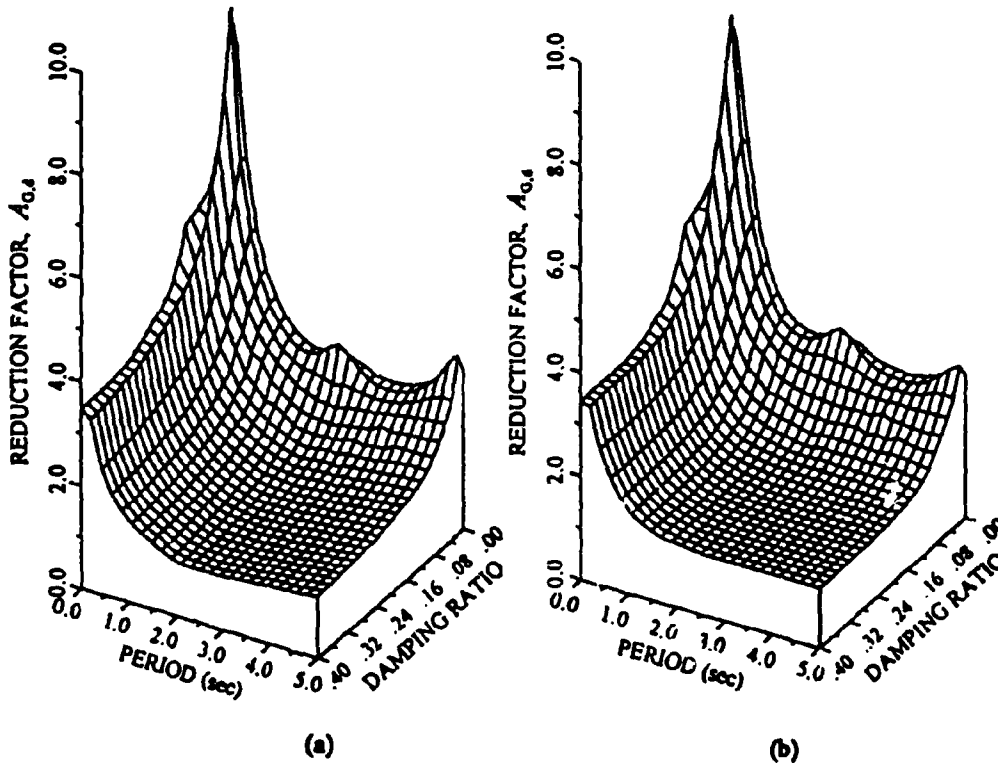


Figure 5.12 Comparison of the global energy-bound reduction factor for the rectangular impulse: (a) data-base, and (b) calibration curve

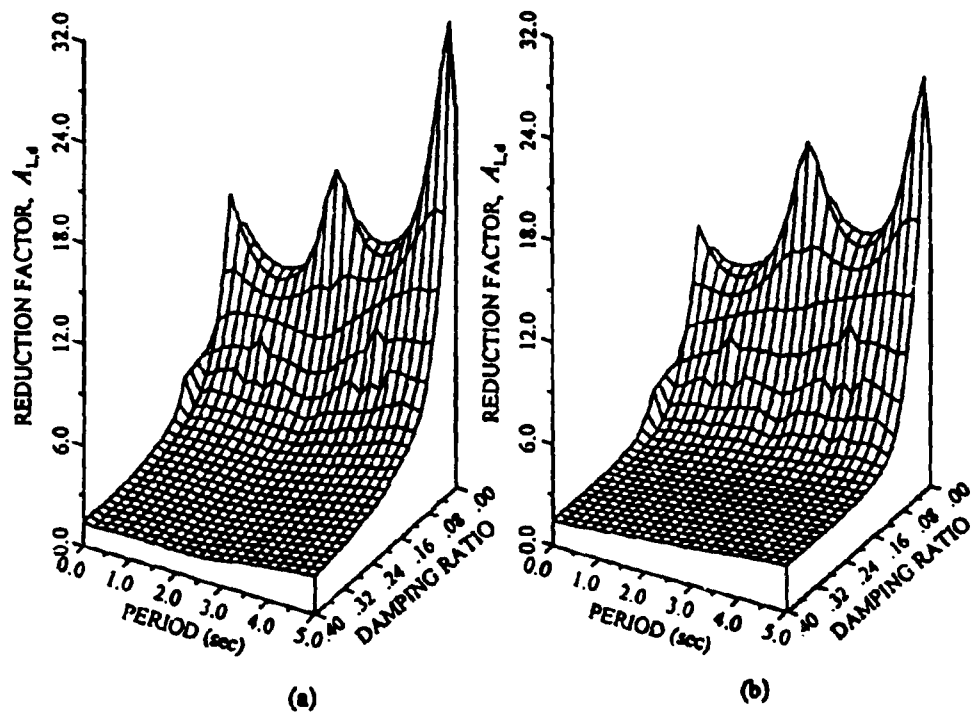


Figure 5.13 Comparison of the local energy-bound reduction factor for the rectangular impulse: (a) data-base, and (b) calibration curve

RGEB or RLEB convex model, once the excitation-specific reduction factors are obtained for each mode, the physical response can be found by combining the adjusted modal responses by the square root of the sum of the squares (SRSS) of the adjusted modal responses (equation (3.11)). This is necessary since the different modes do not achieve their maxima at the same instant in time.

The ten-story frame of Figure 5.14 is used to test the validity of the RGEB convex model. The cross-sectional area and moment of inertia of the beams and columns of the frame are shown in Table 5.2. The damping level is assumed to be 5 % of critical for all modes and only one horizontal degree-of-freedom is considered per floor. Table 5.3 shows the maximum response obtained by: (1) using equation (3.4) for the time-history of the actual record (AR); (2) the GEB convex model; and (3) the RGEB convex model. The 1940 El-Centro earthquake of Figure 4.6(a) is used. The response ratios for the GEB and RGEB models with respect to the actual record (AR) are also shown in Table 5.3. It can be observed that the displacement, velocity, and acceleration response obtained by the original GEB convex model is on average 8.2, 6.5, and 3.7 times larger respectively than that obtained using the actual record from equation (3.4). On the other hand, the differences in the displacement, velocity, and acceleration response obtained by the adjusted RGEB convex model and the actual record (AR) are within 27, 39, and 42 % respectively. On average, the results obtained by the RGEB convex model are 11.3, 15.4, and 25.3 % times larger than the response using a time-history of the actual record for the displacement, velocity, and acceleration respectively. The improvement in the prediction of the maximum response using the RGEB convex model is obvious compared to the GEB

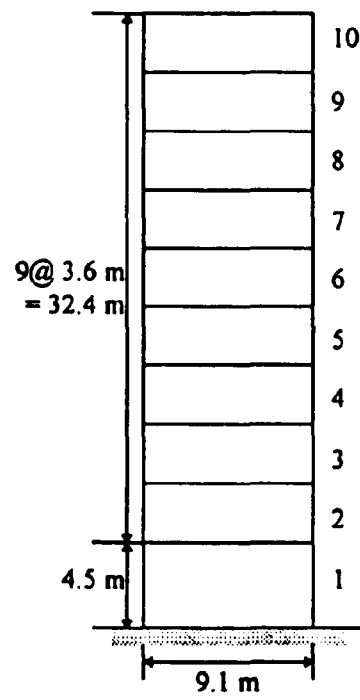


Figure 5.14 Ten-story frame

Table 5.2. Member sizes for ten-story frame

Floor	Beam		Column	
	Area ($\times 10^{-2}, m^2$)	Moment of inertia ($\times 10^{-4}, m^4$)	Area ($\times 10^{-2}, m^2$)	Moment of inertia ($\times 10^{-4}, m^4$)
1	4.02	18.65	4.66	25.03
2-4	3.69	15.69	4.41	22.51
5-7	3.63	15.25	4.15	19.90
8-10	3.17	11.59	3.48	13.96

Table 5.3. Maximum response of the ten-story frame for the 1940 El-Centro earthquake record

Floor	AR	GEB	GEB/AR	RGEB	RGEB/AR
Displacement (cm)					
1	1.37	11.14	8.13	1.74	1.27
2	3.18	26.25	8.25	3.98	1.25
3	5.09	42.79	8.41	6.23	1.22
4	6.89	59.05	8.57	8.23	1.19
5	8.78	74.60	8.50	9.95	1.13
6	10.71	88.77	8.29	11.45	1.07
7	12.57	101.31	8.06	12.84	1.02
8	14.34	112.81	7.87	14.30	1.00
9	15.79	122.15	7.74	15.68	0.99
10	16.84	128.66	7.64	16.75	0.99
Velocity (cm/s)					
1	10.70	63.25	5.91	14.83	1.39
2	22.49	129.61	5.76	30.14	1.34
3	32.96	193.89	5.88	42.85	1.30
4	41.58	253.29	6.09	50.75	1.22
5	49.73	308.43	6.20	54.21	1.09
6	55.68	358.59	6.44	55.31	.099
7	59.19	404.31	6.83	57.10	.096
8	58.61	448.69	7.66	63.03	1.08
9	67.49	488.95	7.24	73.34	1.09
10	77.19	522.41	6.77	83.69	1.08
Acceleration (cm/s ²)					
1	348.59	1584.31	4.54	495.11	1.42
2	541.52	1722.54	3.27	624.28	1.15
3	636.71	1886.39	2.96	734.39	1.15
4	568.89	1973.75	4.47	791.51	1.39
5	576.92	2062.58	3.58	762.08	1.32
6	516.60	2128.05	4.12	733.23	1.42
7	540.96	2236.70	4.13	662.69	1.23
8	576.64	2349.90	4.08	704.30	1.22
9	709.31	2495.88	3.52	827.42	1.17
10	923.82	2876.45	3.11	978.98	1.06

convex model.

The usefulness of the RGEB and RLEB convex models is limited to evaluating the maximum structural response for a given excitation, but for structures with different properties of natural periods and damping. In addition, the RGEB and RLEB convex models are useful in the definition of more general convex models which can predict the maximum structural response for uncertain earthquakes with certain common characteristics, as will be shown in the next section.

Energy-bound Convex Models Using Average Reduction Factor

The results obtained by the RGEB convex model are less conservative than those obtained by the GEB convex model, and the maximum response is within reasonable agreement compared to the actual results from a time-history of the earthquake record. Similar results also can be observed by comparing the RLEB convex model to the LEB convex model. However, the reduction factor obtained by the RGEB or RLEB convex models can be used only for a given earthquake excitation that is not known before it occurs. It should be noted that the reduction factors are independent of the absolute value of the energy bound.

In order to extend the results obtained by the RGEB and RLEB convex models to other unknown earthquakes, it is necessary to have additional information besides the value of the global energy bound. This is necessary because of the variations in frequency content of earthquakes originating at different locations, variations due to soil conditions, topography and others. For an uncertain excitation, an average reduction factor of the global energy-bound convex model (ARGEB) or the local energy-bound convex model

(ARLEB) is defined by using one of three methods: (1) select a set of excitations with a common characteristic such as the eight impulses shown in Figure 5.2 and average the RGEB or RLEB reduction factors of the set; (2) collect a set of actual past earthquake records in the vicinity of the site and average the RGEB or RLEB reduction factors of the set; or (3) construct a set of artificial earthquake records from a known spectrum in the proximity of the site and average the RGEB or RLEB reduction factors of the set. For the RGEB and the RLEB convex models, the reduction factor was obtained as described in the previous section. For the ARGEB and ARLEB convex models, the average reduction factor for each subset is obtained by averaging the earthquake-specific reduction factors for all the earthquake records in the subset. Subsequently, the response obtained from equation (3.10) for the GEB convex model or equation (3.14) for the LEB convex model must be divided by the average reduction factor for each mode (ARGEB or ARLEB), and the final response is obtained using equation (3.11).

The average reduction factors for each set of excitations can be expressed for the ARGEB convex model as

$$B_{G,d} = h_{G,d}(T, \xi); \quad B_{G,v} = h_{G,v}(T, \xi); \quad B_{G,a} = h_{G,a}(T, \xi) \quad (5.6)$$

and for the ARLEB convex model as

$$B_{L,d} = h_{L,d}(T, \xi); \quad B_{L,v} = h_{L,v}(T, \xi); \quad B_{L,a} = h_{L,a}(T, \xi) \quad (5.7)$$

Comparing equations (5.2) and (5.3) with equations (5.6) and (5.7), it can be observed that in the latter equations only two variables need to be considered: the period (frequency) and damping level for each mode of the structure.

The global energy-bound average reduction factor for the set of the impulsive excitations can be expressed using a calibration curve as

$$B_G = c_1(1 + c_2 e^{-c_3 \omega})(1 + c_4 e^{-c_5 t}) \quad (5.8)$$

where the constants, c_1, \dots, c_5 , are equal to: 1.2865, 3.5759, 4.0733, 2.6014, and 28.1952 for the displacement response; 1.7104, 15.7871, 4.4048, 1.9268, and 18.0370 for the velocity response; and 1.7062, 23.6133, 3.6927, 1.5213, and 36.4565 for the acceleration response. Similar expressions can be defined for the seismic records. The average reduction factor for the ARLEB convex model can be obtained by the same way as the ARGEB convex model for each group of excitations.

The average reduction factor of the ARGEB convex model for the impulse set of Figure 5.2 for a structural damping level of 2, 6, and 10 % of critical is shown in Figure 5.15 for the displacement, velocity, and acceleration responses. Comparing the results shown in Figure 5.15 with Figures 5.7 and 5.8, it is clear that the distribution of the values is not exactly the same. However, when the shape and duration of the excitation are unknown, the average reduction factors can be useful for finding an approximation of the maximum actual response using convex models. In the ARGEB or ARLEB model, once the average reduction factors are obtained for each mode, the physical response can be

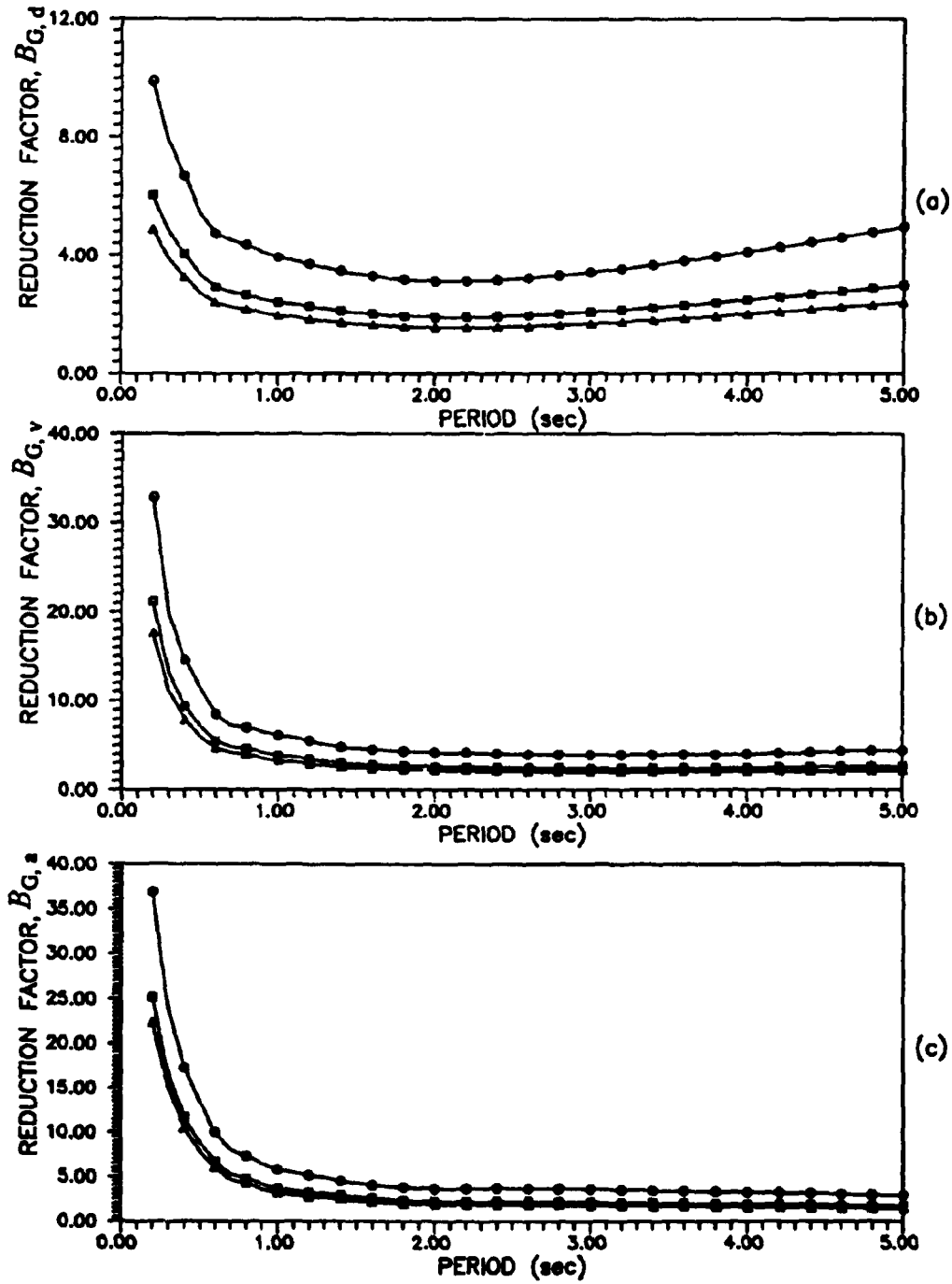


Figure 5.15 Average reduction factor for global energy-bound of impulsive excitations of Figure 5.2: (a) displacement, (b) velocity, and (c) acceleration; \ominus = damping level of 2 % of critical, $\omin�$ = damping level of 6 % of critical, $\omin�$ = damping level of 10 % of critical

found by combining the adjusted modal responses by the SRSS method of equation (3.11).

ARGEB and ARLEB Convex Models for Impulse Excitations

The eight-story building shown in Figure 4.1(a) is used to evaluate the excitation-specific reduction factor of equations (5.2) and (5.3) (RGEB and RLEB convex models) and the average reduction factor of equations (5.6) and (5.7) (ARGEB and ARLEB convex models). A rectangular, a sine wave, and a two peak impulse corresponding to Cases ①, ④, and ⑥, of Figure 5.2 are used to evaluate the maximum response using the actual record (AR), and the response using the convex models.

For the global energy-bound convex model the energy and duration of these impulses are the same, given as $24.01 \text{ m}^2/\text{sec}^3$ and 1 sec, respectively. This is an unusually long impulse duration and it was chosen for illustrative purposes only. However, it should be noted that the reduction factors are the same for impulses of any magnitude of the energy bound. The peak magnitude of the impulse, P_o , is given as 0.5 g, 0.707 g, and 0.677 g for the impulsive forces ①, ④, and ⑥ respectively, where g is the acceleration of gravity.

Table 5.4 shows the maximum displacement at each floor using the time-history of the actual record (AR), the global energy-bound (GEB) convex model, the GEB convex model employing the excitation-specific reduction factor (RGEB) described in equation (5.2), and the GEB convex model using the average reduction factor (ARGEB) described in equation (5.6). Since the global energy bound of the three impulsive forces is the same, it can be observed that the maximum displacements obtained by the GEB convex model are identical for all three impulses. Naturally, this is not true for the response using the

Table 5.4. Displacement response of the eight-story building for impulses with the same global energy-bound

Floor	AR (cm)	GEB (cm)	GEB/AR	RGEB (cm)	RGEB/AR	ARGEB(cm)	ARGEB/AR
Case ① - Rectangular impulse							
1	7.32	26.10	3.57	6.47	0.88	7.31	1.00
2	13.97	51.22	3.67	12.69	0.91	14.35	1.03
3	19.81	74.49	3.76	18.46	0.93	20.88	1.06
4	24.73	95.19	3.85	23.59	0.95	26.69	1.08
5	28.69	112.66	3.93	27.93	0.97	31.60	1.10
6	31.67	126.36	3.99	31.32	0.99	35.44	1.12
7	33.65	135.81	4.04	33.66	1.00	38.09	1.13
8	34.65	140.64	4.06	34.68	1.01	39.44	1.14
Case ② - Sinc wave impulse							
1	8.87	26.10	2.94	7.94	0.90	7.31	0.82
2	17.00	51.22	3.01	15.60	0.92	14.35	0.84
3	24.26	74.49	3.07	22.72	0.94	20.88	0.86
4	30.49	95.19	3.12	29.06	0.95	26.69	0.88
5	35.61	112.66	3.16	34.41	0.97	31.60	0.89
6	39.53	126.36	3.20	38.60	0.98	35.44	0.90
7	42.17	135.81	3.22	41.48	0.98	38.09	0.90
8	43.50	140.64	3.23	42.94	0.99	39.44	0.91
Case ③ - Two-peak impulse							
1	7.44	26.10	3.51	7.04	0.95	7.31	0.98
2	14.48	51.22	3.54	13.81	0.95	14.35	0.99
3	20.93	74.49	3.56	20.09	0.96	20.88	1.00
4	26.58	95.19	3.58	25.67	0.97	26.69	1.00
5	31.28	112.66	3.60	30.39	0.97	31.60	1.01
6	34.93	126.36	3.62	34.08	0.98	35.44	1.01
7	37.46	135.81	3.63	36.63	0.98	38.09	1.02
8	38.74	140.64	3.63	37.93	0.98	39.44	1.02

Table 5.5. Displacement reduction factor for the RGEB and ARGEB convex models for each mode for the eight-story shear building

Impulse		Mode 1	Mode 2	Mode 3	Mode 4	Mode 5	Mode 6	Mode 7	Mode 8
RGEB	Rectangular	4.03	4.12	4.08	4.30	4.25	4.20	4.17	4.15
	Sine wave	3.27	5.40	4.66	5.20	4.97	4.77	4.62	4.55
	Two-peak	3.71	3.78	4.09	4.93	4.81	4.68	4.57	4.52
ARGEB		3.57	3.93	4.03	4.25	4.09	3.98	3.89	3.84

actual record. The displacements obtained by the GEB convex model are on average 3.86, 3.12, and 3.58 times larger than the response to the time-history of the actual record (AR) for the rectangular, sine wave, and two-peak impulses, respectively.

For the GEB convex model adjusted by the reduction factor of each specific impulse shape (RGEB model), the displacements in Table 5.4 were found as follows: The GEB convex modal displacements given by equation (3.10a) were divided by the displacement reduction factor $A_{o,d}(\Gamma, T, \xi)$ as defined in equation (5.2) for each of the eight modes. Table 5.5 shows the reduction factors of each mode for the three impulses. Subsequently, the physical response for the RGEB convex model was obtained by combining the adjusted modal responses using the SRSS method of equation (3.11). The difference in the displacement response obtained by the RGEB convex model and the actual record (AR) was within 12 % for the rectangular impulse, 10 % for the sine wave impulse, and 5 % for the two-peak impulse as shown in Table 5.4.

The responses obtained by the GEB convex model adjusted by the average reduction factor (ARGEB convex model), using the average reduction factor $B_{o,d}(T, \xi)$ of equation (5.6) in Table 5.4, are all the same; this is because the average reduction factor for any impulse of unknown shape has by definition the same value (see Table 5.5 for the reduction factor of each mode). The physical response for the ARGEB model was obtained by combining the adjusted modal responses using the SRSS method of equation (3.11). The difference between the actual displacement response (AR) and the displacement using the ARGEB model was within 14 % for the rectangular impulse, 18 % for the sine wave impulse, and 2 % for the two-peak impulse as shown in Table 5.4.

Figure 5.16 shows the maximum velocity and acceleration response at each floor

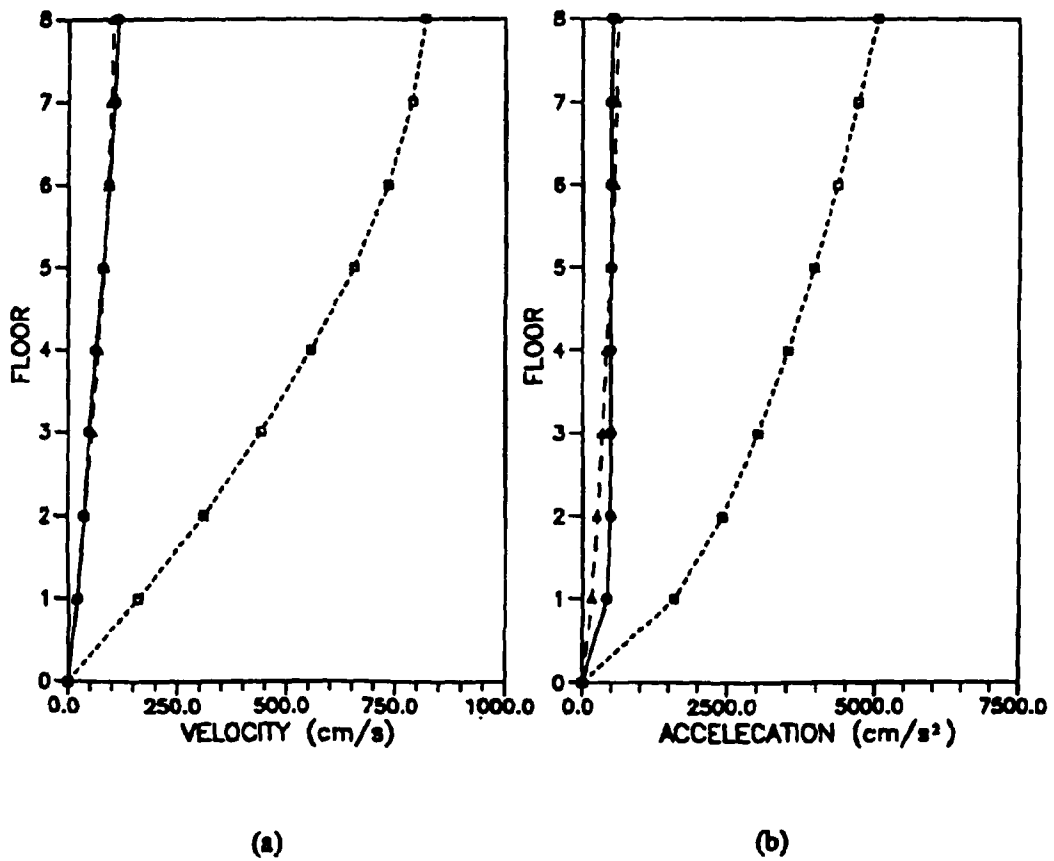


Figure 5.16 Maximum dynamic response of the eight-story building to a rectangular impulse: (a) velocity, (b) acceleration; \ominus = actual response (AR), \square = GEB convex model, \triangle = RGEb convex model

of the eight-story building for the rectangular impulse. It can be observed that the velocity and acceleration obtained by the GEB convex model are much larger than the response to the actual record (AR). However, the difference between the actual record (AR) and the RGEB convex model is reduced appreciably for both the velocity and the acceleration response as shown in Figure 5.16. Similar results are obtained for the sine wave and two-peak impulses.

The difference between the AR and ARGEB (GEB convex model adjusted by the average reduction factor) model is slightly larger than that between the AR and the RGEB model and depends on the actual shape and duration of the impulse. For the rectangular impulse (case ① of Figure 5.2), the displacement, velocity, and acceleration response obtained from the actual response (AR), the RGEB, and ARGEB models are shown in Figure 5.17. Similar results are obtained for the sine wave and two peak impulses. The results obtained by the ARGEB model are still acceptable for an impulse with unknown shape and duration.

The displacement response maxima, using either the RGEB or ARGEB convex model, are seen to be predicted more accurately than the velocity or acceleration maxima for this structure. This behavior can be expected since the reduction factors for velocity and acceleration for the dominant periods of this structure are much larger than those of displacement, as shown in Figure 5.15. For structures with longer dominant periods the results for velocity and acceleration using the RGEB or the ARGEB convex models are expected to be predicted with an accuracy comparable to that for the maximum displacement.

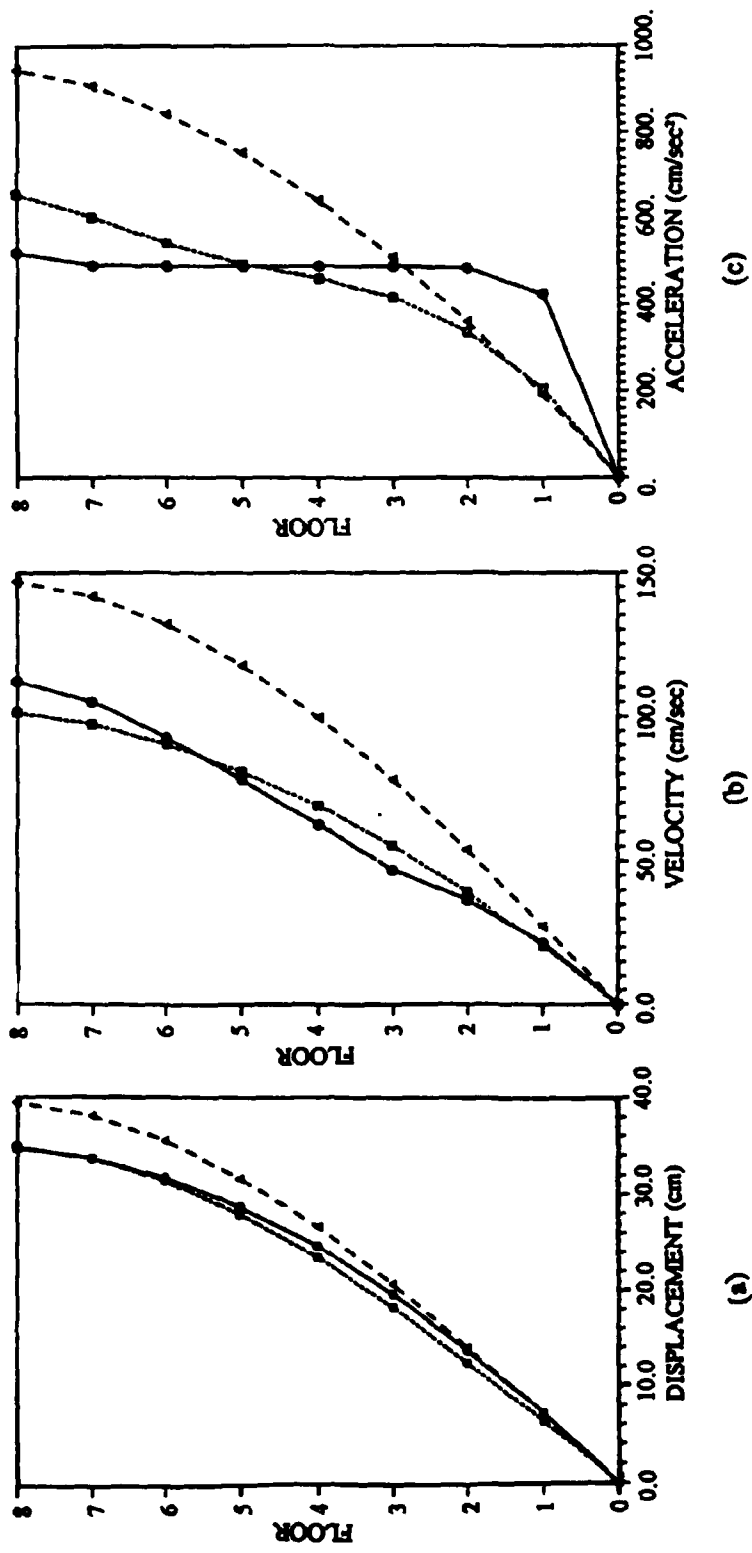


Figure 5.17 Maximum dynamic response of the eight-story building to a rectangular impulse: (a) displacement, (b) velocity, (c) acceleration; \ominus = actual response (AR), \triangle = ARGEB convex model, --- = ARGEB convex model

The comparison of the three impulsive responses using the local energy-bound (LEB) convex model and the results adjusted by the reduction factor and the average reduction factor are shown in Table 5.6. The local energy and duration for impulse case ①, ④, and ⑥ are the same, given as $4.9 \text{ m}^2/\text{sec}^2$ and 1 sec, respectively. The difference in the displacement response obtained by the RLEB model and the actual record (AR) was within 17, 14, and 10 % for the rectangular impulse, sine wave impulse, and two-peak impulse, respectively. The difference between the actual displacement response (AR) and the displacement using the ARLEB model was within 36, 26, and 26 % for the three impulses, respectively. The reduction factors for these three impulses and the average reduction factor of each mode are shown in Table 5.7. Comparing Table 5.4 for the ARGEB convex model and Table 5.6 for the ARLEB convex model it can be observed that the former method is more accurate for this building.

ARGEB Convex Model for Past Earthquake Records

Thirty-two past earthquake records described in Table 5.8 are used to evaluate the performance of the ARGEB convex model. Table 5.9 shows the eight subsets of the above records defined for the purpose of this study. The ten-story frame shown in Figure 5.14 is used for: (1) the time-history of four actual earthquakes, (2) the RGEB convex model, and (3) the ARGEB convex model with several subset excitation records. A response ratio is defined by dividing the response obtained by the convex model to the response obtained using the time-history of the actual record. This ratio is averaged over all floors and is shown in Table 5.10 for both the RGEB and ARGEB convex models.

Table 5.6. Displacement response of the eight-story building for impulses with the same local energy-bound

Floor	AR (cm)	LEB (cm)	LEB/AR	RLEB (cm)	RLEB/AR	ARLEB(cm)	ARLEB/AR
Case ① - Rectangular impulse							
1	7.32	86.86	11.87	6.06	0.83	4.67	0.64
2	13.97	170.74	12.22	11.89	0.85	9.16	0.66
3	19.81	248.76	12.56	17.31	0.87	13.32	0.67
4	24.73	318.29	12.87	22.14	0.90	17.03	0.69
5	28.69	376.99	13.14	26.21	0.91	20.16	0.70
6	31.67	422.88	13.35	29.40	0.93	22.61	0.71
7	33.65	454.39	13.50	31.59	0.94	24.30	0.72
8	34.65	470.42	13.56	32.71	0.94	25.61	0.73
Case ② - Sine wave impulse							
1	6.27	86.86	13.85	5.41	0.86	4.67	0.74
2	12.02	170.74	14.20	10.54	0.88	9.16	0.76
3	17.15	248.76	14.50	15.27	0.89	13.32	0.78
4	21.56	318.29	14.76	19.50	0.90	17.03	0.79
5	25.18	376.99	14.97	23.09	0.92	20.16	0.80
6	27.95	422.88	15.13	25.89	0.93	22.61	0.81
7	29.82	454.39	15.24	27.82	0.93	24.30	0.81
8	30.76	470.42	15.29	28.82	0.94	25.61	0.82
Case ③ - Two-peak impulse							
1	5.50	86.86	15.79	4.90	0.98	4.67	0.74
2	10.69	170.74	15.97	9.61	0.90	9.16	0.76
3	15.46	248.76	16.09	13.97	0.90	13.32	0.78
4	19.63	318.29	16.21	17.83	0.91	17.03	0.79
5	23.09	376.99	16.33	21.09	0.91	20.16	0.80
6	25.79	422.88	16.40	23.66	0.92	22.61	0.81
7	27.66	454.39	16.43	25.43	0.92	24.30	0.81
8	28.61	470.42	16.44	26.34	0.92	25.61	0.82

Table 5.7. Displacement reduction factor for the RLEB and ARLEB convex models for each mode for the eight-story shear building

Impulse		Mode 1	Mode 2	Mode 3	Mode 4	Mode 5	Mode 6	Mode 7	Mode 8
RLEB	Rectangular	14.38	7.03	2.89	2.32	1.96	1.77	1.65	1.59
	Sine wave	15.34	5.02	0.77	3.95	3.25	2.85	2.59	2.47
	Two-peak	17.88	4.73	4.10	3.61	3.06	2.72	2.51	2.40
ARLEB		18.70	6.70	4.37	3.34	2.77	2.45	2.25	2.15

Table 5.8. Past earthquake records used to investigate the ARGEB convex model

No.	Earthquake	Date	Location	Component	Accel. (g)
Earthquakes in California (US)					
1	El-Centro	May 18, 1940	Imperial Valley	S00E	0.348
2				S90W	0.214
3	Taft	July 21, 1952	Kern county (Taft Lincoln school)	S69E	0.179
4				N21E	0.156
5	San Fernando	Feb. 9, 1971	Pacoima Dam	S16E	1.172
6				1.076	1.076
7	Loma Prieta	Oct. 17, 1989	Oakland-outer harbor wharf -channel 1	270°	0.276
8			channel 3	0°	0.220
9			channel 4	270°	0.276
10			channel 5	270°	0.298
11			channel 6	270°	0.305
12			channel 7	0°	0.277
13			channel 8	0°	0.436
14			channel 9	270°	0.296
15			channel 10	270°	0.269
16			channel 12	0°	0.287
17	Northridge	Jan. 17, 1994	Santa Monica - City Hall	90°	0.885
18				0°	0.370
19			Sylmar - County hospital	0°	0.844
20				90°	0.605
21			Newhall - LA County fire station	0°	0.590
22				90°	0.583
23			Pacoima Dam - Downstream	0°	0.434
24				175°	0.415
25			Arleta - Nordoff Ave. fire station	90°	0.344
26				0°	0.308
Earthquakes in Mexico					
27	Mexico City	Sep. 19, 1985	Coast of Buerrero-Michoacan	N90W	0.171
28				S00E	0.100
Earthquakes in Japan					
29	Hachinohe	May, 1968	-	S-N	0.228
30				E-W	0.180
31	Miyagi	June 12, 1978	-	S-N	0.263
32				E-W	0.205

Table 5.9. Subsets of earthquakes used in the ARGEB convex model

Subset	Description	Record (see Table III)
S1	El-Centro, May 18, 1940	1, 2
S2	San Fernando, Feb. 9, 1971	5, 6
S3	Loma Prieta, Oct. 17, 1989	7 - 16
S4	Northridge, Jan. 17, 1994	17 - 26
S5	El-Centro, May 18, 1940 and Taft, July 21, 1952	1 - 4
S6	San Fernando, Feb. 9, 1971 and Northridge, Jan. 17, 1994	5, 6, 17 - 26
S7	California records	1 - 26
S8	California, Mexico City, Sep. 19, '85, Hachinohe, May, '68, and Miyagi, June 12, '78	1 - 32

Table 5.10. Response ratio for maximum response using the RGEB and the ARGEB convex models for past earthquake records

	Max. Displacement	Max. Velocity	Max. Acceleration
1940 El-Centro earthquake (S00E) - AR1			
RGEB/AR1	1.11	1.15	1.25
ARGEB(S1)/AR1	1.07	1.21	1.00
ARGEB(S5)/AR1	1.14	1.10	0.94
ARGEB(S7)/AR1	1.61	1.48	1.14
ARGEB(S8)/AR1	1.56	1.33	0.81
1971 San Fernando earthquake (S16E) - AR2			
RGEB/AR2	1.03	0.94	1.30
ARGEB(S2)/AR2	0.74	0.79	1.26
ARGEB(S4)/AR2	0.79	0.82	1.22
ARGEB(S6)/AR2	0.78	0.81	1.21
ARGEB(S7)/AR2	0.87	0.86	1.05
ARGEB(S8)/AR2	0.85	0.77	0.74
1989 Loma Prieta earthquake - Oakland-outer harbor wharf (channel 8) - AR3			
RGEB/AR3	0.96	0.90	1.20
ARGEB(S3)/AR3	1.27	1.07	0.95
ARGEB(S7)/AR3	0.87	0.80	0.96
ARGEB(S8)/AR3	0.85	0.72	0.67
1994 Northridge earthquake - Santa Monica City Hall (S90N) - AR4			
RGEB/AR4	1.04	1.24	1.96
ARGEB(S2)/AR4	1.00	1.22	1.16
ARGEB(S4)/AR4	1.07	1.27	1.12
ARGEB(S6)/AR4	1.06	1.25	1.12
ARGEB(S7)/AR4	1.18	1.33	0.97
ARGEB(S8)/AR4	1.15	1.19	0.71

It can be observed that the response ratio for the results obtained by the RGEB convex model is within 30 % for all four records, except for the acceleration in the Northridge earthquake (96 %). The response ratio for the results obtained by the ARGEB convex model for the eight subsets defined in Table 5.9, indicates acceptable predictions of the maximum response. As expected, the RGEB convex model yields in general better results than the ARGEB model. For all four actual records in Table 5.10, the accuracy of the prediction of the response progressively worsens as more earthquakes are added from different locations i.e. compare (S7) to (S8). Hence, the reduction factors are sensitive with respect to the location of the subset of earthquakes used to determine the average reduction factor for each mode. However, the results obtained for the San Fernando actual earthquake (S16E) using subsets (S2), (S4), and (S6) are close. Similarly, the results obtained for the 1994 Northridge actual earthquake (Figure 4.8(b)) using subsets (S2), (S4), and (S6) are also close. This shows that the average reduction factors at approximately the same general location are not very sensitive to time.

ARGEB Convex Model for Artificial Earthquakes

The ten-story frame described in the previous section is used to investigate the performance of the RGEB and ARGEB convex models subjected to several artificial earthquakes. Three groups of artificial earthquakes are generated by the SIMQKE program (MIT, 1976). The spectrum of the first group is chosen from the example spectrum of the SIMQKE program to create six artificial earthquakes (G1) shown in Figure 5.18. All records have a peak acceleration of 0.5 g and a duration of 50 secs.

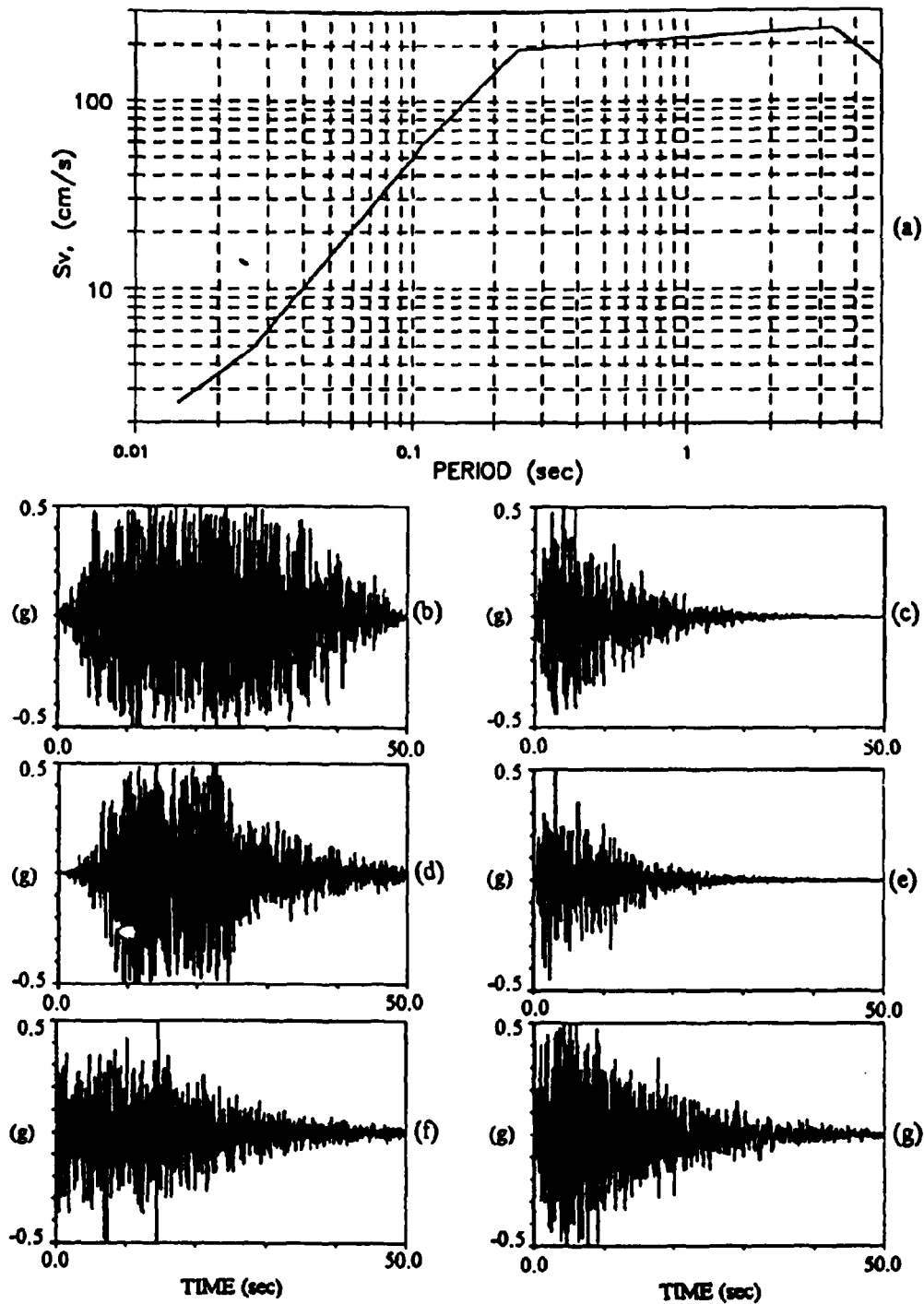


Figure 5.18 Artificial earthquakes of Group 1: (a) spectrum, (b)-(g) artificial earthquakes

However, the global energy bound is not the same; as noted earlier, this fact does not change the values of the reduction factors. Note also that even though the global energy bound is different for the artificial earthquakes, this does not affect the results which are expressed in dimensionless form. The six artificial earthquakes shown in Figure 5.19 are included in the second group (G2) created by the spectrum developed by Housner (1959). The spectrum of Figure 5.20(a) was constructed from the average response of fifteen earthquakes (Vanmarcke et al., 1976). This spectrum was used to create the third group of six artificial earthquakes (G3) as shown in Figures 5.20(b) - (g). The fourth group (G4), considers the set defined by G1, G2, and G3 combined together (see Table 5.11). The average reduction factors are then determined independently for each group of artificial earthquakes stated above.

Table 5.12 shows the response ratio of the RGEB and ARGEB convex models to the time-history analysis of the actual record (AR) for the following artificial earthquakes: 18(c), 18(f), 19(b), 19(d), 20(b), and 20(g). A conclusion can be drawn similar to that for the results shown in Table 5.10. The response ratio for the results obtained by the RGEB convex model is within 10 and 13 % for the displacement and velocity, and 93 % for the acceleration. In general, the response ratios of the ARGEB convex model of Groups 1, 2, and 3 compared with the actual record (AR) are larger than the ratios of the RGEB convex model. However, the response ratio for the results obtained by the ARGEB convex model still yields acceptable predictions of the response for the artificial earthquakes.

The ARGEB convex model of Group 2 (see Table 5.11) is used to predict the

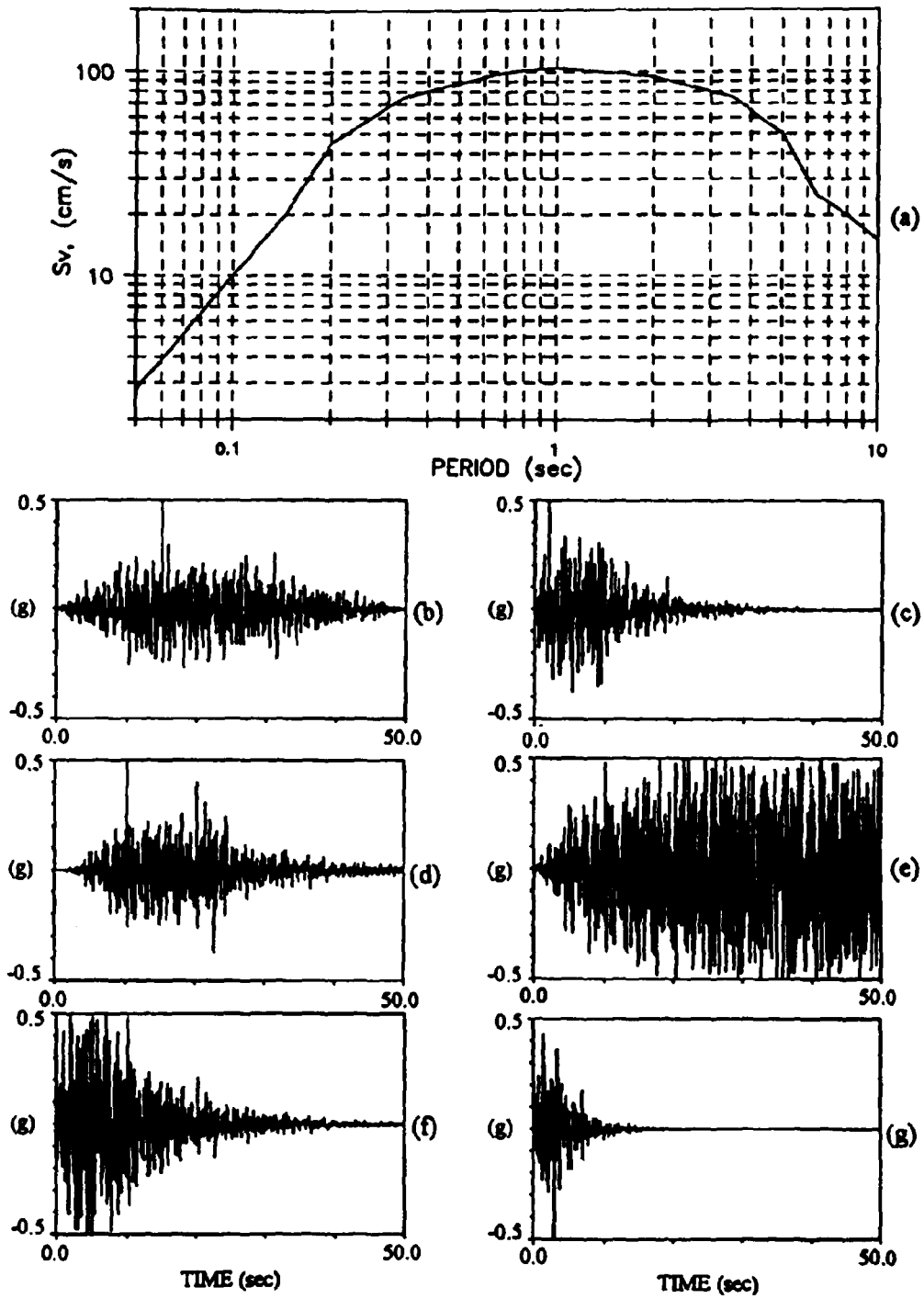


Figure 5.19 Artificial earthquakes of Group 2: (a) spectrum, (b)-(g) artificial earthquakes

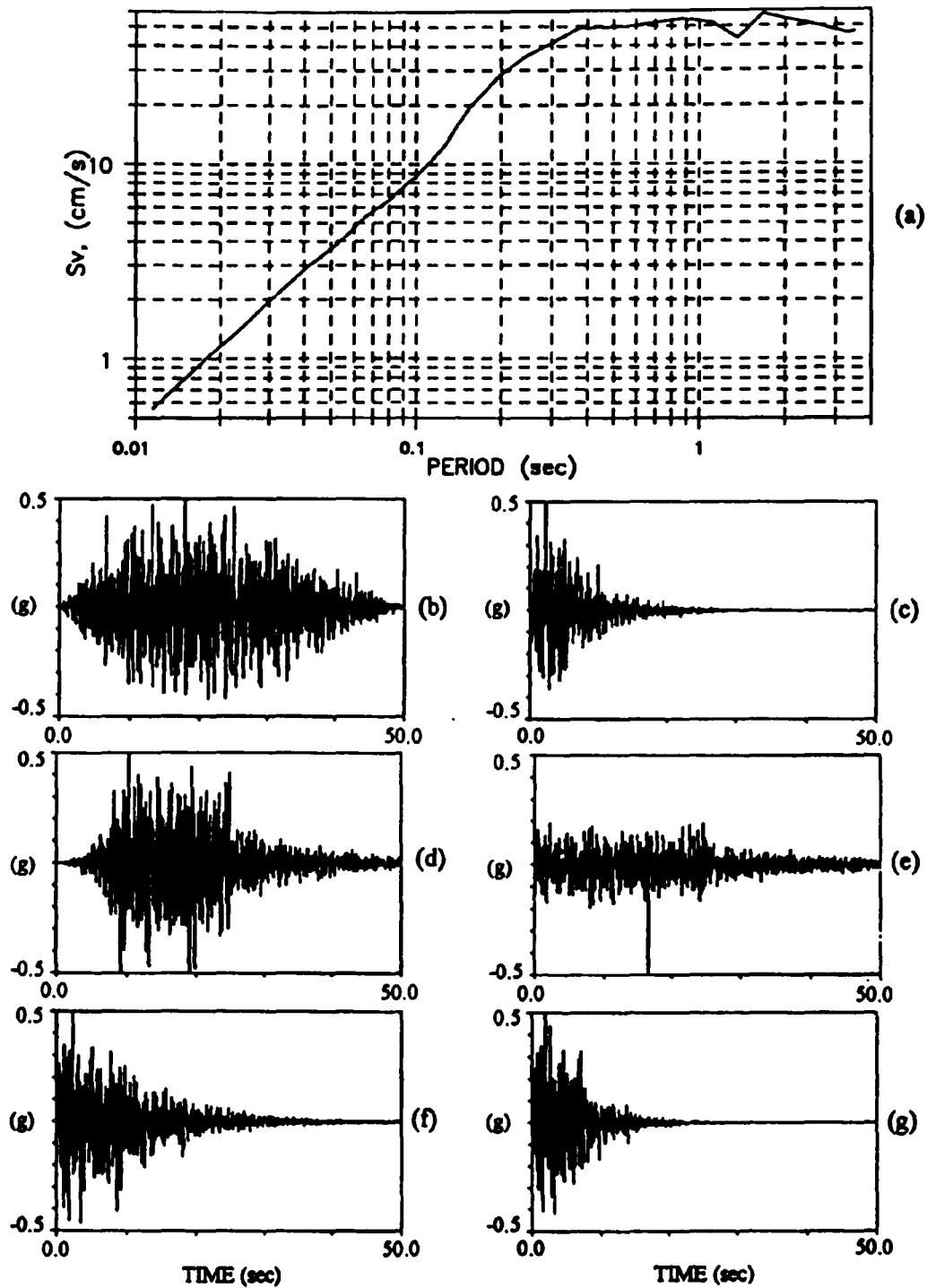


Figure 5.20 Artificial earthquakes of Group 3: (a) spectrum, (b)-(g) artificial earthquakes

Table 5.11. Artificial earthquakes used in the ARGEB convex model

Group	Description	Earthquake records
G1	Created by spectrum shown in Figure 18(a)	Figures 18(b) - (g)
G2	Created by spectrum shown in Figure 19(a)	Figures 19(b) - (g)
G3	Created by spectrum shown in Figure 20(a)	Figures 20(b) - (g)
G4	Includes Groups 1, 2, and 3	Figs. 18(b)-(g), 19(b)-(g), and 20(b)-(g)

Table 5.12. Response ratio for maximum response using the RGEB and the ARGEB convex models for artificial earthquakes

Response	Max. Displacement	Max. Velocity	Max. Acceleration
Artificial earthquake in Group 1 (Fig. 5.18(c)) - AR5			
RGEB/AR5	1.06	1.09	1.86
ARGEB(G1)/AR5	1.21	1.00	1.11
ARGEB(G4)/AR5	1.53	1.24	1.20
Artificial earthquake in Group 1 (Fig. 5.18(f)) - AR6			
RGEB/AR6	1.02	1.04	1.29
ARGEB(G1)/AR6	0.61	0.74	1.80
ARGEB(G4)/AR6	0.78	0.91	1.93
Artificial earthquake in Group 2 (Fig. 5.19(b)) - AR7			
RGEB/AR7	1.07	0.99	1.41
ARGEB(G1)/AR7	1.12	1.29	1.76
ARGEB(G4)/AR7	0.95	1.08	1.75
Artificial earthquake in Group 2 (Fig. 5.19(d)) - AR8			
RGEB/AR8	0.90	1.07	1.32
ARGEB(G2)/AR8	1.44	1.11	1.25
ARGEB(G4)/AR8	1.22	0.93	1.23
Artificial earthquake in Group 3 (Fig. 5.20(b)) - AR9			
RGEB/AR9	1.00	1.13	1.45
ARGEB(G3)/AR9	0.97	1.10	1.74
ARGEB(G4)/AR9	0.85	1.74	1.60
Artificial earthquake in Group 3 (Fig. 5.20(g)) - AR10			
RGEB/AR10	0.99	0.94	1.21
ARGEB(G3)/AR10	1.12	0.98	1.14
ARGEB(G4)/AR10	0.99	0.90	1.04

response for an unknown future excitation which has a known site spectrum and energy-bound. An artificial earthquake which is shown in Figure 5.21 was created by using the spectrum of Figure 5.19(a) and is used to examine the validity of the results. The estimated displacement and velocity obtained by the ARGEB model for Group 2 and the time-history of the actual record are shown in Figure 5.22. It can be observed that the predicted results are slightly underestimated, but the difference between the ARGEB model and the actual record is still within 10 % for both the displacement and velocity response.

Global Energy-bound Convex Model for Active Structural Control

For the global energy-bound (GEB) convex model, the quantities required to obtain the response estimate in the case of an actively controlled structure are: the effective damping ratios (ξ_i^*), the frequencies, and mode-shapes of the controlled structure, and the global energy bound, $E_{\text{GEB}}(\infty)$, of the earthquake. The effective damping can be obtained from equation (3.1b). The modal displacement, velocity, and acceleration can be determined by using the effective damping in equation (3.10); the maximum response in physical coordinates can be approximated by the square root of the sum of the squares (SRSS) of the modal responses (equation (3.11)). Once the maximum velocity, \dot{x}_{max} , is obtained the estimate of the control force using the GEB convex model can be expressed from equation (2.11) as

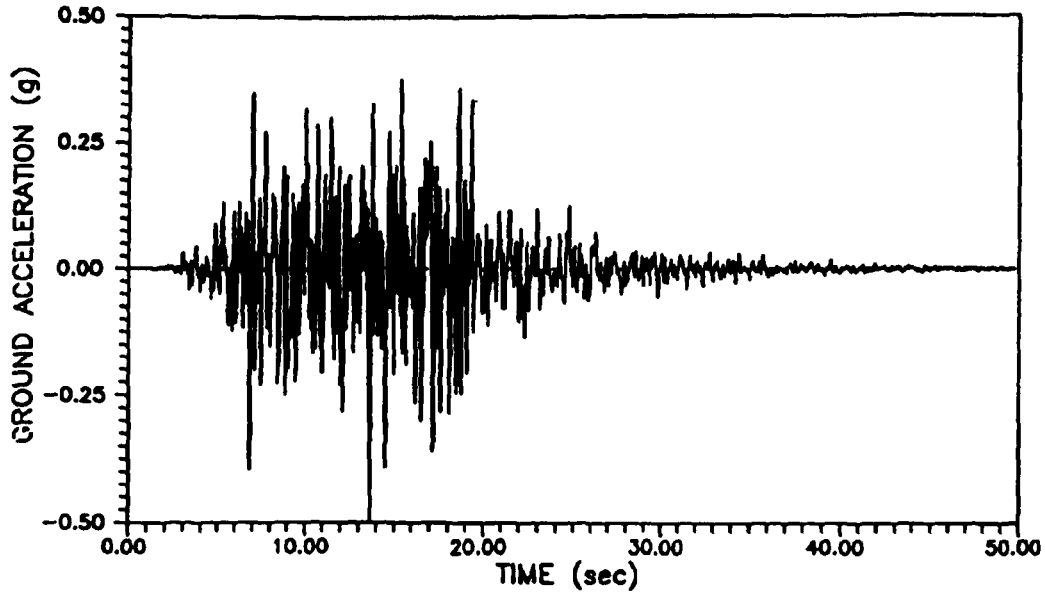


Figure 5.21 Artificial earthquake using the spectrum of Figure 5.19(a)

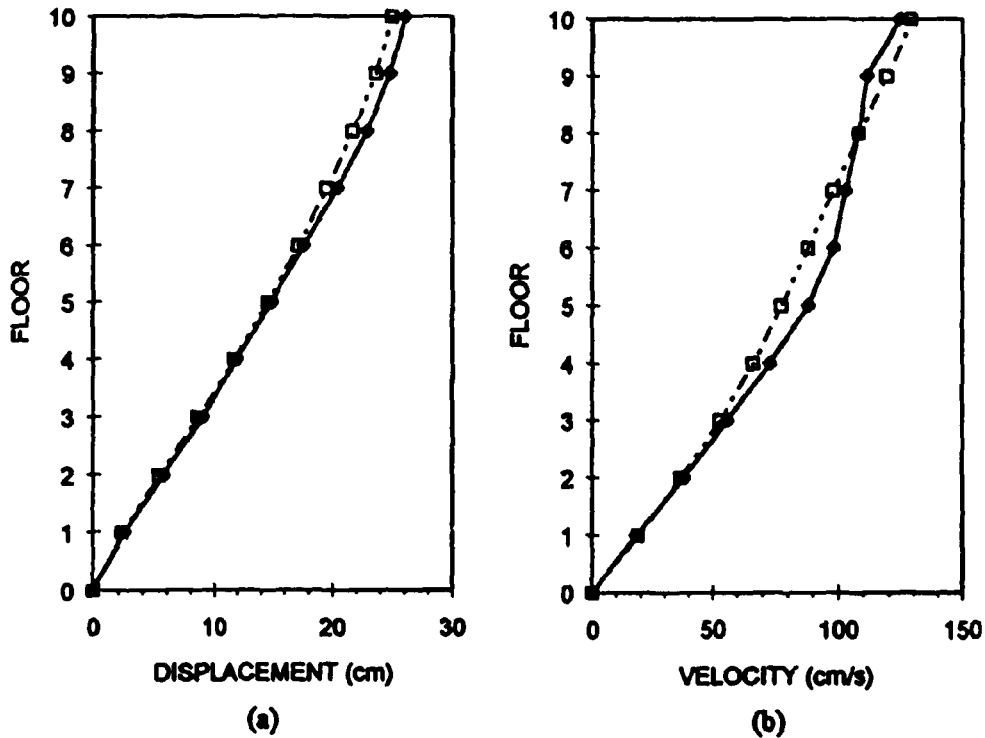


Figure 5.22 Comparison of the predicted response with the actual record: (a) displacement, (b) velocity; —●— = actual record (AR), -□- = estimated results obtained by the ARGEB convex model of artificial earthquakes in Group 2

$$|u_{\max}^{\circ}| = \left| \frac{-\Delta t}{2r} b^T M^{-1} \dot{x}_{\max} \right| \quad (5.9)$$

where M is the mass matrix of the structure; r is a constant which is a scalar multiplier in the diagonal weighting matrix R (see Chapter 2); weighting matrix Q is assigned to be an identity matrix; b was defined in equation (2.8).

The ten-story frame described in Table 5.2 is used to examine the RGEB and ARGEB convex models for the active bracing systems (ABS). One ABS is assumed to be installed on the first floor and one on the second floor of the building. Note that in this application the ABS is used in the form of a retrofit. The maximum responses obtained from the time-history of the actual record (AR), and the RGEB and ARGEB convex models are shown in Table 5.13. The reduction factor used in the RGEB convex model is excitation-specific for the 1940 El-Centro earthquake. The average reduction factor used in the ARGEB convex model is obtained from 26 California records (subset S7 of Table 5.9). The same control parameters are used in the three methods. Note that the control force is affected only by the velocity of the floors as shown in equation (5.9). It can be observed that the ratio of the estimated control forces obtained from the RGEB and ARGEB convex models to the maximum control forces obtained from the actual time history (AR), is approximately equal to the ratio of the velocity of the same floors at the two levels where the ABS are installed. Satisfactory results are obtained using the ARGEB convex model.

Table 5.13. Maximum response of the ten-story frame with two ABS for the 1940 El-Centro earthquake record

Floor	AR	RGEB	RGEB/AR	ARGEB	ARGEB/AR
Displacement (cm)					
1	1.17	1.46	1.25	1.96	1.68
2	2.78	3.37	1.21	4.61	1.66
3	4.59	5.35	1.17	7.47	1.63
4	6.42	7.17	1.12	10.25	1.60
5	8.21	8.80	1.07	12.88	1.57
6	9.85	10.24	1.04	15.28	1.55
7	11.28	11.56	1.02	17.40	1.54
8	12.59	12.88	1.02	19.38	1.54
9	13.64	14.06	1.03	21.01	1.54
10	14.36	14.93	1.04	22.16	1.54
Velocity (cm/s)					
1	7.09	10.50	1.48	11.93	1.68
2	15.66	21.53	1.37	25.84	1.65
3	22.83	31.44	1.38	39.39	1.73
4	30.86	38.88	1.26	51.22	1.66
5	38.90	44.07	1.13	61.55	1.58
6	45.89	48.03	1.05	70.74	1.54
7	51.84	52.10	1.01	79.23	1.53
8	56.10	57.78	1.03	88.02	1.57
9	61.54	64.80	1.05	96.52	1.57
10	68.29	71.24	1.04	103.43	1.51
Acceleration (cm/s ²)					
1	296.35	274.22	0.93	238.18	0.80
2	449.10	406.01	0.90	336.62	0.75
3	542.59	506.83	0.93	427.86	0.79
4	501.20	555.66	1.11	496.43	0.99
5	423.77	554.20	1.31	535.34	1.26
6	407.42	547.83	1.34	573.28	1.41
7	424.85	530.55	1.25	602.33	1.42
8	536.72	565.65	1.05	661.22	1.23
9	631.80	664.82	1.05	737.32	1.17
10	697.33	791.09	1.13	816.16	1.17
Maximum Control Force (kN)					
1	138	204	1.48	232	1.68
2	171	218	1.28	275	1.61

CHAPTER 6

OPTIMAL DESIGN OF CONVENTIONAL AND ACTIVE STRUCTURES

In this chapter, the modified iterated simulated annealing (MISA) method for optimization of structural systems is discussed and compared with three classical optimization methods. The optimal design of the active structure, which includes the conventional structure and the passive and/or active control systems stated in Chapter 2, is performed by using either the time-history analysis of the actual seismic record or the global energy-bound convex model. Both the global energy-bound convex model adjusted with the excitation-specific reduction factor (RGEB) and the convex model using the average reduction factor (ARGEB) are utilized.

Structural Optimization

The optimal design of a ten-bar truss system with static constraints is examined using the modified iterated simulated annealing (MISA) method described in Chapter 3, and is compared with the state space optimization method. This example is carried out in order to evaluate the advantages or disadvantages of the present algorithm, compared to standard methods. For the structures with dynamic constraints, a two-story and a ten-

story frame are designed for dynamic excitations. The results obtained by the MISA method and three classical optimization methods are compared. The design variables are defined as the cross-sectional areas of the structural members. The moment of inertia, I , of the frame members can be obtained using well-known relations as follows (Haug and Arora, 1979):

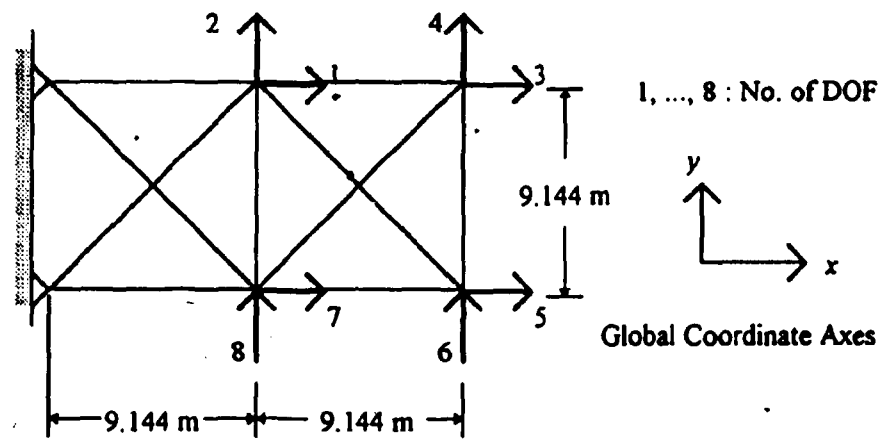
$$\begin{aligned} I_i &= Z_i \times s_i \\ Z_i &= \beta_i \left(\frac{A_i}{\alpha_i} \right)^{3/2} ; s_i = \chi_i \left(\frac{A_i}{\alpha_i} \right)^{1/2} \end{aligned} \quad (6.1)$$

where Z_i , s_i , and A_i are the section modulus, the least radius of gyration, and the cross-sectional area of the i th element; α_i , β_i , and χ_i are constants.

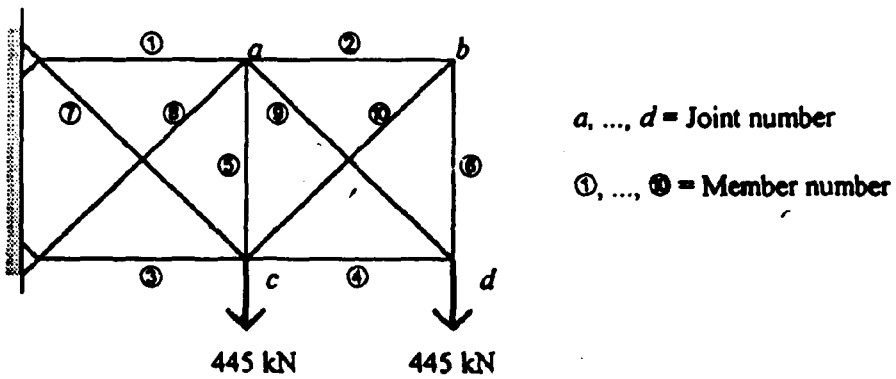
Ten-bar Truss with Static Constraints

The optimal design of the ten-bar truss shown in Figure 6.1 is used to evaluate the performance of the MISA method. Two degrees-of-freedom (DOF), the x and y direction displacement, are considered at each joint. The vertical load is applied at joints c and d and equals 445 kN, respectively. The allowable stress is given as ± 172 MPa, and the displacement constraint is 5.08 cm at all joints in both the x and y directions. The Young's modulus of the material is 68.9 GPa.

First, five design variables are used for the ten-bar truss by linking the cross-sectional area of the truss members in groups of two which have the same areas as



(a)



(b)

Figure 6.1 Ten-bar truss: (a) dimensions and degrees-of-freedom, (b) loading and design variables

follows: ① and ③, ② and ④, ⑤ and ⑥, ⑦ and ⑧, and ⑨ and ⑩ (see Figure 6.1(b)). The iteration histories for the iterated simulated annealing (ISA) method (Ackley, 1987) and the MISA method are shown in Figure 6.2; both stress and displacement constraints are considered. It can be observed that the MISA method converges to the minimum volume in less iterations than the ISA method. The design parameters used in the MISA method are as follows: $M = 8$, $n_1 = 75$, $n_2 = 25$, and $k = 1$. The optimization results are listed in Table 6.1. The number of function calls listed in Table 6.1 for the MISA method is defined as the number of iteration loops required to find the minimum volume. The y direction displacement at joint d is the active constraint for the optimal designs obtained by the two methods. The optimal volume using the MISA method is 7.7 % less than that of the ISA method.

Table 6.2 shows the results for the same problem with ten design variables as shown in Figure 6.1(b). The y direction displacements for nodes b and d are the active constraints found by the MISA method. The y direction displacement for node d is active for the ISA method. In this case, the design parameters, M , n_1 , n_2 , and k , used in the MISA method equal 8, 75, 25, and 1, respectively. The result obtained by the state space optimal (SSO) design method is also shown in Table 6.2 (Haug and Arora, 1979). The y direction displacements at nodes b and d and the axial stress of member 5 are the active constraints in the SSO design method. The minimum volume of the ten-bar truss obtained by the MISA method is only 0.4 % more than the volume obtained from the SSO design method. However, the number of function calls required by the MISA method is larger than the SSO design method as shown in Table 6.2. The optimal results obtained by the

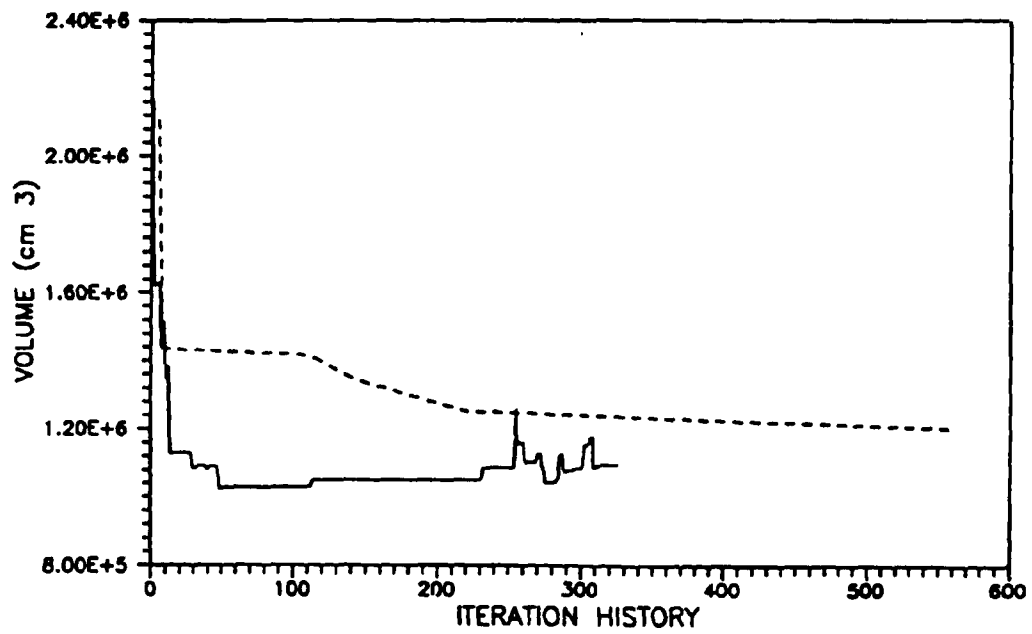


Figure 6.2 Iteration history for five-variable optimal design of ten-bar truss using the ISA method (- - - - -) and the modified iterated simulated annealing (MISA) method (———)

Table 6.1. Five-variable optimal design of ten-bar truss with static constraints

No. of bar	Cross-sectional area (cm ²)		Axial stress (kPa)		DOF	Displacement (cm)	
	ISA	MISA	ISA	MISA		ISA	MISA
①	179.94	221.75	41.92	41.82	1	0.56	0.56
②	54.52	59.86	34.47	7.47	2	-2.16	-1.96
③	179.94	221.75	47.99	38.42	3	1.02	0.66
④	54.52	59.86	47.09	66.84	4	-4.70	-4.47
⑤	72.13	10.08	17.79	81.68	5	-1.27	-1.40
⑥	72.13	10.08	26.06	44.35	6	-5.06	-5.06
⑦	107.29	60.41	66.53	95.33	7	-0.64	-0.51
⑧	89.74	129.21	60.67	52.81	8	-2.41	-3.05
⑨	89.74	129.21	40.47	43.79			
⑩	107.29	60.41	24.82	10.47			
Volume (cm ³)	1,103,175	1,023,870					
Function calls	4960	392					

Table 6.2. Ten-variable optimal design of ten-bar truss with static constraints

No. of bar	Cross-sectional area (cm ²)			Axial stress (MPa)			DOF	Displacement (cm)		
	SSO	ISA	MISA	SSO	ISA	MISA		SSO	ISA	MISA
①	193.75	269.48	201.35	46.42	20.55	44.65	1	0.62	0.28	0.58
②	0.65	79.81	0.65	9.04	10.98	5.30	2	-1.87	-3.05	-1.88
③	150.15	278.45	161.55	58.35	44.06	54.28	3	0.50	0.41	0.53
④	98.62	152.90	95.68	45.07	23.37	46.44	4	-5.08	-3.94	-5.08
⑤	0.65	70.39	0.65	171.44	35.44	161.13	5	-1.37	-0.89	-1.35
⑥	3.23	10.26	4.19	1.63	84.67	11.21	6	-5.06	-5.06	-5.08
⑦	48.18	147.87	49.16	126.86	104.18	124.60	7	-0.78	-0.58	-0.71
⑧	136.64	14.71	131.55	47.10	74.74	48.85	8	-4.15	-2.57	-4.04
⑨	139.47	156.06	134.32	45.07	14.07	46.78				
⑩	0.65	87.74	0.65	12.79	32.41	7.50				
Volume (cm ³)	829,448	1,313,103	832,526							
Function calls	15	2,504	392							

Note : SSO - State space optimal method

ISA - Ackley's iterated simulated annealing method

ISA method did not reach the global minimum. As a result, the volume obtained in the ISA method is about 58 % larger than the other two methods.

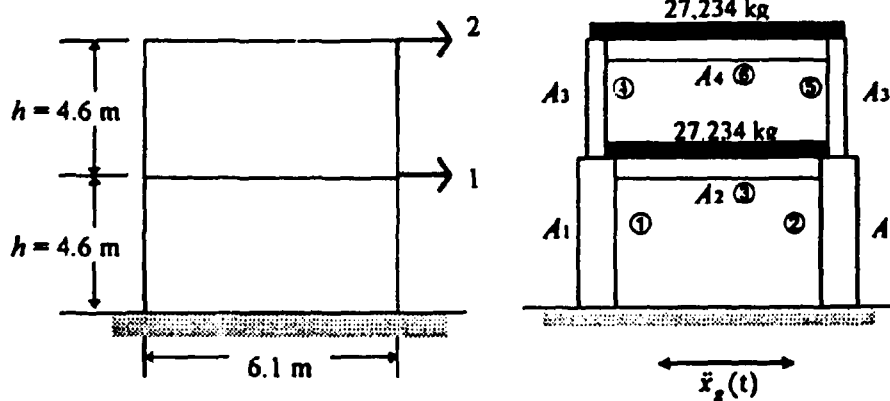
It can be seen that the MISA method performs better than the ISA method and requires less function calls. However, the MISA method requires more function calls than the state space optimal design method for the present problem with static constraints.

Two-story Frame with Dynamic Constraints

Figure 6.3(a) shows a one-bay two-story frame with a 6.1 m width and a 4.6 m height for each floor, which is used to evaluate the performance of the MISA method for optimization problems with dynamic constraints. The structural analysis of the frame is based on the direct stiffness method, with a capability for computing the strength ratio of column to beam, and the combined axial and bending stress in the members. Elastic response of the frame is assumed throughout the iteration history. The total dynamic degrees-of-freedom are reduced from 12 to 2 (Figure 6.3(a)) by the Guyan reduction method (1965), and the lumped mass procedure is used for the solution of the dynamic problem. The lumped mass for each floor is given as 27,234 kg and 5 % critical damping is assumed in each of the two vibrational modes.

Two artificial excitations (Figure 6.4) are created by using a sinusoidal function multiplied by an amplitude function. These excitations are applied as an earthquake ground motion. The artificial ground acceleration is expressed as

$$\ddot{x}_{g,1}(t) = eF(t)[\sin(5t) + \sin(10t) + \sin(20t)] \quad (6.2a)$$



A_1, \dots, A_4 = Cross-sectional area of frame member
 ①, ..., ④ = Member number
 1, 2 = No. of DOF

(a)

(b)

Figure 6.3 Two-story frame: (a) dimensions and degrees-of-freedom, (b) loading and design variables

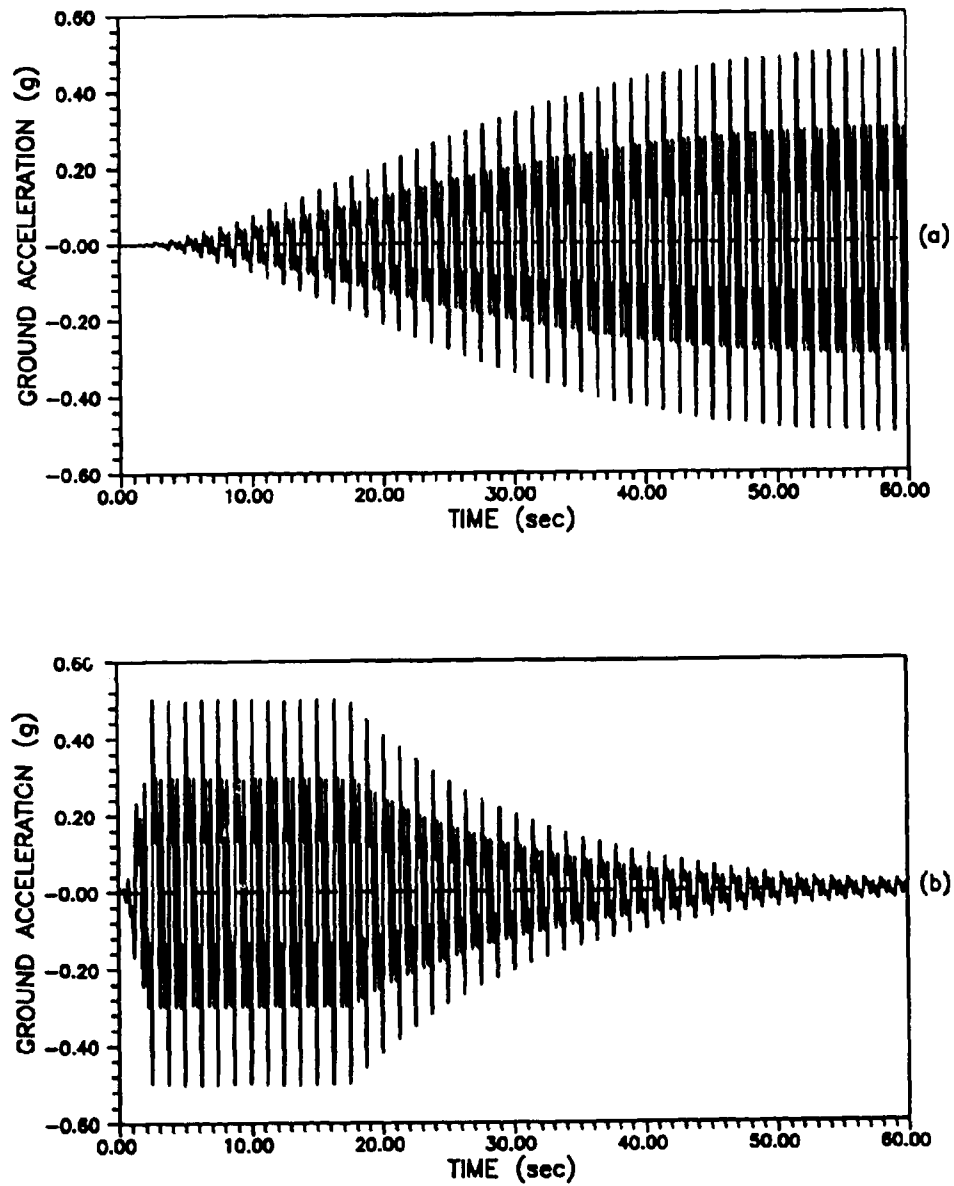


Figure 6.4 Artificial excitation using an amplitude envelope function: (a) artificial earthquake I (equation (6.2b)), (b) artificial earthquake II (equation (6.2c))

For the first excitation (artificial earthquake I) shown in Figure 6.4(a), the amplitude function is chosen as

$$F_1(t) = \left(\frac{t}{t_0}\right)^2 \exp\left[2\left(1 - \frac{t}{t_0}\right)\right] \quad (6.2b)$$

where e is a constant which is chosen to achieve a peak ground acceleration equal to $0.5g$; $g = 9.81 \text{ m/sec}^2$, and t_0 is proportional to the duration of the excitation which is defined as 60 sec. in this case. The amplitude function chosen for the second excitation (artificial earthquake II) shown in Figure 6.4(b) is (Jennings et al., 1969)

$$\begin{aligned} F_2(t) &= t^2 / 4; & 0 \leq t \leq 2 \\ &= 1; & 2 \leq t \leq 17.5 \\ &= e^{[-0.07153(t-17.5)]}; & 17.5 \leq t \leq 40 \\ &= 0.05 + 0.000375(60-t)^2; & 40 \leq t \leq 60 \end{aligned} \quad (6.2c)$$

The function $F_2(t)$ in equation (6.2c) has been modified from that of the original result of Jennings et al. (1969), so that the earthquake duration is comparable with the other excitation. Figure 6.5 shows the amplitude function of equation (6.2c).

A two-parameter design is used by assigning the columns of the two floors of the two-story frame to be identical (A_1) and the beams on each floor to have the same size (A_2) (Figure 6.3(b)). The allowable stress (combined axial and bending stress) for each frame member is assumed as 150 Mpa (60 % of the yielding stress of 250 MPa), and the

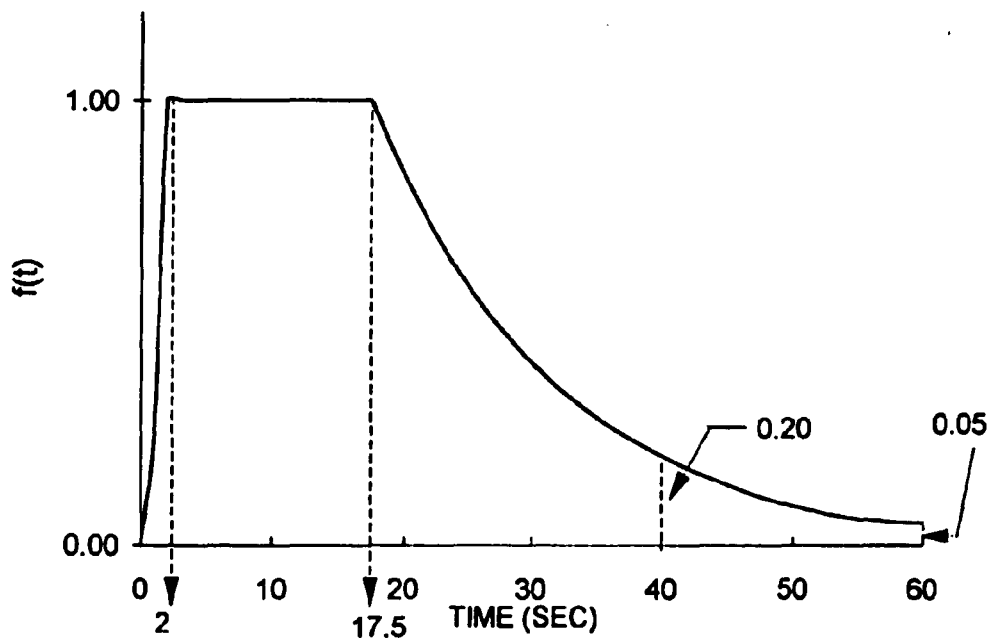


Figure 6.5 Time-dependent variation of amplitude envelope function (equation (6.2c)) for artificial earthquake

interstory drift constraints for each floor are set equal to $h/180$ or 2.54 cm. The constants, α_i , β_i , and χ_i , in equation (6.1) equal 0.58, 0.58, and 0.67, respectively (Haug & Arora, 1979). For this optimization problem, a disjoint feasible region is found for the structure subjected to artificial earthquake I as shown in Figure 6.6. The two portions of the feasible region for this two-story frame are constrained by the second floor drift and the stress in the two columns of the first floor.

The resulting optimal design for the present optimization problem is shown in Table 6.3. The constants M , n_1 , and n_2 used in the present algorithm were chosen as 8, 75, and 25, respectively; k is equal to 1 for this design. The same structural optimization problem was solved using classical optimization techniques. The results from program DOT (Design Optimization Tools) developed by VMA Engineering (1993) are also shown in Table 6.3. Three classical algorithms are presented in Table 6.3 using the DOT program; the first is the modified feasible directions (MFD) method, the second is the sequential linear programming (SLP) method, and the third is the sequential quadratic programming (SQP) method (Appendix E). Table 6.3 shows that in essence all four algorithms yield the same answer. However, for different initial values of the design variables, the results obtained from the classical optimization methods are different, as shown in Table 6.4.

As can be seen from Table 6.4, the classical methods sometimes converge to local minima. For certain initial values, the design converges to point (2), located in the upper part of the feasible region (see Figure 6.6), which is the stress constraint for the first floor columns; for some other initial values, the design converges to point (1), located in the

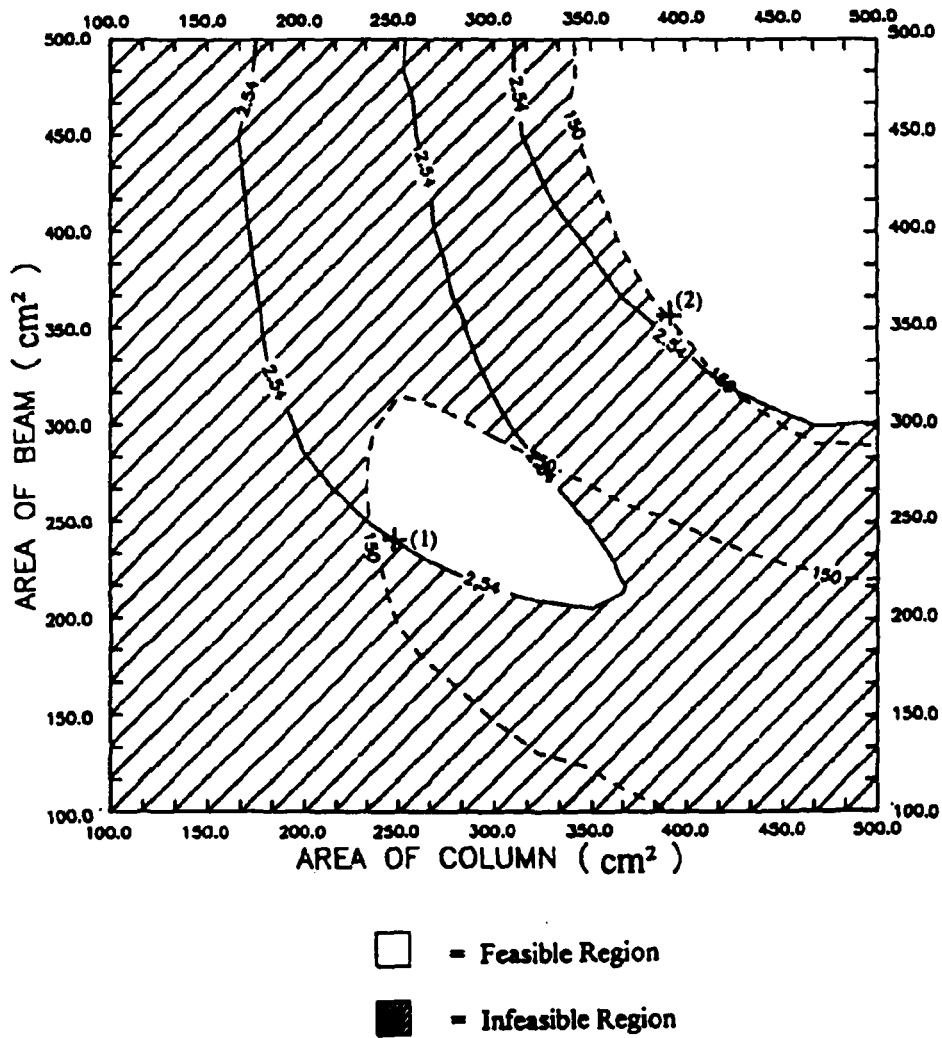


Figure 6.6 Disjoint feasible region of the two-story frame subjected to artificial earthquake I; — 2.54 — = second floor drift constraint, - - - - 150 - - - - = combined stress constraint in columns of the first floor

Table 6.3. Optimal design of the two-story frame subjected to artificial earthquake I

Frame Group	Cross-section area (cm ²)			Member No.	Combined stress (MPa)			Floor	Interstory drift (cm)				
	MFD	SLP	SQP		MISA	MFD	SLP		SQP	MISA	MFD	SLP	SQP
A ₁	245.20	245.22	245.24	245.28	①	141	141	141	140	2.30	2.30	2.30	2.28
A ₂	236.25	236.23	236.22	236.33	②	142	142	142	141	2.54	2.54	2.54	2.53
					③	132	132	131	131				
					④	79	79	79	79				
Volume (cm ³)	736,456	736,464	736,498	736,715	⑤	79	79	79	79				
					⑥	84	84	84	84				

Note : MFD - Modified feasible directions method

SLP - Sequential linear programming method

SQP - Sequential quadratic programming method

Table 6.4. Results for two-story frame subjected to artificial earthquake I for different initial designs

	Initial Design	Optimal Design Method			
		MFD	SLP	SQP	MISA
Column Area (cm ²)	500	386.69	-	386.97	245.28
Beam Area (cm ²)	500	365.08	-	365.45	236.33
Volume (cm ³)	1,524,000	1,152,289	-	1,151,557	736,715
Function calls		66	151	16	320
Active Constraint		Point (2)	-	Point (2)	Point (1)
Column Area (cm ²)	400	386.68	245.22	386.74	247.75
Beam Area (cm ²)	400	365.11	236.23	365.03	234.97
Volume (cm ³)	1,219,200	1,152,291	736,464	1,152,176	739,567
Function calls		33	34	28	1056
Active Constraint		Point (2)	Point (1)	Point (2)	Point (1)
Column Area (cm ²)	300	245.20	-	245.24	247.78
Beam Area (cm ²)	300	236.25	-	236.22	234.74
Volume (cm ³)	914,400	736,456	-	736,498	739,338
Function calls		33	151	20	530
Active Constraint		Point (1)	-	Point (1)	Point (1)

Note: Point (1) is when the second floor drift is active

Point (2) is when the stress in the columns of the first floor is active

Table 6.4. Results for two-story frame subjected to artificial earthquake I for different initial designs

	Initial Design	Optimal Design Method			
		MFD	SLP	SQP	MISA
Column Area (cm ²)	500	386.69	-	386.97	245.28
Beam Area (cm ²)	500	365.08	-	365.45	236.33
Volume (cm ³)	1,524,000	1,152,289	-	1,151,557	736,715
Function calls		66	151	16	320
Active Constraint		Point (2)	-	Point (2)	Point (1)
Column Area (cm ²)	400	386.68	245.22	386.74	247.75
Beam Area (cm ²)	400	365.11	236.23	365.03	234.97
Volume (cm ³)	1,219,200	1,152,291	736,464	1,152,176	739,567
Function calls		33	34	28	1056
Active Constraint		Point (2)	Point (1)	Point (2)	Point (1)
Column Area (cm ²)	300	245.20	-	245.24	247.78
Beam Area (cm ²)	300	236.25	-	236.22	234.74
Volume (cm ³)	914,400	736,456	-	736,498	739,338
Function calls		33	151	20	530
Active Constraint		Point (1)	-	Point (1)	Point (1)

Note: Point (1) is when the second floor drift is active

Point (2) is when the stress in the columns of the first floor is active

lower portion of the feasible region (see Figure 6.6), which is the second floor drift constraint; point (1) is the global minimum. The SLP method even failed to find a local minimum for certain initial values of the design variables as shown in Table 6.4. However, the MISA method always came very close to the global minimum regardless of the initial values of the design variables. This is because of the random nature of the selection of the new design at each iteration. Because of this randomness, the MISA method requires, on average, more function calls than classical optimization methods. However, with the increasing computational speed found in present day computers this becomes less of a disadvantage. The main program for the MISA algorithm and the function of each program component are shown in Appendix F.

Similar results are obtained for this two-story frame when it is subjected to the artificial earthquake II excitation (Figure 6.4(b)). Figure 6.7 shows the disjoint feasible region which is also constrained by the second floor drift and the stress in the two columns of the first floor. The resulting optimal designs obtained by the MISA method and three classical optimization techniques (MFD, SLP, and SQP methods) are shown in Table 6.5. The constants M , n_1 , and n_2 used in the present algorithm were chosen as 8, 75, and 25, respectively; k is equal to 1 for this design. The results obtained by using the different initial values of the design variables are shown in Table 6.6. Similar to the previous case of the two-story frame subjected to the artificial earthquake I, a local minimum is found in point (2) of Figure 6.7. The local minimum is obtained for some initial designs by the classical optimal design methods in the upper portion of the feasible region.

A four-parameter design is formulated by assigning the two columns of the first

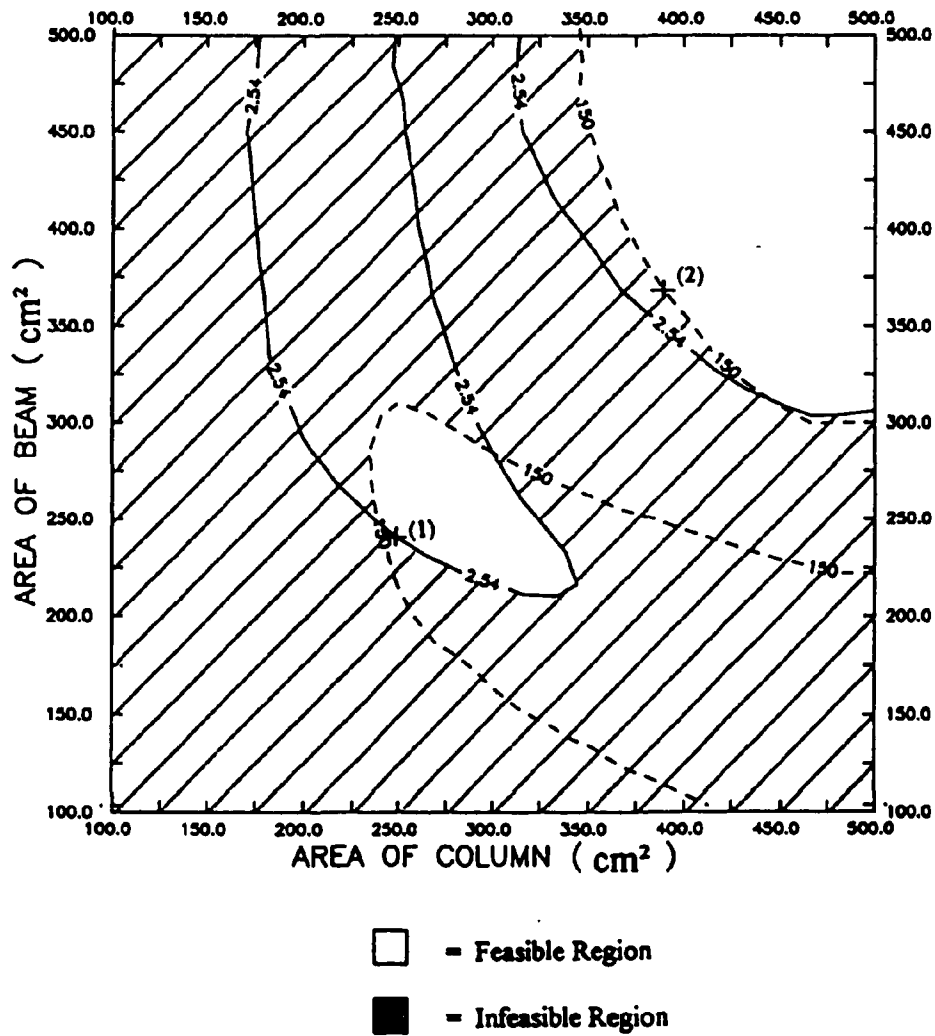


Figure 6.7 Disjoint feasible region of the two-story frame subjected to artificial earthquake II; — 2.54 — = second floor drift constraint, - - - - 150 - - - - = combined stress constraint in columns of the first floor

Table 6.5. Optimal design of the two-story frame subjected to artificial earthquake II

	Optimal Design Method			
	MFD	SLP	SQP	MISA
Column Area (cm ²)	246.06	246.09	246.09	246.78
Beam Area (cm ²)	237.00	236.99	236.98	236.56
Volume (cm ³)	738,938	738,991	736,214	739,726
Function calls	39	19	15	744
Active Constraint	2nd fl. drift	2nd fl. drift	2nd fl. drift	2nd fl. drift

Table 6.6. Results for two-story frame subjected to artificial earthquake II for different initial designs

	Initial Design	Optimal Design Method			
		MFD	SLP	SQP	MISA
Column Area (cm ²)	750	390.63	-	246.08	248.54
Beam Area (cm ²)	750	368.53	-	239.98	236.78
Volume (cm ³)		1,163,702	-	738,963	743,213
Function calls		63	151	33	2064
Active Constraint		Point (2)	-	Point (1)	Point (1)
Column Area (cm ²)	500	390.52	-	390.90	247.84
Beam Area (cm ²)	500	368.37	-	368.08	236.45
Volume (cm ³)	1,524,000	1,163,296	-	1,163,250	741,530
Function calls		60	159	16	5312
Active Constraint		Point (2)	-	Point (2)	Point (1)
Column Area (cm ²)	400	390.51	391.76	390.48	246.78
Beam Area (cm ²)	400	368.37	366.60	368.39	236.56
Volume (cm ³)	1,219,200	1,163,293	1,163,412	1,163,289	739,726
Function calls		33	67	47	744
Active Constraint		Point (2)	Point (2)	Point (2)	Point (1)
Column Area (cm ²)	300	246.07	-	246.09	248.87
Beam Area (cm ²)	300	236.99	-	236.98	235.28
Volume (cm ³)	914,400	738,948	-	738,633	741,990
Function calls		39	151	18	720
Active Constraint		Point (1)	-	Point (1)	Point (1)

Note: Point (1) is when the second floor drift is active

Point (2) is when the stress in the columns of the first floor is active

floor to be identical, (A_1), and the two columns of the second floor as having the same size, (A_3). The beams on each floor have a different size, (A_2, A_4), as shown in Figure 6.3(b). The strong column-weak beam philosophy is implemented in the program by computing the strength ratio of column to beam, which reflects current design code requirements for earthquake design. The 1940 El-Centro earthquake shown in Figure 4.6(a) is used.

The present structural optimization problem was solved using the MISA method and other classical optimization techniques. Table 6.7 shows the optimization results by using the MISA, MFD, and SQP methods for the problem with dynamic constraints. For all methods, the drift of the second floor is the active constraint. The volume of the two-story frame obtained by the MISA method is 0.7 % more than the volume obtained by the MFD and SQP methods. However, some local minima were found for certain initial design variables when the MFD and SQP method were used. The minimum values of the volume at the local minima were found to be 17 to 35 % higher than the global minimum. It should be noted that the SLP method failed to find the optimal structure regardless of the initial values of the design variables.

Table 6.7. Optimal design of two-story frame for the 1940 El-Centro earthquake

Group of Frame	Cross-section area (cm ²)			Member No.	Combined stress (MPa)			Fl.	Drift (cm)		
	MFD	SQP	MISA		MFD	SQP	MISA		MFD	SQP	MISA
A_1	270.9	267.6	268.8	①	108.97	112.86	111.33	1st	1.70	1.77	1.75
A_2	263.1	259.7	257.6	②	109.47	113.39	111.86	2nd	2.54	2.54	2.54
A_3	193.1	196.3	211.6	③	103.29	106.59	106.71				
A_4	190.8	193.6	180.2	④	78.97	79.01	67.92				
Volume (cm ³)				⑤	79.06	79.09	68.00				
	700,896	00,683	706,083	⑥	81.80	81.8	87.55				

Note : MISA - Modified iterated simulated annealing

MFD - Modified feasible directions

SQP - Sequential quadratic programming

Figure 6.8 shows the iteration history using the MISA method for the two-story frame optimal design subjected to the 1940 El-Centro earthquake. Because of the random search of the design variables, there exist intermediate iterations for which the volume increases. Note that the constants, m , n_1 , and n_2 in the MISA program were kept as 8, 75, and 25 which are identical to the parameter values used in the other case.

Ten-story Frame with Dynamic Constraints

A ten-story frame (Figure 6.9(a)) with a 9.1 m width and a 4.6 m height for the first floor, and a 3.66 m height for floors above the first is used to test the MISA method for dynamic constraints. The allowable stress for each frame member is assumed as 150 MPa, and the allowable interstory drift for each floor is given as $h/180$ which is 2.5 cm for the first floor, and 2.0 cm for the second up to the tenth floors. The inherent structural damping level is assumed to 5 % of critical at all modes. The strong column-weak beam philosophy is implemented in the program, which reflects current building code requirements for earthquake design.

In the first case, a design with only two variables is used by defining the cross-sectional areas of the columns in every floor to be the same, and the cross-sectional areas of the beams in each floor as identical. The lumped mass for each floor is given as 34,034 kg and 5 % critical damping is assumed in each of the ten vibration modes. The excitation is chosen as the 1940 El-Centro earthquake which is shown in Figure 4.6(a).

There are 30 combined stress constraints, and 10 interstory drift constraints in this case. Figure 6.10 shows the feasible region which is constrained by the drift limits for the

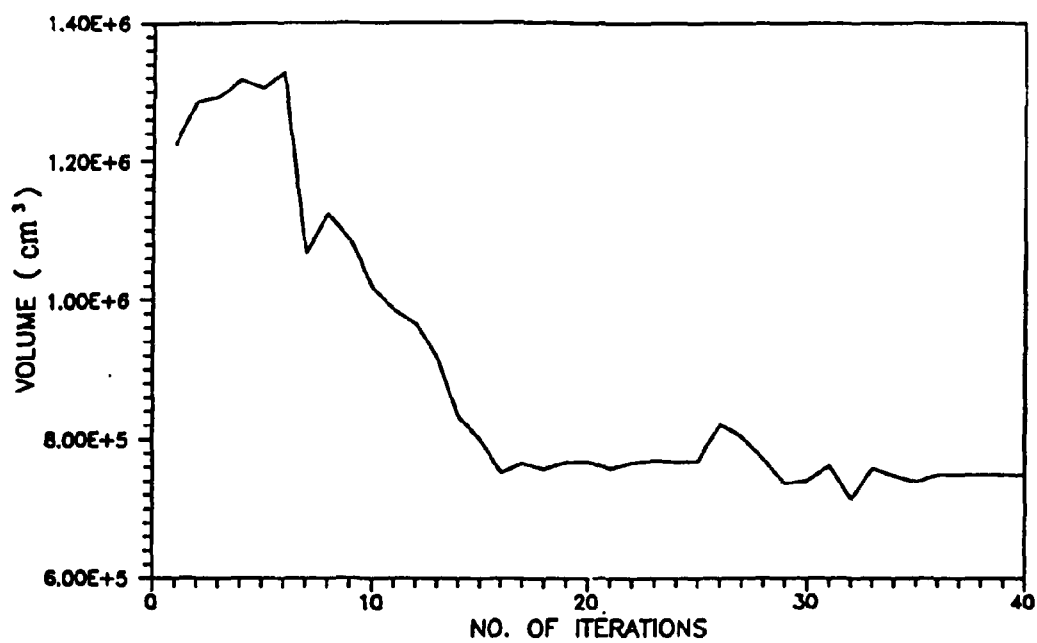
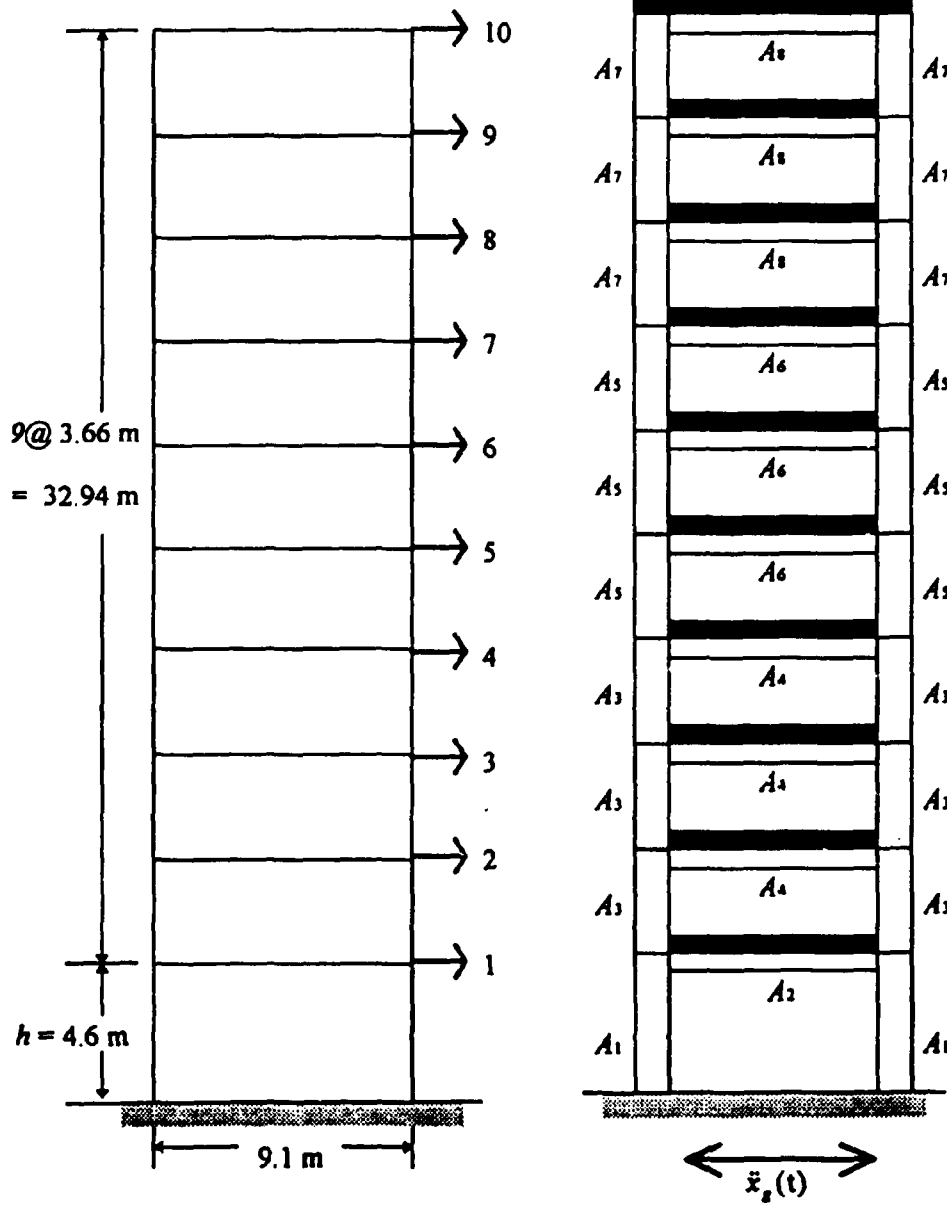


Figure 6.8 Iteration history for four-variable optimal design of two-story frame using the MISA method



A_1, \dots, A_8 = Cross-sectional area of frame member
 1, ..., 10 = No. of DOF
 Lumped mass = 34,034 kg for each floor

(a)

(b)

Figure 6.9 Ten-story frame: (a) dimensions and degrees-of-freedom, (b) loading and design variables

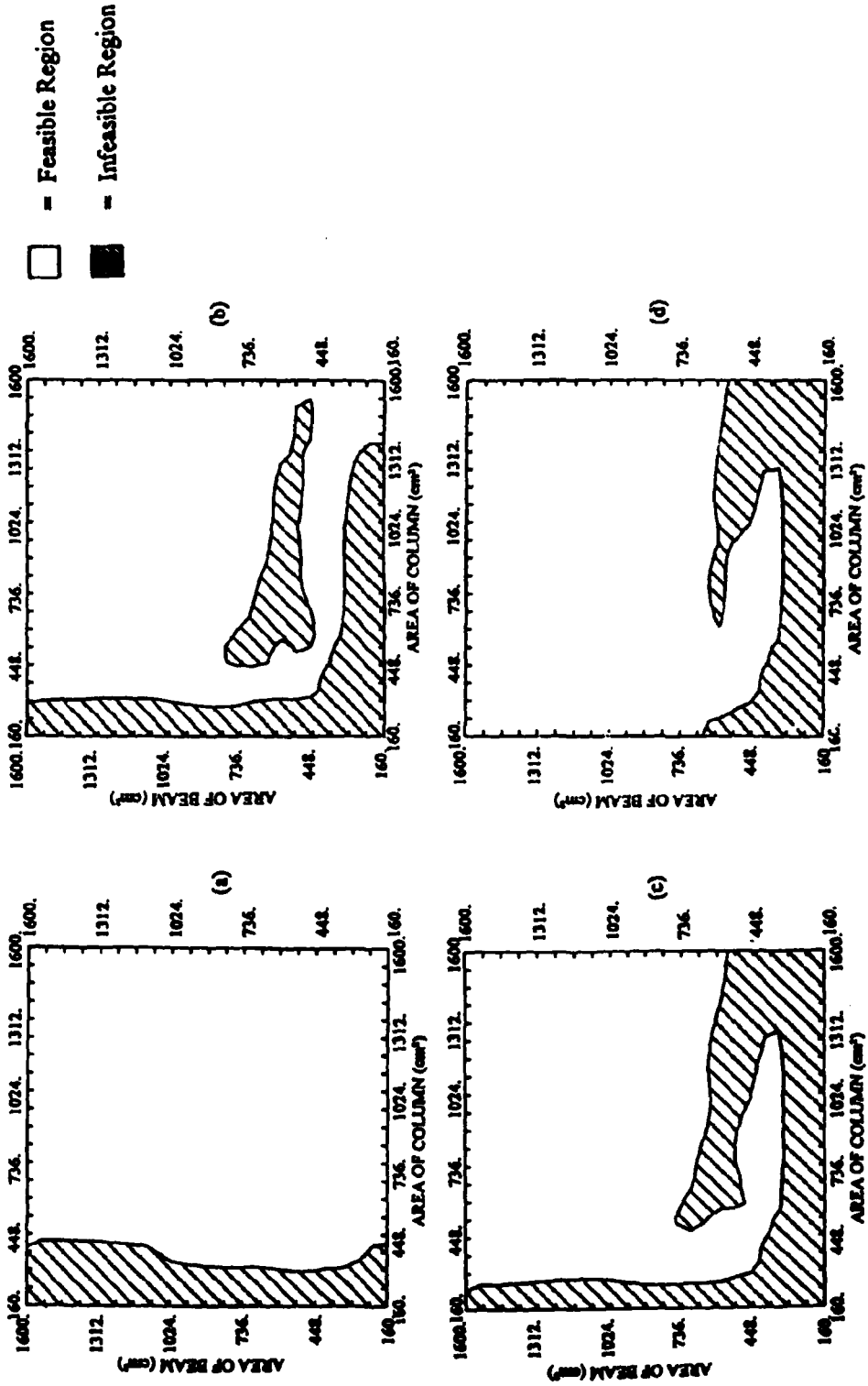


Figure 6.10 Feasible region of ten-story frame constrained by drift on: (a) first, (b) third, (c) fourth, and (d) fifth floors

first, third, fourth, and fifth floors. The feasible region is also constrained by the combined stresses of the columns on the first floor as shown in Figure 6.11. The disjoint feasible region is found when all the drift and stress constraints are considered together for the optimization problem stated above. This results in a feasible region with three disjoint portions as shown in Figure 6.12, which is formed by the drift constraint on the third, fourth, and fifth floors, and the stress constraint in the columns of the first floor.

Table 6.8 shows the optimization results by using the MISA method and three classical optimal design methods (MFD, SLP, and SQP). The minimum volume of the ten-story frame found by the MISA method is slightly larger than that obtained by the SLP and SQP methods. In the present algorithm the following parameters were used: $M = 8$, $n_1 = 75$, $n_2 = 25$, and $k = 1$. In this case, the number of function calls required by the MISA method is less than that for the classical optimal design methods and is due to the randomness inherent in the method. However, in general the MISA method requires a larger number of iterations as compared to classical methods. The design found by the MFD method, after at least six optimization runs with different initial values for the design variables, failed to produce an active constraint. It should be noted that some local minima are found by the MFD method at points (3), (4), (5), (7), and (8) in the three portions of the feasible region shown in Figure 6.12. Similarly, local minima located at points (2) and (6) were found by the SQP method for certain initial values of the design variables. Similar to the case of the two-variable two-story frame, the SLP method failed to find even a local minimum for certain initial values of the design variables. However, the MISA method came very close to the global minimum (point (1) in Figure 6.12).

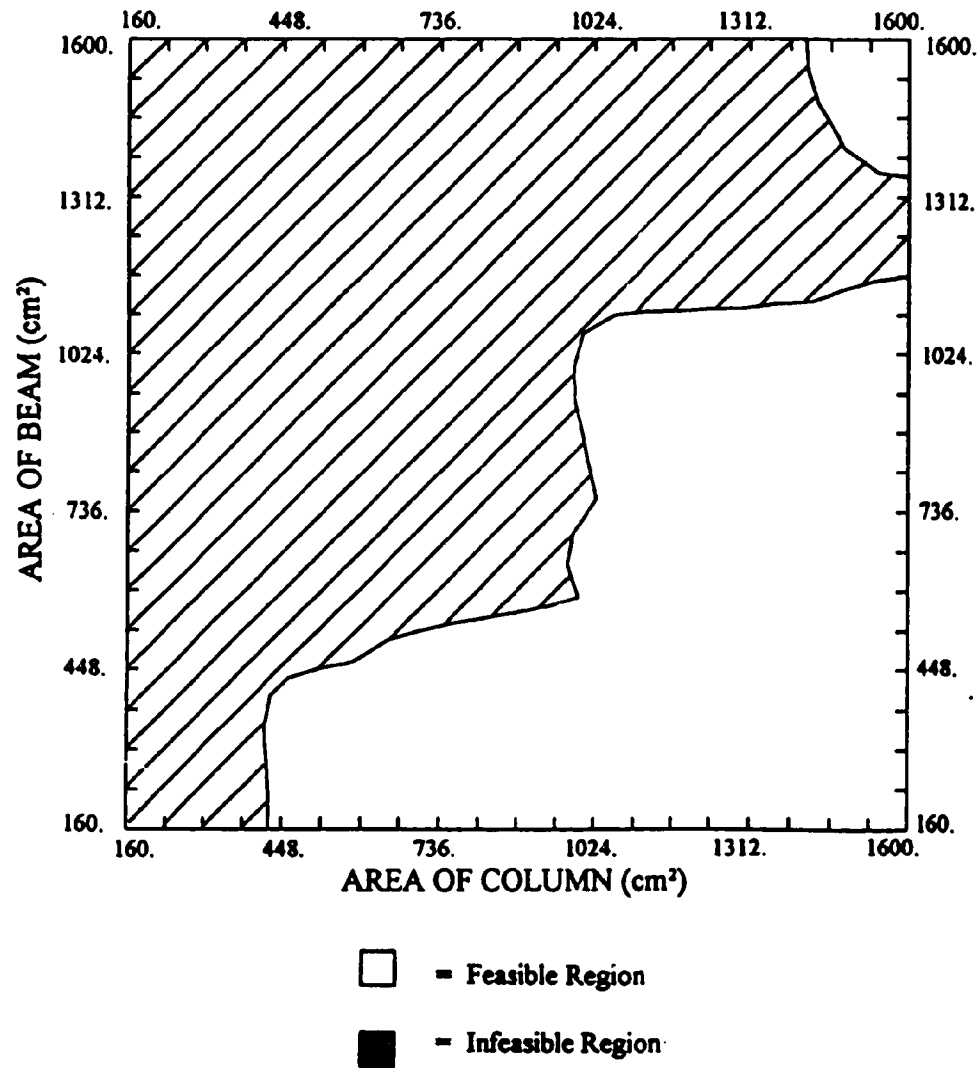


Figure 6.11 Feasible region of ten-story frame constrained by combined stress in columns of the first floor.

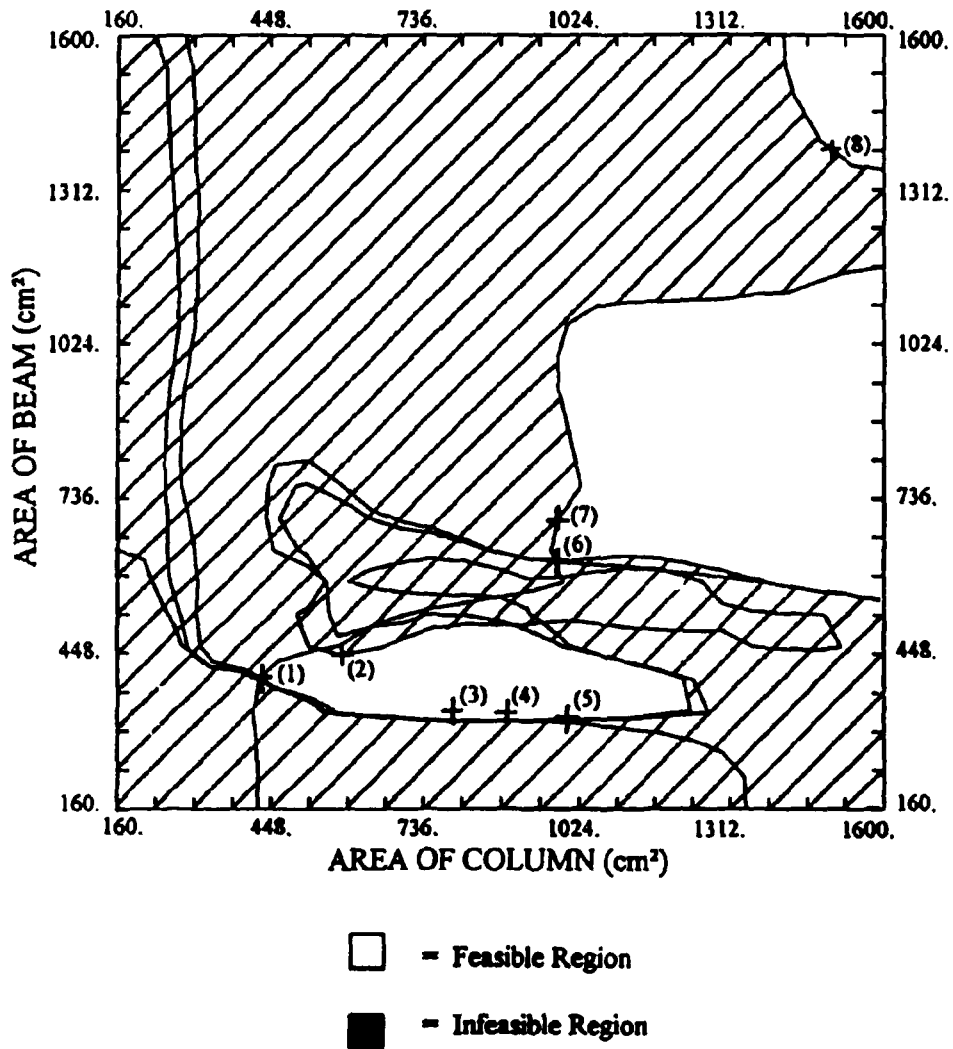


Figure 6.12 Disjoint feasible region of the ten-story frame constrained by the drift constraint on the third, fourth, and fifth floors and the combined stress constraint in columns of the first floor

Table 6.8. Two-variable optimal design of ten-story frame subjected to the 1940 El-Centro earthquake

	Optimal Design Method			
	MFD	SLP	SQP	MISA
Column Area (cm ²)	449	432	431	438
Beam Area (cm ²)	382	377	377	378
Volume (cm ³)	6,852,646	6,684,985	6,685,878	6,736,125
Function calls	21	42	26	24
Active Constraint	none	4, 5 fl. drift	4, 5 fl. drift	3,4, fl. drift

A second case for the ten-story frame with eight different groups for the cross-sectional areas is also presented in this example. The eight groups are shown in Figure 6.9(b). The allowable stresses and allowable interstory drifts are the same as stated above. The 1940 El-Centro earthquake record is also used as the excitation for the present case. The results of the optimal design are listed in Table 6.9. In this design, the design parameters using in the MISA method are: $M = 8$, $n_1 = 75$, $n_2 = 25$, and $k = 3$. Similar to the previous studies, the results obtained by the classical optimal design methods depend on the initial values of the design variables. Different initial values of the design variables produce different results or even fail to obtain a local minimum as shown in Table 6.10.

Table 6.9. Eight-variable optimal design of ten-story frame subjected to the 1940 El-Centro earthquake

	Optimal Design Method			
	MFD	SLP	SQP	MISA
Area (cm ²) - A_1	533	464	426	445
A_2	376	383	373	381
A_3	493	418	418	427
A_4	365	373	372	375
A_5	392	394	398	410
A_6	365	367	372	364
A_7	403	389	322	407
A_8	287	288	314	284
Volume (cm ³)	6,445,092	6,228,547	6,129,459	6,291,178
Function calls	216	95	71	904
Active Constraint	5, 6, 8 fl. drift	5, 6, 8 fl. drift	4, 5, 8 fl. drift	5, 6, 8 fl. drift

Table 6.10. Results for eight-variable ten-story frame for different initial designs

	Initial Design	Final Design			
		MFD	SLP	SQP	MISA
Area (cm ²) - A ₁	1600	1330	-	870	540
A ₂	1500	1229	-	738	425
A ₃	1500	851	-	804	430
A ₄	1400	619	-	680	375
A ₅	1400	750	-	746	413
A ₆	1300	590	-	667	365
A ₇	1300	653	-	517	375
A ₈	1200	430	-	490	338
Volume (cm ³)	22,751,000	11,782,700	-	11,046,000	6,518,109
Function calls		282	459	148	808
Active constraint		5-8 fl. drift	-	8 fl. drift col. stress (1st)	5 fl. drift
Area (cm ²) - A ₁	1200	987	984	919	651
A ₂	720	620	622	616	392
A ₃	960	929	902	916	424
A ₄	600	619	619	616	374
A ₅	720	674	697	649	378
A ₆	480	612	619	563	352
A ₇	480	609	643	649	349
A ₈	480	457	448	419	327
Volume (cm ³)	10,776,000	10,955,470	11,017,670	10,645,570	6,369,010
Function calls		176	149	41	776
Active constraint		3, 5-8 fl. drift col. stress (1st)	3-6, 8 fl. drift col. stress (1st)	2-5, 8 fl. drift col. stress (1st)	5-8 fl. drift
Area (cm ²) - A ₁	600	616	-	-	465
A ₂	550	469	-	-	402
A ₃	550	500	-	-	441
A ₄	500	353	-	-	369
A ₅	500	420	-	-	415
A ₆	450	353	-	-	363
A ₇	450	372	-	-	348
A ₈	400	302	-	-	317
Volume (cm ³)	8,047,100	6,592,121	-	-	6,311,531
Function calls		147	465	100	1016
Active constraint		5, 8 fl. drift	-	-	5, 8 fl. drift
Area (cm ²) - A ₁	600	533	-	-	864
A ₂	360	376	-	-	409
A ₃	480	493	-	-	421
A ₄	300	365	-	-	375
A ₅	360	392	-	-	404
A ₆	240	365	-	-	349
A ₇	240	403	-	-	347
A ₈	240	287	-	-	335
Volume (cm ³)	5,387,900	6,445,092	-	-	6,645,938
Function calls		216	460	56	816
Active constraint		5, 6, 8 fl. drift	-	-	5 fl. drift

Note: col. stress (1st) = combined stress in the columns of the first floor

The latter was observed for the SLP and SQP classical methods. However, the results obtained by the MISA method always came very close to the global minimum design.

Optimal Structures Using Convex Models

The ten-story frame shown in Figure 6.9 is used to evaluate the performance of the global energy-bound convex model adjusted with the excitation-specific reduction factor (RGEB) and the global energy-bound convex model adjusted with the average reduction factor (ARGEB). These designs also compared with the results obtained using the time-history of the actual seismic records. The structural analysis of the frame is based on the direct stiffness method, with a capability for computing the strength ratio of column to beam which reflects current design code requirements for earthquake design, and the axial and bending stresses in the members. Three degrees-of freedom (DOF), the rotation, and the x and y direction displacements are considered at each joint, but only the horizontal displacement is used for determining the dynamic constraints. The allowable stress for each member is assumed as 60 % of the yielding stress of 250 Mpa, and the interstory drift constraints for each floor are equal to $h/180$ or 2.54 cm. The lumped mass for each floor is given as 27,234 kg and 5 % critical damping is assumed in each of the two vibrational modes. The constants α_i , β_i , and χ_i in equation (6.1) equal 0.58, 0.58, and 0.67, respectively. Three excitations, the S00E component of the May 18, 1940 El-Centro earthquake, the S16E component of the Feb. 17, 1971 San Fernando earthquake, and an artificial earthquake (III) shown in Figure 5.19(d) are considered.

Optimal Design of Conventional Structure for El-Centro Earthquake

The optimal design using the time-history response for the 1940 El-Centro earthquake (AR) and the optimal designs for the global energy-bound convex model adjusted with the excitation-specific reduction factor (RGEB), and the average reduction factor (ARGEB) are shown in Table 6.11. The values shown for stress and drift are the maxima obtained at the final design. The active constraints for each optimal design are shaded in Table 6.11. The reduction factor for the RGEB convex model is discussed in Chapter 5 which is excitation-specific and can be used only for the 1940 El-Centro earthquake (S00E component). The average reduction factor for the ARGEB convex model is the average value of the reduction factors from 26 California records (subset S7 of Table 5.9).

The minimum volume obtained by the RGEB convex model is 3.3 % less than that obtained by using the time-history analysis of the actual record (AR). The result obtained by using the ARGEB convex model is 49 % more than that obtained by the AR procedure. From the definition of the global energy-bound convex model adjusted with the average reduction factor (ARGEB) in Chapter 5, the result obtained in Table 6.11 for the ARGEB convex model could be used for any other excitation in California which has the same global energy bound as the 1940 El-Centro earthquake.

The time-history analysis of three earthquake records and that for the 1940 El-Centro earthquake are used to verify the designs using the AR procedure and the ARGEB convex model (see Table 6.11). A scaled record of the S16E component of the 1971 San Fernando earthquake, the S90N component of the 1994 Northridge earthquake (Santa

Table 6.11. The optimal design of the ten-story conventional structure subjected to the 1940 El-Centro earthquake

Frame Group	Cross-sectional area (cm ²)			Fl.	Combined stress for beam (MPa)			Combined stress for column (MPa)			Interstory Drift (cm)		
	AR	RGEb	ARGEB		AR	RGEb	ARGEB	AR	RGEb	ARGEB	AR	RGEb	ARGEB
A1	448.31	603.52	820.57	1	84.98	88.86	103.55	118.21	112.71	138.82	1.35	1.21	1.22
A2	379.26	292.64	598.10	2	92.49	100.26	124.99	77.31	79.22	109.09	1.72	1.64	1.79
A3	430.38	529.49	694.98	3	87.77	92.25	125.91	64.52	63.14	88.60	1.80	1.68	1.99
A4	375.54	453.80	574.74	4	85.75	80.88	119.23	53.63	50.18	76.98	1.89	1.50	1.98
A5	402.90	278.79	667.91	5	90.13	88.75	110.24	60.34	87.19	69.26	1.99	1.94	1.92
A6	360.52	263.78	551.26	6	88.82	78.42	99.42	55.44	55.89	59.98	1.97	1.98	1.81
A7	353.38	267.66	429.92	7	80.92	75.55	91.74	49.71	42.79	47.31	1.87	1.84	1.67
A8	310.48	253.01	351.54	8	70.64	78.74	95.76	43.92	48.20	70.19	1.98	1.94	1.95
Volume (cm ³)	6,232,048	6,028,142	9,285,281	9	53.27	70.22	76.98	39.63	49.60	51.65	1.76	1.93	1.90
				10	32.73	47.14	49.80	26.32	41.87	35.98	1.24	1.51	1.42

Note : AR - Maximum response using the time-history of the actual record

RGEb - Global energy-bound convex model adjusted with the excitation-specific reduction factor

ARGEB - Global energy-bound convex model adjusted with the average reduction factor from subset S7 on Table 5.9

Monica City Hall), and an artificial earthquake (IV) (Figure 6.13), all having the same global energy bound as the 1940 El-Centro earthquake, are considered. The peak acceleration, duration, and global energy bound of the four excitations are shown in Table 6.12. Note that the artificial earthquake is created using a sinusoidal function multiplied by the amplitude envelope function as shown in Figure 6.5. The artificial ground acceleration is expressed as

$$\ddot{x}_g(t) = bf(t) \sum_{k=1}^{25} \bar{a}_k \sin(\bar{\omega}_k t) \quad (6.3)$$

where \bar{a}_k and $\bar{\omega}_k$ are the values of the 25 highest peak amplitudes and frequencies chosen from the 1940 El-Centro earthquake record; b is a constant chosen to give the same global energy bound as the 1940 El-Centro earthquake. It should be noted that the artificial excitation of Figure 6.13 was not used in the evaluation of the reduction factors of the ARGEB convex model.

Figure 6.14(a) shows the interstory drift response for the structure designed using the time-history of the actual 1940 El-Centro earthquake record (Building I); Figure 6.14(b) shows the interstory drift response for the structure designed by the ARGEB

Table 6.12. Peak acceleration and global energy-bound of the excitations for verifying the structure designed by the ARGEB convex model of subset S7 of Table 5.9

Excitations	Peak accel. (g)	Duration (sec)	Global energy-bound (m ² /sec ³)
1940 El-Centro	0.348	53.0	11.38
Scaled San Fernando	0.545	41.0	11.38
Scaled Northridge	0.706	60.0	11.38
Artificial earthquake IV	0.252	60.0	11.38

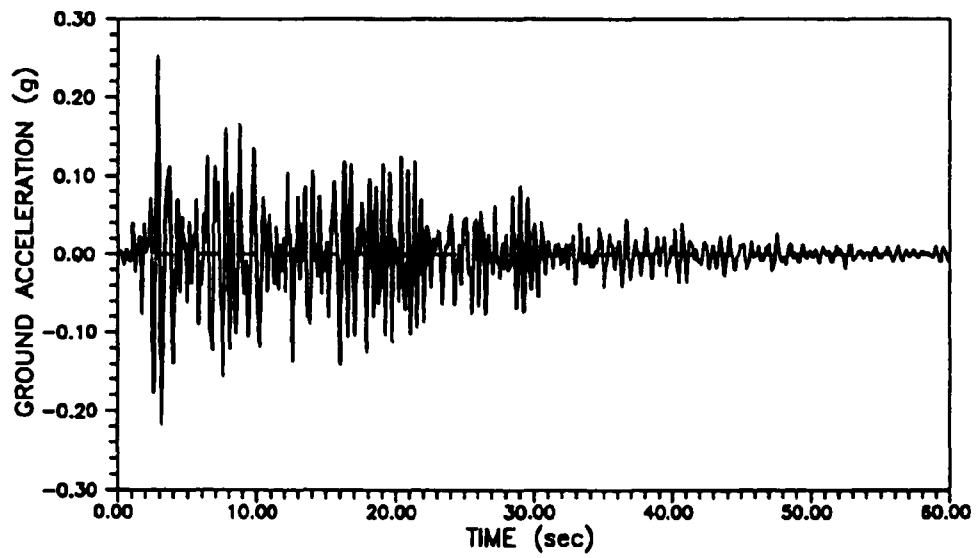


Figure 6.13 Artificial earthquake IV using the amplitude envelope function of equation (6.2c)

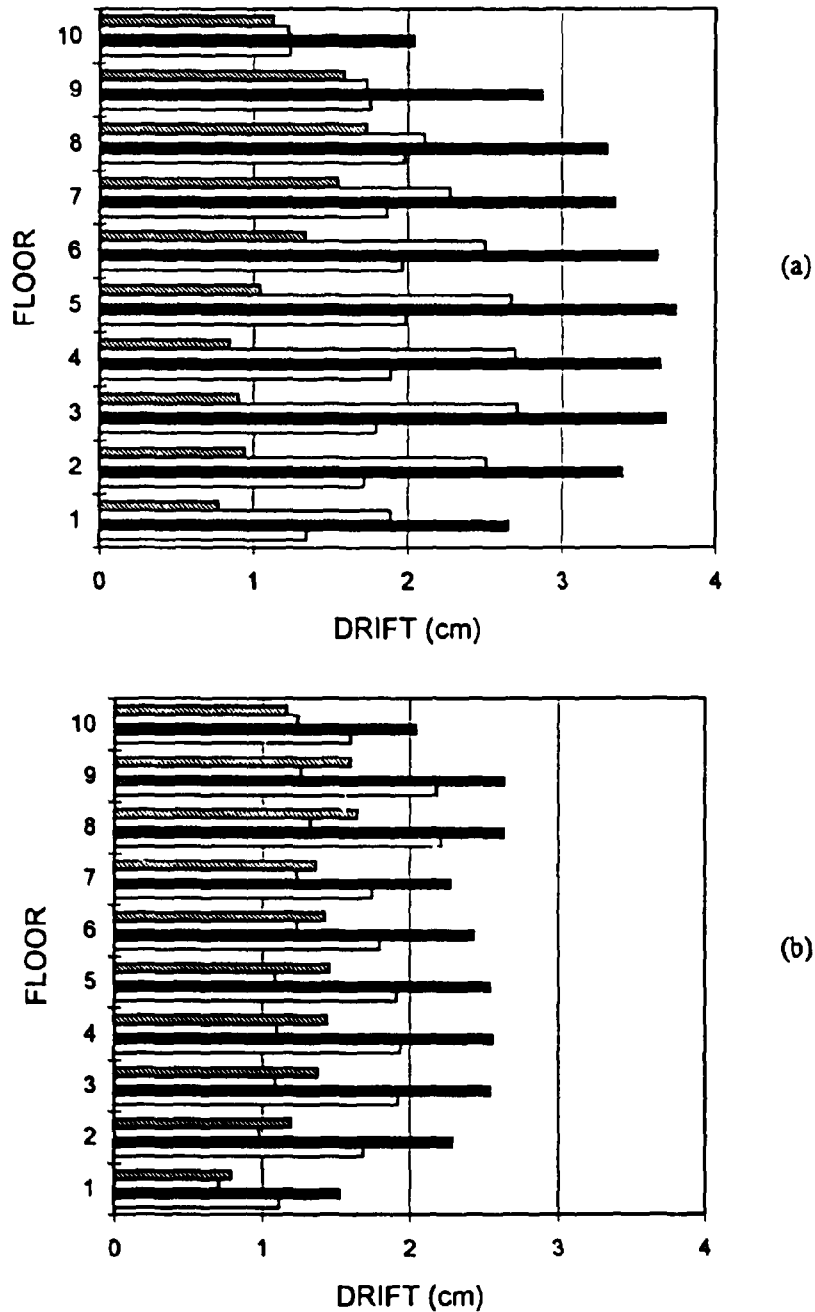


Figure 6.14 Interstory drift of the ten-story frame: (a) AR design for 1940 El-Centro of Table 6.11 (Building I) and (b) ARGEB convex model design of Table 6.11 (Building II); ▨ = artificial earthquake shown in Figure 6.13, □ = scaled record of 1994 Northridge earthquake, ■ = scaled record of 1971 San Fernando earthquake, □ = 1940 El-Centro earthquake record

convex model (Building II). It can be observed that Building I exceeds the allowable drift at all floors for the scaled record of the 1971 San Fernando earthquake, and at seven floors for the scaled record of the 1994 Northridge earthquake. The maximum drift of Building I is 84 and 36 % more than the allowable drift when the structure is subjected to the scaled records of the San Fernando and Northridge earthquakes. Building II which was designed by the ARGEB convex model has a better response than Building I for both scaled records. The maximum drift is only 32 and 11 % larger than that of the allowable drift in the scaled record of the San Fernando earthquake and the actual record of the 1940 El-Centro earthquake. It should be noted that the drift response to the artificial earthquake (IV) of Figure 6.13 for both Buildings I and II remains within the allowable limits.

Optimal Design of Conventional Structure for San Fernando Earthquake

The optimal design for the actual record of the 1971 San Fernando earthquake and the optimal designs using the RGEB and ARGEB convex models are listed in Table 6.13. The reduction factor used in the RGEB convex model is excitation-specific, valid only for the 1971 San Fernando earthquake (S16E component). The average reduction factor used in the ARGEB convex model was obtained from the 12 records of the 1971 San Fernando and 1994 Northridge earthquakes (subset S6 of Table 5.9). The active constraints for each optimal design are shown shaded in Table 6.13.

The minimum volume obtained by the RGEB convex model is 2.0 % more than that obtained from the time-history of the actual record (AR). The minimum volume obtained

Table 6.13. The optimal design of the ten-story conventional structure subjected to the 1971 San Fernando earthquake

Frame Group	Cross-sectional area (cm ²)			Fl.	Combined stress for beam (MPa)			Combined stress for column (MPa)			Interstory Drift (cm)		
	AR	RGEB	ARGEb		AR	RGEB	ARGEb	AR	RGEB	ARGEb	AR	RGEB	ARGEb
A1	1,334.31	1,587.42	2,649.55	1	100.69	106.38	78.80	132.40	143.99	126.41	0.91	0.95	0.54
A2	876.97	900.01	2,508.64	2	142.31	139.56	115.88	148.39	145.77	149.10	1.65	1.60	1.01
A3	962.99	1,002.77	1,588.74	3	145.12	146.20	133.12	115.01	118.69	120.79	1.95	1.94	1.45
A4	839.02	834.34	1,241.68	4	134.45	140.03	135.51	97.36	98.57	98.85	1.93	1.99	1.60
A5	906.10	926.20	1,239.37	5	118.34	126.80	130.44	86.54	95.91	112.47	1.84	1.95	1.73
A6	782.88	834.10	1,173.85	6	96.08	112.25	118.68	73.27	80.00	92.61	1.73	1.81	1.70
A7	606.58	643.84	977.81	7	77.80	103.31	112.96	48.21	62.18	71.23	1.66	1.68	1.62
A8	572.07	523.38	660.66	8	78.47	109.95	124.43	63.31	83.98	89.30	1.97	1.94	1.89
Volume (cm ³)	13,656,970	13,933,900	21,097,000	9	68.61	89.43	106.71	46.49	59.67	57.90	1.88	1.92	1.96
				10	52.77	59.35	76.38	45.74	42.30	41.74	1.39	1.49	1.59

Note: ARGEb - Global energy-bound convex model adjusted with the average reduction factor from subset S6 of Table 5.9

by the ARGEB convex model is 54 % more than that obtained by the AR procedure. It can also be observed that the minimum volume of the structure designed for the 1971 San Fernando is 2.2 times larger than that for the 1940 El-Centro earthquake shown in Table 6.11, which is approximately equal to the square root of the ratio of the global energy bound for these two earthquakes.

The structure designed by the AR procedure (referred to as Building III) and the ARGEB convex model (referred to as Building IV) are also verified by a dynamic analysis for the 1971 San Fernando and scaled 1994 Northridge earthquakes shown in Table 6.14. Figure 6.15 shows the interstory drift of the structures subjected to the actual record of the 1971 San Fernando earthquake, and the scaled record of the 1994 Northridge earthquake with the same global energy bound. It can be observed that Building III has much larger drifts than Building IV when the structures are subjected to the scaled record of the 1994 Northridge earthquake. The maximum drifts are 76 and 12 % larger than the allowable drift for Buildings III and IV. Figures 6.14 and 6.15 show that in general, the structures designed by the ARGEB convex model respond well for other excitations which have the same global energy-bound. However, this is not true for structures designed for a single earthquake.

Table 6.14. Peak acceleration and global energy-bound of the excitations for verifying the structure designed by the ARGEB convex model of subset S6 of Table 5.9

Excitations	Peak accel. (g)	Duration (sec)	Global energy-bound (m ² /sec ²)
1971 San Fernando	1.172	41.0	52.61
Scaled Northridge	1.517	60.0	52.61

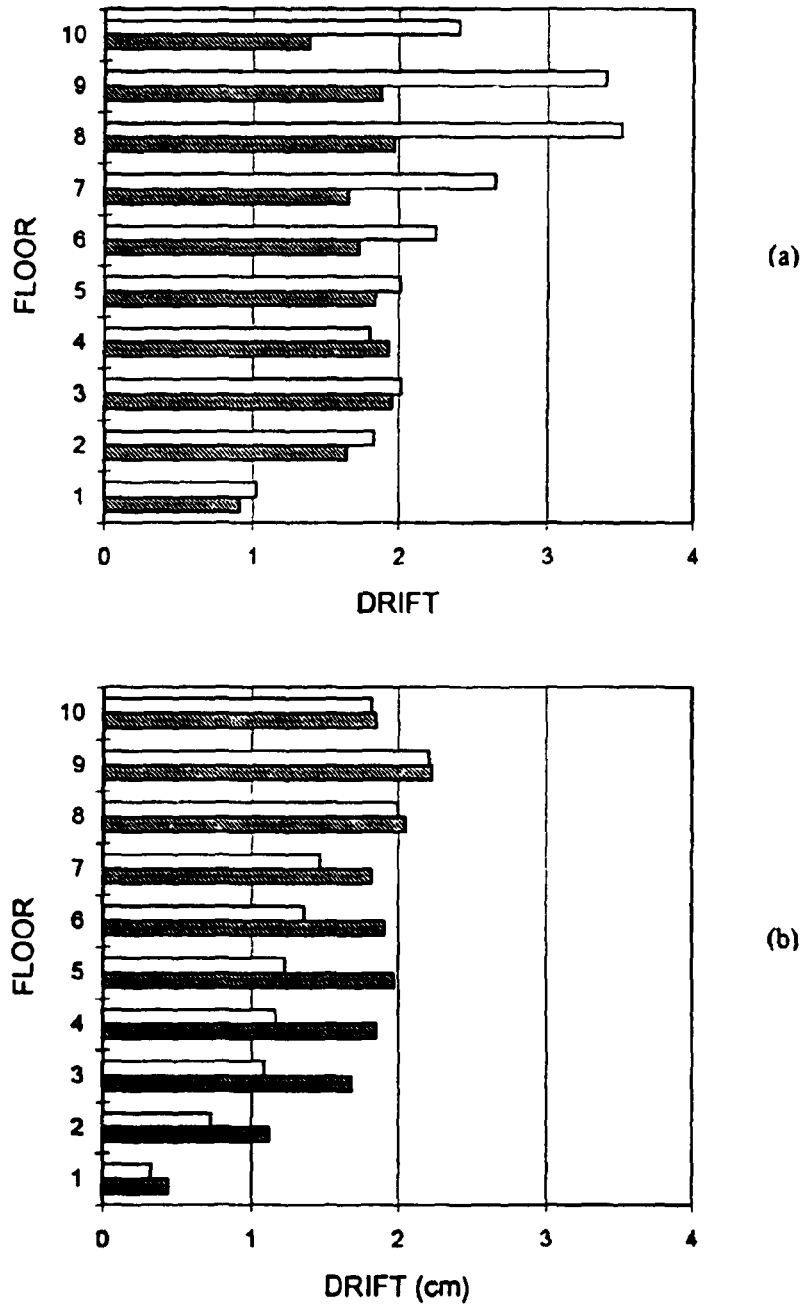


Figure 6.15 Interstory drift of the ten-story frame: (a) AR design for 1971 San Fernando of Table 6.13 (Building III) and (b) ARGEB convex model design of Table 6.13 (Building IV); □ = scaled record of 1994 Northridge earthquake, ▨ = 1971 San Fernando earthquake record

Optimal Design of Conventional Structure for Artificial Earthquake

The optimal designs for the actual record of an artificial earthquake (Artificial earthquake III, see Figure 5.19(d)), are shown in Table 6.15. The reduction factors used in the RGEB convex model were the excitation-specific values valid only for this excitation. The average reduction factors used in the ARGEB convex model were determined from 6 excitation records with the same spectrum (subset G2 of Table 5.11). It can be observed from Table 6.15 that the minimum volume obtained by the RGEB convex model is 24 % less than that obtained by the time-history of the actual record (AR). The reason for the larger difference between the RGEB convex model and the AR analysis in this case is that the interstory drift used for the design was not directly obtained from the RGEB convex model. From the definition of the global energy-bound convex model, the maximum displacement, velocity, and acceleration were formulated, and the interstory drift was obtained by subtracting the maximum displacement at each floor. The minimum volume obtained from ARGEB convex model is 9 % more than the AR optimal design which is acceptable.

Optimal Design of Active Structure for El-Centro Earthquake

In this section the optimal design of an active structure with one active bracing system (ABS) on the first floor and one ABS on the second floor of the ten-story frame is presented. The control force is constrained to a maximum of 20 % of the excitation's effective lateral force. The effective lateral force is determined by multiplying the total mass of the structure by the peak acceleration of the excitation.

Table 6.15. The optimal design of the ten-story conventional structure subjected to the artificial earthquake III

Frame Group	Cross-sectional area (cm ²)		Fl.	Combined stress for beam (MPa)		Combined stress for column (MPa)		Interstory Drift (cm)					
	AR	RGEB		ARGEB	AR	RGEB	ARGEB	AR	RGEB	ARGEB			
A1	818.80	767.75	902.65	1	69.50	63.53	81.39	80.79	72.16	98.41	0.84	0.83	0.95
A2	460.50	358.74	489.55	2	103.92	98.09	113.42	97.85	91.53	98.09	1.62	1.67	1.66
A3	486.81	394.19	606.32	3	102.44	98.85	118.79	68.90	63.13	76.29	1.91	1.97	1.97
A4	393.65	322.20	464.21	4	86.72	91.85	114.35	62.18	54.17	63.71	1.98	1.93	1.99
A5	436.58	353.31	564.52	5	82.81	84.36	107.50	44.30	54.41	59.68	1.95	1.88	1.97
A6	393.35	311.87	437.20	6	76.67	75.66	98.43	62.82	47.00	53.04	1.80	1.73	1.88
A7	400.04	249.25	367.93	7	56.95	70.47	91.42	38.37	37.29	42.50	1.92	1.59	1.75
A8	376.67	195.28	284.69	8	54.49	76.55	92.38	30.48	52.65	61.43	1.95	1.88	2.00
Volume (cm ³)	7,261,152	5,492,297	7,904,052	9	51.04	67.69	75.34	32.70	37.03	46.19	1.77	1.96	1.94
				10	38.46	49.54	50.74	33.28	33.57	33.89	1.30	1.59	1.42

Note: ARGEB - Global energy-bound convex model adjusted with the average reduction factor from group G2 of Table 5.11

Table 6.16 shows the optimal design using the time-history analysis of the 1940 El-Centro earthquake record, the RGEB convex model with the excitation-specific reduction factor, and the ARGEB convex model with the average reduction factor from 26 California records (subset S7 of Table 5.9). It can be observed that the minimum volume obtained by the RGEB convex model is 0.7 % more than that obtained by using the time-history of the actual record (AR) for the 1940 El-Centro earthquake. The minimum volume obtained by the ARGEB convex model is 64 % more than that of the AR design. However, note that compared to the design of the structure without structural control the present designs required on the average 15 % less volume.

The performance of the structure designed by the time-history of the actual El-Centro earthquake record (Building V) and the structure designed by the ARGEB convex model (Building VI) are examined using a time-history analysis of the four excitations shown in Table 6.12 with the same global energy-bound. The same control parameters are used in the design of Buildings V and VI. The interstory drifts for these two buildings are shown in Figure 6.16. Similar results are obtained as observed in Figures 6.14 and 6.15. Building VI responds much better than Building V for all excitations, especially for the scaled record of the San Fernando earthquake. The maximum control forces of both ABS in Buildings V and VI (Figure 6.17) are on average 19 and 11 % of the excitation effective lateral force, respectively.

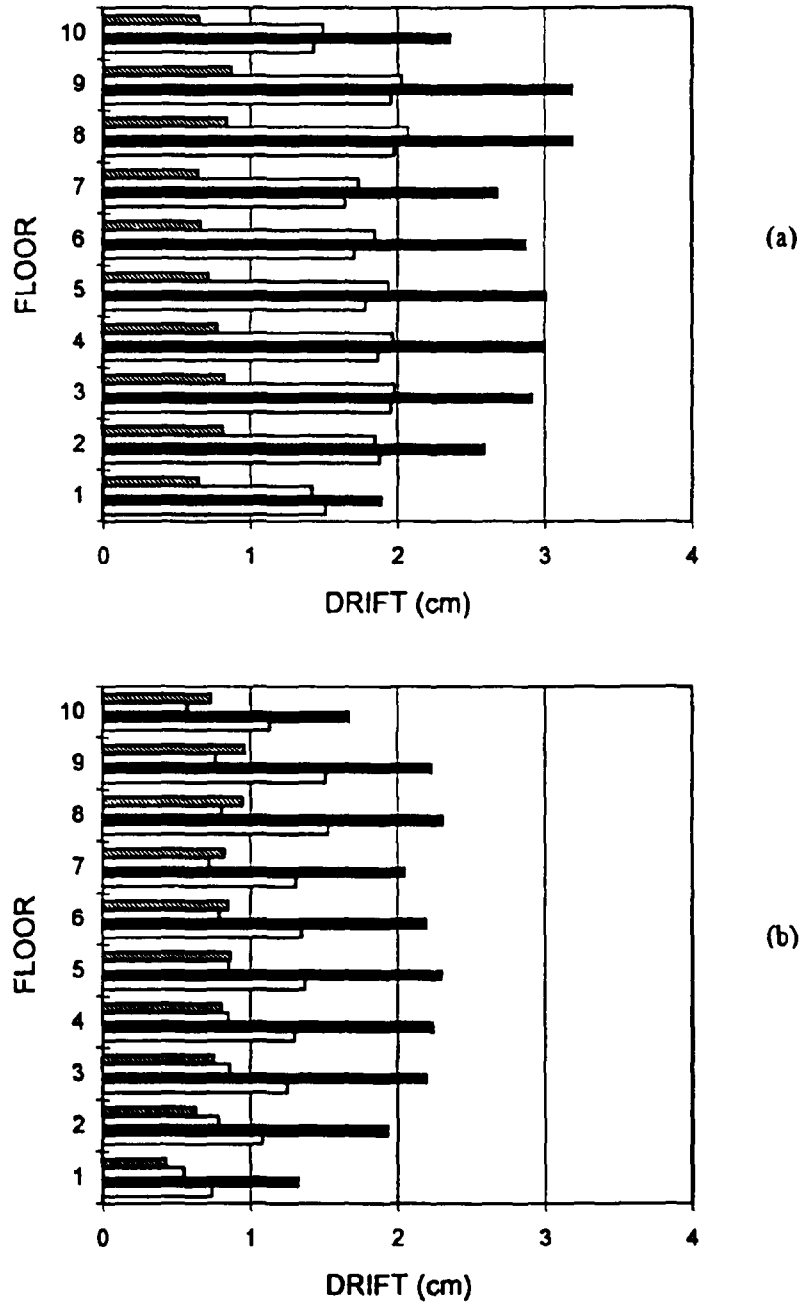


Figure 6.16 Interstory drift of the ten-story frame with two ABS: (a) AR design for 1940 El-Centro of Table 6.16 (Building V) and (b) ARGEB convex model design of Table 6.16 (Building VI); ▨ = artificial earthquake shown in Figure 6.13, □ = scaled record of 1994 Northridge earthquake, ■ = scaled record of 1971 San Fernando earthquake, ◻ = 1940 El-Centro earthquake record

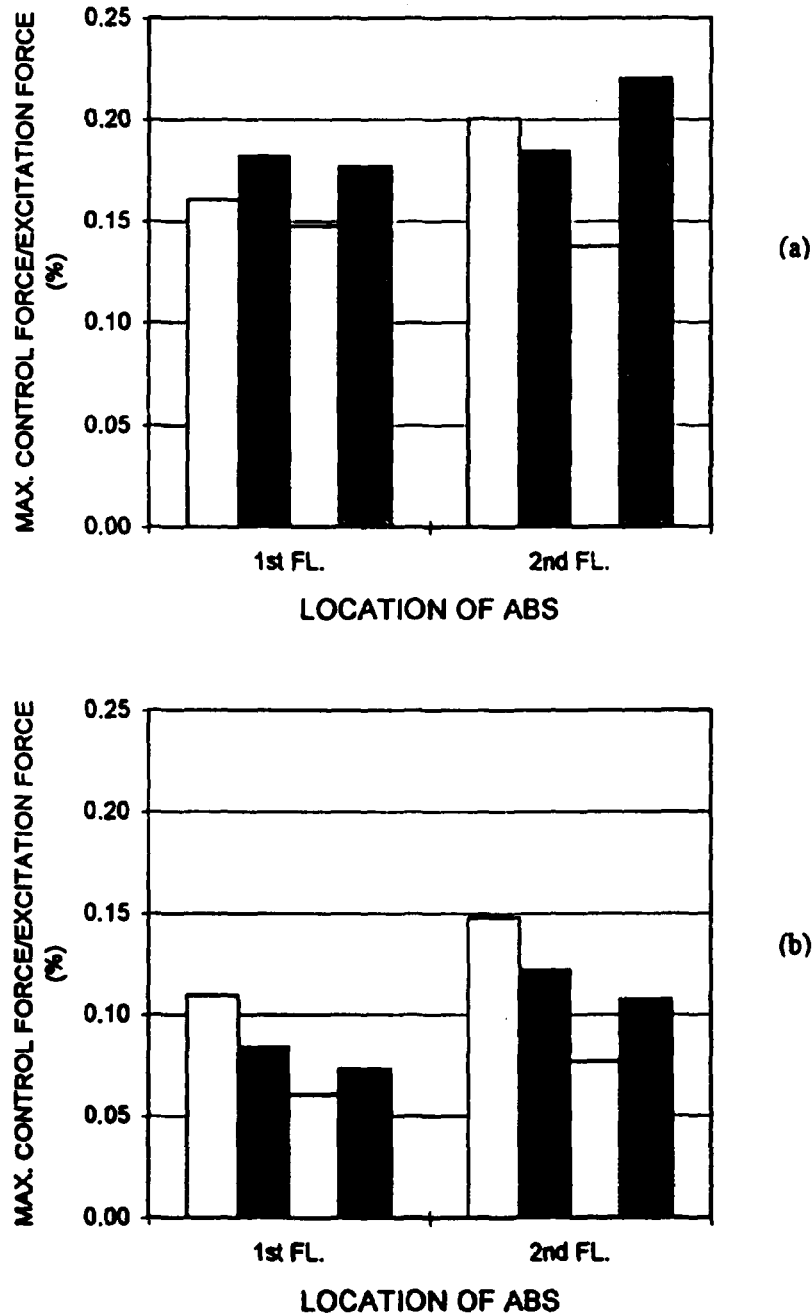


Figure 6.17 Maximum control force of the ten-story frame with two ABS: (a) Building V (AR analysis for 1940 El-Centro) and (b) Building VI (ARGEB convex model); \blacksquare = artificial earthquake shown in Figure 6.13, \square = scaled record of 1994 Northridge earthquake, \blacksquare = scaled record of 1971 San Fernando earthquake, \square = 1940 El-Centro earthquake record

Optimal Design of Active Structure for San Fernando and
Artificial Earthquakes

Two ABS were assumed to be installed in the ten-story frame as described in the last section. The optimal designs for the 1971 San Fernando earthquake are shown in Table 6.17. The minimum volume obtained by the RGEB convex model is 3.3 % less than the minimum volume for the actual record (AR) for the 1971 San Fernando earthquake. For the results obtained by the ARGEB convex model, the subset S6 of Table 5.9 is used in Table 6.17. The minimum volume results obtained by the ARGEB convex model is 59 % more than the minimum volume obtained using the actual record (AR) for the San Fernando earthquake. Table 6.18 shows the optimal designs for the time-history analysis of the artificial earthquake III shown in Figure 5.19(d), and the RGEB and ARGEB convex models. The minimum volumes obtained by the RGEB convex model is 7.2 % less than the actual record (AR) of the artificial earthquake III. The results obtained by the ARGEB convex model (subset G2 of Table 5.11) is 25 % more than those obtained by the AR.

These values, as well as that obtained for the conventional structures, indicate that in general the results obtained by the RGEB convex model are closer to those of the time-history of the actual record (AR). The results obtained by the ARGEB convex model are further away as compared to the RGEB convex model from those of the AR procedure. However, the ARGEB convex model results are most of the time on the conservative side and within reasonable margins. In general, the structures designed by the ARGEB convex model respond better to other excitations than the structures designed by the time-history analysis for a specific excitation. The computational advantage of using convex models is

Table 6.18. The optimal design of the ten-story active structure subjected to the artificial earthquake III

Frame Group	Cross-sectional area (cm ²)			Fl.	Combined stress for beam (MPa)			Combined stress for column (MPa)			Interstory Drift (cm)		
	AR	RGEB	ARGEB		AR	RGEB	ARGEB	AR	RGEB	ARGEB	AR	RGEB	ARGEB
A1	397.31	484.30	587.50	1	85.77	75.88	95.15	114.42	92.82	121.77	1.43	1.15	1.30
A2	353.79	343.72	445.54	2	97.50	90.78	110.93	79.00	73.56	80.99	1.88	1.70	1.80
A3	374.67	386.87	562.68	3	94.68	89.41	110.92	64.90	57.29	64.34	1.98	1.83	1.96
A4	331.14	329.32	423.01	4	85.45	85.23	105.73	59.47	50.80	56.32	1.93	1.79	1.93
A5	341.00	357.34	501.94	5	76.61	82.26	99.50	50.22	48.55	53.85	1.96	1.80	1.93
A6	313.21	297.70	385.93	6	72.72	76.60	91.02	45.48	42.79	48.30	1.91	1.75	1.84
A7	322.06	245.87	294.97	7	67.32	72.41	83.80	41.44	34.65	39.21	1.74	1.64	1.70
A8	293.97	179.39	271.35	8	55.85	77.27	83.98	41.39	51.10	63.01	1.93	1.95	1.98
Volume (cm ³)	5,538,400	5,142,305	6,892,113	9	35.25	66.21	66.00	30.70	35.72	50.00	1.81	2.00	1.86
				10	18.42	47.04	40.78	15.86	28.87	35.02	1.32	1.56	1.34
Note: ARGEB - Global energy-bound convex model adjusted with the average reduction factor from group G2 of Table 5.11													
Maximum Control Force (kN)													
Floor	AR	RGEB	ARGEB										
1	204	239	265										
2	254	251	251										

obvious in the case of buildings with a large number of design variables, such as tall buildings. In that case, the calculations involved in obtaining the active structure using the time-history analysis of the actual record are quite expensive. However, the convex model solutions could be obtained with less effort because of the static nature of the constraints.

Optimal Designs of Active Structures

In this section, the ten-story frame shown in Figure 6.9 with different levels of inherent structural damping is used. Three cases are discussed: (1) one active bracing system (ABS) installed on the first floor and one ABS on the second floor, (2) one viscoelastic (VE) damper on the first floor and one VE damper on the second floor, and (3) one ABS on the first floor and one VE damper on the second floor. The allowable stress for each frame member is assumed as 150 MPa, and the allowable interstory drift for each floor is given as $h/180$ which is 2.5 cm for the first floor, and 2.0 cm for the second up to the tenth floors. The strong column-weak beam philosophy is also implemented. The constants α_i , β_i , and χ_i in equation (6.1) equal 0.58, 0.58, and 0.67, respectively. Note that for Cases (1) and (3) the maximum control forces of ABS are limited to be equal or less than 20 % of the excitation lateral force. The thickness of the VE dampers equals 0.0127 m, and the cross-sectional area of the VE dampers equals 0.032 m² which is chosen to achieve the similar performance as the ABS structural control. The material properties of the VE dampers are described in Chapter 4.

The optimal designs of the conventional structure with inherent structural damping

levels of 1, 2, 3, and 4 % of critical are shown in Table 6.19. The time-history analysis method is used with the 1940 El-Centro earthquake as the excitation. The active constraints for each optimization design are shaded in Table 6.19. It can be observed that the minimum volume of the optimal structure is decreased as the inherent structural damping is increased. Note that the optimal design of the structure with inherent structural damping of 5 % of critical was shown in the previous section (Building I in Table 6.11).

The optimal designs for the three active structures stated above are shown in Tables 6.20, 6.21, and 6.22. The inherent structural damping levels are assumed to 1, 2, 3, 4, and 5 % of critical at all modes for each of the three cases. The 1940 El-Centro earthquake is used. The effective damping level, includes the inherent structural damping and the damping introduced by the structural control. The minimum volume of the active structures are compared with the conventional structures of Table 6.19 and Building I of Table 6.11, and are shown in Figures 6.18, 6.19, and 6.20. It can be observed that the volume of the optimal structures are decreased as the effective damping level is increased for active structures as well as conventional structures.

The relationship between the effective damping ratios and the optimal volume of the active structures can be depicted more clearly by comparing Cases 1 - 3 of Figures 6.18 - 6.20 as shown in Figure 6.21. It can be observed that in general the minimum volume of the active structure is inversely proportional to the effective damping ratio for all three structural control cases. A comparison of the additional damping introduced by the control systems in the three cases with respect to the inherent structural damping is

Table 6.19. Optimal designs of the ten-story frame with different levels of the inherent structural damping

Frame Group	Cross-sectional area (cm ²)				Fl.	Combined stress of beam (MPa)				Combined stress of column (MPa)				Interstory Drift (cm)			
	1 %	2 %	3 %	4 %		1 %	2 %	3 %	4 %	1 %	2 %	3 %	4 %	1 %	2 %	3 %	4 %
A ₁	960.02	622.72	620.10	582.49	1	103.68	92.16	66.47	67.10	103.68	116.43	86.77	87.49	1.16	1.22	0.90	0.94
A ₂	385.27	496.31	443.06	397.98	2	119.62	112.02	81.86	83.70	59.17	102.53	77.27	80.46	1.82	1.86	1.38	1.48
A ₃	921.62	474.25	462.13	426.82	3	116.08	100.77	82.30	82.47	41.56	78.25	61.91	64.41	1.97	1.97	1.59	1.65
A ₄	369.86	410.38	410.54	376.31	4	104.11	80.39	85.79	84.84	25.77	64.36	53.26	52.67	1.98	1.97	1.72	1.84
A ₅	882.75	436.77	427.69	409.74	5	97.47	86.29	88.33	91.98	28.59	41.31	64.96	65.34	1.94	2.00	1.79	1.95
A ₆	368.88	396.08	394.14	371.40	6	87.88	89.12	79.28	89.45	33.14	70.43	55.15	59.02	1.95	1.85	1.74	1.90
A ₇	527.37	429.35	409.55	360.67	7	80.59	69.77	67.49	79.83	12.97	49.40	43.75	49.41	1.94	1.86	1.86	1.88
A ₈	327.42	388.03	313.64	321.08	8	78.86	54.25	58.74	71.43	40.42	37.12	30.86	43.98	1.98	1.77	1.97	1.98
Volume (cm ³)	9,272,500	7,241,799	6,891,800	6,456,335	9	64.64	39.06	44.88	54.67	32.65	32.08	29.20	41.98	1.88	1.45	1.82	1.75
					10	45.78	22.19	28.72	32.72	22.36	18.64	18.99	26.84	1.49	1.03	1.37	1.24

Note: Allowable stress = 150 Mpa, Allowable interstory drift = 2.5 cm for the 1st floor, 2.0 cm for the other floors.

Table 6.20. Optimal designs of ten-story frame with two ABS

Frame Group	Cross-sectional area (cm ²)					Fl.	Combined stress of beam (MPa)					Combined stress of column (MPa)				
	1%	2%	3%	4%	5%		1%	2%	3%	4%	5%	1%	2%	3%	4%	5%
A ₁	458.26	486.14	461.38	381.57	379.16	1	89.63	84.06	85.21	86.19	87.92	118.74	105.79	103.61	114.27	114.75
A ₂	366.19	366.20	342.97	335.21	323.01	2	101.57	99.55	100.04	95.88	94.35	74.50	74.68	68.01	75.64	69.58
A ₃	439.93	445.39	442.93	366.30	373.55	3	103.60	100.86	100.10	93.31	90.56	67.24	61.86	53.74	63.91	55.02
A ₄	365.98	361.50	329.25	334.38	317.52	4	99.65	97.29	94.56	87.75	85.93	58.16	54.72	48.52	56.92	54.09
A ₅	402.88	355.45	390.10	351.65	358.61	5	94.70	91.29	86.08	82.72	75.62	56.15	63.09	48.89	49.21	49.29
A ₆	338.90	336.73	316.08	297.72	312.28	6	83.43	80.22	75.77	73.73	65.18	50.50	56.29	43.71	43.39	40.42
A ₇	315.07	311.88	236.12	283.60	254.21	7	72.02	68.52	65.63	65.31	58.31	40.94	44.94	34.10	35.38	33.11
A ₈	272.51	249.86	222.23	204.91	192.23	8	60.67	59.70	59.69	57.95	58.95	39.10	34.40	44.36	31.76	36.69
Volume (cm ³)	5,976,381	5,822,353	5,461,975	5,149,726	5,061,958	9	43.00	43.45	41.79	43.03	54.51	31.93	29.84	35.41	26.35	27.06
						10	26.18	26.95	23.01	27.80	41.79	20.65	19.06	20.62	16.96	26.82
Mode	Total damping ratio (%)					Fl.	Interstory drift (cm)					Max. control force (kN)				
	1%	2%	3%	4%	5%		1%	2%	3%	4%	5%	1%	2%	3%	4%	5%
1	4.91	5.56	7.61	9.6	10.60	1	1.40	1.26	1.31	1.47	1.51	206	189	194	215	215
2	10.75	11.05	13.30	16.33	16.82	2	1.85	1.77	1.82	1.88	1.88	265	256	261	261	268
3	13.08	13.90	18.03	20.73	23.30	3	1.99	1.94	1.97	1.95	1.96	-	-	-	-	-
4	11.76	12.53	15.37	19.11	20.09	4	1.98	1.93	1.94	1.88	1.87	-	-	-	-	-
5	10.83	11.23	14.37	18.06	19.12	5	1.98	1.99	1.89	1.85	1.78	-	-	-	-	-
6	13.70	13.69	16.47	24.13	25.60	6	1.87	1.85	1.73	1.87	1.71	-	-	-	-	-
7	19.09	17.94	17.96	31.90	29.02	7	1.70	1.71	1.65	1.81	1.64	-	-	-	-	-
8	23.19	22.98	35.24	34.66	39.52	8	1.93	2.00	1.99	1.96	1.98	-	-	-	-	-
9	23.23	20.52	35.27	35.06	40.27	9	1.78	1.93	2.00	1.82	1.96	-	-	-	-	-
10	17.64	29.56	28.09	21.58	23.21	10	1.26	1.42	1.41	1.34	1.43	-	-	-	-	-

Table 6.2.1. Optimal designs of ten-story frame with two VE dampers

Frame Group	Cross-sectional area (cm ²)					Fl.	Combined stress of beam (MPa)					Combined stress of column(MPa)				
	1%	2%	3%	4%	5%		1%	2%	3%	4%	5%	1%	2%	3%	4%	5%
A1	509.02	472.15	413.03	414.89	373.37	1	61.88	67.29	74.59	74.86	74.40	88.05	93.83	100.68	97.41	101.75
A2	406.40	396.47	341.02	327.63	321.05	2	78.54	83.93	90.44	90.27	88.61	72.97	75.75	67.88	64.21	68.24
A3	420.36	402.16	396.51	398.29	354.76	3	85.25	90.89	98.06	97.42	94.61	66.77	70.47	69.37	64.03	69.90
A4	367.27	357.53	340.00	326.21	320.24	4	88.91	91.81	95.88	95.25	89.98	57.85	59.69	57.85	53.36	58.72
A5	385.91	386.27	384.94	341.59	335.88	5	91.06	90.97	89.01	87.37	81.86	65.02	59.97	53.16	58.69	54.72
A6	355.82	345.15	323.01	313.16	305.96	6	85.72	83.13	77.42	74.27	69.87	56.76	53.60	47.21	50.68	47.89
A7	373.96	351.59	272.44	314.40	237.23	7	78.49	73.91	64.97	61.75	58.23	47.79	44.28	38.01	39.31	37.13
A8	292.48	280.08	268.18	230.89	232.34	8	71.91	66.13	51.49	51.39	47.88	38.70	35.66	39.76	27.86	40.75
Volume (cm ³)	6,213,347	5,992,279	5,557,062	5,380,169	5,026,639	9	55.88	51.02	34.77	35.53	39.74	35.41	33.68	30.18	23.91	18.48
						10	37.14	32.84	19.73	21.24	33.15	25.22	22.95	18.77	13.36	30.65
Mode	Total damping ratio (%)					Interstory drift (cm)					Area of VE damper (cm ²)					
	1%	2%	3%	4%	5%	1%	2%	3%	4%	5%	1%	2%	3%	4%	5%	
1	4.46	5.65	7.37	8.29	9.60	1	0.91	1.00	1.17	1.17	1.23	320	320	320	320	320
2	6.69	7.92	9.74	10.55	11.87	2	1.35	1.45	1.60	1.61	1.64	320	320	320	320	320
3	6.32	7.90	9.20	10.39	11.84	3	1.69	1.81	1.93	1.93	1.95	-	-	-	-	-
4	4.85	6.07	7.38	8.53	9.80	4	1.86	1.95	2.00	1.99	1.97	-	-	-	-	-
5	3.36	4.53	5.82	6.85	8.20	5	1.96	1.98	1.94	1.98	1.90	-	-	-	-	-
6	2.97	4.17	5.45	6.39	7.68	6	1.91	1.89	1.81	1.89	1.91	-	-	-	-	-
7	3.10	4.27	5.07	6.36	7.16	7	1.90	1.83	1.73	1.81	1.81	-	-	-	-	-
8	3.10	4.19	5.68	6.34	8.02	8	1.99	1.98	1.99	1.95	1.98	-	-	-	-	-
9	2.56	4.06	5.80	5.79	8.06	9	1.81	1.83	1.82	1.94	1.88	-	-	-	-	-
10	3.38	4.11	4.93	6.68	7.75	10	1.32	1.32	1.25	1.46	1.32	-	-	-	-	-

Table 6.22. Optimal designs of ten-story frame with one ABS and one VE damper

Frame Group	Cross-sectional area (cm ²)					Fl.	Combined stress of beam (MPa)					Combined stress of column(MPa)				
	1%	2%	3%	4%	5%		1%	2%	3%	4%	5%	1%	2%	3%	4%	5%
A1	425.21	412.68	430.73	400.83	357.83	1	78.63	78.69	80.41	79.58	80.60	118.26	115.99	107.01	108.61	119.27
A2	368.21	365.30	327.20	322.79	308.10	2	91.96	91.07	93.49	92.03	87.88	66.55	65.62	58.46	61.25	59.47
A3	407.46	399.57	424.18	383.77	348.14	3	100.00	98.52	99.50	97.92	93.53	74.81	70.03	59.54	63.80	66.85
A4	355.49	343.63	319.22	312.85	307.80	4	97.88	96.57	96.32	93.69	89.49	61.22	58.40	49.08	53.27	58.70
A5	387.10	354.51	398.43	349.86	334.22	5	91.73	89.94	88.77	85.03	78.75	58.61	59.40	47.33	52.39	53.68
A6	341.13	323.87	306.46	300.55	301.69	6	81.11	78.70	77.74	73.32	67.30	51.76	52.50	42.15	45.71	44.67
A7	316.15	303.81	268.65	246.53	264.70	7	69.33	67.20	66.76	62.34	57.71	42.66	42.16	33.40	35.67	36.87
A8	279.62	241.41	232.59	225.50	203.74	8	58.42	57.31	55.59	53.38	60.27	38.65	33.21	36.17	37.01	29.34
Volume (cm ³)	5,841,290	5,526,547	5,442,562	5,114,119	4,918,403	9	41.21	40.73	37.84	36.50	57.87	31.60	27.94	29.47	29.20	34.24
						10	24.61	25.21	21.61	21.22	39.25	20.05	17.64	17.17	18.20	26.02
Mode	Total damping ratio (%)					Interstory drift (cm)					Max. control force (kN) (Area of VE damper, cm ²)					
	1%	2%	3%	4%	5%	1%	2%	3%	4%	5%	1%	2%	3%	4%	5%	
1	5.67	6.66	7.98	9.05	10.55	1	1.33	1.34	1.31	1.34	1.50	263	265	261	259	257
2	10.99	12.01	13.11	14.21	15.78	2	1.63	1.63	1.67	1.69	1.71	(320)	(320)	(320)	(320)	(320)
3	14.40	16.49	17.85	19.11	21.75	3	1.93	1.93	1.95	1.98	1.99	-	-	-	-	-
4	15.59	18.25	19.18	20.17	22.52	4	2.00	1.99	1.99	2.00	1.99	-	-	-	-	-
5	14.63	17.40	18.55	19.53	21.15	5	1.98	1.99	1.94	1.94	1.92	-	-	-	-	-
6	14.14	16.68	18.40	19.26	20.97	6	1.85	1.84	1.81	1.89	1.88	-	-	-	-	-
7	11.86	14.20	14.07	15.00	17.59	7	1.69	1.73	1.74	1.80	1.80	-	-	-	-	-
8	9.76	11.91	15.38	16.58	15.77	8	1.86	1.94	1.90	1.98	2.00	-	-	-	-	-
9	8.05	9.00	12.27	13.53	13.85	9	1.70	1.90	1.83	1.78	1.88	-	-	-	-	-
10	5.18	8.24	7.74	10.21	9.90	10	1.20	1.40	1.31	1.26	1.36	-	-	-	-	-

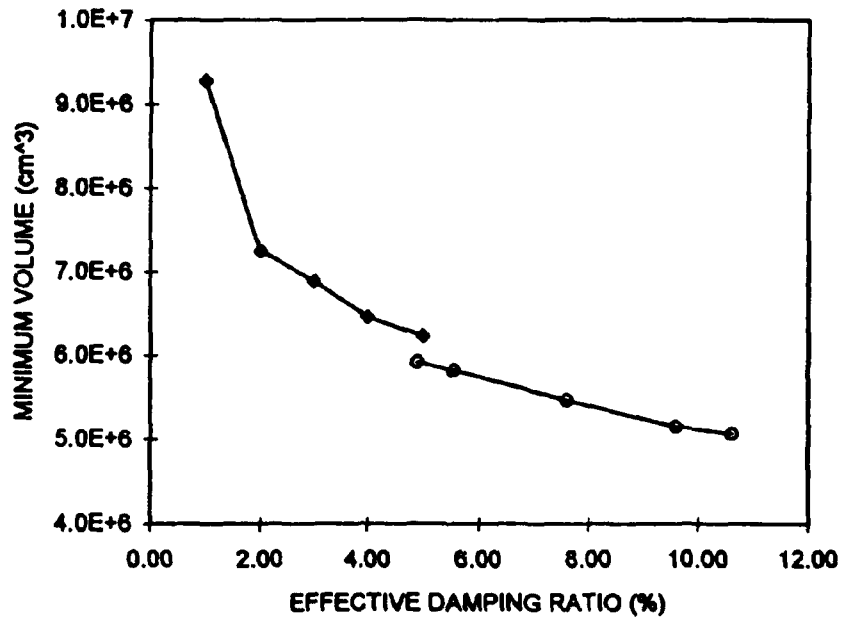


Figure 6.18 Comparison of the effective damping vs. optimal volume: \blacklozenge = conventional structure, \ominus = active structure with two ABS

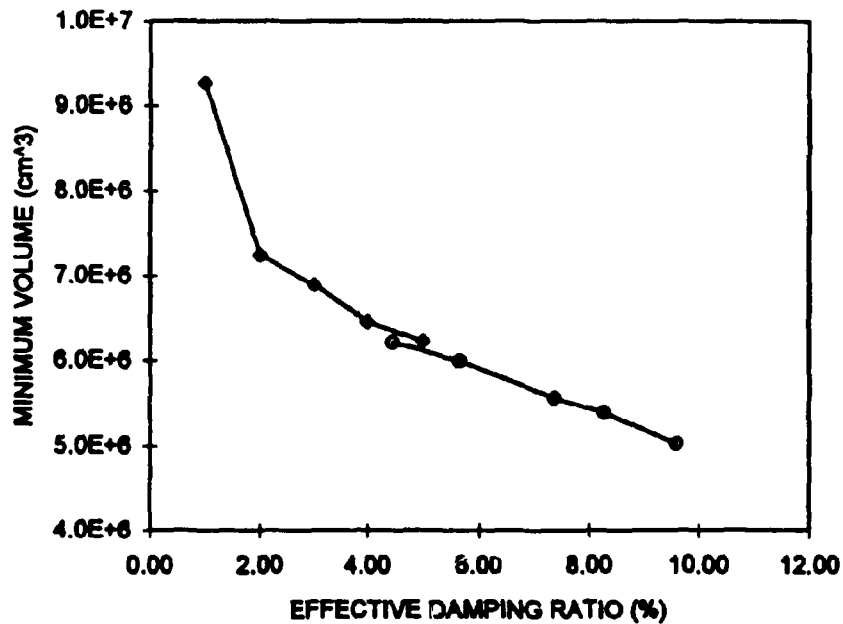


Figure 6.19 Comparison of the effective damping vs. optimal volume: \blacklozenge = conventional structure, \ominus = active structure with two VE dampers

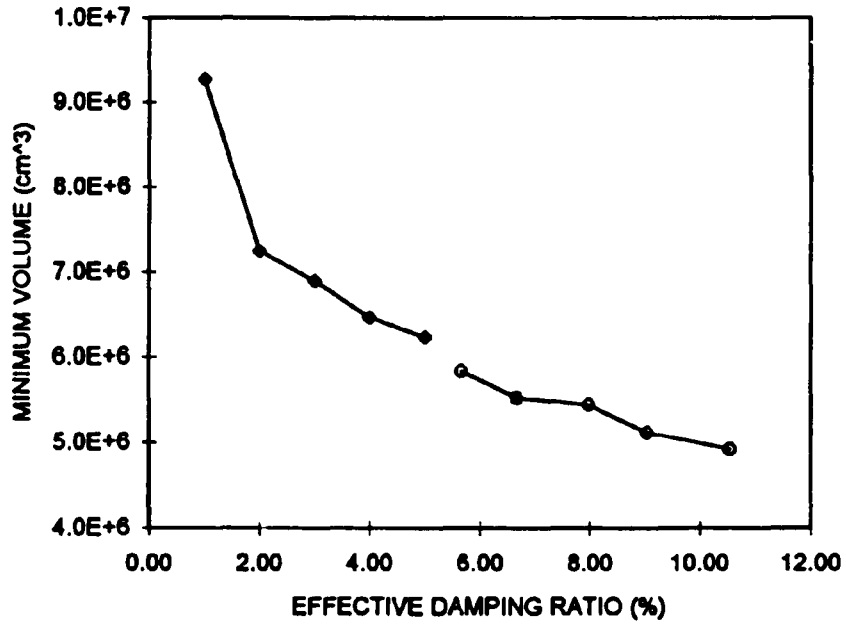


Figure 6.20 Comparison of the effective damping vs. optimal volume: \blacklozenge = conventional structure, \ominus = active structure with one ABS and one VE

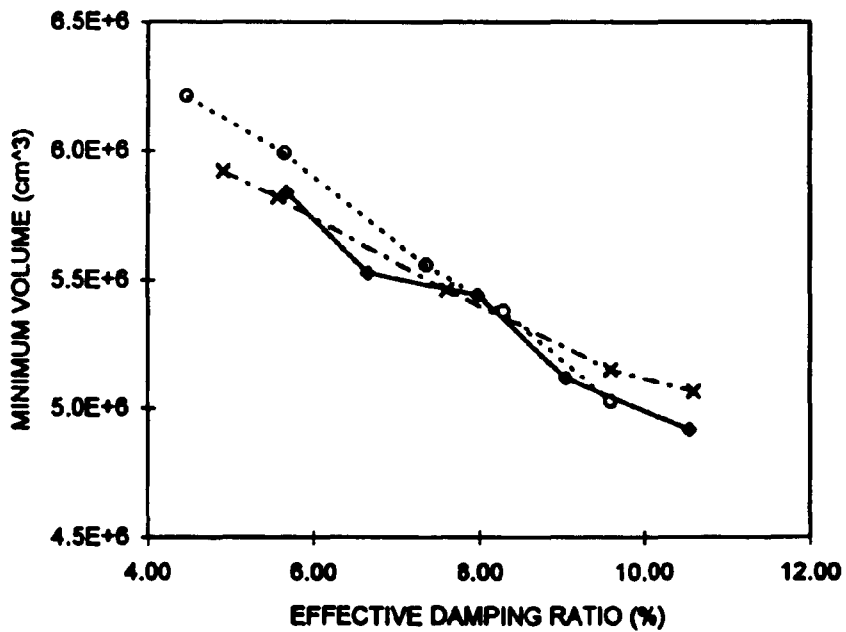


Figure 6.21 Comparison of the effective damping vs. optimal volume of active structures: $\cdots \times \cdots$ = two ABS, \blacklozenge = two VE dampers, $\cdots \ominus \cdots$ = one ABS and one VE damper

shown in Figure 6.22. It can be observed that for the same level of inherent structural damping, the additional damping introduced by the VE dampers (Case 2) on average is 0.6 and 0.9 % less than that of the active bracing systems (Case 1) and that of the combined system (Case 3), respectively.

However, the structural control systems reduce the optimal volume of the active structures on average by 23 % as compared to the reduction of the optimal conventional structures for the different levels of inherent structural damping. Figure 6.23 shows the ratios of the optimal volume of the active structures to that of the conventional structures. For the structure with the inherent structural damping level of 1 % of critical, the reduction of the structural volume can be achieved more efficiently (35 % on average) by the active structure. Note that the reduction of the three active structures, structures equipped with two ABS, two VE dampers, or one ABS and one VE damper, on average for all inherent damping ratios is 23, 21, and 25 % less than the conventional structure's optimal volume. However, a specific cross-sectional area of VE dampers and the maximum control force of the ABS are chosen for the active structures to achieve a comparable level. The intention of those comparisons is not to run a competition among the three cases of active structures, but to demonstrate that the reduction of the structural volume can be achieved in more than one way.

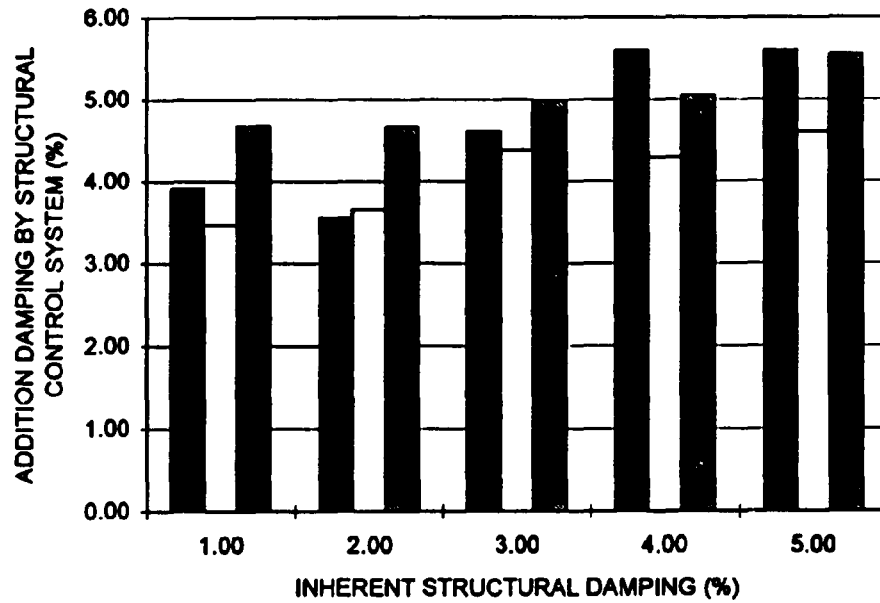


Figure 6.22 Additional damping of the active structures; ■ = two ABS (Case 1), □ = two VE dampers (Case 2), ▨ = one ABS and one VE damper (Case 3)

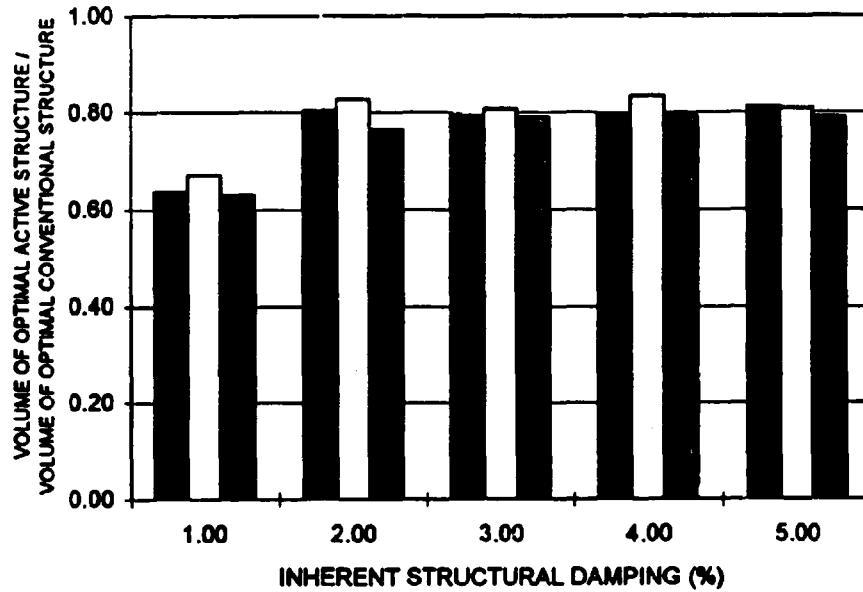


Figure 6.23 Reduction of the structural volume; ■ = two ABS (Case 1), □ = two VE dampers (Case 2), ▨ = one ABS and one VE damper (Case 3)

CHAPTER 7

INELASTIC ANALYSIS OF CONVENTIONAL AND ACTIVE STRUCTURES

An inelastic analysis is carried out in this Chapter using the finite element software DRAIN2DX (Prakash et al., 1993) for both conventional and active structures. A bilinear elastic-plastic model is used for the inelastic analysis. The response of the elastic and inelastic models is compared in terms of the displacement, velocity, acceleration, permanent deformation, control force requirements, and energy of the structural systems. The advantage of using active structures is shown by comparing the structural response and number of yield events.

Inelastic Analysis of Framed Structures

A simple inelastic element for modelling the frame elements of the structure (Powell, 1993), which includes beam and beam-column components, is used in this research. An elastic beam with two rigid-plastic hinges at its ends is considered. Yielding takes place only in the plastic hinges. The yield moment capacity is specified for positive and negative bending at the two ends of the element (Figure 7.1). The value of this yield

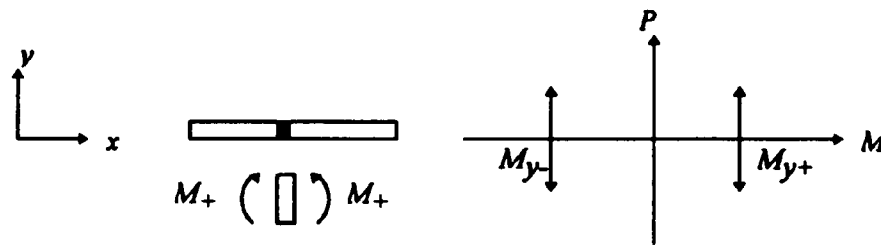


Figure 7.1 Yield surface and sign convention for moment

moment can be calculated in terms of the yield stress, σ_y , as

$$M_y = \int_0^d \int_0^b z \sigma_y dz dy \quad (7.1)$$

where d and b are the width and the depth of the beam or column element, and z is the coordinate in the in-plane direction.

The effects of the inelastic axial and shear deformations are ignored. The strain hardening in bending is modelled by assuming that the element consists of elastic and plastic components in parallel as shown in Figure 7.2. It is assumed that if the bending moment on the element is constant, the moment-rotation relationship has the same shape as the moment-curvature relationship. Thus, the strain hardening ratio is defined as a proportion of Young's modulus.

The input energy imparted to an inelastic system by a dynamic excitation is dissipated by viscous damping and by the yielding behavior of the structure. The energy terms can be defined by integrating the equation of motion of an inelastic system as (Chopra, 1995)

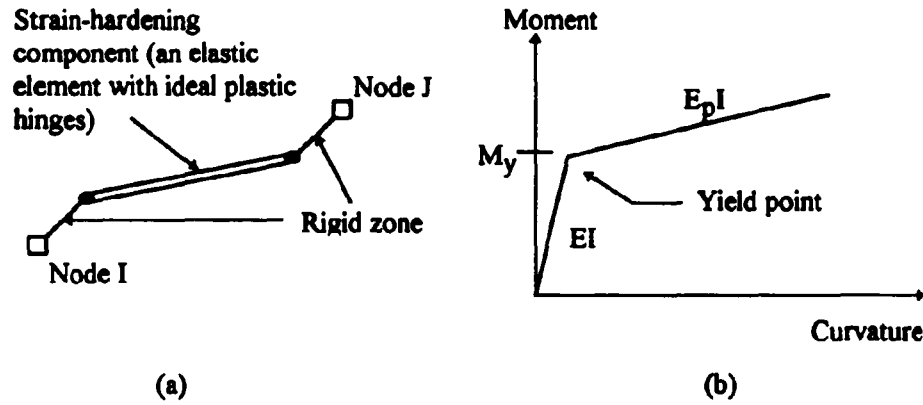


Figure 7.2 Bilinear model for the inelastic structure; (a) parallel components, (b) moment-curvature relationship

$$\int_0^x m\ddot{x}(t)dx + \int_0^x c\dot{x}dx + \int_0^x f_s(x, \dot{x})dx = -\int_0^x m\ddot{x}_g(t)dx \quad (7.2)$$

where $f_s(x, \dot{x})$ is the resisting force for an inelastic (in this case elastoplastic) system. Equation (7.2) can be described in terms of the energy dissipated by viscous damping, yielding, and the recoverable strain energy of the system as

$$E_K(t) + E_C(t) + E_T(t) + E_S(t) = E_I(t) \quad (7.3)$$

where $E_K(t)$, $E_C(t)$, $E_T(t)$, $E_S(t)$, and $E_I(t)$ are the kinetic energy associated with the motion of the structure relative to the ground, the damping energy, the yield strain energy, the elastic strain (the recoverable strain) energy, and the input energy. These energies are defined as

$$E_I(t) = -\int_0^x m\ddot{x}_g(t)dx = \int_0^t m\ddot{x}_g(t)\dot{x}(t)dt \quad (7.4a)$$

$$E_k(t) = \int_0^x m\ddot{x}(t)dx = \int_0^t m\dot{x}(t)d\dot{x} = \frac{m\dot{x}(t)^2}{2} \quad (7.4b)$$

$$E_c(t) = \int_0^x c\dot{x}(t)dx = \int_0^t c[\dot{x}(t)]dt \quad (7.4c)$$

$$E_p(t) = \int_0^x f_s(x, \dot{x})dx - E_s(t) = \int_0^t \dot{x}(t)f_s(x, \dot{x})dt - E_s(t) \quad (7.4d)$$

$$E_s(t) = \frac{[f_s(t)]^2}{2k} = \frac{kx^2}{2} \quad (7.4e)$$

Conventional Structures

Building V where properties are shown in Table 6.16 is used to investigate the inelastic behavior of the elastic-plastic structure. The strain hardening ratio is assumed as 0.0588, and the structural damping level equals 5 % of critical for all the modes. The beam and beam-column components of the structure are assumed to be structural steel W-shapes. The yield moments and moments of inertia of the structural element are shown in Table 7.1. The yield moments for positive and negative bending are assumed to be the same. The actual record of the S16E component of the 1971 San Fernando earthquake is used. Scaled records of the S00E component of the 1940 El-Centro

Table 7.1 Moments of inertia and yield moments of the structural elements of Building V in Table 6.15

Structural element	Cross-sectional Area (m ²)	Moment of inertia (m ⁴)	Yield Moment (N-m)
1st floor columns	.050902	2.9931E-3	1.7619E+6
1st floor beam	.040640	1.9079E-3	1.4111E+6
2nd-4th floors columns	.042036	2.0412E-3	1.4589E+6
2nd-4th floors beams	.036727	1.5582E-3	1.2771E+6
5th-7th floors columns	.038591	1.7204E-3	1.3410E+6
5th-7th floors beams	.035582	1.4625E-3	1.2378E+6
8th-10th floors columns	.037396	1.6155E-3	1.3000E+6
8th-10th floors beams	.028248	9.8819E-4	1.0203E+6

earthquake and the S90N component of the 1994 Northridge earthquake (Santa Monica City Hall), both having the same global energy bound as the 1971 San Fernando earthquake, are also considered. The peak acceleration, duration, and global energy bound of the three excitations are shown in Table 7.2.

The maximum response in terms of displacement, drift, velocity, and acceleration at each floor is shown in Figures 7.3 - 7.14 for the three excitations. It can be observed that the displacement, drift, velocity, and acceleration response obtained by the elastic analysis are on average 27, 31, 33, and 20 % larger than those obtained by the inelastic analysis for the 1971 San Fernando earthquake, and 13, 9, 5, and 1 % for the scaled record of the El-Centro earthquake. For the scaled record of the Northridge earthquake, the displacement, drift, and velocity response obtained by the elastic analysis are on average 2, 1, and 11 % larger than those obtained by the inelastic analysis. The acceleration response obtained from the elastic and inelastic analyses are almost the same for the scaled record of the Northridge earthquake. In general, it can be found that the maximum responses obtained from the elastic analysis were more conservative than those obtained from the inelastic analysis if significant yield events had occurred. However, the permanent deformations can only be determined from the inelastic analysis.

Table 7.2. Peak acceleration and global energy-bound of the excitations for investigating the inelastic behavior of Building V in Table 6.15

Excitations	Peak accel. (g)	Duration (sec)	Global energy-bound (m ² /sec ³)
1971 San Fernando	1.172	41.0	52.61
Scaled El-Centro	0.748	53.0	52.61
Scaled Northridge	1.518	60.0	52.61

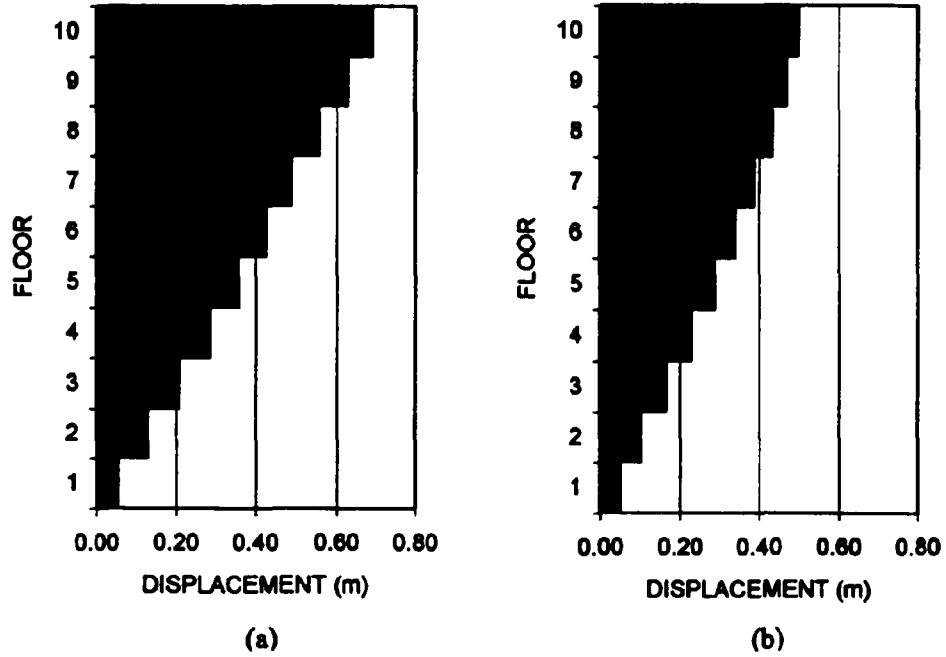


Figure 7.3 Maximum displacement of the ten-story frame for the 1971 San Fernando earthquake; (a) elastic analysis, (b) inelastic analysis

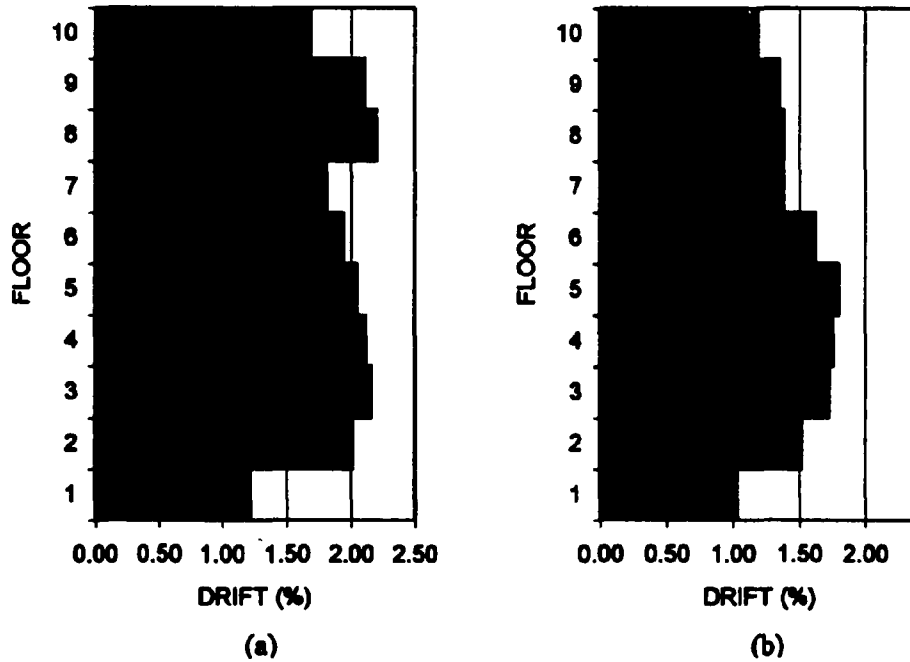


Figure 7.4 Maximum drift of the ten-story frame for the 1971 San Fernando earthquake; (a) elastic analysis, (b) inelastic analysis

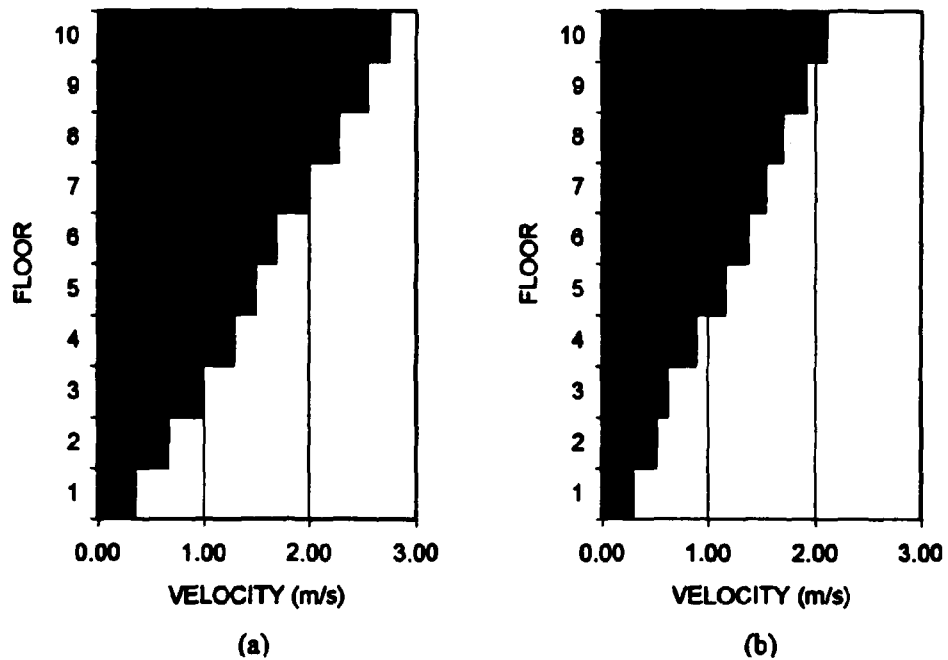


Figure 7.5 Maximum velocity of the ten-story frame for the 1971 San Fernando earthquake; (a) elastic analysis, (b) inelastic analysis

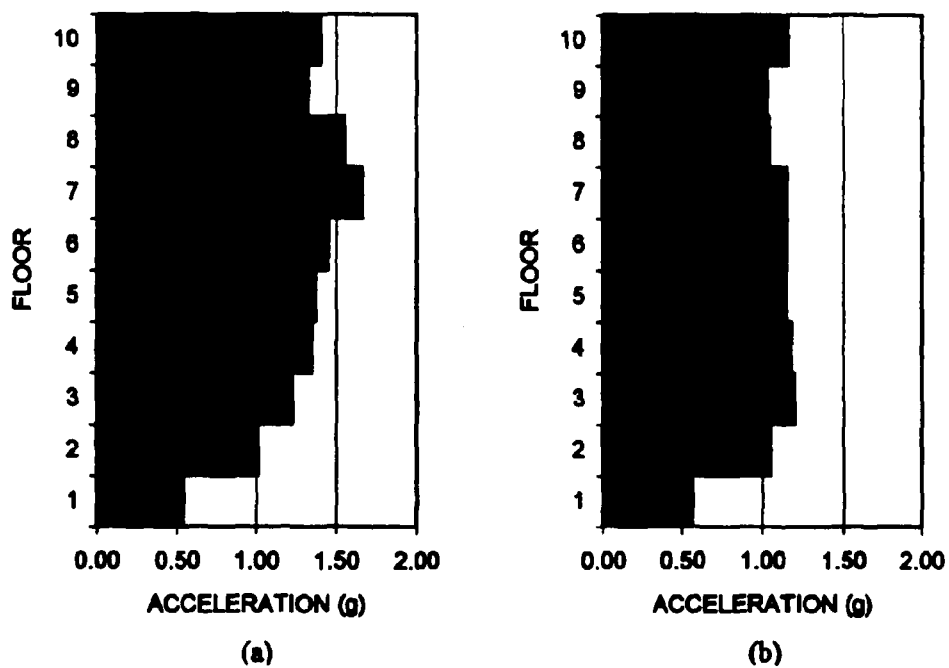


Figure 7.6 Maximum acceleration of the ten-story frame for the 1971 San Fernando earthquake; (a) elastic analysis, (b) inelastic analysis

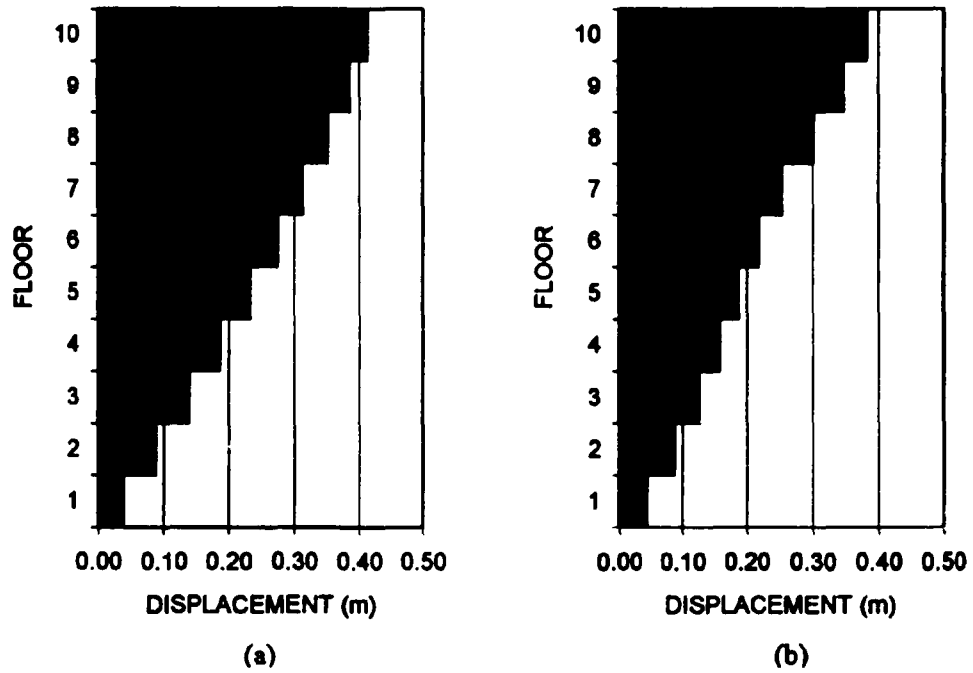


Figure 7.7 Maximum displacement of the ten-story frame for the scaled record of El-Centro earthquake; (a) elastic analysis, (b) inelastic analysis

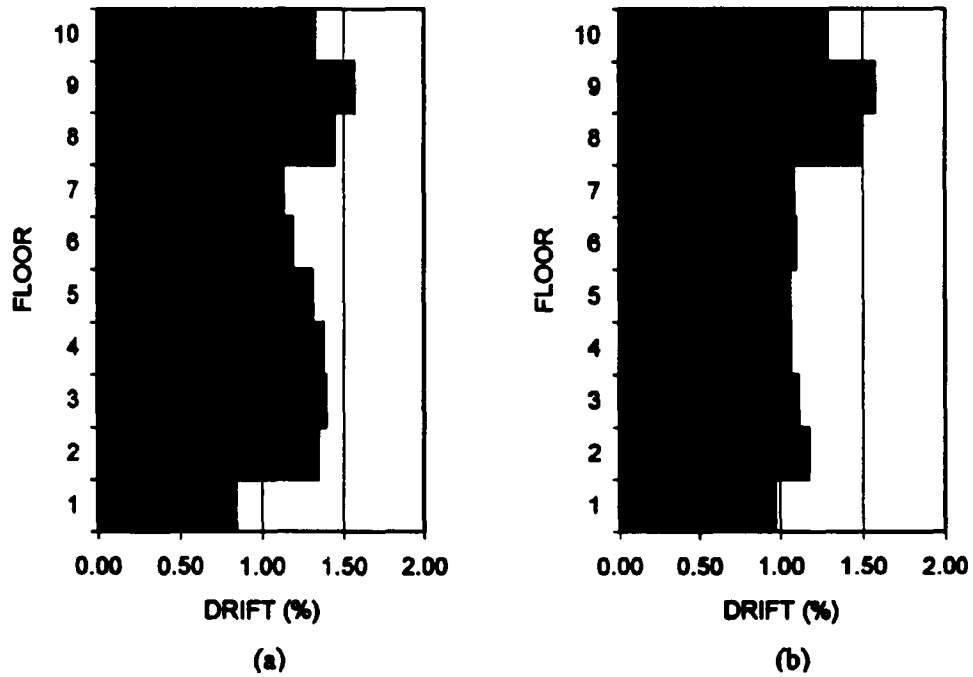


Figure 7.8 Maximum drift of the ten-story frame for the scaled record of El-Centro earthquake; (a) elastic analysis, (b) inelastic analysis

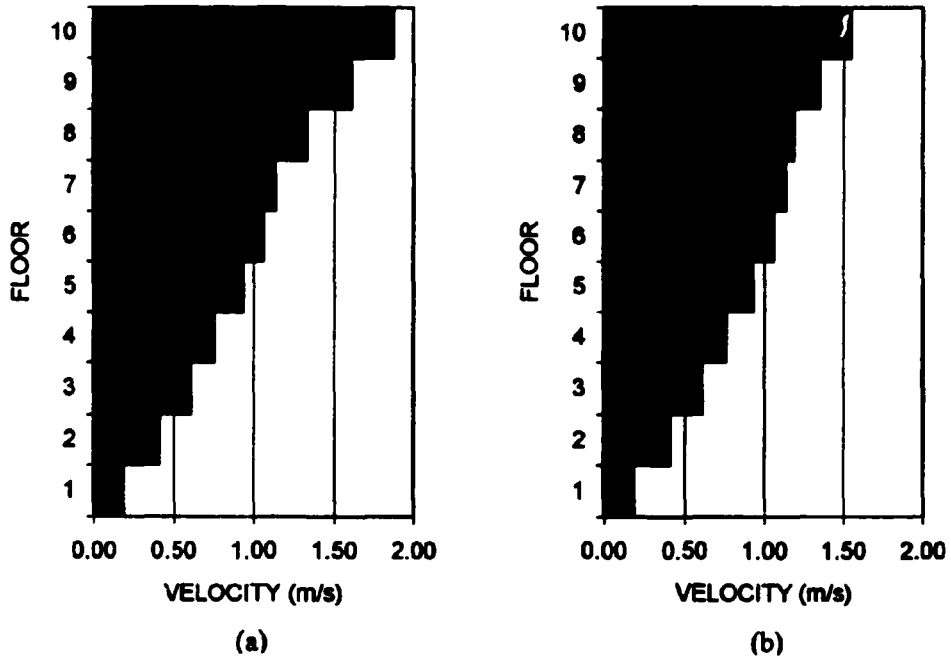


Figure 7.9 Maximum velocity of the ten-story frame for the scaled record of El-Centro earthquake; (a) elastic analysis, (b) inelastic analysis

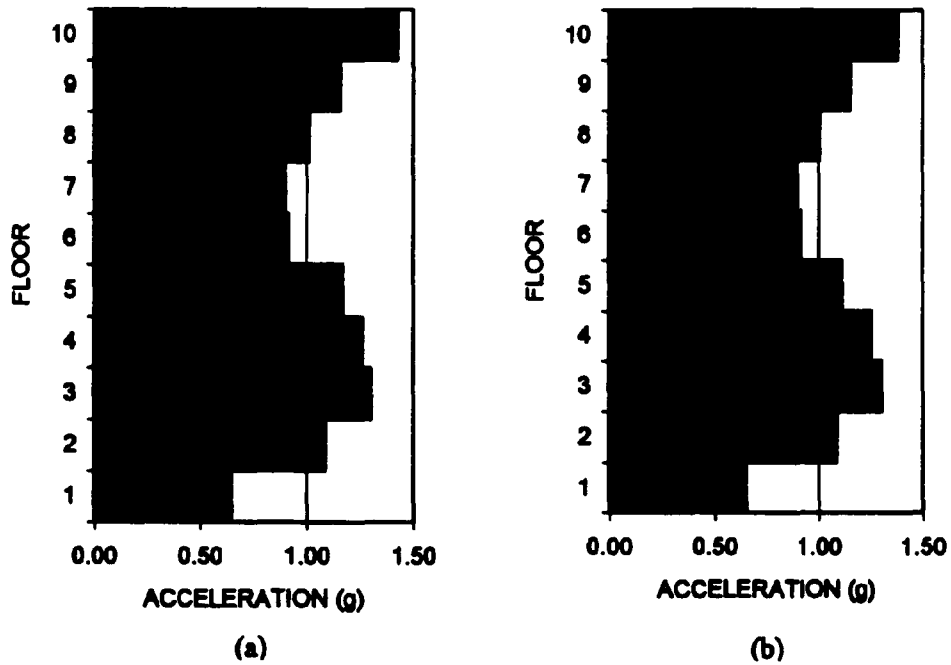


Figure 7.10 Maximum acceleration of the ten-story frame for the scaled record of El-Centro earthquake; (a) elastic analysis, (b) inelastic analysis

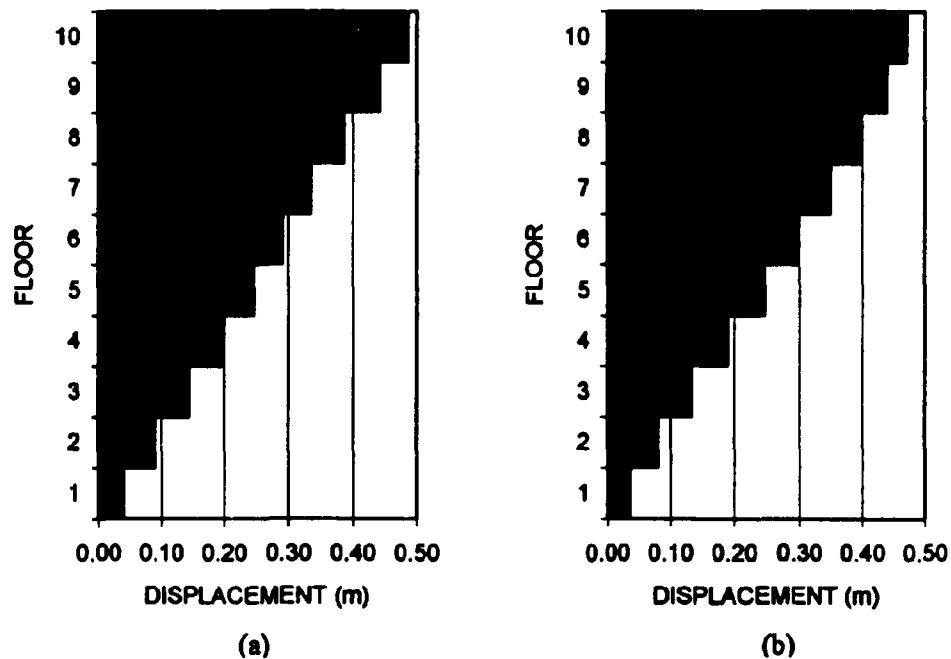


Figure 7.11 Maximum displacement of the ten-story frame for the scaled record of Northridge earthquake; (a) elastic analysis, (b) inelastic analysis

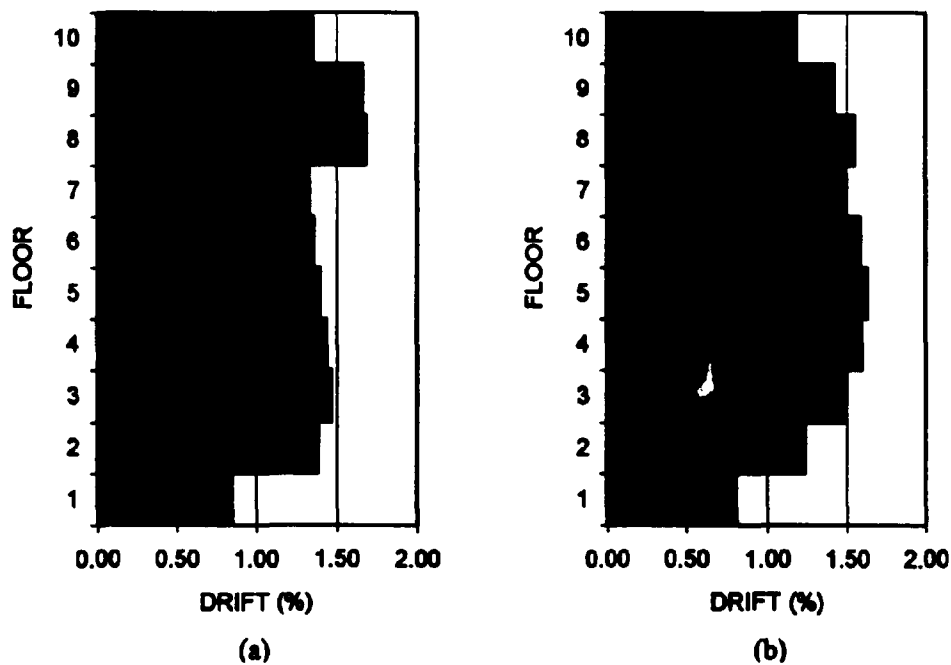


Figure 7.12 Maximum drift of the ten-story frame for the scaled record of Northridge earthquake; (a) elastic analysis, (b) inelastic analysis

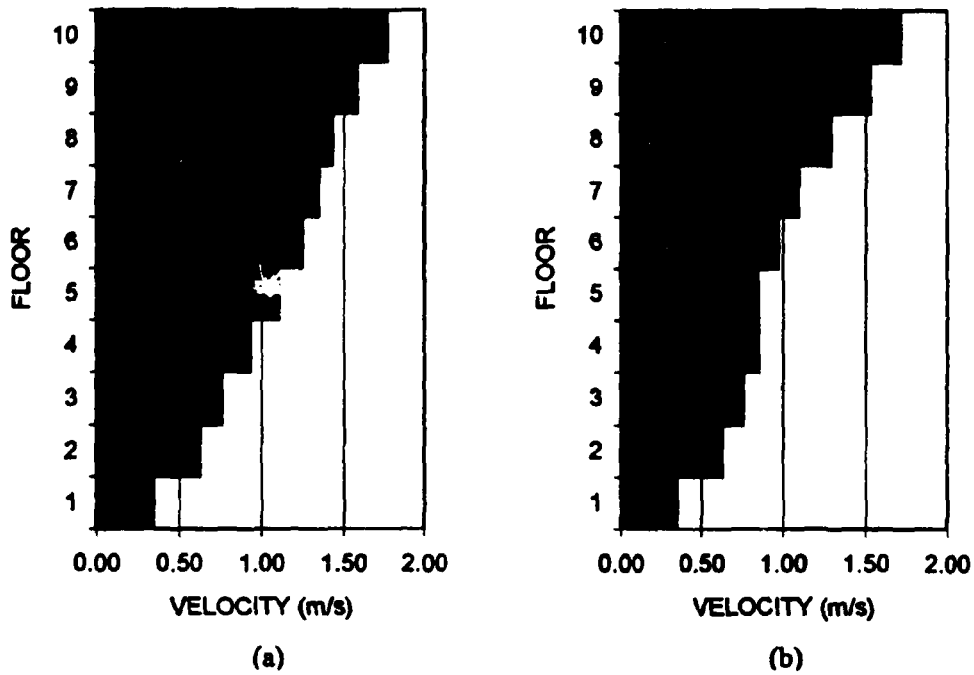


Figure 7.13 Maximum velocity of the ten-story frame for the scaled record of Northridge earthquake; (a) elastic analysis, (b) inelastic analysis

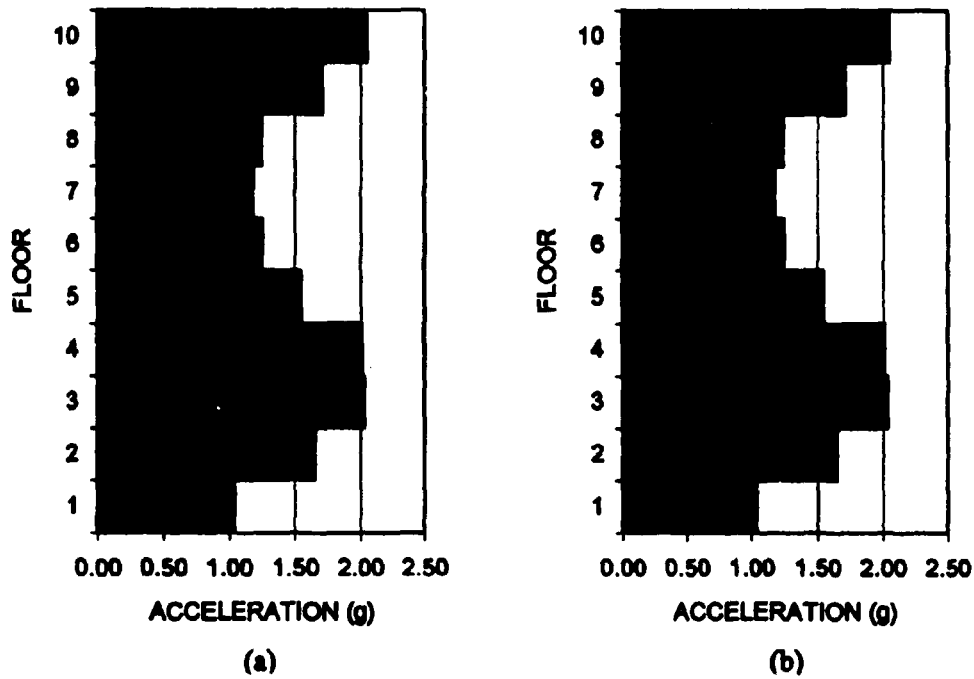


Figure 7.14 Maximum acceleration of the ten-story frame for the scaled record of Northridge earthquake; (a) elastic analysis, (b) inelastic analysis

Figure 7.15 shows the time-history record of the 10th floor displacement obtained from the three excitations shown in Table 7.2 for both elastic and inelastic analyses. It can be observed that after the peak ground acceleration occurs the structure maintains some permanent deformation for the inelastic case. The permanent deformation for each floor of the structure is shown in Figure 7.16. It can be found that the permanent deformation for the structure subjected to the scaled record of the 1994 Northridge earthquake is larger compared to the other two earthquake records.

The energy time-histories of the elastic and inelastic analyses for the structure subjected to the 1971 San Fernando earthquake and the scaled records of the 1940 El-Centro and 1994 Northridge earthquakes are compared as shown in Figures 7.17 - 7.19. It can be observed that the damping energy is reduced when yielding occurs. In the inelastic analysis, the input energy is dissipated by structural damping as well as yielding. In general, the input energy in the elastic analysis is greater than that of the inelastic analysis. This fact can also be observed from the velocity response of the structure shown in Figures 7.5, 7.9, and 7.13.

Active Structures

Two active structures with elastic-plastic behavior are studied in this section. In the first case, the ten-story frame in Table 7.1 equipped with an active bracing system (ABS) on the first and second floors is used. The control force is constrained to a maximum of 20 % of the excitation's effective lateral force. The effective lateral force is determined by multiplying the total mass of the structure by the peak acceleration of the

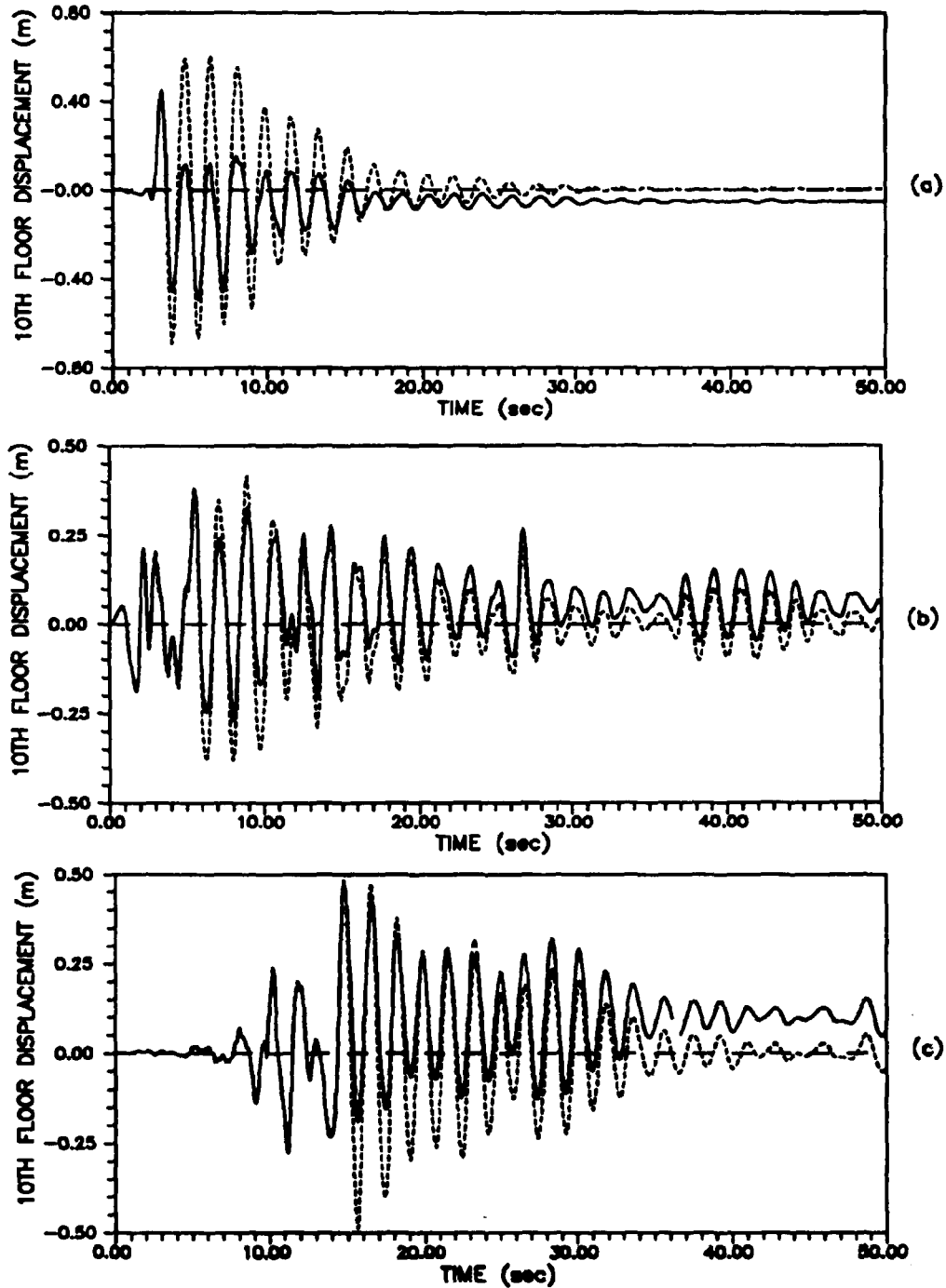
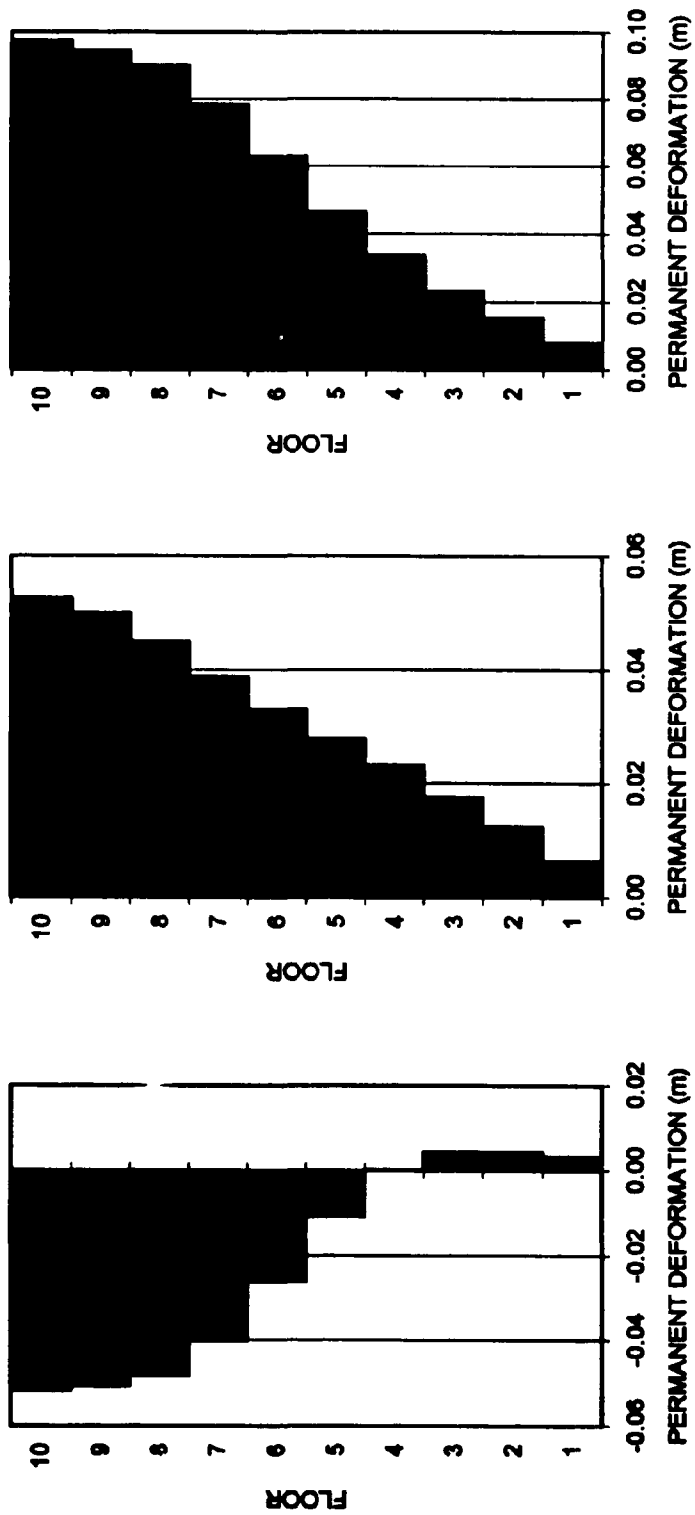


Figure 7.15 Displacement time-history of the 10th floor of the structure: (a) 1971 San Fernando earthquake, (b) scaled record of 1940 El-Centro earthquake, (c) scaled record of 1994 Northridge earthquake; = elastic analysis, — = inelastic analysis



(a) (b) (c)
 Figure 7.16 Permanent deformation of the elastic-plastic structure; (a) the 1971 San Fernando earthquake, (b) the scaled record of the 1940 El-Centro earthquake, (c) the scaled record of the 1994 Northridge earthquake

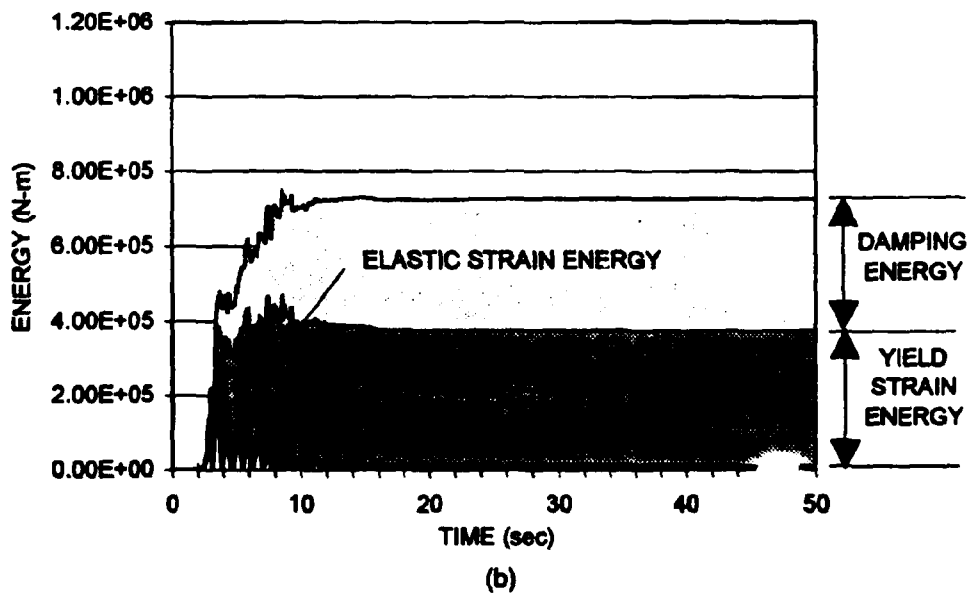
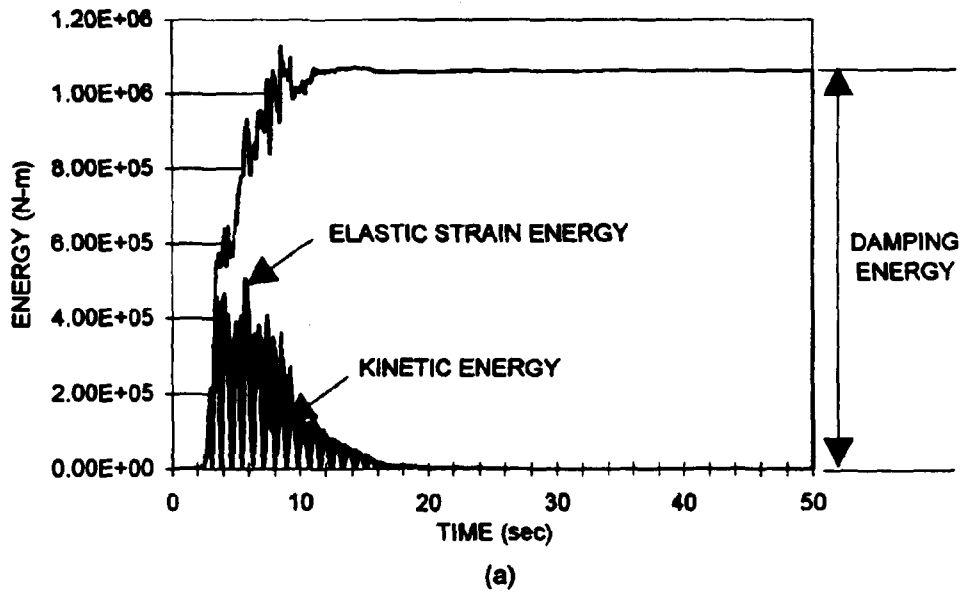
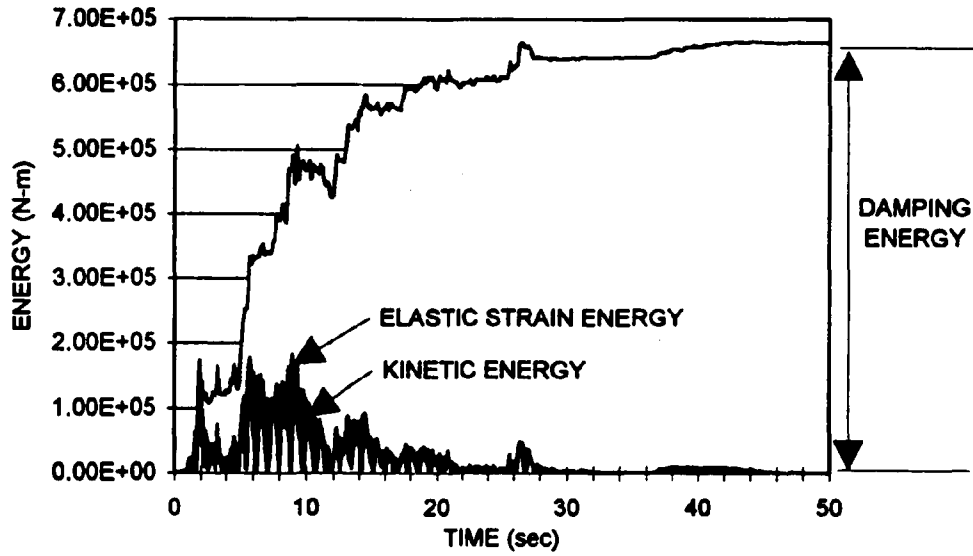
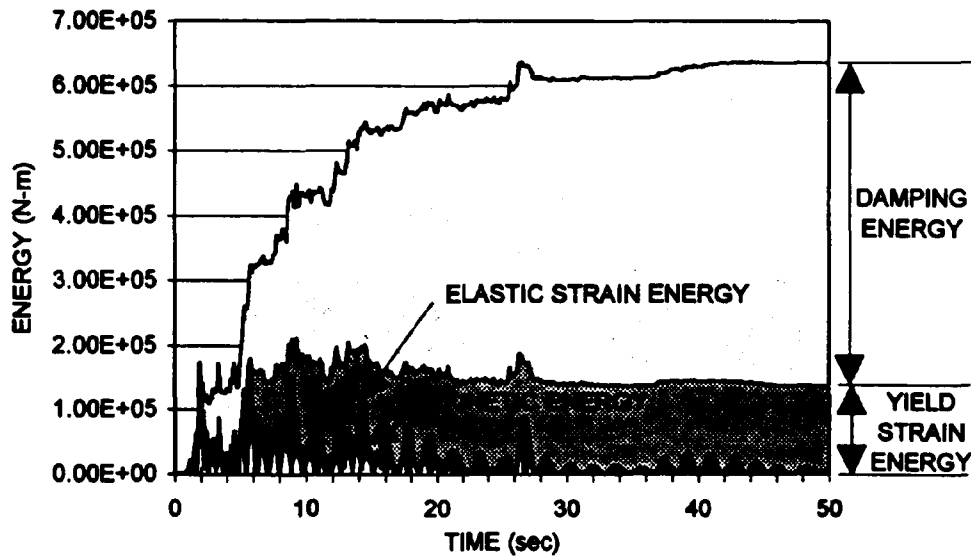


Figure 7.17 Energy time-history for the 1971 San Fernando earthquake: (a) elastic analysis; (b) inelastic analysis

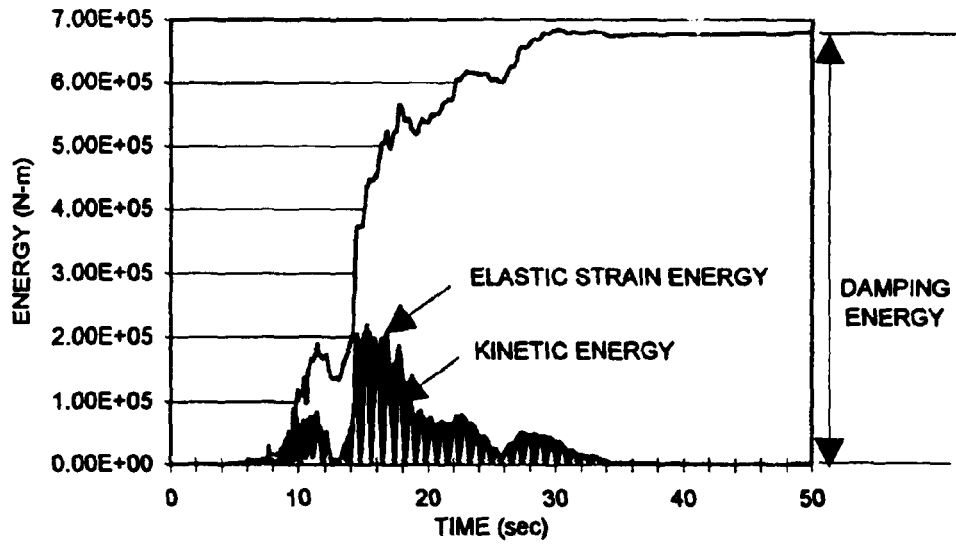


(a)

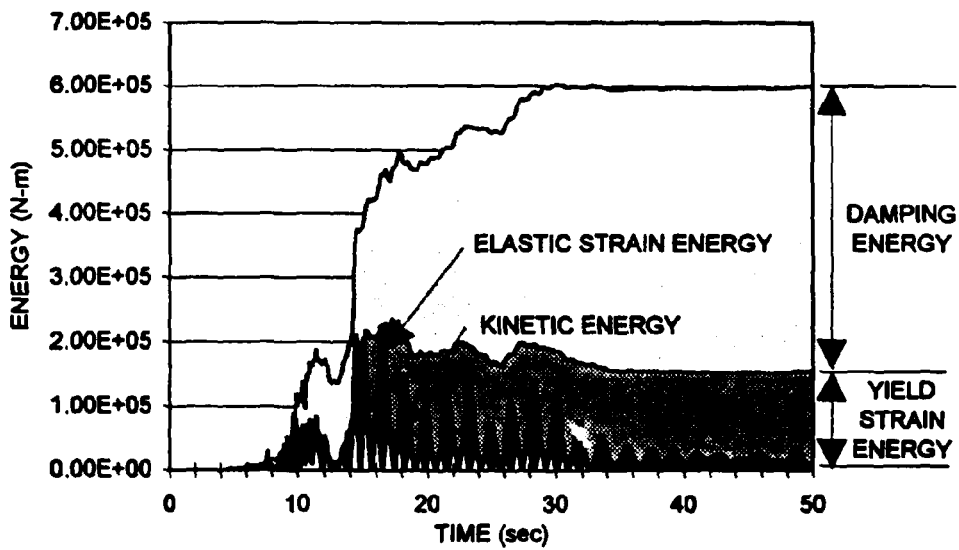


(b)

Figure 7.18 Energy time-history for the scaled record of the 1940 El-Centro earthquake: (a) elastic analysis; (b) inelastic analysis



(a)



(b)

Figure 7.19 Energy time-history for the scaled record of the 1994 Northridge earthquake: (a) elastic analysis; (b) inelastic analysis

excitation. The effective damping level for the first two modes of this active structure equals 10.6 and 16.8 % of critical, respectively. In the second case, the ten-story frame in Table 7.1 is equipped with an ABS on the first, second, third, and fourth floors. The control force is also constrained to a maximum of 20 % of the excitation's effective lateral force. The effective damping level for this active structure equals 20.6 and 27.6 % of critical for the first and second modes, respectively.

The structural response for the cases stated above is compared to the structure without the ABS structural control. The displacement, drift, velocity, and acceleration response reduction obtained for the earthquake records of Table 7.2 is shown in Table 7.3. In general, the structure with four ABS structural controls can reduce the response even more compared to the structure with only two ABS. It can be observed that the displacement response of the structure with two ABS structural controls was on average 9 - 16 % less than that of the structure without control. The displacement response of the structure with four ABS structural controls was reduced about 29 - 35 % on average.

More importantly, the additional structural control system not only reduces the dynamic response of the structure, it also reduces the yield events of the structure. Figure 7.20 shows the number of yield events as a function of time for the three structures stated above in the 1971 San Fernando earthquake. It can be observed that the total yielding

Table 7.3 Average response ratios as compared to the uncontrolled structure with the addition of active bracing systems

Excitation	ABS on the 1st and 2nd floors				ABS on the 1st, 2nd, 3rd, and 4th floors			
	Disp.	Drift	Vel.	Accel.	Disp.	Drift	Vel.	Accel.
San Fernando	0.84	0.88	0.91	0.98	0.71	0.73	0.83	1.00
Scaled El-Centro	0.87	0.79	0.87	0.90	0.72	0.66	0.77	0.84
Scaled Northridge	0.91	0.83	0.85	0.95	0.65	0.62	0.73	0.96

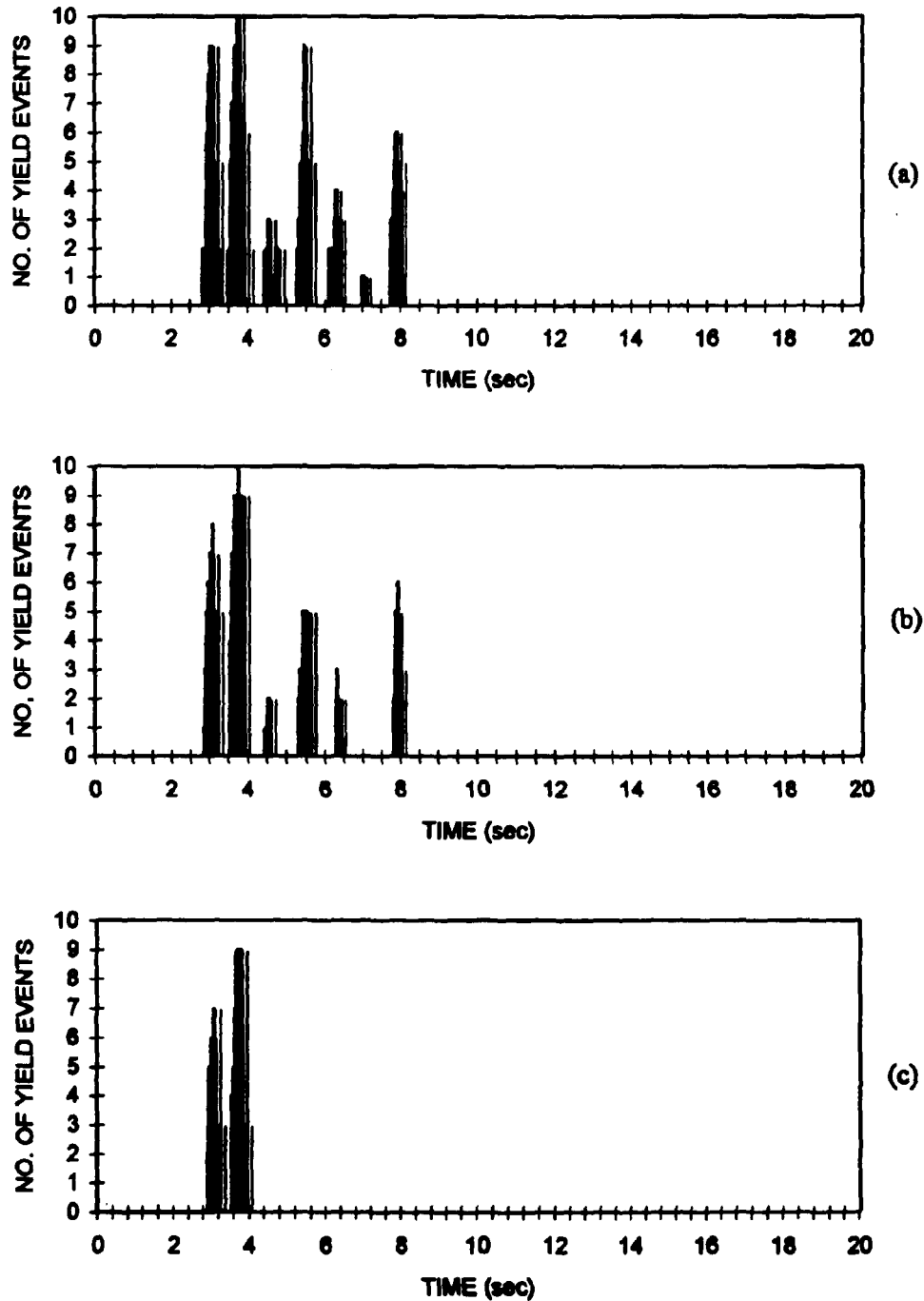


Figure 7.20 Yield events of the inelastic ten-story frame subjected to the actual record of 1971 San Fernando earthquake: (a) no control, (b) structure with two ABS structural controls, (c) structure with four ABS structural controls

events are only two-thirds of those of the no control system for the structure equipped with two ABS, and only one-third for the structure with four ABS. Figures 7.21 and 7.22 show a breakdown of the yield events with respect to the beam and column members of the structure. It should be noted that yielding in the columns occurred only in the columns of the first floor. Similar results can also be observed from the scaled records of the 1940 El-Centro earthquake and the 1994 Northridge earthquake that are shown in Figures 7.23 - 7.28. The total yielding events for the three cases are shown in Table 7.4. It can be seen that total yield events for the active structure with two ABS are reduced to one half compared to the conventional structure. The yield events for the active structure with four ABS are much less than those of the conventional structure.

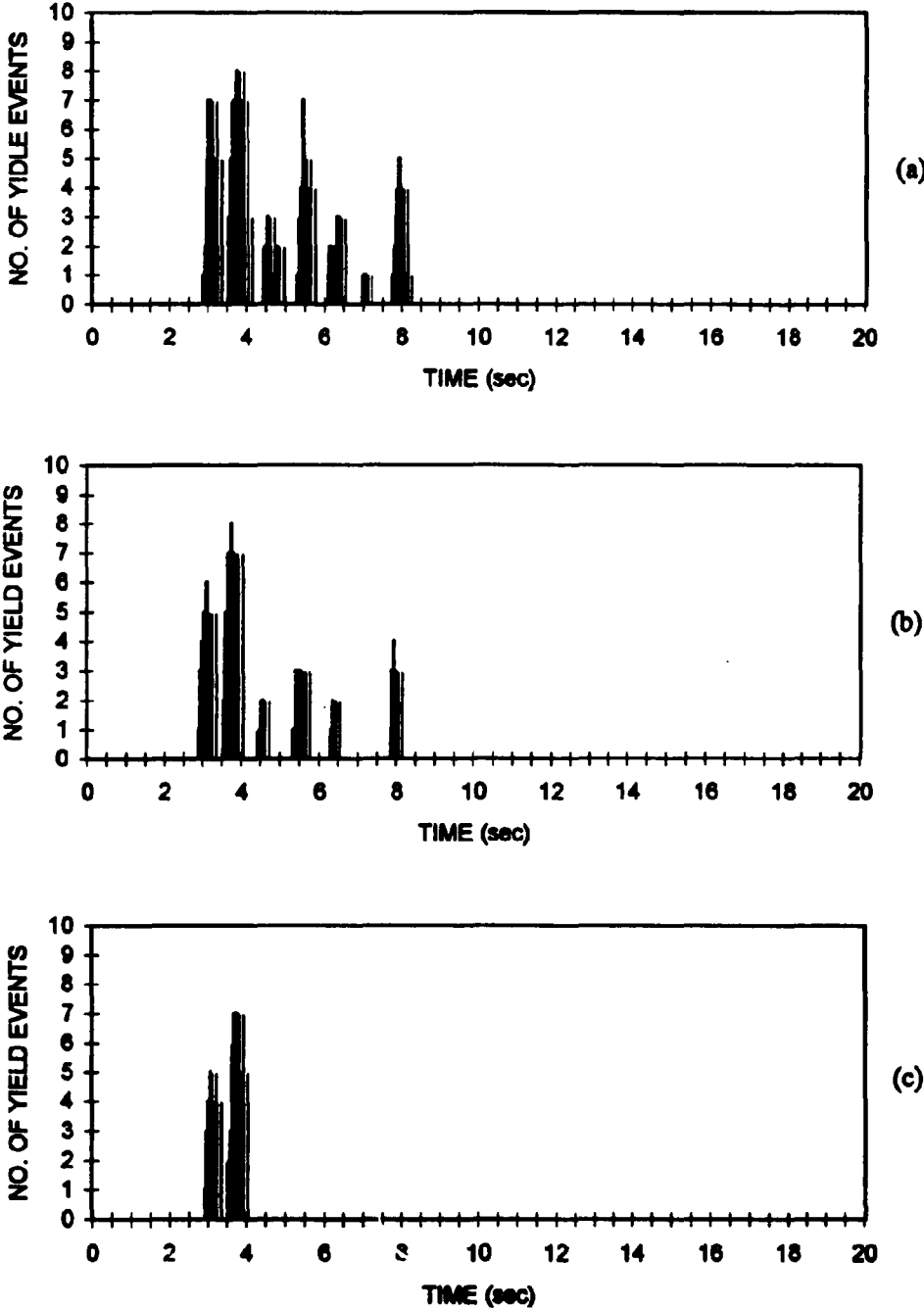


Figure 7.21 Yield events occurring in the beam members of the inelastic ten-story frame subjected to the actual record of 1971 San Fernando earthquake: (a) no control, (b) structure with two ABS structural controls, (c) structure with four ABS structural controls

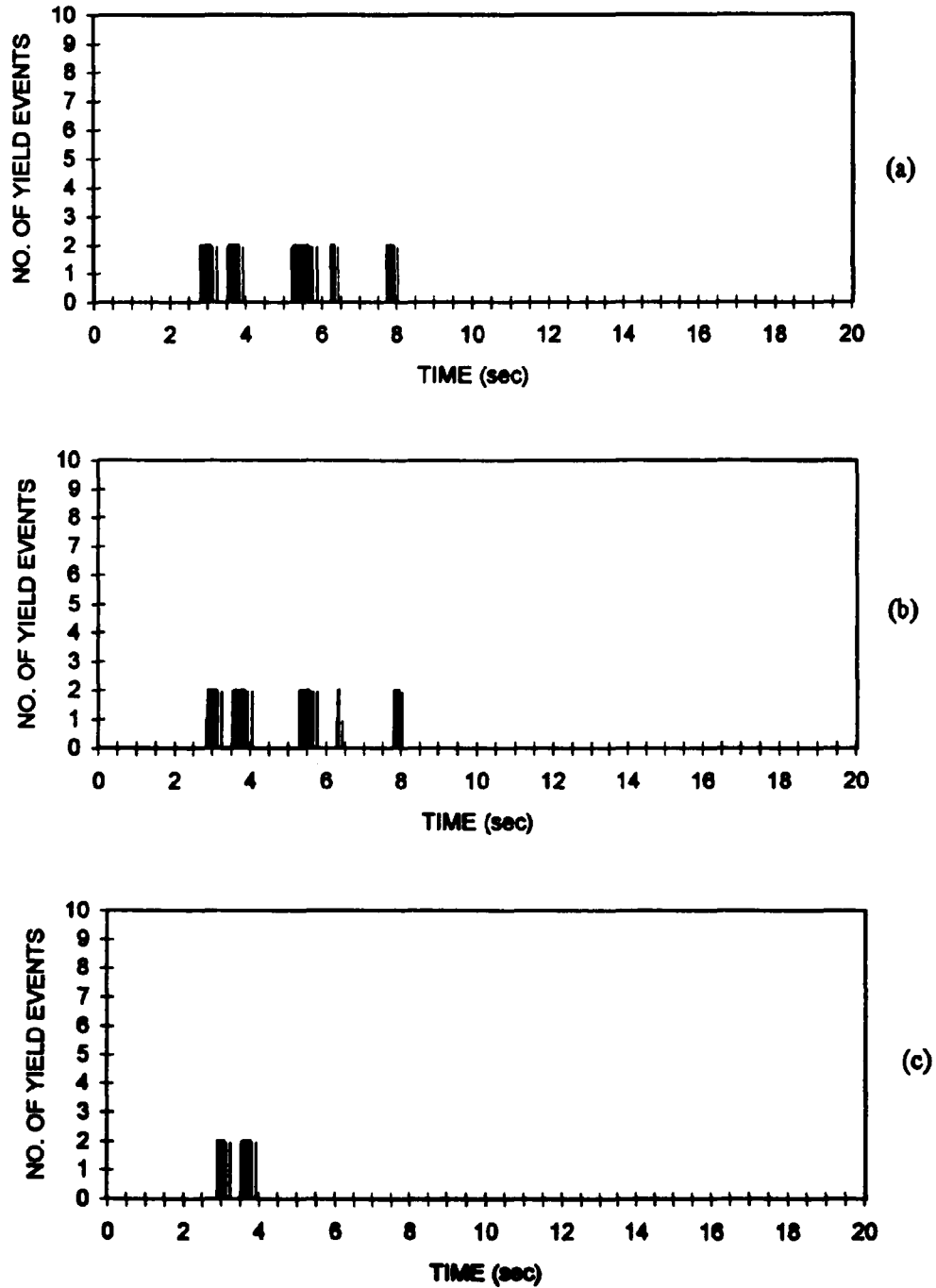


Figure 7.22 Yield events occurring in the column members of the inelastic ten-story frame subjected to the actual record of 1971 San Fernando earthquake: (a) no control, (b) structure with two ABS structural controls, (c) structure with four ABS structural controls

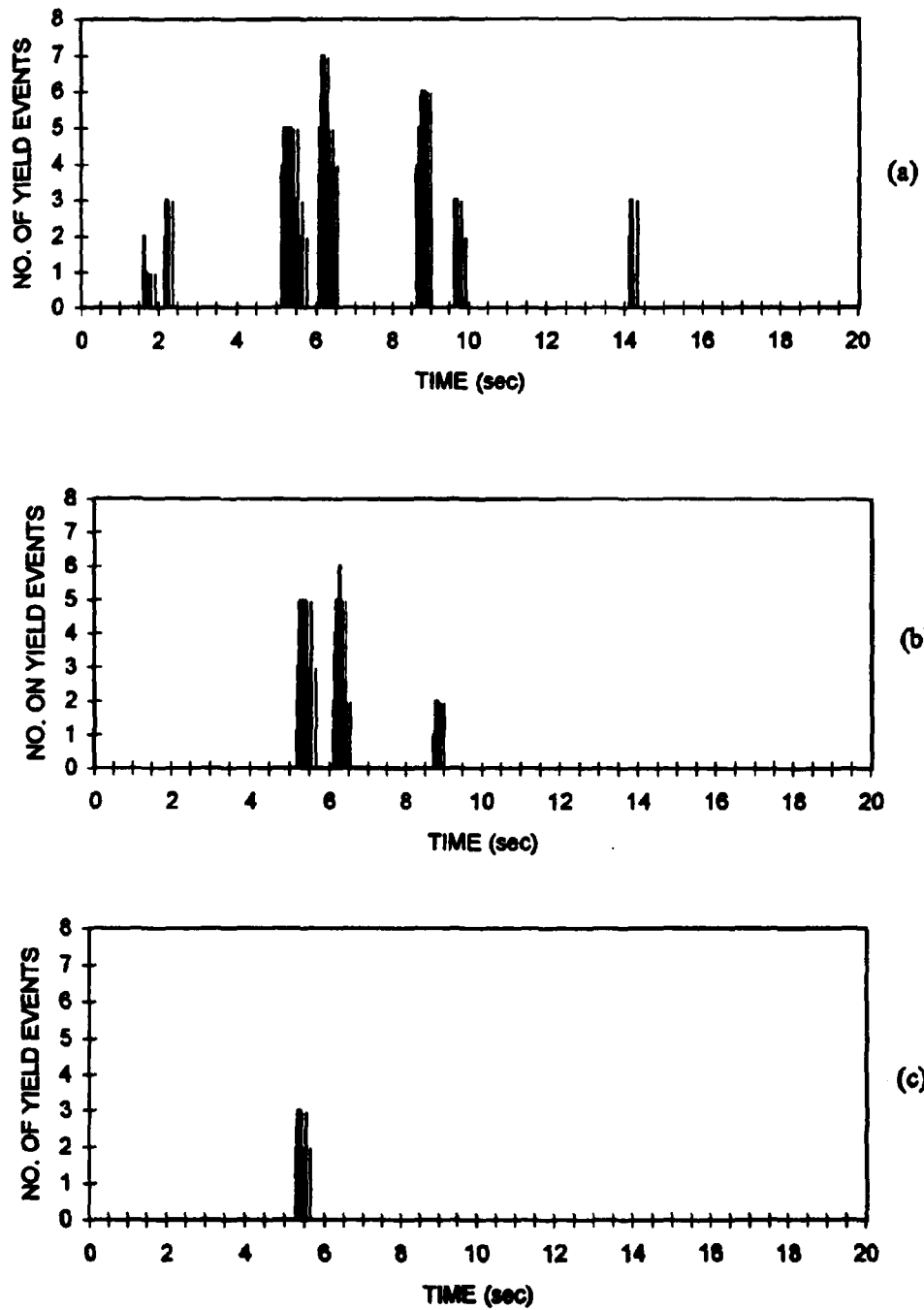


Figure 7.23 Yield events of the inelastic ten-story frame subjected to the scaled record of 1940 El-Centro earthquake: (a) no control, (b) structure with two ABS structural controls, (c) structure with four ABS structural controls

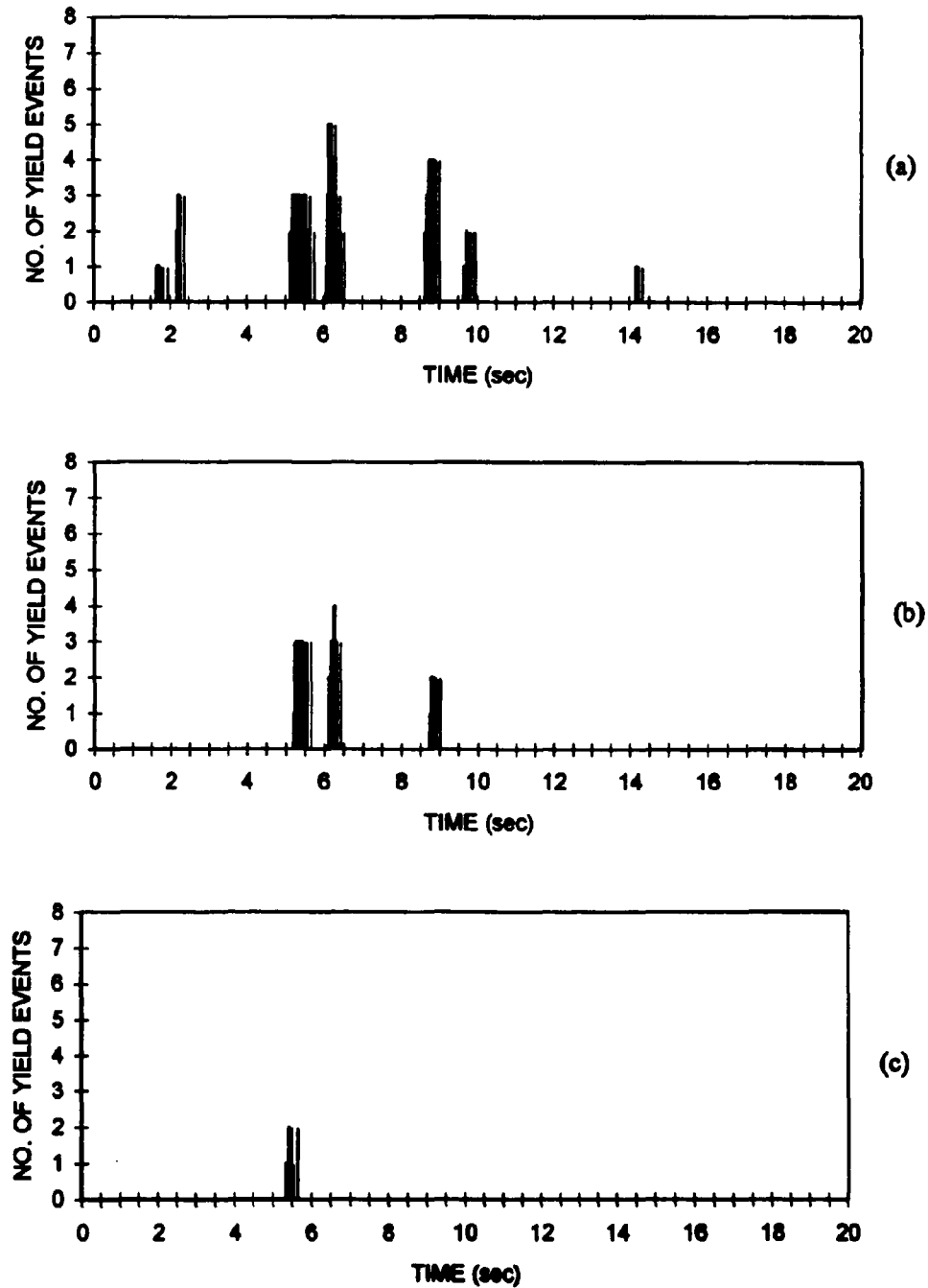


Figure 7.24 Yield events occurring in the beam members of the inelastic ten-story frame subjected to the scaled record of 1940 El-Centro earthquake: (a) no control, (b) structure with two ABS structural controls, (c) structure with four ABS structural controls

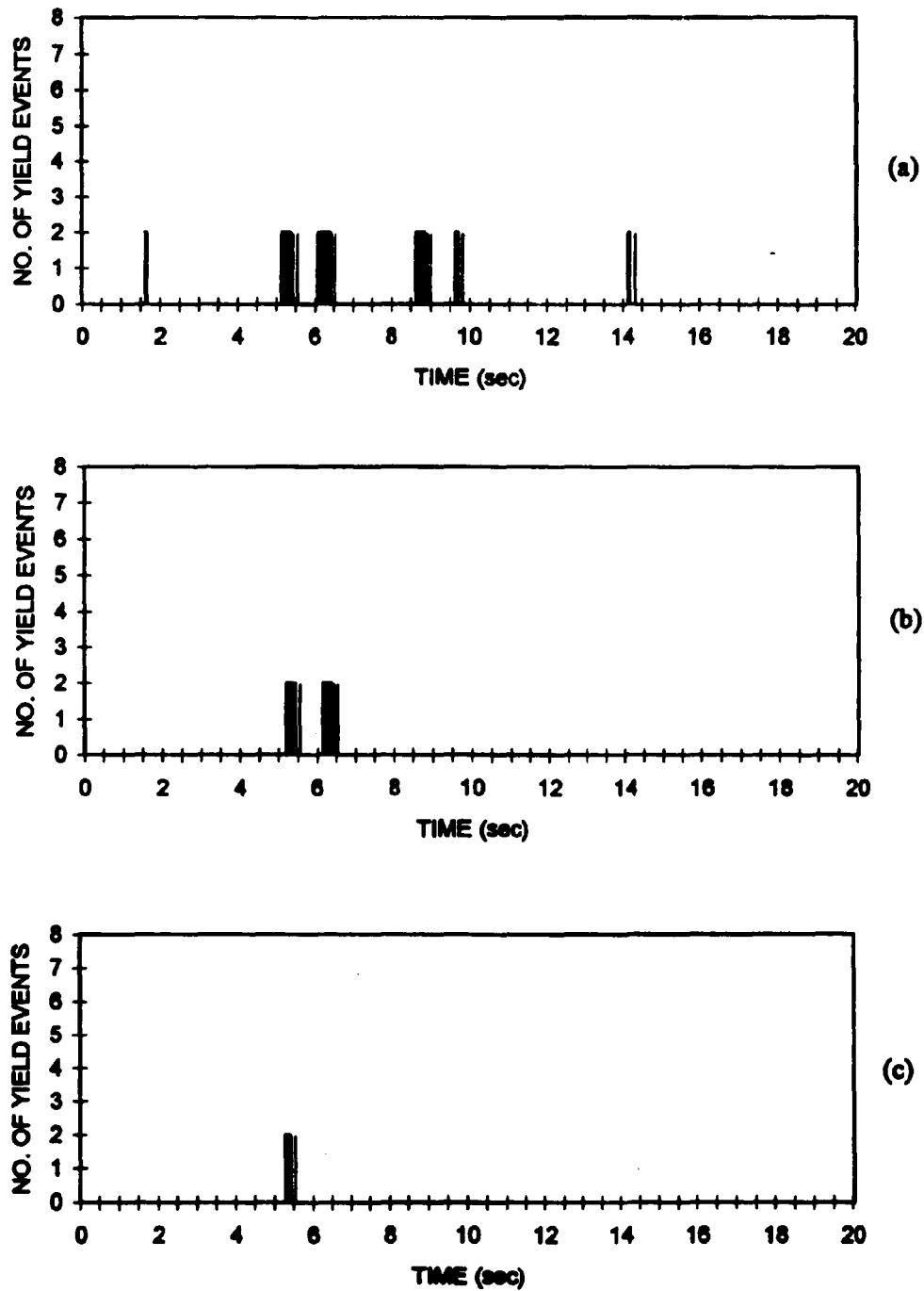


Figure 7.25 Yield events occurring in the column members of the inelastic ten-story frame subjected to the scaled record of 1940 El-Centro earthquake: (a) no control, (b) structure with two ABS structural controls, (c) structure with four ABS structural controls

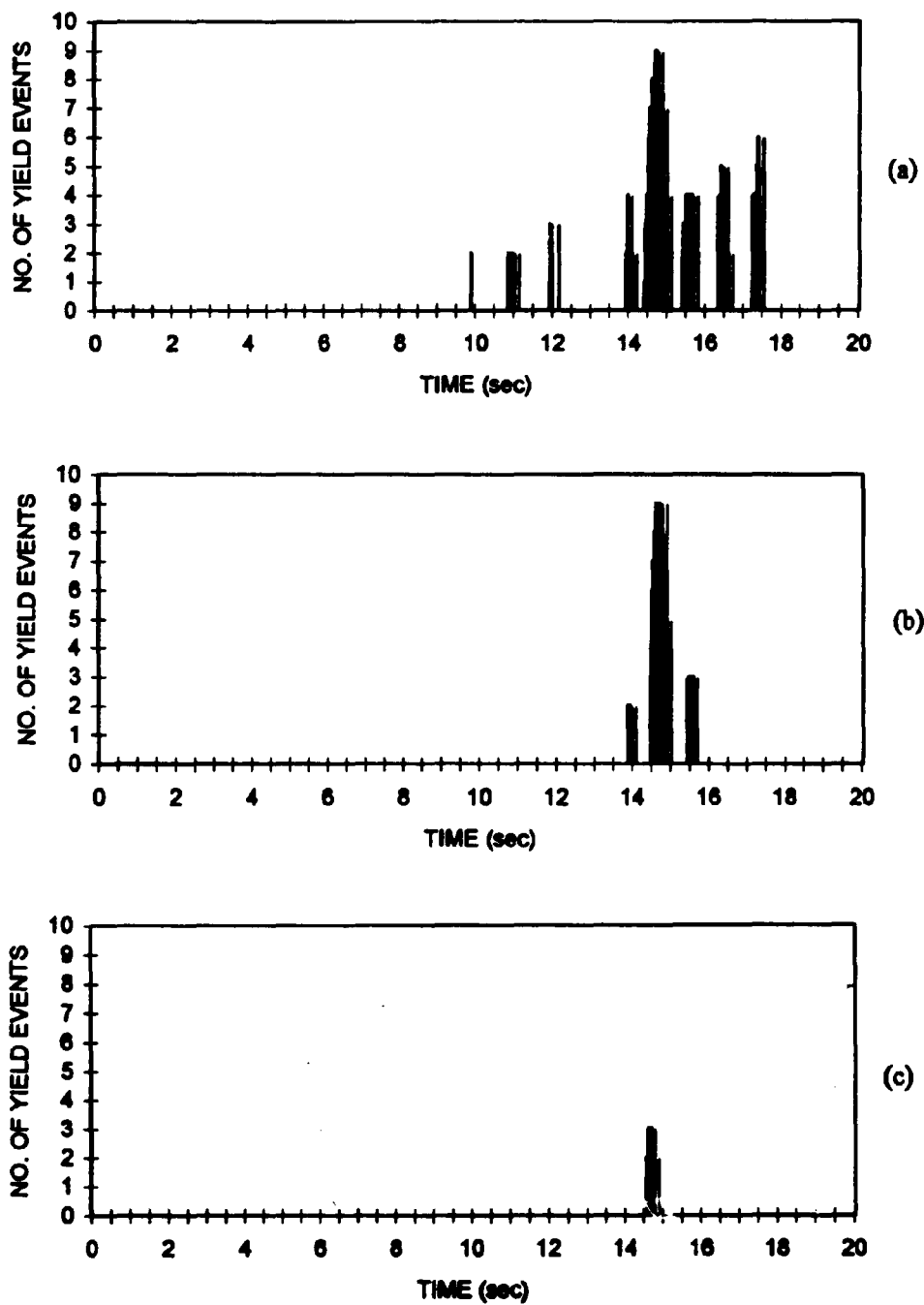


Figure 7.26 Yield events of the inelastic ten-story frame subjected to the scaled record of 1994 Northridge earthquake: (a) no control, (b) structure with two ABS structural controls, (c) structure with four ABS structural controls

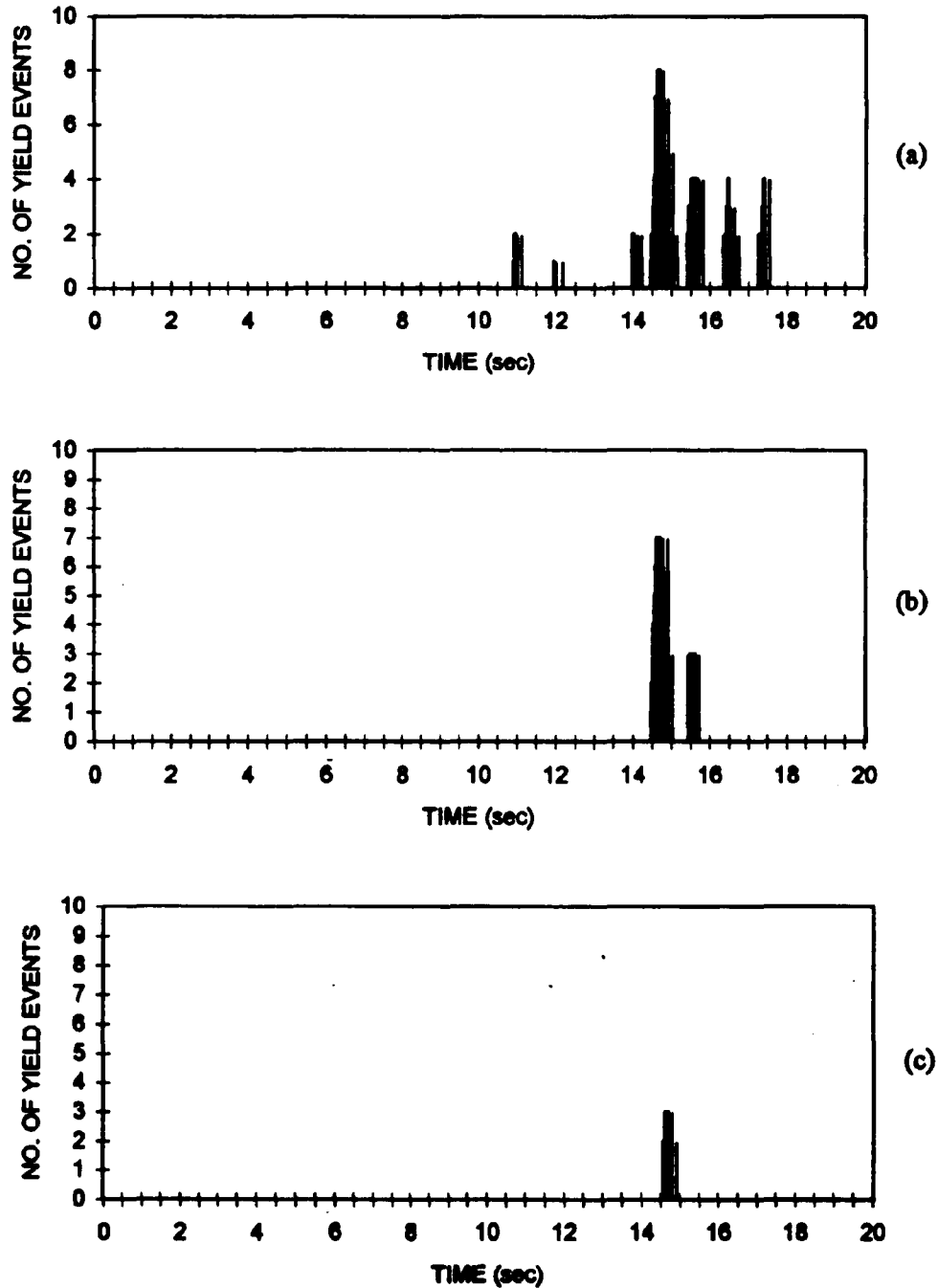


Figure 7.27 Yield events occurring in the beam members of the the inelastic ten-story frame subjected to the scaled record of 1994 Northridge earthquake: (a) no control, (b) structure with two ABS structural controls, (c) structure with four ABS structural controls

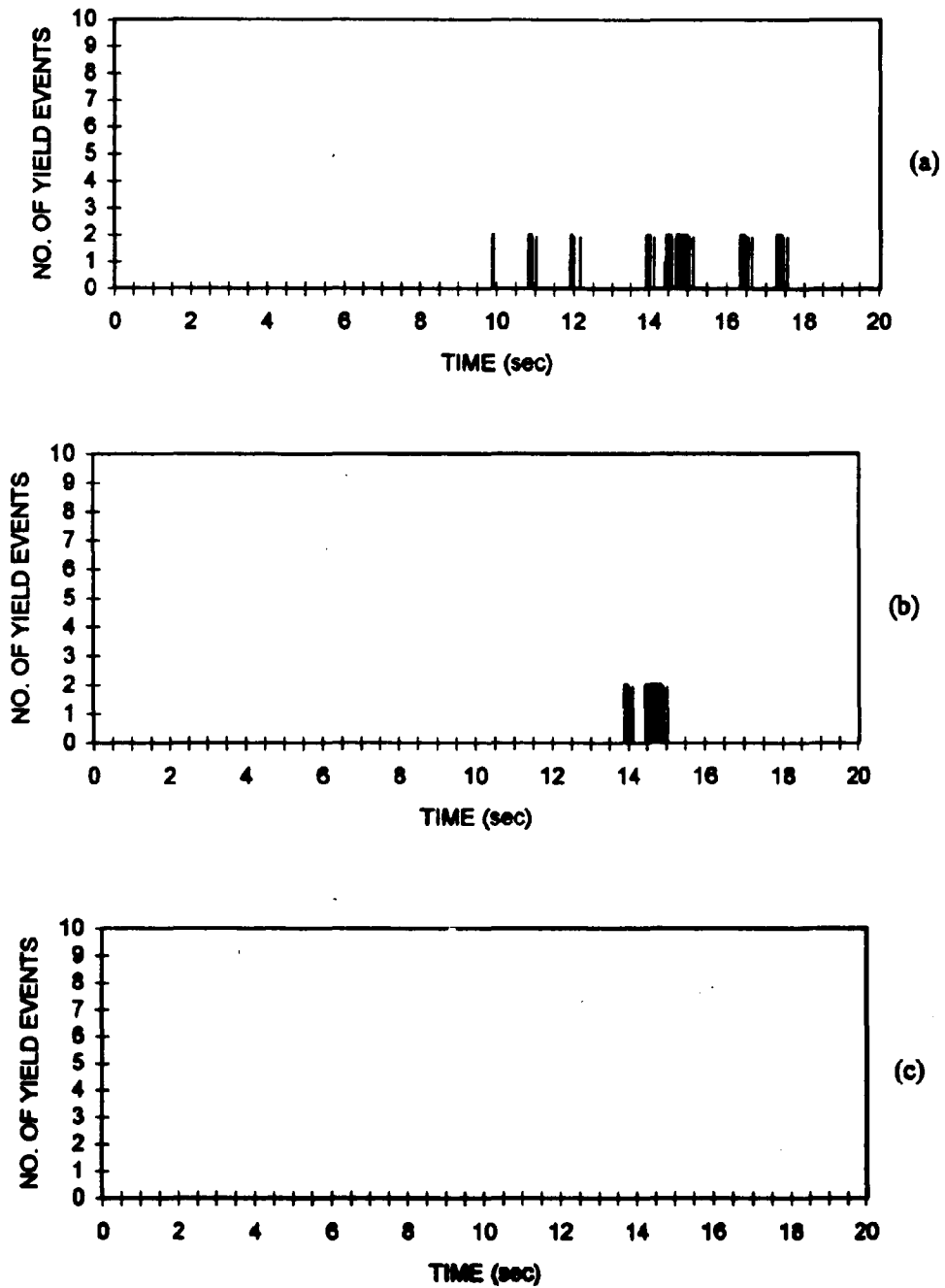


Figure 7.28 Yield events occurring in the column members of the the inelastic ten-story frame subjected to the scaled record of 1994 Northridge earthquake: (a) no control, (b) structure with two ABS structural controls, (c) structure with four ABS structural controls

Table 7.4 Yielding events of the inelastic structure equipped with a certain number of active bracing systems

Excitation	w/o control			2 ABS			4 ABS		
	Total	Beam	Column	Total	Beam	Column	Total	Beam	Column
San Fernando	451	341	110	324	230	94	159	117	42
Scaled El-Centro	259	167	92	117	73	44	16	6	10
Scaled Northridge	330	241	89	176	126	50	21	21	0

CHAPTER 8

CONCLUSIONS

The performance of viscoelastic (VE) dampers and active bracing systems (ABS) when they are used for structural control was studied. A structural frequency dependent property of the VE damper is employed to obtain the effective damping ratio introduced in a structure equipped with VE dampers. An optimization method is developed to design the minimum size of VE dampers for achieving an expected effective damping ratio of the structure. A performance index using drift as the criterion, and another using velocity and acceleration feedback are proposed for the ABS structural control. These algorithms were found to reduce floor accelerations better than the instantaneous optimal control algorithm, but require higher levels of control force. A method based on the Lyapunov function for obtaining the weighting matrix of an ABS structural control is introduced that reduces the required control force for certain control algorithms.

Structural displacements can be reduced to a desired level by using different arrangements of VE dampers and ABS structural controls having the same effective damping ratio. For the same response reduction, the addition of a VE damper to a structure equipped with an ABS structural control reduces the required control force and

damper is improved in the presence of the ABS structural control. The elastic strain and kinetic energy of a seismic structure is decreased by using the ABS-VE hybrid structural control system.

An energy-bound convex model is used for estimating the maximum response of a structural system subjected to dynamic loads. The estimated structural response using the energy-bound convex models is rather conservative when compared to the time-history of the response using the actual earthquake record. The energy-bound convex model results are slightly improved as the damping level of the structure is increased. A reduction factor is defined for a structure subjected to a specific earthquake record and is a function of the structure's natural periods and modal damping ratios (global energy-bound convex model adjusted with an excitation-specific reduction factor, RGEB convex model).

The results are extended for finding the maximum response of a structure to an unknown excitation but known energy-bound. An average reduction factor is defined by taking the average of the reduction factors at the modal level from a set of earthquake records. Numerical simulations show that the response obtained by the global energy-bound convex model adjusted by the average reduction factor (ARGEB convex model) is not as close to the actual response as that obtained by the excitation-specific RGEB convex model. However, the ARGEB convex model still yields an acceptable prediction of the maximum response for unknown earthquakes of a given global energy-bound. The reduction factor remains constant for different levels of the energy-bound.

It has been found that the average reduction factor is sensitive to the location of

the records that defines the subset from which the factor was determined. In addition, it was found that the average reduction factor for records in the same general location is not sensitive to time. Thus, for a certain location if sufficient records of previous earthquakes are available, regardless of the chronology of the event, the average reduction factor can be determined with some confidence. An alternative procedure is to determine the average reduction factor from site-specific spectra whenever they are available.

A modified iterated simulated annealing (MISA) method with sensitivity analysis and automatic reduction of the search range is presented for the structural optimization process. The method is based on simulated annealing which is an algorithm that has the ability to find the global optimum. First-order sensitivity analysis is used to identify which design variables need to be modified in order to decrease a certain constraint in the most economical way. Even though the actual values of the new design variables are determined randomly, the knowledge of which design variables to modify avoids the expense of multiple trials and improves the efficiency of the present method considerably. The automatic reduction of the search range helps reduce the extent of the search for the new design variables. As a result, the computational effort for successive iterations is greatly reduced.

The MISA method was found to be advantageous for optimization of structural systems with dynamic constraints, as compared to classical optimal design methods. For dynamically constrained problems, where the feasible region is usually disjoint, the MISA method has the advantage of converging in the proximity of the global minimum even when infeasible initial designs are used, and for practically any choice of the initial values

of the design variables. In addition, the method proceeds to the global minimum even when intermediate design iterations are worse than previous iterations, since design iterations use random sequences of candidate designs. By contrast, some of the classical optimization methods may converge to local optimal points or not even reach these local optimal points because of the disjoint nature of the feasible region.

The optimal design of conventional as well as active structures using the energy-bound convex models yields static member sizes that are different from those obtained using a historic actual earthquake record. The minimum volume required for conventional or active structures designed by the average reduction factor convex model (ARGEB) is approximately 50 % larger than the volume required by the optimal structure designed for a single historic earthquake record. One advantage of using convex models to perform the structural optimization is that they represent a more general excitation than a single historic earthquake. Thus, the structures designed using the ARGEb convex model respond well for other excitations, which might occur in the future, and having the same global energy-bound; by contrast, structures designed for a specific historic earthquake record do not respond as well for other possible future earthquakes. This is true for either conventional or active structures. Another advantage of using convex models is that the computational effort required for the optimization, when using the energy-bound convex models, is much less than that required when using actual historic earthquake records. That is the case since the constraints are transformed from dynamic to static ones.

For a certain number of VE dampers or a limited control force of the ABS structural control, the optimal design of the active structure yields a minimum volume on

average twenty percent less than the optimal volume of the conventional structure for different levels of inherent structural damping. The constraints for joint displacements and member stresses are kept the same for either the optimal conventional or active structures. In this respect, active structures are seen to be more efficient by combining the conventional static members with the active members.

Finally, inelastic analysis based on a bilinear elastic-plastic model is used to investigate the behavior of conventional as well as active structures. In general, the maximum responses obtained from the elastic analysis were more conservative than those obtained from the inelastic analysis if significant yielding events had occurred. However, the permanent deformations can only be determined from the inelastic analysis. The inelastic behavior of the structure can also be observed from the reduced structural damping and input energy requirements which are offset by external damping as well as yielding in the inelastic analysis. The active structure with the additional structural control system can reduce the response compared to the conventional structure. More importantly, it also reduces the yield events experienced by the structure.

APPENDIX A

ACTIVE CONTROL ALGORITHMS

Research in the area of active control of civil structures subjected to dynamic loads has been focused on the development of a number of certain control algorithms based on different performance indexes. Discussion in this appendix is focused on some basic results of modern control theory as they relate to the results presented in Chapter 2.

Linear Quadratic Regulator (LQR) Method

In classical linear optimal control the control vector, $u(t)$, is chosen by defining the performance index, J , as (Soong, 1990)

$$J = J_1[z(t_0), z(t_f), t_0, t_f] + \int_{t_0}^{t_f} J_2(z, \dot{z}, u, \dot{u}, t) dt \quad (\text{A.1})$$

The first term, J_1 , is the initial stage which is used to evaluate the index at the initial and final times of the control interval $[t_0, t_f]$. The second term, J_2 , is an integral evaluation over the control period. $z(t)$ and $u(t)$ are the state vector and the control force vector as shown in equation (2.8).

The performance index chosen for the study of the structural control problem is quadratic in vectors, $z(t)$ and $u(t)$. Setting the initial time equal to zero, the performance index can be represented as in equation (2.7). To find the optimal results one minimizes the index of equation (2.7) subject to the constraint of equation (2.8a). The Lagrangian L is formed by adjoining these two equations with a time-varying Lagrange multiplier, $\lambda(t)$. This can be expressed as (Soong, 1990)

$$L = \int_0^{t_f} \left\{ z^T(t)Qz(t) + u^T(t)Ru(t) + \lambda^T(t)[Az(t) + Bu(t) + HF(t) - \dot{z}(t)] \right\} dt \quad (\text{A.2})$$

Let

$$\mathcal{H}(z, u, \lambda, t) = z^T(t)Qz(t) + u^T(t)Ru(t) + \lambda^T(t)[Az(t) + Bu(t) + HF(t)] \quad (\text{A.3})$$

Therefore, the Lagrangian can be simplified as

$$L = \int_0^{t_f} \left[\mathcal{H}(z, u, \lambda, t) + \dot{\lambda}^T(t)z(t) \right] dt - \lambda^T(t)z(t) \Big|_0^{t_f} \quad (\text{A.4})$$

The necessary condition for the optimal control can be obtained by finding the first variation of the Lagrangian with respect to the control variables and setting it to zero.

The first variation of equation (A.4) can be obtained as

$$\delta L = \int_0^{t_f} \left[\frac{\partial \mathcal{H}}{\partial u} \delta u + \left(\frac{\partial \mathcal{H}}{\partial z} + \dot{\lambda}^T \right) \delta z \right] dt \quad (\text{A.5})$$

By requiring $\delta L = 0$, one obtains

$$\frac{\partial \mathcal{H}}{\partial u} = 0, \quad \text{when } 0 \leq t \leq t_f \quad (\text{A.6a})$$

$$\dot{\lambda}^T + \frac{\partial \mathcal{H}}{\partial z} = 0 \quad (\text{A.6b})$$

and the boundary condition

$$\lambda^T(t_f) = 0 \quad (\text{A.6c})$$

Substituting equation (A.3) into equations (A.6a) and (A.6b), one can obtain

$$u(t) = -\frac{1}{2} R^{-1} B^T \lambda \quad (\text{A.7a})$$

$$\dot{\lambda} = -A^T \lambda(t) - 2Qz(t) \quad (\text{A.7b})$$

Considering a closed-loop control, the control vector is regulated by the state vector which is expressed as (Sage and White, 1977)

$$\lambda(t) = P(t)z(t) \quad (\text{A.8})$$

Substituting equation (A.8) into equation (A.7), one can obtain

$$u(t) = -\frac{1}{2} R^{-1} B^T P(t)z(t) = G(t)z(t) \quad (\text{A.9a})$$

$$P(t)\dot{z}(t) = -\dot{P}(t)z(t) - A^T P(t)z(t) - 2Qz(t) \quad (\text{A.9b})$$

The control vector $u(t)$ is linear in $z(t)$, and the matrix $G(t) = -\frac{1}{2} R^{-1} B^T P(t)$ is the control gain. Recalling equation (2.8) and pre-multiplying it by matrix $P(t)$

$$P(t)\dot{z}(t) = P(t)Az(t) + P(t)Bu(t) + P(t)HF(t) \quad (\text{A.10})$$

Therefore, the unknown matrix $P(t)$ can be determined by substituting equation (A.9) into (A.10). In addition, the boundary condition of equation (A.6c) can be obtained from equation (A.8). The expression for finding $P(t)$ is obtained as

$$\begin{aligned} & \left[\dot{P}(t) + P(t)A + A^T P(t) + 2Q - \frac{1}{2} P(t)BR^{-1}B^T P(t) \right] z(t) + P(t)HF(t) = 0 \\ & P(t_r) = 0 \end{aligned} \quad (\text{A.11})$$

When $F(t) = 0$, equation (A.11) reduces to

$$\dot{P}(t) + P(t)A + A^T P(t) + 2Q - \frac{1}{2} P(t)BR^{-1}B^T P(t) = 0, \quad P(t_r) = 0 \quad (\text{A.12})$$

Equation (A.12) is called the matrix Riccati equation in optimal control theory, and $P(t)$ is the Riccati matrix. Usually, the Riccati matrix, $P(t)$, does not yield an optimal solution unless the excitation force $F(t)$ is zero within the control period $[0, t_r]$ (Sage and White, 1977). In the applications of structural control to civil structures, numerical computations have shown that the Riccati matrix remains constant over the control period and drops to zero rapidly at the end of the interval. Therefore, in most of the cases $P(t)$ can be approximated by a constant matrix P . Equation (A.12) can be simplified as

$$PA + A^T P + 2Q - \frac{1}{2} PBR^{-1}B^T P = 0 \quad (\text{A.13})$$

and the control gain $G(t)$ is also a constant matrix expressed from equation (A.9a) as

$$G(t) = -\frac{1}{2} R^{-1} B^T P \quad (\text{A.14})$$

Instantaneous Optimal Control (IOC) Method

Since the classical optimal control, the linear quadratic regulator method, is not truly optimum by ignoring the seismic excitation term in the Riccati equation, other algorithms have been proposed. A time-dependent performance index $J(t)$ was defined by Yang et al. (1987) as shown in equation (2.10). The optimal solution can be obtained by minimizing $J(t)$ at every time instant t for the total control period ($0 \leq t \leq t_r$).

The instantaneous optimal control algorithm is used to successively evolve the state vector $z(t)$ through a small time interval Δt . Assuming that matrix A shown in equation (2.8) possesses distinct eigenvalues, the state vector can be expressed through the transformation

$$z(t) = Tw(t) \quad (\text{A.15})$$

where T is a $2n \times 2n$ modal matrix whose columns are the eigenvectors of matrix A ; $w(t)$ is

the “modal” state vector (Soong, 1990). Substituting equation (A.15) into equation (2.8) and pre-multiplying by the inverse of the modal matrix T^{-1} both sides of the equation, one can obtain

$$\dot{w}(t) = \Lambda w(t) + \Omega(t) \quad (\text{A.16a})$$

$$\Lambda = T^{-1}AT, \quad \Omega(t) = T^{-1}[Bu(t) + HF(t)] \quad (\text{A.16b})$$

where Λ is a diagonal matrix whose diagonal elements are the complex eigenvalues of matrix A . Solving equation (A.16a) over a small time interval Δt , the “modal” state vector $w(t)$ can be expressed as

$$w(t) = \int_0^t e^{\Lambda(t-\tau)} \Omega(\tau) d\tau \quad (\text{A.17})$$

According to the trapezoidal rule

$$\int_0^t f(\tau) d\tau = \sum_{k=1}^{n-1} f(k \cdot \Delta t) \cdot \Delta t + \frac{f(t) \cdot \Delta t}{2} \quad (\text{A.18})$$

Therefore, equation (A.17) can be reduced

$$w(t) = \sum_{k=1}^{n-1} e^{\Lambda(n-k)\Delta t} \Omega(k \cdot \Delta t) \Delta t + \Omega(t) \frac{\Delta t}{2} \quad (\text{A.19})$$

Let

$$D(t - \Delta t) = \sum_{k=1}^{n-1} e^{\Lambda(n-k)\Delta t} \Omega(k \cdot \Delta t) \Delta t \quad (\text{A.20})$$

Equation (A.20) can be rewritten as

$$\begin{aligned} D(t - \Delta t) &= \sum_{k=1}^{n-2} e^{\Lambda(n-k)\Delta t} \Omega(k \cdot \Delta t) \Delta t + e^{\Lambda \Delta t} \Omega(t - \Delta t) \Delta t \\ &= e^{\Lambda \Delta t} [D(t - 2\Delta t) + \Omega(t - \Delta t) \Delta t] \end{aligned} \quad (\text{A.21})$$

Substituting equation (A.20) into equation (A.19), one can obtain

$$D(t - \Delta t) = w(t) - \Omega(t) \frac{\Delta t}{2}; \quad \text{and} \quad D(t - 2\Delta t) = w(t - \Delta t) - \Omega(t - \Delta t) \frac{\Delta t}{2} \quad (\text{A.22})$$

Equation (A.21) can be written as

$$D(t - \Delta t) = e^{\Lambda \Delta t} \left[w(t - \Delta t) + \frac{\Delta t}{2} \Omega(t - \Delta t) \right] \quad (\text{A.23})$$

and

$$w(t) = e^{\Lambda \Delta t} \left[w(t - \Delta t) + \frac{\Delta t}{2} \Omega(t - \Delta t) \right] + \frac{\Delta t}{2} \Omega(t) \quad (\text{A.24})$$

For the state vector $z(t)$, equations (A.15) and (A.24) lead to

$$\begin{aligned} z(t) &= T \left\{ e^{\Lambda \Delta t} w(t - \Delta t) + \frac{\Delta t}{2} [e^{\Lambda \Delta t} \Omega(t - \Delta t) + \Omega(t)] \right\} \\ &= T \Theta(t - \Delta t) + \frac{\Delta t}{2} [B u(t) + H F(t)] \end{aligned} \quad (\text{A.25a})$$

$$\Theta(t - \Delta t) = e^{\Lambda \Delta t} T^{-1} \left\{ z(t - \Delta t) + \frac{\Delta t}{2} [B u(t - \Delta t) + H F(t - \Delta t)] \right\} \quad (\text{A.25b})$$

A similar procedure as given in the last section is used, for the minimization of the performance index $J(t)$ given in equation (2.10). The Hamiltonian is

$$\mathcal{H} = z^T(t) Q z(t) + u^T(t) R u(t) + \lambda^T(t) \left\{ z(t) - T \Theta(t - \Delta t) - \frac{\Delta t}{2} [B u(t) + H F(t)] \right\} \quad (\text{A.26})$$

The necessary conditions for the minimization are

$$\frac{\partial \mathcal{H}}{\partial z} = 0, \quad \frac{\partial \mathcal{H}}{\partial u} = 0, \quad \frac{\partial \mathcal{H}}{\partial \lambda} = 0$$

which yield

$$2Qz(t) + \lambda(t) = 0 \quad (\text{A.27a})$$

$$2Ru(t) - \frac{\Delta t}{2} B^T \lambda(t) = 0 \quad (\text{A.27b})$$

$$z(t) = T\Theta(t - \Delta t) + \frac{\Delta t}{2} [Bu(t) + HF(t)] \quad (\text{A.27c})$$

Using the closed-loop control, $\lambda(t) = P(t)z(t)$ (equation (A.8)), equation (A.27a)

gives

$$P(t) = -2Q \quad (\text{A.28a})$$

and equation (A.27b) can be expressed as

$$u(t) = -\frac{\Delta t}{2} R^{-1} B^T Q z(t) \quad (\text{A.28b})$$

The response state vector $z(t)$ is

$$\begin{aligned} z(t) &= T\Theta(t - \Delta t) + \frac{\Delta t}{2} \left[-\frac{\Delta t}{2} BR^{-1} B^T Q z(t) + HF(t) \right] \\ &= \left[I + \frac{\Delta t^2}{2} BR^{-1} B^T Q \right]^{-1} \left[T\Theta(t - \Delta t) + \frac{\Delta t}{2} HF(t) \right] \end{aligned} \quad (\text{A.29})$$

The above expressions of equation (A.28b) and (A.29) are used to calculate the control force and the response of structures with active controls using the IOC algorithm.

APPENDIX B

RUNGE-KUTTA METHOD

A high-order local truncation error of the Taylor methods is used for evaluation of the derivatives of function $f(t, z)$ which is called the Runge-Kutta method (Burden and Faires, 1985). The order of all of the partial derivatives of function $f(t, z)$ is assuming to be less than or equal to $n+1$ and be continuous on the domain $D = \{(t, z) | a \leq t \leq b, c \leq z \leq d\}$. Let $(t_0, z_0) \in D$. Therefore, for every $(t, z) \in D$ there exists a ζ between t and t_0 and an η between z and z_0 with (Burden and Faires, 1987)

$$f(t, z) = P_n(t, z) + R_n(t, z) \quad (\text{B.1a})$$

$$\begin{aligned} P_n(t, z) = & f(t_0, z_0) + \left[(t - t_0) \frac{\partial f}{\partial t}(t_0, z_0) + (z - z_0) \frac{\partial f}{\partial z}(t_0, z_0) \right] \\ & + \left[\frac{(t - t_0)^2}{2} \frac{\partial^2 f}{\partial t^2}(t_0, z_0) + (t - t_0)(z - z_0) \frac{\partial^2 f}{\partial t \partial z}(t_0, z_0) + \frac{(z - z_0)^2}{2} \frac{\partial^2 f}{\partial z^2}(t_0, z_0) \right] \\ & + \dots + \left[\frac{1}{n!} \sum_{j=0}^n \binom{n}{j} (t - t_0)^{n-j} (z - z_0)^j \frac{\partial^n f}{\partial t^{n-j} \partial z^j}(t_0, z_0) \right] \end{aligned} \quad (\text{B.1b})$$

$$R_n(t, z) = \frac{1}{(n+1)!} \sum_{j=0}^{n+1} \binom{n+1}{j} (t - t_0)^{n+1-j} (z - z_0)^j \frac{\partial^{n+1} f}{\partial t^{n+1-j} \partial z^j}(\zeta, \eta) \quad (\text{B.1c})$$

where P_n is called the Taylor polynomial of degree n in two variables for the function f , R_n is the remainder term associated with $P_n(t, z)$.

The first step of the Runge-Kutta method is to determine the parameters, α_1 , α_1 , and β_1 of $a_1 f(t + \alpha_1, z + \beta_1)$, which approximates

$$T^{(2)}(t, z) = f(t, z) + \frac{h}{2} \dot{f}(t, z) \quad (\text{B.2})$$

with error no greater than $O(h^2)$, the local truncation error for the Taylor method of order two. Note that $\dot{f}(t, z)$ in equation (B.2) is the derivative of the function $f(t, z)$ and

$$\dot{f}(t, z) = \frac{\partial f}{\partial t}(t, z) + \frac{\partial f}{\partial z}(t, z) \cdot \dot{z}(t); \text{ and } \dot{z}(t) = f(t, z) \quad (\text{B.3})$$

Therefore, equation (B.2) can be expressed as

$$T^{(2)}(t, z) = f(t, z) + \frac{h}{2} \frac{\partial f}{\partial t}(t, z) + \frac{h}{2} \frac{\partial f}{\partial z}(t, z) \cdot f(t, z) \quad (\text{B.4})$$

Expanding $f(t + \alpha_1, z + \beta_1)$ into the first degree, the Taylor polynomial is

$$a_1 f(t + \alpha_1, z + \beta_1) = a_1 f(t, z) + a_1 \alpha_1 \frac{\partial f}{\partial t}(t, z) + a_1 \beta_1 \frac{\partial f}{\partial z}(t, z) + a_1 \cdot R_1(t + \alpha_1, z + \beta_1) \quad (\text{B.5a})$$

$$R_1(t + \alpha_1, z + \beta_1) = \frac{\alpha_1^2}{2} \frac{\partial^2 f}{\partial t^2}(\zeta, \eta) + \alpha_1 \beta_1 \frac{\partial^2 f}{\partial t \partial z}(\zeta, \eta) + \frac{\beta_1^2}{2} \frac{\partial^2 f}{\partial z^2}(\zeta, \eta) \quad (\text{B.5b})$$

for a certain ζ between t and $t + \alpha_1$, and η between $z + \beta_1$.

From equations (B.4) and (B.5), the parameters a_1 , α_1 , and β_1 are obtained as

$$a_1 = 1; \quad \alpha_1 = \frac{h}{2}; \quad \beta_1 = \frac{h}{2} f(t, z) \quad (\text{B.6})$$

and

$$T^{(2)}(t, z) = f\left(t + \frac{h}{2}, z + \frac{h}{2}f(t, z)\right) - R_1\left(t + \frac{h}{2}, z + \frac{h}{2}f(t, z)\right) \quad (\text{B.7a})$$

$$R_1\left(t + \frac{h}{2}, z + \frac{h}{2}f(t, z)\right) = \frac{h^2}{8} \frac{\partial^2 f}{\partial t^2}(\zeta, \eta) + \frac{h^2}{4} f(t, z) \frac{\partial^2 f}{\partial t \partial z}(\zeta, \eta) + \frac{h^2}{8} (f(t, z))^2 \frac{\partial^2 f}{\partial z^2}(\zeta, \eta) \quad (\text{B.7b})$$

A similar procedure can be used to obtain the higher order Runge-Kutta method.

The most common Runge-Kutta method in use is of order four and is given as

$$z_0 = \alpha, \quad (\text{B.8a})$$

$$z_{i+1} = z_i + \frac{1}{6}(k_1 + 2k_2 + 2k_3 + k_4) \quad (\text{B.8b})$$

where

$$k_1 = hf(t_i, z_i), \quad (\text{B.8c})$$

$$k_2 = hf\left(t_i + \frac{h}{2}, z_i + \frac{1}{2}k_1\right), \quad (\text{B.8d})$$

$$k_3 = hf\left(t_i + \frac{h}{2}, z_i + \frac{1}{2}k_2\right), \quad (\text{B.8e})$$

$$k_4 = hf(t_{i+1}, z_i + k_3) \quad (\text{B.8f})$$

The α in equation (B.8a) is the initial value of the function $z(a)$ at time equal a ($a \leq t \leq b$).

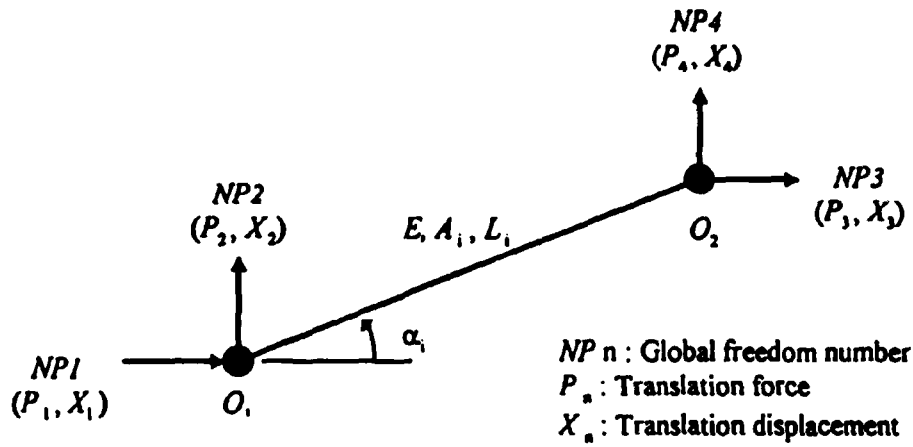
APPENDIX C

**DIRECT STIFFNESS METHOD
AND GUYAN REDUCTION**

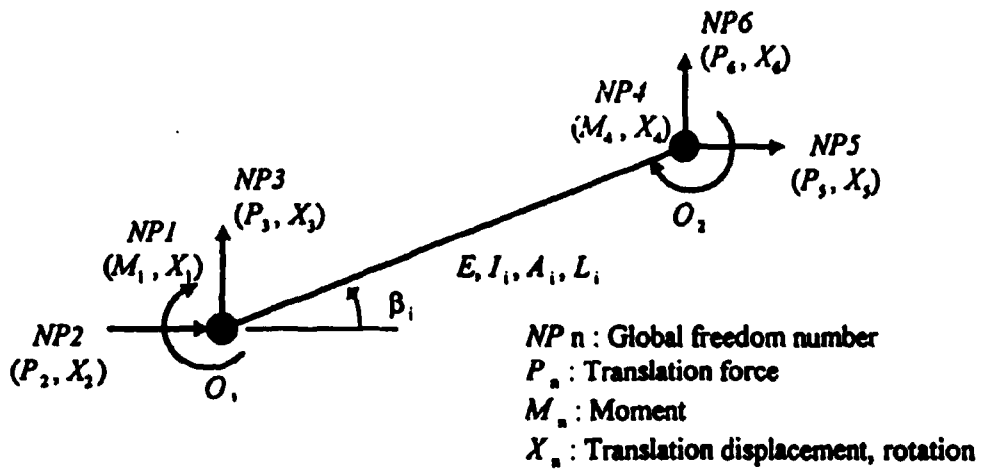
Generally, two methods, the force method and the displacement method, are used for the structural analysis. In the force method, the redundant forces are primary unknowns that can be solved from the compatibility conditions only for the statically indeterminate structures (Wang, 1986). In the displacement method, the displacement of all the joints in the structure are the primary unknowns that can be solved from the equilibrium conditions for both statically determinate and indeterminate structures. Usually, the force method is used to analyze the statically indeterminate trusses. For building frames, the displacement method is often implemented because of two reasons. First, the degree of indeterminacy for the frames is often equal to or sometimes much larger than the number of joint displacements. Second, the compatibility equation involving the redundant forces is more difficult to formulate than the equilibrium equations involving the joint displacements.

In this study, the displacement method is used to analyze both the truss and frame structures. The direct stiffness method uses the direct contribution of each element. The global stiffness matrix is obtained from the local stiffness matrix of each element in the structure (Wang, 1986). The local stiffness matrix has four degrees-of-freedom for each truss element and six degrees-of-freedom for each frame element (see Figure C.1).

The local stiffness includes two translations at each end of the truss element and can be expressed as



(a)



(b)

Figure C.1 Local freedom numbers for: (a) truss and (b) frame elements

$$[k]_i = \frac{EA_i}{L_i} \begin{bmatrix} \cos^2 \alpha_i & & \text{symmetric} \\ \cos \alpha_i \sin \alpha_i & \sin^2 \alpha_i & \\ -\cos^2 \alpha_i & -\cos \alpha_i \sin \alpha_i & \cos^2 \alpha_i \\ -\cos \alpha_i \sin \alpha_i & -\sin^2 \alpha_i & \cos \alpha_i \sin \alpha_i & \sin^2 \alpha_i \end{bmatrix} \quad (C.1)$$

where E is the Young's modulus of the material, A_i , L_i , and α_i are the cross-sectional area, length, and declining angle of the i th element. The local stiffness of the frame element includes two translations and a rotation at each end and can be expressed as

$$[k]_i = \begin{bmatrix} 4T_1 & & & & & & \text{symmetric} \\ T_2 & T_4 + T_9 & & & & & \\ -T_3 & -T_5 + T_8 & -T_6 + T_7 & & & & \\ 2T_1 & T_2 & -T_3 & 4T_1 & & & \\ -T_3 & -T_4 - T_9 & T_5 - T_8 & -T_2 & T_4 + T_9 & & \\ T_3 & T_3 - T_8 & -T_6 - T_7 & T_2 & -T_5 + T_8 & T_6 + T_7 & \end{bmatrix} \quad (C.2)$$

$$T_1 = \frac{EI_i}{L_i}; \quad T_2 = \frac{6EI_i}{L_i^2} \sin \beta_i; \quad T_3 = \frac{6EI_i}{L_i^2} \cos \beta_i;$$

$$T_4 = \frac{12EI_i}{L_i^3} \sin^2 \beta_i; \quad T_5 = \frac{12EI_i}{L_i^3} \sin \beta_i \cos \beta_i; \quad T_6 = \frac{12EI_i}{L_i^3} \cos^2 \beta_i;$$

$$T_7 = \frac{EA_i}{L_i} \sin^2 \beta_i; \quad T_8 = \frac{EA_i}{L_i} \sin \beta_i \cos \beta_i; \quad T_9 = \frac{EA_i}{L_i} \cos^2 \beta_i;$$

where I_i and β_i are the moment of inertia and the declining angle of the i th frame element. The global stiffness matrix can be obtained by using the superposition method from the known global freedom number, NP_n (shown in Figure C), of each element corresponding to the local matrix. A simple procedure can be used for the computer program to assemble the global stiffness matrix

```

do loop1 = 1, n
  do loop2 = 1, n
    GlobalStiff[NP(loop1),NP(loop2)] = GlobalStiff[NP(loop1),NP(loop2)] + k{loop1, loop2}
  end loop2
end loop1

```

where $n = 4$ for the truss structure; and $n = 6$ for the frame structure. One must repeat this procedure for every element of the structure.

Once the global stiffness matrix has been established by using the direct stiffness method, the displacement method of truss/frame analysis can be solved through the force-displacement relationships as

$$[X] = [K]^{-1} [P] \quad (C.3)$$

where $[K]^{-1}$ is the inverse form of the global stiffness matrix; vectors $[X]$ and $[P]$ are the global displacement and applied force to the structural system.

Guyan Reduction

For the dynamic analysis, Guyan's condensation method (1965) is used to reduce the degrees-of-freedom of the structural system to only translations in the horizontal direction. A state reduction is used. The equations of equilibrium for free displacement, equation (C.3) can be expressed as

$$\begin{bmatrix} K_{AA} & K_{AB} \\ K_{BA} & K_{BB} \end{bmatrix} \begin{bmatrix} X_A \\ X_B \end{bmatrix} = \begin{bmatrix} P_A \\ P_B \end{bmatrix} \quad (C.4)$$

The subscript A in equation (C.4) denotes the displacements that are to be eliminated, and subscript B refers to those that will be retained which are the translations in the horizontal direction in this case. Equation (C.4) can be written as two sets of equations as follows:

$$K_{AA}X_A + K_{AB}X_B = P_A \quad (\text{C.5a})$$

$$K_{BA}X_A + K_{BB}X_B = P_B \quad (\text{C.5b})$$

The *dependent displacements* (Weaver and Johnston, 1987), X_A , can be solved from equation (C.5a) as

$$X_A = K_{AA}^{-1}(P_A - K_{AB}X_B) \quad (\text{C.6})$$

Substituting equation (C.6) into equation (C.5b), one can obtain

$$K_{BB}^*X_B = P_B^* \quad (\text{C.7a})$$

$$K_{BB}^* = K_{BB} - K_{BA}K_{AA}^{-1}K_{AB} \quad (\text{C.7b})$$

$$P_B^* = P_B - K_{BA}K_{AA}^{-1}P_A \quad (\text{C.7c})$$

The *independent displacements*, X_B , can be solved by pre-multiplying the inverse matrix of the reduced stiffness matrix, K_{BB}^* , on both sides of equation (C.7a). Once the independent displacements are obtained, the dependent displacements can be solved by the back-substitution formula in equation (C.6).

APPENDIX D

SENSITIVITY ANALYSIS FOR STRUCTURAL DESIGN

The first-order sensitivity analysis is used to modify the structural design in an optimal way (Grierson, 1994). The equations of equilibrium in matrix form can be expressed as

$$KX = P \quad (D.1)$$

where K is the stiffness matrix of the structure, and vectors, X and P , are the nodal displacements and the applied forces at the nodal degrees-of-freedom. Consider a particular displacement, e_j , which is related to the vector of nodal displacements as

$$e_j = b_j^T X \quad (D.2)$$

where b_j is a vector with the values of ones or zeros which depend on the nature of the displacement e_j . For example, e_j could be the horizontal drift between two floors. The first-order sensitivity of displacement e_j is calculated by taking the first-derivative of equation (D.2) with respect to the design variables (the cross-sectional area of the structural members, A_j , in this problem), which can be expressed as

$$\frac{\partial e_j}{\partial A_j} = b_j^T \frac{\partial X}{\partial A_j} + X^T \frac{\partial b_j^T}{\partial A_j} = b_j^T \frac{\partial X}{\partial A_j} \quad (D.3)$$

Similarly by taking the first-derivative of equation (D.1) with respect to \underline{A}_j , one can obtain

$$K \frac{\partial X}{\partial \underline{A}_j} + \frac{\partial K}{\partial \underline{A}_j} X = \frac{\partial P}{\partial \underline{A}_j} \quad (\text{D.4})$$

The right-hand side of equation (D.4) equals zero by assuming that the applied loads P are invariant with the cross-sectional area of the structural members. Equation (D.4) can be rewritten as

$$\frac{\partial X}{\partial \underline{A}_j} = -K^{-1} \frac{\partial K}{\partial \underline{A}_j} X \quad (\text{D.5})$$

Therefore, equation (D.3) becomes

$$\frac{\partial e_j}{\partial \underline{A}_j} = -b_j^T K^{-1} \frac{\partial K}{\partial \underline{A}_j} X \quad (\text{D.6})$$

Equation (D.6) defines the first-order sensitivity of displacement with respect to the changing variables. The sign of the sensitivity indicates the relationship of the displacement and the variables. For the structural design problem, the negative sign of the sensitivity ($\partial e_j / \partial \underline{A}_j$ in equation (D.6)) means that the displacement e_j will decrease as \bar{A}_j increases. This is useful for the design procedure since one needs to change only the size of the members that will decrease a given displacement and not the size of all the members.

APPENDIX E

CLASSICAL OPTIMIZATION METHODS

In this section, the three classical optimization methods used in Chapter 6, i.e., the modified feasible directions method (MFD), the sequential linear programming method (SLP), and sequential quadratic programming method (SQP) are described. An optimization program, Design Optimization Tools (DOT), was developed by VMA Engineering (1993) which includes three numerical optimization search methods for constrained problems and is used here to compare with MISA.

Modified Feasible Directions Method (MFD)

In general, the optimization problem is stated as follows (Vanderplaats, 1984 b):

Minimize or maximize

$$O(\underline{A}) \qquad \text{Objective function} \qquad \text{(E.1)}$$

Subject to:

$$g_j(\underline{A}) \leq 0; \quad j = 1, \dots, N; \quad \text{Inequality constraints} \qquad \text{(E.2a)}$$

$$\underline{A}_i^L \leq \underline{A}_i \leq \underline{A}_i^U; \quad i = 1, \dots, N_{dv}; \quad \text{Side constraints} \qquad \text{(E.2b)}$$

where \underline{A}_i , \underline{A}_i^L , and \underline{A}_i^U are the i th design variable, and the lower and upper bound of the i th design variable; N is the number of constraints; N_{dv} is the number of design variables.

In the method of feasible directions, one will first find a search direction S and then move in this direction to update the design variables (\underline{A}). This procedure can be

expressed as

$$\underline{A}^q = \underline{A}^{q-1} + \alpha^* \mathcal{S}^q \quad (\text{E.3})$$

where α^* is a scalar and the search direction \mathcal{S}^q is defined as

$$\mathcal{S}^q = -\nabla O(\underline{A}^{q-1}) + \epsilon \mathcal{S}^q \quad (\text{E.4a})$$

$$\epsilon = \frac{|\nabla O(\underline{A}^{q-1})|^2}{|\nabla O(\underline{A}^{q-2})|^2} \quad (\text{E.4b})$$

The basic concept of the feasible directions method is to obtain an α^* that will minimize $O(\underline{A}^{q-1} + \alpha^* \mathcal{S}^q)$ subject to the constraints. The MFD method of the DOT program (VMA, 1993) creates a first order Maclaurin series approximation to the objective function in terms of α^* . Substituting equation (E.3) into equation (E.1), one can obtain

$$O(\underline{A}^q) = O(\underline{A}^{q-1} + \alpha^* \mathcal{S}^q) \quad (\text{E.5})$$

Thus, an approximation to $O(\underline{A}^q)$ is

$$O(\underline{A}^q) = O(\underline{A}^{q-1}) + \sum_{i=1}^n \frac{\partial O(\underline{A}^{q-1})}{\partial A_i} \left(\frac{\partial A_i}{\partial \alpha^*} \right) \alpha^* \quad (\text{E.6})$$

or

$$O(\underline{A}^*) \approx O(\underline{A}^{*+1}) + \frac{dO(\underline{A}^{*+1})}{d\alpha^*} \alpha^* \quad (\text{E.7})$$

where $\frac{\partial O(\underline{A}^{*+1})}{\partial \underline{A}_i}$ is the i th entry of gradient of the objective function, $\nabla O(\underline{A}^{*+1})$ which can

be derived by finite differences as

$$\nabla O(\underline{A}) = \left\{ \begin{array}{c} \frac{O(\underline{A} + \delta \underline{A}_1) - O(\underline{A})}{\delta \underline{A}_1} \\ \frac{O(\underline{A} + \delta \underline{A}_2) - O(\underline{A})}{\delta \underline{A}_2} \\ \dots \\ \dots \\ \frac{O(\underline{A} + \delta \underline{A}_N) - O(\underline{A})}{\delta \underline{A}_N} \end{array} \right\} = \left\{ \begin{array}{c} \frac{\partial O(\underline{A})}{\partial \underline{A}_1} \\ \frac{\partial O(\underline{A})}{\partial \underline{A}_2} \\ \dots \\ \dots \\ \frac{\partial O(\underline{A})}{\partial \underline{A}_N} \end{array} \right\} \quad (\text{E.8})$$

and

$$\frac{\partial \underline{A}_i}{\partial \alpha^*} = S_i \quad (\text{E.9})$$

Therefore

$$\frac{dO(\underline{A}^{*+1})}{d\alpha^*} = \nabla O(\underline{A}^{*+1})^T S^* \quad (\text{E.10})$$

Since the gradient and the search direction are available, the slope of the function can be obtained from equation (E.10). The objective function $O(\underline{A}^q)$ is expected to reduce by some fraction, say 10 %, and is expressed by using a linear approximation

$$\begin{aligned} O(\underline{A}^q) &\approx O(\underline{A}^{q+1}) + \frac{dO(\underline{A}^{q+1})}{d\alpha^*} \alpha^* \\ &= O(\underline{A}^{q+1}) - 0.1|O(\underline{A}^{q+1})| \end{aligned} \quad (\text{E.11})$$

Thus, an estimate of α^* which will reduce the objective function by 10 % can be obtained as

$$\alpha_{est}^* = \frac{-0.1|O(\underline{A}^{q+1})|}{\left[\frac{dO(\underline{A}^{q+1})}{d\alpha^*} \right]} \quad (\text{E.12})$$

However, since the gradients of some constraints are also available, the approach by driving $g_j(\underline{A}^q)$ to zero can be used instead of reducing by 10 % the value of the objective function (equation (E.11)). Thus, a linear approximation to find $g_j(\underline{A}^q) = 0.0$ is

$$g_j(\underline{A}^q) = g_j(\underline{A}^{q+1}) + \frac{dg_j(\underline{A}^{q+1})}{d\alpha^*} \alpha^* = 0.0 \quad (\text{E.13})$$

and an estimate for α^* is

$$\alpha_{\max}^* = \frac{-g_j(\underline{A}^{k+1})}{\left[\frac{dg_j(\underline{A}^{k+1})}{d\alpha^*} \right]} \quad (\text{E.14})$$

Therefore, even at the beginning of the search, a considerable amount of information is available to direct the process. Using similar approximations, an upper bound of α^* can be derived by driving the design variables to their lower or upper bounds, and this would provide a maximum value for α^* to be allowed.

Sequential Linear Programming Method (SLP)

The sequential linear programming method (SLP) instead of using the original nonlinear functions, uses a Taylor Series approximation for the optimization. The DOT program (VMA, 1993) creates the Taylor Series expansion in the form of

$$\tilde{O}(\underline{A}) = O(\underline{A}^{k+1}) + \nabla O(\underline{A}^{k+1})^T \delta \underline{A} \quad (\text{E.15a})$$

$$\tilde{g}_j(\underline{A}) = g_j(\underline{A}^{k+1}) + \nabla g_j(\underline{A}^{k+1})^T \delta \underline{A}; \quad j \in J_n \quad (\text{E.15b})$$

where

$$\delta \underline{A} = \underline{A}^q - \underline{A}^{k+1} \quad (\text{E.16})$$

and J_n is the set of retained constraints.

Equation (E.15) can be rewritten as

$$\tilde{O}(\underline{A}) = \tilde{O}^0 + \nabla O(\underline{A}^{*1})^T \underline{A}^1 \quad (\text{E.16a})$$

$$\tilde{g}_j(\underline{A}) = \tilde{g}_j^0 + \nabla g_j(\underline{A}^{*1})^T \underline{A}^1; \quad j \in J_n \quad (\text{E.16b})$$

where

$$\tilde{O}^0 = O(\underline{A}) - \nabla O(\underline{A}^{*1})^T \underline{A}^{*1} \quad (\text{E.17a})$$

$$\tilde{g}_j^0 = \tilde{g}_j(\underline{A}) - \nabla g_j(\underline{A}^{*1})^T \underline{A}^{*1}; \quad j \in J_n \quad (\text{E.17b})$$

Thus, the linear approximation optimization problem can be solved by minimizing $\tilde{O}(\underline{A}^1)$

subject to

$$\tilde{g}_j(\underline{A}^1) \leq 0; \quad (\text{E.18})$$

$$\tilde{\underline{A}}_i^L \leq \underline{A}_i \leq \tilde{\underline{A}}_i^U; \quad i = 1, \dots, Ndv; \quad (\text{E.19})$$

where

$$\tilde{\underline{A}}_i^L = \underline{A}_i - \vartheta |\underline{A}_i| \quad (\text{E.20a})$$

$$\tilde{\underline{A}}_i^U = \underline{A}_i + \vartheta |\underline{A}_i| \quad (\text{E.20b})$$

The multiplier ϑ in equation (E.20) is a variable number which is dependent on the progress of the optimization.

Sequential Quadratic Programming Method (SQP)

The basic concept of the sequential quadratic programming method is very similar to the sequential linear programming method. A Taylor Series approximation is also created for the objective and constraint functions. However, instead of minimizing the linearized objective, a quadratic approximate objective function is created by the form

$$\text{Minimize: } V(S) = O^0 + \nabla O^T S + \frac{1}{2} S^T D S \quad (\text{E.21})$$

$$\text{Subject to: } (\nabla g_j)^T S + g_j^0 \leq 0; \quad j = 1, \dots, N \quad (\text{E.22})$$

where matrix D is a positive definite matrix, vector S is the search direction as described in the modified feasible directions method (MFD). This subprogram is solved using the MFD program. Usually, matrix D is initially defined as an identity matrix, and is updated to approach the Hessian of the Lagrangian function. The updated D matrix can be expressed as

$$D' = D - \frac{D(\delta\Delta)(\delta\Delta)^T D}{(\delta\Delta)^T D(\delta\Delta)} + \frac{\eta\eta^T}{(\delta\Delta)^T \eta} \quad (\text{E.23})$$

where

$$\delta \underline{A} = \underline{A}^n - \underline{A}^{n-1} \quad (\text{E.24a})$$

$$\eta = \theta \Gamma + (1 - \theta) D \delta \underline{A} \quad (\text{E.24b})$$

$$\Gamma = \nabla_{\underline{A}} \Psi^n - \nabla_{\underline{A}} \Psi^{n-1} \quad (\text{E.24c})$$

$$\Psi^n = \alpha(\underline{A}) + \sum_{j=1}^N v_j^n \max[0, g_j(\underline{A})] \quad (\text{E.24d})$$

$$v_j^n = \max\left[|\lambda_j|, \frac{1}{2}(v_j^{n-1} + |\lambda_j|)\right] \quad (\text{E.24e})$$

$$\theta = \begin{cases} 1.0 & \text{if } (\delta \underline{A})^T \Gamma \geq 0.2(\delta \underline{A})^T D(\delta \underline{A}) \\ \frac{0.8(\delta \underline{A})^T D(\delta \underline{A})}{(\delta \underline{A})^T D(\delta \underline{A}) - (\delta \underline{A})^T \Gamma} & \text{if } (\delta \underline{A})^T \Gamma < 0.2(\delta \underline{A})^T D(\delta \underline{A}) \end{cases} \quad (\text{E.24f})$$

In the search process of the SQP method in DOT program, the approximations are made by using the components of Ψ . This function has discontinuous derivatives at the constraints boundaries which has smooth components.

The convergence criteria for the MFD, SLP, and SQP methods should satisfy either the maximum iterations allowed or the Kuhn-Tucker conditions (Zangwill, 1969). The Kuhn-Tucker conditions dictate that the Lagrangian function must have a vanishing gradient at the optimum design denoted by \underline{A}^* . The Kuhn-Tucker necessary conditions for optimality are:

1. \underline{A}^* is feasible (all $g_j(\underline{A}^*) \leq 0$) (E.25a)

2. The product of Lagrange multipliers, λ_j , and $g_j(\underline{A}^*)$ equals zero

$$\lambda_j g_j(\underline{A}^*) = 0; \quad j = 1, \dots, N \quad (\text{E.26})$$

3. The gradient of the Lagrangian vanishes

$$\nabla O(\underline{A}) + \sum_{j=1}^N \lambda_j \nabla g_j(\underline{A}) = 0 \quad (\text{E.27a})$$

$$\lambda_j \geq 0; \quad j = 1, \dots, N \quad (\text{E.27b})$$

APPENDIX F

THE MISA PROGRAM

The MISA program includes several subroutines required to implement the developed algorithm. Figure F.1 shows the order of execution of the MISA program. In Figure F.1, the boxes with solid lines indicate the name of the subroutine and the function of the subroutine is described near the box. The boxes with dashed lines are the judgment procedures in the MISA program. Finally, the required input data of the MISA is listed in Tables F.1 and F.2. The name of the input file can be any string with a maximum of twelve characters. The input data must follow the line set order shown in Table F.1. One set of data may include as many lines as needed to specify the required data. A free formatted data is used. A comma (,) or a blank space is used to separate the input data at the same line. The data type and data description are shown in Table F.2. Data type is declared as type I or R. Type I is integer, and type R is real. It should be noted that the analysis method and the dynamic excitation are input from the keyboard.

Table F.1 Input order for required data in the MISA program

Line set	Description	Note
1	Program initiation.	
2	Material properties.	
3	External static loads.	
4	Frame element definition.	Omit if there are no frame elements.
5	Truss element definition.	Omit if there are no truss elements.
6	Lumped mass and response constraints.	
7	Damping matrix/Damping ratio.	
8	Control parameter for ABS.	Omit if there are no ABS structural controls.
9	Location of ABS.	Omit if there are no ABS structural controls.
10	Side constraints.	
11	Size and location of VE dampers.	Omit if there are no VE dampers.

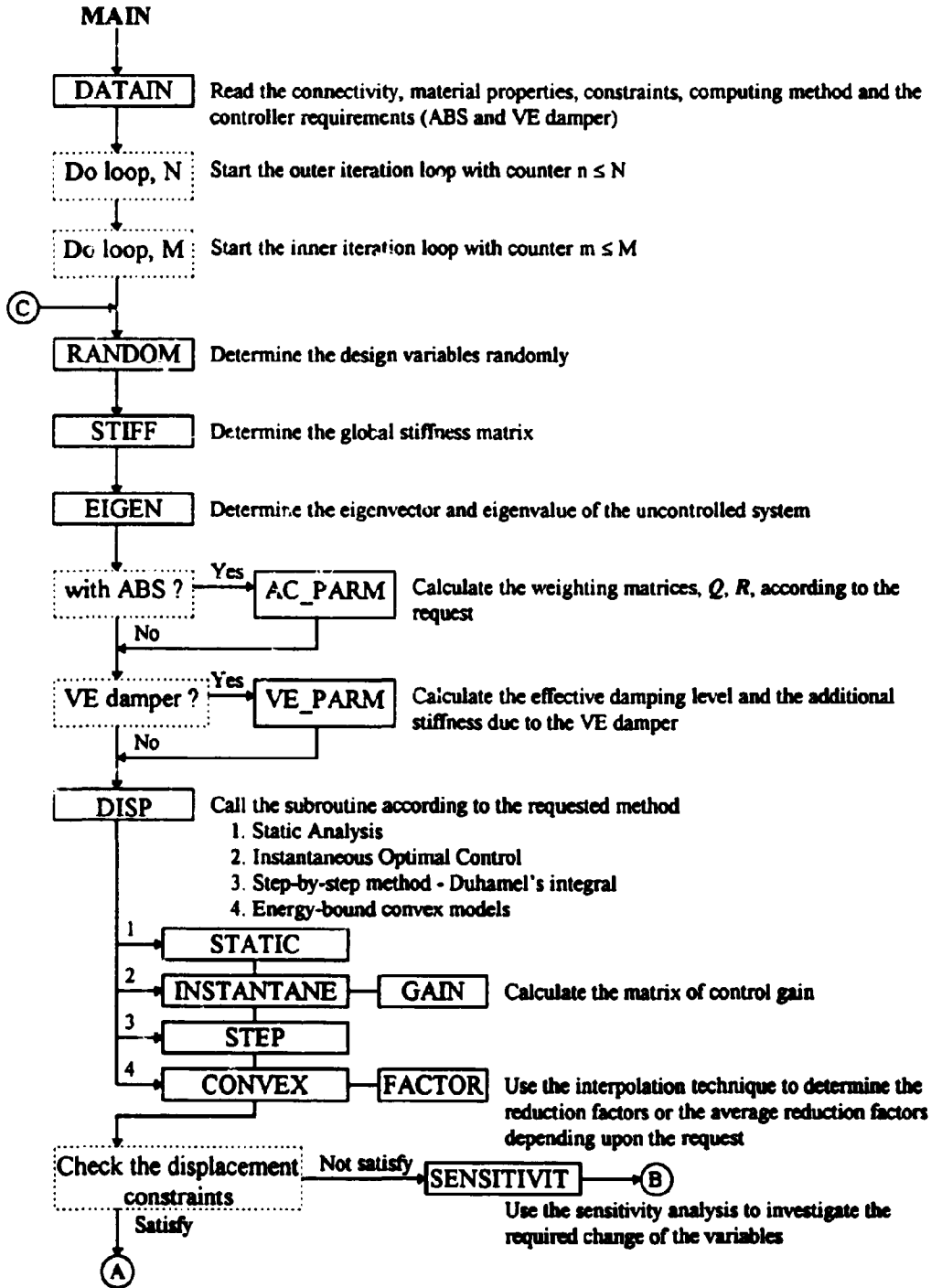


Figure F.1 Execution order of the MISA program

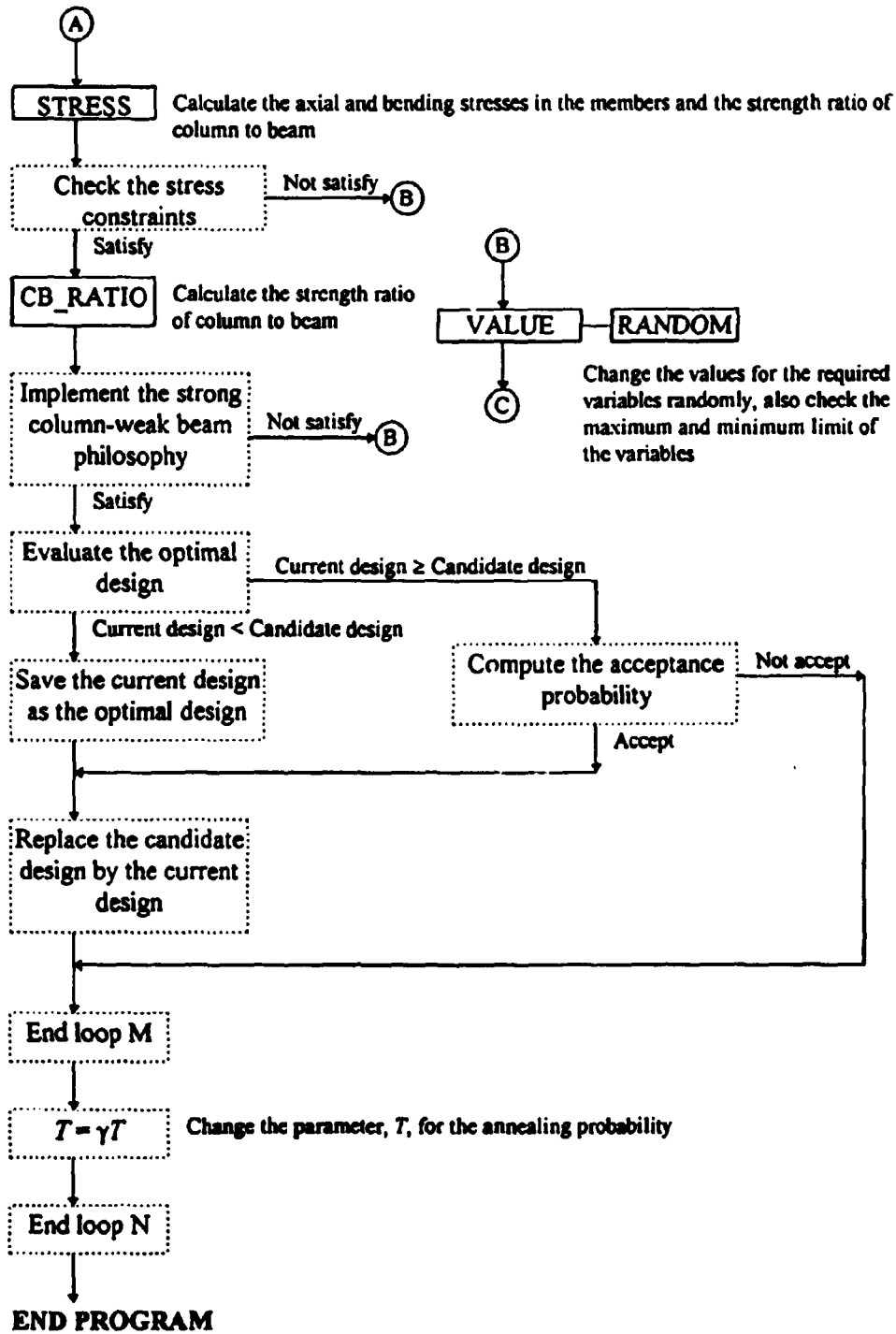


Figure F.1 (Continued)

Table F.2 Description for input data in the MISA program

Variable	Data type	Line #	Description	Note
NS	I	1	Number of stories for the structure.	
NB	I	1	Number of bays for the structure.	
NM	I	1	Number of frame elements.	Includes beams, column.
NP	I	1	Degree-of-freedom of the structure.	
ITURSS	I	1	Number of truss elements.	
IC	I	1	(a) 1 : Input the damping matrix. (b) 2 : Input the inherent damping ratio.	
IUNIT	I	1	(a) 1 : SI units. (b) 2 : US units.	
IMAT	I	1	Number of design variables.	
MAC	I	1	Number of ABS.	0 : no ABS.
ICF	I	1	(a) 0 : no ABS or using the initial control parameter. (b) 1 : changing the control parameter to achieve the required control force.	
IVE	I	1	Number of VE dampers.	0 : no VE dampers.
E	R	2	Elastic modulus.	
P	R	3	External static load at each DOF.	P(i), I = 1, NP.
NO	I	4a	Element number.	a - first line of this set.
MATERIAL	I	4a	Variable number.	
XL	R	4a	Length of current element.	
ANG	R	4a	Angle of current element with horizontal.	Degrees.
SLIMIT	R	4a	Yield stress for current element.	
NPE (1)	I	4b	DOF's number of horizontal translation direction @ end I.	b - second line of this set.
NPE (2)	I	4b	DOF's number of vertical translation direction @ end I.	
NPE (3)	I	4b	DOF's number of rotation direction @ end I.	
NPE (4)	I	4b	DOF's number of horizontal translation direction @ end J.	
NPE (5)	I	4b	DOF's number of vertical translation direction @ end J.	
NPE (6)	I	4b	DOF's number of rotation direction @ end J.	
FNP (1)	R	4b	Node/Span loads in horizontal direction @ end I.	
FNP (2)	R	4b	Node/Span loads in vertical direction @ end I.	
FNP (3)	R	4b	Node/Span moment @ end I.	
FNP (4)	R	4b	Node/Span loads in horizontal direction @ end J.	
FNP (5)	R	4b	Node/Span loads in vertical direction @ end J.	
FNP (6)	R	4b	Node/Span moment @ end J.	

Table F.2 (Continued)

Variable	Data type	Line #	Description	Note
NO	I	5	Element number.	
MATERIAL	I	5	Variable number.	
NPE (1)	I	5	DOF's number of horizontal translation direction @ end <i>I</i> .	
NPE (2)	I	5	DOF's number of vertical translation direction @ end <i>I</i> .	
NPE (3)	I	5	DOF's number of horizontal translation direction @ end <i>J</i> .	
NPE (4)	I	5	DOF's number of vertical translation direction @ end <i>J</i> .	
XL	R	5	Length of current element.	
ANG	R	5	Angle of current element with horizontal.	Degrees.
SLIMIT	R	5	Yield stress for current element.	
LUMPM (<i>k</i>)	R	6	Lumped mass @ floor <i>k</i> .	NS lines are needed in this set. (<i>K</i> = 1, NS)
XLIMIT (<i>k</i>)	R	6	Displacement constraint @ floor <i>k</i> .	
VLIMIT (<i>k</i>)	R	6	Velocity constraint @ floor <i>k</i> .	
ALIMIT (<i>k</i>)	R	6	Acceleration constraint @ floor <i>k</i> .	
Z0 (<i>k</i>)	R	6	Initial displacement.	
Z0(<i>k</i> +NS)	R	6	Initial velocity.	
DAMP	R	7	(a) Damping matrix. (b) Damping ratio.	Damp(<i>i,j</i>), <i>j</i> = 1, NS. NS lines are needed for this input data. Damp(<i>i,i</i>), <i>i</i> = 1, NS.
R	R	8	Scale factor for identity weighting matrix.	
FLOOR	I	9	Location of ABS. 0 : no ABS at this floor. 1 : an ABS at this floor.	Floor(<i>i</i>), <i>i</i> = 1, NS.
MAXRANGE	R	10	Upper bound of design variable.	IMAT lines are needed in this set.
MINRANGE	R	10	Lower bound of design variable.	
RANGE	R	10	Initial value of design variable.	
VE_T	R	11	Thickness of VE damper.	IVE lines are needed in this set. Radian.
VE_AREA	R	11	Area of VE damper.	
VE_A	R	11	Angle of VE bracing system with horizontal.	
N_VE (1)	I	11	DOF's number of horizontal translation direction @ end <i>I</i> .	
N_VE (2)	I	11	DOF's number of vertical translation direction @ end <i>I</i> .	
N_VE (3)	I	11	DOF's number of horizontal translation direction @ end <i>J</i> .	
N_VE (4)	I	11	DOF's number of vertical translation direction @ end <i>J</i> .	
L VE	I	11	Location of VE damper (Floor number).	

REFERENCES

- Ackley, D. H. (1987). "An empirical study of bit vector function optimization." *Genetic algorithms and simulating annealing*, D. Lawrence, ed., Morgan Kaufmann Publishers, Los Altos, CA, 170-271.
- ASCE 7-88 Standard. (1990). *Minimum design loads for buildings and other structures*. ASCE, New York, NY.
- ATC 17-1. (1993). *Proceedings of seminar on seismic isolation, passive energy dissipation, and active control*. Applied Technology Council, San Francisco, CA., March 11-12.
- Balling, R. J. (1991). "Optimal steel frame design by simulated annealing." *J. Struct. Engrg.*, 117(6), 1780-1795.
- Balling, R. J., Pister, K. S., and Ciampi, V. (1983). "Optimal seismic-resistant design of a planar steel frame." *Earthq. Engrg. Struct. Dyn.*, 11, 541-556.
- Ben-Haim, Y. (1994 a). "Fatigue lifetime with load uncertainty represented by a convex model." *J. Engrg. Mech., ASCE*, 120(3), 445-462.
- Ben-Haim, Y. (1994 b). "A non-probabilistic concept of reliability." *Structural Safety*, 14, 227-245.
- Ben-Haim, Y., Chen, G., and Soong, T. T. (1995). "Maximum structural response using convex models." *J. Engrg. Mech., ASCE*, In print.
- Ben-Haim, Y., and Elishakoff, I. (1990). *Convex models of uncertainty in applied mechanics*. Elsevier, New York, NY.
- Bhatti, M. A., and Pister, K. S. (1981). "A dual critical approach for optimal design of earthquake-resistant structural systems." *Earthq. Engrg. Struct. Dyn.*, 9, 557-572.
- Burden, R. L. and Faires, J. D. (1985). *Numerical analysis*. Prindle, Weber & Schmidt, Boston.
- Cassis, J. H. (1974). "Optimum design of structures subjected to dynamic loads." *UCLA-ENG-7451*, UCLA School of Engineering and Applied Science, Los Angeles, CA.

- Cassis, J. H., and Schmit, L. A. Jr. (1976). "Optimal structural design with dynamic constraints." *J. Struct. Engrg., ASCE*, 102(ST10), 2053-2071.
- Cha, J. Z., Pitarresi, J. M., and Soong, T. T. (1988). "Optimal design procedure for active structures." *J. Struct. Engrg., ASCE*, 114(12), 2710-2723.
- Chang, K. C., Soong, T. T., Oh, S-T., and Lai, M. L. (1992). "Effect of ambient temperature of viscoelastically damped structure." *J. Struct. Engrg., ASCE*, 118(7), 1955-1973.
- Chang, K. C., Chen, K. L., Soong, T. T., and Lai, M. L. (1994). "Seismic retrofit of a reinforced concrete frame with added viscoelastic dampers." *Fifth U. S. National Conference on Earthquake Engineering*, Vol. II, Chicago, July 10-14, 707-716.
- Chang, K. C., Soong, T. T., and Oh, S.-T., and Lai, M. L. (1995). "Seismic behavior of steel frame with added viscoelastic dampers." *J. Struct. Engrg., ASCE*, 121(10), 1418-1426.
- Chen, G-S., Bruno, R. J., and Salama, M. (1991). "Optimal placement of active/passive members in truss structures using simulated annealing." *AIAA J.*, 29(8), 1327-1334.
- Cheng, F. Y., and Pantelides, C. P. (1986). "Optimal control of seismic structures." *Dynamic response of structures*, G. C. Hart and R. B. Nelson, eds., ASCE, New York, NY, 764-771.
- Cheng, F. Y., and Pantelides, C. P. (1988). "Combining structural optimization and structural control." *Technical report NCEER 88-0006*, State University of New York, Buffalo, NY, Jan.
- Clark, A. J. (1994), MTS Systems Corporation, Minneapolis, Minnesota, Personal Communication, Feb. 10.
- Clough, R. W., and Penzien, J. (1975). *Dynamics of structures*. McGraw-Hill Book Co., New York, NY.
- Der Kiureghian, A. (1980). "Structural response to stationary excitation." *J. Engrg. Mech. Div., ASCE*, 106, 1195-1213.
- Dobbs, M. W., and Nelson, R. B. (1976). "Application of optimality criteria to automated structural design." *AIAA J.*, 14(10), 1436-1443.
- Drenick, R. F. (1970). "Model-free design of aseismic structures." *J. Engrg. Mech. Div., Proc. ASCE*, 96, EM4, 483-493.

- Drenick, R. F. (1973). "Aseismic design by way of critical excitation." *J. Engrg. Mech. Div., Proc. ASCE*, 99, EM4, 649-667.
- Elishakoff, I. (1990). "Convex versus probabilistic methods of uncertainty in structural dynamics." *Structural dynamics: recent advances*, M. Petyt, H. F. Wolfe, and C. Mei, eds., Elsevier Science Publishers, London, England, 3-21.
- Elishakoff, I. (1994). "A new safety factor based on convex modelling." *Uncertainty modelling and analysis*, B. M. Ayyub and M. M. Gupta, Eds., Elsevier Science Publishers, Amsterdam, Netherlands, 145-172.
- Elishakoff, I. (1995). "Essay on uncertainties in elastic and viscoelastic structures: from A. M. Freudenthal's criticisms to modern convex modeling." *Computers & structures* 56(6), 871-895.
- Elishakoff, I., and Ben-Haim, Y. (1990). "Dynamics of a thin cylindrical shell under impact with limited deterministic information on its initial imperfections." *Structural Safety*, 8, 103-112.
- Elishakoff, I., Elisseeff, P., and Glegg, S. A. L. (1994). "Nonprobabilistic, convex-theoretic modelling of scatter in material properties." *AIAA J.*, 32(4), 843-849.
- Elishakoff, I., and Zhu, L. P. (1994). *Probabilistic and convex modelling of acoustically excited structures*. Elsevier Science Publishers, Amsterdam, Netherlands.
- ENR (1990). "Active dampers create a stir - Japanese mass driver raises questions of active vs. passive damping." *ENR Feature*, Feb. 8, 39-40.
- Fleury, C. (1980). "An efficient optimality criteria approach to the minimum weight design of elastic structures." *J. Computers and Structures*, 11, 163-173.
- Gasparini, D. A. and Vanmarcke, E. H. (1976). "Simulated earthquake motions compatible with prescribed response spectra." *Research Report R76-4, Order No. 527*, Department of Civil Engineering, Constructed Facilities Division, Massachusetts Institute of Technology, Cambridge, Massachusetts.
- Gellatly, R. A., and Berke, L. (1971). "Optimal structural design." *AFFDL-TR-70-165*, Feb.
- Gellatly, R. A., and Gallagher, R. H. (1966). "A procedure for automated minimum weight structural design." *Aeronautical quarterly*, 17(3), 216-230 and 17(4), 332-342.
- Goldberg, E. D. (1989). *Genetic algorithms in search, optimization and machine learning*. Addison-Wesley, Reading, MA.

- Grierson, D. E. (1994). "Structural analysis for structural design." *Proceedings of the 11th analysis and computation conference*, F. Y. Cheng Ed., ASCE, Structures Congress '94 and IASS International Symposium '94, Atlanta, Georgia, Apr. 24-28, 133-144.
- Guyan, R. J. (1965). "Reduction of stiffness and mass matrices." *AIAA J.*, 13(2), 380.
- Haftka, R. T., Martinovic, Z. N., and Hallauer, W. (1985). "Enhanced vibration controllability by minor structural modifications." *AIAA J.*, 23, Aug., 1260-1266.
- Haftka, R. T., *et al.*, (1986). "Sensitivity of optimized control systems to minor structural modifications." *AIAA Paper No. 85-0801-CP*, presented at *AIAA/ASME/ASCE/ AHS 26th Structures, Structural Dynamics, and Materials Conference*, Orlando, Fl., Apr.
- Hale, A. L., Lisowski, R. J., and Dahl, W. L. (1985). "Optimal simultaneous structural and control design of maneuvering flexible spacecraft." *AIAA J. Guidance, Dynamics, and Control*, 8(1), 86-93.
- Hardy, G. H., Littlewood, J. E., and Pólya, G. (1934). *Inequalities*. Cambridge University Press.
- Haug, E. I., and Arora, J. S. (1979). *Applied optimal design - Mechanical and structural systems*. John Wiley & Sons, New York, NY.
- Heldenfels, R. R. (1973). "Automating the design process: progress, problems, prospects, potential." *AIAA, Paper 73-353*, March.
- Housner, G. W. (1959). "Behavior of structures during earthquake." *J. Engrg. Mech. Div., ASCE*, 85, 109-129.
- Housner, G. W., and Jennings, P. C. (1964). "Generation of artificial earthquake." *J. Engrg. Mech. Div., ASCE*, 90, EM1, 113-150.
- Housner, G. W., Soong, T. T., and Masri, S. F. (1994). "Second generation of active structural control in civil engineering." Position paper, *Proc. 1st World Conf. Struct. Control*, Los Angeles, CA, Aug. 3-5, Panel-3 - Panel-18.
- Humar, J. L. (1990). *Dynamics of structures*. Prentice Hall, Englewood Cliffs, New Jersey.
- Jennings, P. C., Housner, G. W., and Tsai, N. C. (1969). "Simulated earthquake motions for design purposes." *Proc. Fourth World Conf. Earthq. Engrg.*, 145-160.
- Johnson, E. H. (1976). "Disjoint design spaces in the optimization of harmonically excited structures." *AIAA J.*, 14(2), 259-261.

- Johnson, E. H., Rizzi, P., Ashley, H., and Segenreich, S. A. (1976). "Optimization of continuous one-dimensional structures under steady harmonic excitation." *AIAA J.*, 14(12), 1690-1698.
- Kasai, K., Munshi, J. A., Lai, M. L., and Maison, B. F. (1993). "Viscoelastic damper hysteretic model: Theory, experiment, and application." *ATC 17-1, Proc. Seminar on Seismic Isolation, Passive Energy Dissipation, and Active Control*, Applied Technology Council, San Francisco, CA., March 11-12, 521-532.
- Kelley, H. J. (1960). "The cutting plane method for solving complex programs." *SIAM J.*, 8, 703-712.
- Khot, N. S., Berke, L., and Venkayya, V. B. (1979). "Comparison of optimality criteria: algorithms for minimum weight design of structures." *AIAA J.*, 17(2), 182-190.
- Kirkpatrick, S., Gelatt, C. D. Jr., and Vecchi, M. P. (1983). "Optimization by simulated annealing." *Science*, 220(4598), 671-680.
- Kirsch, U., and Moses, F. (1977). "Optimization of structures with control forces and displacement." *Engrg. Optim.*, 3(1), 37-44.
- Kiusalaas, J. (1972). "Minimum weight design of structures via optimality criteria." *NASA TND-7115*.
- Kobori, T. (1994). "Future direction on research and development of seismic response controlled structure." Position paper, *Proc. 1st World Conf. Struct. Control*, Los Angeles, CA, Aug. 3-5, Panel-19 - Panel-31.
- Komkov, V. (1983). "Simultaneous control and optimization for elastic systems." *Proc. workshop applic. Distributed system theory control large space structures*, G. Rodriguez, ed., JPL Publication, 83-146, July.
- Lai, M. L., Chang, K. C., Soong, T. T., Hao, D. S., and Yeh, Y. C. (1995). "Full-scale viscoelastically damped steel frame." *J. Struct. Engrg., ASCE*, 121(10), 1443-1447.
- Lindberg, H. E. (1992 a). "An evaluation of convex modeling for multimode dynamic buckling." *J. Appl. Mech., ASME*, 59, 929-936.
- Lindberg, H. E. (1992 b). "Convex models for uncertain imperfection control in multimode dynamic buckling." *J. Appl. Mech., ASME*, 59, 937-945.
- Martin, C. R., and Soong, T. T. (1976). "Modal control of multistory structures." *J. Engrg. Mech. Div., Proc. ASCE*, 102, EM4., Aug., 613-623.

- Mills-Curran, W. C., and Schmit, L. A. (1985). "Structural optimization with dynamic behavior constraints." *AIAA J.*, 23(1), 132-138.
- MIT. (1976). *SIMQKE - A program for artificial motion generation user's manual and documentation*. Department of Civil Engineering, Massachusetts Institute of Technology.
- Nemhauser, G. L., and Wolsey, L. A. (1988). *Integer and combinatorial optimization*. John Wiley and Sons Ltd., New York, NY.
- Norris, C. H., Hansen R. J., Holley, M. J. Jr., Biggs, J. M., Namyet, S., and Minami, J. K. (1959). *Structural design for dynamic loads*. McGraw-Hill Book Company, Inc., New York.
- Pantelides, C. P. (1987). "Optimal design of seismic and wind structures with active controls." *Ph. D. Diss.*, Department of Civil Engineering, University of Missouri-Rolla, Rolla, MO.
- Pantelides, C. P. (1990). "Optimal design of active controlled structures." *Earthq. Engrg. Struct. Dyn.*, 19, 583-596.
- Pantelides, C. P. (1991). "Synthesis of lateral structural bracing with active tendons." *Mech. Computing in 1990's and Beyond*, ASCE, H. Adeli and R. L. Sierakowski, eds., 2, May, 766-770, Columbus, OH.
- Powell, G. H. (1993). "DRAIN-2DX: Element description and user guide for element type01, type02, type04, type06, type09, and type15." *Report No. UCB/SEMM-93/18*, Department of Civil Engineering, University of California, Berkeley, CA, Dec.
- Prager, W., and Marcal, P. (1971). "Optimality criteria in structural design." *AFFDL-TR-70-166*, May.
- Prakash, V., Powell, G. H., and Campbell, S. (1993). "DRAIN-2DX: Base program description and user guide." *Report No. UCB/SEMM-93/17*, Department of Civil Engineering, University of California, Berkeley, CA, Nov.
- Reinhorn, A. M., Soong, T. T., Lin, R. C., Riley, M. A., Wang, Y. P., Aizawa, S., and Higashino, M. (1992). "Active bracing system: A full scale implementation of active control." *Report No. NCEER-92-0020*, Aug. 14.
- Riley, M. A., Subramaniam, R., Nagarajaiah, S., and Reinhorn, A. M. (1993). "Hybrid control of sliding base isolated structures." *ATC 17-1, Proc. Seminar on Seismic Isolation, Passive Energy Dissipation, and Active Control*, Applied Technology Council, San Francisco, CA., March 11-12, 799-810.

- Sage, A. P. and White, C. C. III (1977). *Optimum systems control*. Prentice Hall, Englewood Cliff, NJ.
- Salama, M., Bruno, R., Chen, G-S., and Garba, J. (1988). "Optimal placement of excitations and sensors by simulated annealing." NASA/Air Force Symposium on Recent Experiences in Multidisciplinary Analysis and Optimization, Hampton, VA, Sept.
- Schmit, L. A. (1981). "Structural synthesis - Its genesis and development." *AIAA J.*, 19(10), 1249-1263.
- Shinozuka, M. (1970). "Maximum structural response to seismic excitations." *J. Engrg. Mech. Div., Proc. ASCE*, 96, EM5, 729-738.
- Soong, T. T. (1990). *Active structural control: theory and practice*. Longman Scientific and Technical, John Wiley and Sons, Inc., New York, NY.
- Soong, T. T., and Manolis, G. D. (1987). "Active structures." *J. Struct. Engrg., ASCE*, 113(11), 2290-2302.
- Soong, T. T., and Reinhorn, A. M. (1993). "Case studies of active control and implementation issues." *ATC 17-1, Proc. Seminar on Seismic Isolation, Passive Energy Dissipation, and Active Control*, Applied Technology Council, San Francisco, CA, 701-713.
- Soong, T. T., Reinhorn, A. M., Wang, Y. P., and Lin, R. C. (1991). "Full scale implementation of active control. I: Design and simulation." *J. Struct. Engrg., ASCE*, 117, 3516-3636.
- Taylor, J. (1969). "Optimal design of structural systems: an energy formulation." *AIAA J.*, 7, 1404-1406.
- Thomas, H. L., and Schmit, L. A. Jr. (1991). "Control-augmented structural synthesis with dynamic stability constraints." *AIAA J.*, 29(4), 619-626.
- Truman, K. Z., and Petruska, D. J. (1992). "Parametric optimal design of steel structures." *Proc. 10th World Conf. Earthquake Engrg.*, Madrid, Spain, 4453-4458.
- Tzan, S-R., and Pantelides, C. P. (1994). "Hybrid structural control using viscoelastic dampers and active control systems." *Earthq. Engrg. Struct. Dyn.*, 23(12), 1369-1388 (1994).
- Uang, C. M. (1988). "Use of energy as a design criterion in earthquake-resistant design." *Report No. UCB/EERC - 88/18*, Earthquake Engineering Research Center, U. of California, Berkeley, CA, Nov.

- UBC (1994), International Conference of Building Officials. *Uniform building code. Vol. 2*, Whittier, CA, 2.362.
- U. S. National Workshop on Structural Control Research (1990), G. W. Housner and S. F. Masri, eds., USC, Los Angeles, CA.
- Vanderplaats, G. N. (1984 a). "An efficient feasible directions algorithm for design synthesis." *AIAA J.*, 22(11), 1633-1640.
- Vanderplaats, G. N. (1984 b). *Numerical optimization techniques for engineering design: with applications*. McGraw Hill, New York, NY.
- Vanmarcke, E. H., Biggs, J. M., Frank, R., Gasparini, D., Gazetas, G., Arnold, P., and Luyties W. (1976). "Comparison of seismic analysis procedures for elastic multiple-degree system." *Research Report R76-5, Order No. 528*, Department of Civil Engineering, Constructed Facilities Division, Massachusetts Institute of Technology, Cambridge, Massachusetts.
- Venkayya, V. (1971). "Design of optimum structures." *J. Computers and Structures*, 1(1/2), 265-309.
- VMA Engineering. (1993). *Design optimization tools - DOT users manual*. Vanderplaats, Miura & Associates, Inc., Goleta, CA.
- Wang, C-K. (1986). *Structural analysis on microcomputers*. Macmillan Publishing Company, NY.
- Weaver, W. Jr. and Johnston, P. R. (1987). *Structural dynamics by finite elements*. Prentice-Hall, Inc., Englewood Cliffs, NJ.
- Wiesner, K. B. (1986). "Taming lively building." *Civil Engrg., ASCE*, 56(6), 54-57.
- Xia, C., Hanson, R. D., and Wight, J. K. (1990). "A study of ADAS element parameters and their influence on earthquake response of building structures." *Report No. ECS 8821735*, The University of Michigan, Ann Arbor, Michigan.
- Yamakawa, H. (1984). "Optimum structural designs for dynamic response." *New directions in optimum structural design*, A. Atrek, R. G. Gallagher, K. M. Kagsdell, and O. C. Zienkiewicz, eds., John Wiley & Sons Ltd., New York, NY, 249-266.
- Yang, J. N. (1982). "Control of tall buildings under earthquake excitation." *J. Engrg. Mech. Div., ASCE*, 108(EM5), 833-849.
- Yang, J. N., Akbarpour, A., and Ghaemmaghami, P. (1987). "New optimal control algorithms for structural control." *J. Engrg. Mech., ASCE*, 113(9), 1369-1386.

- Yang, J. N., Danielians, A., and Liu, S. C. (1991). "Aseismic hybrid control systems for building structures." *J. Engrg. Mech., ASCE*, 117(4), 836-753.
- Yang, J. N., Li, Z., and Liu, S. C. (1992 a). "Stable controllers for instantaneous optimal control." *J. Engrg. Mech., ASCE*, 118(8), 1612-1630.
- Yang, J. N., Li, Z., and Liu, S. C. (1992 b). "Control of hysteretic system using velocity and acceleration feedbacks." *J. Engrg. Mech., ASCE*, 118(11), Nov., 2227-2245.
- Yang, J. N., Li, Z., and Vongchavalitkul, S. (1993). "Nonlinear control of building using hybrid systems." *ATC 17-1, Proc. Seminar on Seismic Isolation, Passive Energy Dissipation, and Active Control*, Applied Technology Council, San Francisco, CA., March 11-12, 811-822.
- Yang, J. N., Long, F. X., and Wong, D. (1988). "Optimal control of nonlinear structures." *J. Appl. Mech., Trans., ASME*, 55, 931-938.
- Yang, J. N. and Samali, B. (1983). "Control of tall buildings in along-wind motion." *J. Struct. Engrg., ASCE*, 109(1), 50-68.
- Yao, J. T. P. (1972). "Concept of structural control." *J. Struct. Engrg., Div. ASCE*, 98, 1567-1564.
- Zangwill, W. I. (1969). *Nonlinear programming: a unified approach*. Prentice-Hall, Englewood Cliffs, N.J.
- Zhang, R. (1990). "Structural response control by additive viscoelastic dampers." Ph. D. Diss., State University of New York at Buffalo, NY.
- Zhang, R., Soong, T. T., and Mahmoodi, P. (1989). "Seismic response of steel frame structures with added viscoelastic dampers." *Earthq. Engrg. Struct. Dyn.*, 18, 389-396.
- Zhang, R., and Soong, T. T. (1992). "Seismic design of viscoelastic dampers for structural applications." *J. Struct. Engrg., ASCE*, 118(5), 1375-1392.
- Zoutendijk, G. (1960). *Methods of feasible directions*. Elsevier, Amsterdam, Netherlands.